Stability and Toxicity of Silver Nanomaterials

Bey Fen Leo

Submitted for the fulfilment of the degree of Doctor of Philosophy (PhD),

Imperial College London

DEPARTMENT OF MATERIALS

IMPERIAL COLLEGE LONDON

APRIL 2015

Author's Declaration

I hereby declare that I am the sole author of this thesis. The work was carried out in the Department of Materials, Imperial College London on my own, unless otherwise stated. Wherever contributions of others are involved, every effort is made to indicate this, with due reference to literature and acknowledgements of collaborative research and discussions.

Some of the results presented in this thesis have been published in the following publication:

Leo, B. F.; Chen, S.; Kyo, Y.; Herpoldt, K. L.; Terrill, N. J.; Dunlop, I. E.; McPhail, D. S.; Shaffer, M. S.; Schwander, S.; Gow, A.; Zhang, J. F.; Chung, K. F.; Tetley, T. D.; Porter, A. E.; Ryan, M. P., The Stability of Silver Nanoparticles in a Model of Pulmonary Surfactant. *Environmental Science & Technology* 2013, 47, 11232-11240.

The research work presented in this thesis was conducted under the guidance of Professor Mary Ryan, Dr. Alex Porter and Dr. David McPhail at Imperial College London.

Bey Fen Leo

March 2015

Declaration of Copyright

Abstract

Understanding the electrochemical stability or corrosion behaviour of metallic nanoparticles in aqueous environments is of central importance in the fields of catalysis, sensing and nano-electronics. The electrochemical stability of silver nanoparticles (AgNPs) was investigated as a function of applied potential, pH and particle size. The direct voltammetric measurements of the Ag oxidation potential indicate that the electrochemical stability of nanoparticles (NPs) is different from their bulk metal, suggesting that theoretically derived energy diagrams for a bulk material might not always be accurate for NPs. In order to understand interactions of nanomaterials (NMs) with biological systems, the cellular environment can be considered as an electrochemical cell, since metal ion release is a major pathway underlying their potential toxicity. NPs inhaled from the air into the deep lung first contact with the lung lining fluid where they have the potential to translocate into other organs like the brain, liver, spleen and heart *via* blood circulation. Here, this thesis specifically focuses on the impact of AgNMs on two major organs, the lung and brain.

AgNMs as potential occupational and environmental hazards may raise health and safety concerns. For this reason, there is a need to assess the interaction of NMs with biological systems for early prediction of their cytotoxicity. The stability of AgNPs in dipalmitoylphosphatidylcholine (DPPC), the major component of lung surfactant, was investigated as a function of pH. TEM images revealed that the AgNPs were coated with a DPPC layer serving as a semi-permeable layer, improving their dispersion and delaying ions release in the lung. Furthermore, these studies suggested that size, stability and chemical composition of NP have to be taken into account in the evaluation of NP cytotoxicity. These observations have important implications for predicting the potential reactivity of AgNPs in the lung and the environment.

In response to potential neurotoxicity, studies have shown that AgNPs can cross the blood brain barrier (BBB) *via* the systemic blood supply and then localise inside the brain, causing neurodegeneration, but much less is known about the distribution of AgNMs and their interaction with protein complexes inside the brain cells. Interaction of microglia with AgNMs, as well as their uptake,

cytotoxicity and processing inside cells were investigated. The findings demonstrate that Ag_2S formation acts as an ion trap for free Ag^+, significantly limiting short term toxicity effects with important consequences for the neuro safety of AgNMs. In order to manipulate particular NPs features with favourable bio-availability and bio-distribution, not only NP uptake into cells, but also a fundamental understanding of the NPs-protein complex is necessary.

Table of Contents

Acknowledgements

I would like to express my heartfelt gratitude to my supervisors, Professor Mary Ryan, Dr. Alexandra Porter and Dr. David McPhail, for their continued encouragement, suggestions and criticisms throughout my PhD. I am indebted to them for giving me a chance to work in such a wonderful environment surrounding with intelligent and passionate people. This thesis would never come to fruition without their guidance, mentorship, and their abundance of patience and unfailing support during the high tides of the work.

I would like to thank Dr. Sarah Fearn, Dr. Richard Chater, Dr. Mahmoud Ardakani and Dr. Ecaterina Ware who taught me experimental techniques and provided invaluable discussion in characterising my samples. I would like to extend my sincere thanks to my research groups - Dr. Shu Chen, Dr. Ong Zhan Yuin, Dr. Pakatip Ruenraroengsak, Dr. Angela Goode, Dr. Michal Klosowski, Dr. Catriona McGilvery and Mr. Ioannis Theodorou for their discussions and constructive comments in the *in vitro* research. Besides, the guidance and assistance in electrochemistry works that I have received from Dr. Geoff Nelson, Dr. Qi Jia Hui, Dr. Stephen Tay, Dr. Evgeniy Donchev and Ms. Emily Brooke are highly appreciated. The support and friendship of my entire research group's members have contributed to a most enjoyable working environment in the Imperial College London (ICL) – all of them are the wonderful scientists who make science a fun thing to explore.

During my PhD study, thanks to my supervisors for providing me an excellent experience by working in different projects leading to collaborative opportunities, which were extremely productive. A special acknowledgement goes to Prof. Milo Shaffer, Prof. Terry Tetley, Prof. Fan Chung, Prof. David Dexter, Dr. David Payne, Dr. Daniel Gonzalez, Dr. Mark Perry, Dr. Sinbad Sweeney and Dr. Joanna Seiffert for providing me the chance to work with the talented researchers, who have varied backgrounds and interests. That allows me to learn new things and deal with fascinating and complex interdisciplinary problems in my research.

I would like to express my sincere appreciation to my best friends, Dr. Romi Korotana and Dr. Monica Patel who laughed and cried with me throughout my best and worst time in my life. I owe a great deal of gratitude to my past mentors and

supervisors who always inspiring me not only on my research, but also on many aspect of my life. I am truly grateful to Assoc. Prof. Mohd Rafie Johan, Assoc. Prof. Tony Centony, Prof. Mohd Hamdi, Dr. Phuah Chin, Dr. Basma Othman, Dr. Jing Pang and Mr. Bob.

Most importantly, my family has been an incredible support to me throughout my PhD studies and my entire life. I can't express how grateful I am to have my parents and sisters who always by my side to comfort me when I experience low. Their deepest loves and understanding encourage me to achieve my life goals, no matter how much obstacles I might be facing in the future. Thank you, Travis for his boundless faith in me and his calming presence while listening to my problems. His unconditional love and understanding have supported me, in person and in spirit.

Lastly, thank you to all my family, colleagues and friends who have been so kind and supportive throughout my PhD. Thank you for all the given inspiration and encouragement that has shaped me to grow into a better person for my future careers.

Publications

1. **Leo, B. F.**; Chen, S.; Kyo, Y.; Herpoldt, K. L.; Terrill, N. J.; Dunlop, I. E.; McPhail, D. S.; Shaffer, M. S.; Schwander, S.; Gow, A.; Zhang, J. F.; Chung, K. F.; Tetley, T. D.; Porter, A. E.; Ryan, M. P., The Stability of Silver Nanoparticles in a Model of Pulmonary Surfactant. *Environmental Science & Technology* 2013, 47, 11232-11240.

2. Mukherjee, D., **Leo, B.F.**, Royce, S.G., Porter, A.E., Ryan, M.P., Schwander, S., Chung, K.F., Tetley, T.D., Zhang, J., Georgopoulos, P.G., Modeling Physicochemical Interactions Affecting In Vitro Cellular Dosimetry of Engineered Nanomaterials: Application to Nanosilver. J. Nanopart. Res. 2014, 16, 2616.

3. Seiffert, J., Hussain, F., Wiegman, C., Li, F., **Leo, B.F.**, Baker, W., Porter, A., Ryan, M., Chang, Y., Gow, A., Zhang, J., Tetley, T., Chung, K.F., Pulmonary Toxicity of Instilled Silver Nanospheres: Influence of Size, Coating and Rat Strain. PLOS ONE. 2015, PONE-D-14-26669R1.

4. Botelho, D., **Leo, B.F.**, Massa, C., Sarkar, S., Tetley, T., Chung, K.F., Chen,S., Ryan, M., Porter, A., Zhang, J., Schwander, S., Gow, A., Low Dose AgNPs Reduce Lung Mechanical Function and Innate Immune Defense in the Absence of Cellular Toxicity. Nanotoxicology. 2015, TNAN-2014-0286.R2.

5. **Leo, B.F.**, Gonzalez, C.D., Ruenraroengsak, P., Chen, S., Theodorou, I.G., McPhail, D.S., Shaffer, M. S., Ryan, M.P., Porter, A. E., Neurotoxicology: Microglia Response to Silver Nanomaterials and Their Interaction with Enzymes in the Central Nervous System. (Submitted to journal)

6. Sarkar, S., **Leo, B.F.,** Chen, S., Santiago, C. R., Porter, A.E., Ryan, M.P., Gow, A., Chung, K.F., Tetley, T.D., Zhang, J., Georgopoulos, P.G., Strickland, P.A., Schwamder, S. Modulation of Human Antimycobacterial Immune Responses by Silver Nanoparticles. (*Submitted to journal*)

7. Heras, M.L., Theodorou, I.G., **Leo, B.F**., Ryan, M.P., Porter, A.E., Towards Understanding the Antibacteria Activity of Ag Nanoparticles: Analysis of the materials-biology interface in the pathologic lung. (*Submitted to journal*)

8. Sweeney, S., **Leo, B.F**., Chen, S., Thomas, N.A., Zambianchi, M., Thorley, A.J., Gow, A., Schwander, S., Zhang, J., Shaffer, M.S., Chung, K.F., Ryan, M.P., Porter, A.E., Tetley, T., Pulmonary Surfactant Mitigates Silver Nanoparticle Toxicity in Human Alveolar Type-I Epithelial Cells. (*Submitted to journal*)

9. **Leo, B. F.,** Nelson, G.W., Brooke, E. R., McPhail, D.S., Porter, A.E., Payne, D.J., Ryan, M.P., Size-Dependent Electrochemical Stability of Silver Nanoparticles. (*In preparation*)

10. **Leo, B. F.,** Ruenraroengsak, P., Fearn, S., Chater, R. J., Chen, S., Goode, A., Gonzalez, C.D., Shaffer, M. S., McPhail, D.S., Porter, A. E., Ryan, M.P., A Comparative Study of Imaging Techniques on the Cellular Uptake of Silver Nanomaterials. (*In preparation*)

List of Tables

List of Figures

List of Appendices

List of Abbreviation

AgNPs	Silver Nanoparticles
AgNWs	Silver Nanowires
AVG	Average
BDD	Boron - doped Diamond
BF-TEM	Bright - field Transmission Electron Microscopy
BSA	Bovine Serum Albumin
CBS	Cystathionine - β - synthase
CNS	Central Nervous System
CSE	Cystathionine Gamma-lyase
CV	Cyclic voltammetry
DCCM	Dendritic Cells Culture Medium
DCFH-DA	Dichlorofluorescin - Diacetate
DMEM	Dulbecco's Modified Eagle Medium
DPPC	Dipalmitoylphosphatidylcholine
EDX	Energy Dispersive X - ray spectroscopy
EELS	Electron Energy Loss Spectroscopy
ENMs	Engineered Nanomaterials
FEG	Field Emission Gun
FIB	Focused Ion Beam
HAADF-STEM	High Angle Annular Dark Filed - Scanning Transmission Electron Microscopy
ICP - MS	Inductively Coupled Plasma - Mass spectroscopy
ICP - OES	Inductively Coupled Plasma - Optical Emission spectroscopy
IL - 6	Interleukin - 6
LDH	Lactate dehydrogenase
LLF	Lung Lining Fluid

MPST	3 - Mercaptopyruvate Sulfurtransferase
MT	Metallothionine
NHE	National Health Executive
NIOSH	National Institute for Occupational Safety and Health
NMs	Nanomaterials
PVDF	Polyvinylidene fluoride
PVP	Polyvinylpyrrolidone
ROS	Reactive oxygen species
SAED	selected area electron diffraction
SAXS	Small Angle X-ray Scattering
SEM	Scanning Electron Microscopy
SF - RPMI	Serum Free - Roswell Park Memorial Institute medium
TNFα	Tumor necrosis factor alpha
TOF-SIMS	Time - of - Flight Secondary Ion Mass Spectrometry
UV - vis	Ultraviolet-visible spectroscopy
XPS	X - ray Photoelectron Spectroscopy
XRD	X - ray powder diffraction

1.0 Introduction

The worldwide commercial nanotechnology market is predicted to increase tremendously and reach $ 1 trillion by 2015[1]. Currently, silver nanoparticles (AgNPs) are one of the types of nanomaterial that are under the most scrutiny. They are becoming increasingly popular due to their unique physical and chemical properties compared to their bulk analogues. Since NPs have been widely used in various applications in electroanalysis, understanding their corrosion behaviour in aqueous environments is vital to retain their useful properties in long-term applications.

Stability against oxidation, or loss of effective surface area of a particular metal in a specific environment, can be predicted from an E_H-pH diagram, also known as a Pourbaix diagram[2]. Marcel Pourbaix produced a series of E_H-pH diagrams of metal elements and published the 'Atlas of Electrochemical Equilibria', first in French in 1963 and then in an English translation version in 1966. Pourbaix diagrams are thermodynamic charts constructed using the Nernst equation, predicting conditions under which corrosion can be prevented by adjusting the potential/pH. Thus, these diagrams are extensively used for materials selection or corrosion control in the fields of fuel cells, batteries, electroplating and corrosion engineering. However, due to the fact that NPs are between a free diffusion atom and a bulk metal, the electrochemical stability of these metallic NPs may act differently from their bulk analogues[3, 4]. Therefore, the outstanding behaviour of NMs may go beyond the scope of conventional thermodynamic theories.

Fundamental understanding of nano-thermodynamics not only offers us the opportunity to tune NMs intrinsic physical properties, but also to provide information that goes beyond the expectation and description of the classical approaches. For instance, scientists or engineers may extend the suitability range of the classic thermodynamic theory by considering the size dependence physical and chemical properties of surfaces in the NMs-related theoretical calculation. For the case of Pourbaix diagram for NMs, it is necessary to understand the size dependence of the electrochemical stability of NPs as a function of pH and potential in order to choose the right conditions for their practical applications. Also it will be of paramount importance to predict their long term persistence behaviour and assess their safety in different environmental conditions.

The advantages of nanoparticles, such as the increased solubility of nanosuspensions and their low production costs have resulted in their rapid commercialisation for medical applications (*e.g*. drug delivery)[5]. The increasing use and manufacture of engineered nanomaterials (ENMs) in biosensing, clothing, sunscreen, paint, cosmetics and medical device applications raise concerns regarding their safety for human health and the environment[6, 7]. Inhalation of high levels of nanoparticles in air pollution has been associated with pulmonary and neurological toxicity[8, 9]. Occupational and environmental hazards of NPs must be assessed before their production is spread more widely. Understanding the interactions between living cells and nanomaterials (NMs) or how NMs are processed by cells also guides the development of diagnostics and medicine.

Several studies have identified the potential cytotoxicity of AgNMs in different biological systems, such as fungi, bacteria and mammalian cells. Their cytotoxicity has been attributed to different possible mechanisms, including generation of reactive oxygen species (ROS), damage to cell-membrane integrity, proteins and DNA[10, 11]. The toxicity mechanism of NPs can be related to the physicochemical properties of NPs, such as surface area, shape, surface charge, capping agent and particle purity[12, 13]. These properties might affect the ion release rate from NPs and the intracellular production of ROS, which are predictors for the toxicity of NPs[14]. Upon dispersion in biological media, NPs do not behave as an inert particle or as soluble molecules but they can either agglomerate or even aggregate, altering the particle size and the available surface area[15, 16]. Moreover, experimental parameters such as ionic strength or pH of buffer media and the presence of plasma proteins may further modify NMs properties, leading to inaccurate assessment of NPs toxicity if compared to *in-vivo* response.

Although no clear consensus has yet been reached on the entry pathways for nanoparticles into cells, it has been suggested that nanoparticle-cell interactions are associated with the protein coating or 'corona' on the surface of the NPs[17]. When NPs are suspended in biological media (*e.g.* lung lining fluid (LLF), blood plasma and cerebrospinal fluid), they are known to be coated by proteins or associated with biomolecules which may decrease their surface energy and also affect their colloidal stability in the suspension media[18]. Evidence has suggested that AgNPs lead to

neuroinflammation, however much less is known about their interaction with proteins which may modify their neurotoxicity by changing the surface chemistry of the AgNMs[19, 20]. Furthermore, the interaction of AgNMs with sulphide species, including hydrogen sulphide gas (H_2S), sulphide (S^{2-}) and HS^-, form very stable Ag_2S due to its extremely low solubility (k_{sp}= 5.92 x 10^{-51}) and could act as a potential detoxification mechanism[21]. So far, most of the toxicity studies performed on AgNMs have overlooked their possible sulfidation reaction, how they are processed by, and transformed, inside cells or cytotoxicity assays. This knowledge will shed light on how protein/NP/sulfide species interactions affect the cellular response, becoming a key element for interpreting experimental results accurately.

1.1 Research Objectives

The main aim of this study is to investigate the stability of AgNMs and their *in vitro* toxicity in biologically relevant environments. The specific objectives of this project are:

I. To assess the electrochemical stability of AgNPs as a function of applied potential, pH and particle size and compare the experimental studies with thermodynamic calculations.
II. To study the effect of pH, particle size and surface chemistry on the stability of AgNPs and their interaction with lung lining fluid (DPPC).
III. To assess how DPPC disperses the AgNPs and how this may impact their bio-availability and lung function under varying pH conditions.
IV. To investigate the response of microglia cells to silver nanomaterials (AgNMs) of two morphologies (spheres and wires), as well as their cytotoxicity and uptake in brain cells.
V. To assess the activation of H_2S producing enzymes through interactions with AgNMs and investigate the transformation of these materials which may affect their impact on human physiology and short-term toxicity in brain cells.

1.2 Organisation of Thesis

This thesis is organised in seven chapters. *Chapter 2 Literature Review* discusses literature related to this project. *Chapters 3 to 6* describe the experimental techniques used in the thesis and the results of the project. The results of the electrochemical

stability of silver nanoparticles (AgNPs) as a function of applied potential, pH and particle size are presented in *chapter 3*. The effect of size and surface functionalization on the stability of AgNPs and their interactions with dipalmitoylphosphatidylcholine (DPPC), the main component of pulmonary surfactant, is described in *chapter 4*. *Chapter 5* presents the results from the studies on microglial uptake of AgNMs (particles and wires) and their transformation inside the brain cells. *Chapter 6 Conclusions and Future work* highlights the key contributions of this research work to the field and proposes some ideas for future experiments. *Chapter 7.0 References* outlines a list of references used in the thesis chapter sections.

2.0 Literature Review

2.1 Nanotechnology: An Overview

The terminology 'nano' originates from the Greek word meaning '*dwarf*'. It represents one billionth (10^{-9}) of a metre, which is as tiny as length of ten hydrogen atoms. Physicist Richard Feynman promoted the concepts of nanotechnology with a talk entitled "There's Plenty of Room at the Bottom" at an American Physical Society meeting at the California Institute of Technology on 29th December 1959[22]. He described "a technological vision of extreme miniaturization" and invited researchers to explore this relatively new scientific field[23]. The terminology 'nanotechnology' was first used by Professor Norio Taniguchi in a 1974 conference paper, "On the Basic Concept of 'Nanotechnology"[24] to describe precision engineering with tolerances of a micron or less[25]. Dr. K Eric Drexler developed the concept and the technological significance of nano-scale phenomena further[26].

Nanotechnology began taking off in the 1980s with three major discoveries, the invention of the scanning tunnelling microscope (STM) in 1981 and fullerenes in 1985[27], as well as carbon nanotubes (CNTs) in 1991[28]. In the 2000s, this field of research invited growing interest and spurred on many industries to commercialise consumer products containing nano-materials. Recent reports suggest that the nanotechnology industry will become a one-trillion-dollar market by 2015 and the silver nanoparticles (AgNPs) domain is the most commercialised nanomaterials by far[29].

2.1.1 Silver Nanomaterials: Sources and Toxicity

Engineered silver nanomaterials (AgNMs) are of great scientific interest due to their remarkable properties, including their excellent electrical and thermal conductivity, as well as their unique optical and antimicrobial properties[30-34]. However, due to the large production volume of manufactured AgNPs, in particular in airborne products (*e.g.* disinfectant sprays) and a wide variety of consumer products (*e.g.* water purification, air filters, nanoAg textiles[35], toothpaste and deodorants), Ag may be released into the environment either as soluble ions, nanoparticles (NPs) or NPs aggregates, during handling, washing, disposal or abrasion[7]. Since AgNPs are prevalent in consumer products, these release routes

raise concerns about the potential toxic effects of AgNPs to the environment and human health[36].

Many recent publications have shown that AgNMs are toxic to bacteria, cause the development of deformities in zebra fish, inflammatory response in rats, neurotoxicity in mice and cytotoxicity to human lung cells[37-39]. For over a decade, researchers have debated the main mechanism of AgNPs toxicity, *i.e.* whether the toxicity is due to the direct particle-specific biological effects or due to the release of Ag^+ ionic species or the combination of these effects. AgNPs have high surface energies, given the increase in their surface area per unit volume as their particle size decreases. In specific environmental conditions, Ag can be oxidized and dissolved to release Ag^+ ions, which are considered the main active and reactive species[40]. For instance, Zong *et al.* reported that the toxicity or antimicrobial activity of AgNPs can be solely attributed to an Ag^+ ion dose dependent response and that no direct particle-specific effects were observed[41]. Nevertheless, some studies have shown that AgNPs exerted higher toxic effects to the organism than the Ag^+ ions released from the corresponding AgNPs in the extracellular media[42-44]. Taglietti *et al.* pointed out that two different processes need to be considered as a "long distance mechanism" *i.e.* the release of Ag^+ ions from the NPs and a ''short-distance mechanism'', involving the nanomechanical action of a particle on the bacterial membrane[45]. The "short distance" effect arises when particles close to the bacterial surfaces, which have an acidic pH and oxidising environment, facilitating AgNPs dissolution and release of Ag^+ ions[46].

Recent studies have provided a new insight into the important role of the particle-cell interface in the antibacterial action of AgNPs. A synergistic effect between AgNPs and Ag^+ ions is required where the AgNPs can deliver a localised ionic dose to the cell and enhance the amount of internalised Ag^+ ions released from the particle surface[46, 47]. Olesja *et al.*[48] and Gliga *et al.*[37] demonstrated that 'Ag- ion' and 'particle-specific' mechanisms are not competing but that they are synergistic. They suggested cellular uptake of Ag was significantly higher when cells were exposed to NPs rather than ions. AgNPs facilitate Ag^+ uptake *via* endocytosis or a 'Trojan horse' mechanism, which increases the intracellular bioavailability of Ag. Moreover, a direct contact between the bacterial cell and AgNPs have been shown to enhance the toxicity of AgNPs against bacterial strains due to the increased

dissolution of Ag^+ ions, which could be driven by the proton motive force of the bacterial membrane that decreases the local pH to as low as 3[47]. The findings provided by the literatures show the importance of membrane interactions of AgNPs, as they translocate across, and become internalised, directly through the cytoplasm or inside vesicles, leading to high local concentrations of Ag^+ ions inside the cells.

2.1.2 Effect of Physicochemical Properties on AgNP Toxicity

To date, some studies have demonstrated that the physicochemical properties of AgNPs (*e.g.* size, shape, surface functionalisation, surface charge, Ag ions released and solution chemistry) could play pivotal roles in affecting the toxicity of AgNPs to organisms. Recently, Liu and Hart have shown that the dissolution of AgNPs is a cooperative oxidation that involves both protons (H^+) and dissolved oxygen (O_2) [49]. In addition, Zhang *et al*.[50] developed a kinetic model to describe Ag^+ release, based on the hard sphere theory using the Arrhenius equation. The authors showed that Ag^+ ions release rates depended not only on the primary particle size, but also on their concentration and environmental factors (*e.g.* dissolved oxygen and pH).

It is well known that AgNPs can be oxidised in the medium exposure to air by reaction with dissolved O_2 and mediated by H^+ as shown in the reaction below:

$$\mathrm{Ag(s)} + \frac{1}{2} O_{2(aq)} + 2H^+_{(aq)} \leftrightarrow Ag^+_{(aq)} + H_2O_{(l)} \qquad (2.1)$$

AgNPs can be assumed as soluble reactants due to their small size and the oxidation reaction can be expressed by first-order reaction kinetics. Using the Arrhenius equation, $(\frac{dm}{dt})_{Ag}$ can be described as follows [50]:

$$(\frac{dm}{dt})_{Ag} = k\,[AgNPs]\,[O_2]^{1/2}[H^+]^2 \qquad (2.2)$$

$$k = A \exp(\frac{-E_a}{RT}) \qquad (2.3)$$

$$(\frac{dm}{dt})_{Ag} = A \exp(\frac{-E_a}{RT})\,[AgNPs]\,[O_2]^{1/2}[H^+]^2 \qquad (2.4)$$

where $(\frac{dm}{dt})_{Ag}$ is the Ag^+ release rate (mol/L.h); k is the reaction rate constant (mol/h); [AgNP] , [O], $[H^+]$ are the molar concentrations (mol/L) of AgNPs, dissolved

oxygen and protons, respectively; E is the activation energy (J); T is temperature (298 K); and A is the frequency factor.

The molar concentration of AgNPs ([AgNPs]) can be replaced by the mass-based concentration ([Ag]):

$$[\text{AgNPs}] = \frac{[Ag]}{N_A \rho \frac{4}{3}\pi r^3} \quad (2.5)$$

where ρ is the density of AgNPs (~ 10.5 g/cm^3), r is the AgNPs radius (nm) and N_A is the Avogadro constant (~6.023x10^{23} mol^{-1}).

$$(\frac{dm}{dt})_{Ag} = A \exp(\frac{-E}{RT}) \frac{[Ag]}{N_A \rho \frac{4}{3}\pi r^3} [O_2]^{1/2}[H^+]^2 \quad (2.6)$$

Equation (2.6) reveals that $(\frac{dm}{dt})_{Ag}$ increases with increasing [Ag], $[O_2]$, or $[H^+]$ and is inversely proportional to the radius of AgNPs. Furthermore, an increase of temperature could significantly increase $(\frac{dm}{dt})_{Ag}$.

These equations show that factors such as ionic strength and composition of the dispersion medium[51, 52], pH[44, 53], dissolved organic matter[54], relative humidity[55], dissolved oxygen concentration[14] and temperature[56], can lead to alterations in the NPs properties and dissolution rates. Therefore, stability assays can be used to relate the physicochemical properties of AgNPs to Ag^+ ion release and consequently, to predict their toxicology[57, 58]. Therefore, it is of great importance to understand and predict how AgNPs behave in the environment and to understand the thermodynamics driving their dissolution, which is related to the physicochemical properties of AgNPs (*e.g.* varying size, coating and surface properties) and environmental conditions (such as dissolved oxygen and pH). Further research is needed to understand the exact physicochemical properties and cellular mechanism underlying the induced toxicity and how they can be exploited to design safe NMs or therapeutic AgNPs.

2.1.3 Importance of Materials Characterisation

Characterisation of the physicochemical properties of AgNPs in *in vivo* and *in vitro* studies at the point of exposure is paramount in order to draw conclusions on their biological activity accurately. Inductively coupled plasma sources (ICP-OES and

ICP-MS) and atomic absorption spectroscopy (AAS) techniques are generally used to correlate the dissolution rate of AgNPs with their toxicity profiles. There are some discrepancies in the toxicity data provided by different authors, probably due to the use of inconsistent methodologies, an improper NPs characterisation or the lack of dose response considerations in *in vitro* systems. Table 2.1 shows a wide variety of experimental setups and analytical methodologies employed in *in vitro* studies, in order to quantify the amount of Ag^+ ions released from NPs. This might explain, to some extent, why inconsistent dissolution rates are observed even the same types of AgNPs are used. For example, in the case of 10 nm citrate-AgNPs, the % dissolution of Ag provided by UV-vis absorption spectroscopy and AAS (which required a previous centrifugation step) were very different. These small size of NPs could not be effectively separated from solution using centrifugation and the values obtained by AAS were anomalously high[46].

My research group has recently suggested the limitation of using ICP-OES to analyse Ag^+ ions dissolution in cell culture media[59]. This study demonstrated that Ag^+ ions act differently from other metal ions (*e.g.* Zn and Fe) and are likely to bind with complex protein thiol groups or ligands in the medium such as Cl^-, PO_4^{3-}, S^{2-} and SO_4^{2-}, and to form insoluble silver compounds, *e.g.* silver oxide and silver chloride (Fig. 2.1 A,B). These compounds would reduce the bioavailability of released silver ions to a greater extent than that of AgNPs. This could confound the interpretation of Ag^+ ion released rate *via* ICP studies. We compared the percentage of free Ag^+ ion that can be measured when $AgNO_3$ is added in DI water to different culture media (RPMI, DMEM and DCCM), as shown in Fig. 2.1C. Although 100 % of Ag^+ ions were measured by ICP-OES in DI-water, the recovery of ionic Ag was less than 5 % in cell media.

The same study also investigated how different sources of sulphur in the cellular environment can lead to transformations of the surface chemistry of AgNWs, using a set of spatially resolved analytical TEM techniques. The formation of silver sulphide (Ag_2S) crystals on the surface of AgNWs within 1 h of incubation in DCCM-1 was easily identified by high resolution TEM (Fig. 2.1D, E). Nevertheless, the incubation of AgNWs in RPMI-1640 or DMEM did not lead to sulfidation. These findings highlight the need to consider the effects of cell culture media in the analysis of

toxicity assays, as well as the potential of high resolution analytical TEM in detecting insoluble Ag species, in contrast to ICP-OES[59].

In the *in vitro* studies, non-interacting perchlorate buffer solutions are used when examining the dissolution rates of Ag, with an understanding that significant sequestering of free Ag^+ ion will occur in the *in vivo* environment. Prior to the ICP analysis, 2 kDa filter tubes (Sartorius Stedim VIVACON 500) were used to filter NPs < 20 nm from the supernatant. Whereas, 10kDa filter tubes (Milipore) were applied to separate NPs < 50 nm from the solutions. In the study, ICP-OES (Thermo Scientific ThermoFlex-900) was chosen to study dissolution of NPs as a function of pH due to the machine availability and also its higher sensitivity and detection limits compared to the AAS.

Determining the fundamental physicochemical properties of AgNPs in biological systems will be vital to understanding their bioreactivity and antibacterial activity. When performing biological assays, it is necessary to study the oxidation kinetics of AgNPs under the same biological conditions employed in the assay. To achieve this, standardized protocols need to be developed, that combine different techniques including high resolution imaging, ICP and UV-vis. There is also an urgent need to develop methods to quantify the oxidation rates of AgNPs inside cells since the effects induced by either AgNPs or Ag^+ ions is difficult to distinguish. This is because NPs dissolution may occur in the extracellular medium before uptake or intracellularly following ingestion. Thus, the development of a sensitive and selective colorimetric Ag^+ detection method could provide fundamental insight into the mechanism of AgNPs toxicity by deconvoluting the effects of particles and Ag^+ ions.

Table 2.1: Dissolution studies on Ag^+ ions release performed using different experimental conditions and methodologies.

Type of AgNPs	Experimental Setup	Analytical Methodology and Analysis Technique	Released Ag^+ ions	Reference
10.5 ± 4.3 nm PVP-AgNPs	10 µg/ml of AgNPs incubated in test media (half-strength NaCl-free lysogeny broth (LB)) for 4 h at 30°C [pH 7]	Ultracentrifugation (1 h at 390,000 g) AAS	4.4 %	[47]
14 ± 1.6 nm Citrate-AgNPs	25 µg/ml of AgNPs incubated in non-interacting perchlorate (ClO_4) buffer solutions for 336 h [pH 5]	Ultrafiltration through 2 kDa filter membranes (13,000 rpm) ICP-OES	~2 %	[60]
20 nm Citrate-AgNPs	300 µg/ml of AgNPs incubated in quarter-strength Hoagland media for 24 h and 336 h (Contains S^{2-}; pH 5.7)	Ultrafiltration through 3 kDa filter membranes (40 min at 5000 g) ICP-MS	17 % (24 h) 40%(336 h)	[50]
20 nm Citrate-AgNPs	12.5 µg/ml of AgNPs incubated in BEGM cell media for 24 h at 37°C	Centrifugation (1 h at 15,000 rpm) ICP-OES	~4.3 %	[61]
40 nm Citrate-AgNPs	10 µg/ml of AgNPs incubated in BEGM cell media at pH 4.5 for 24 h at 37°C	Centrifugation (1 h at 15,000 rpm) AAS	~7 %	[37]
PVP-AgNWs 129±74 nm in diameter and a bimodal length of 2.8± 2.4 µm and 7.0±2.0 µm	10 µg/ml of AgNPs incubated in DMEM, RPMI1640 and DCCM-1[contains S] cell media for 168 h at 37°C	Ultrafiltration through 2 KDa filter membranes (13,000 rpm) ICP-OES	n.q.	[59]
10 nm Citrate-AgNPs	12.5 µg/ml of AgNPs incubated in bacterial growth media(Luria-Bertani, LB, Lennox) for 24 h at 37°C [contains NaCl; pH 4.5]	UV-vis Centrifugation (1 h at 21,000 g) AAS	3.5% (DI water) 7% (bacterial growth media) 16.1% (DI water) 26% (bacterial growth media)	[46]

n.q.: not quantified
ICP-MS: Inductively coupled plasma mass spectrometry
ICP-OES: Inductively coupled plasma optical emission spectroscopy
AAS: Atomic absorption spectroscopy

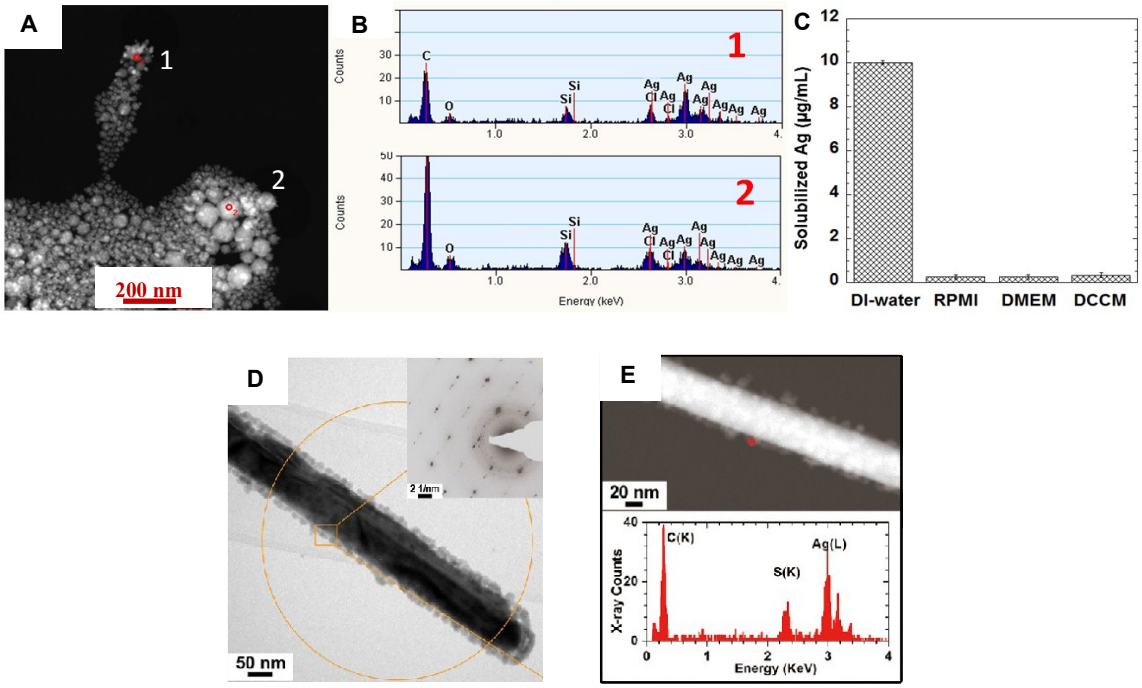

Fig. 2.1: (A) HAADF-STEM image of precipitates formed after the incubation of 17.0 µg/mL $AgNO_3$ in RPMI-1640 at 37˚C for 0.5 h. (B) The corresponding STEM-EDX spectra 1-2 were collected from area 1-2 marked in A. (C) ICP-OES analysis of solubilized silver concentrations of 17.0 µg/mL $AgNO_3$ in different cell culture media, incubated at 37˚C for 0.5 h (n = 3). Physicochemical characterization of AgNWs incubated for 6 h at 37˚C in small molecule solutes and salts extracted from DCCM-1 (D, E). A representative BF-TEM image of the AgNWs. The inset is a SAED pattern obtained from the circled area (aperture size ~550 nm) (D). HAADF-STEM image obtained from the same area marked in D (E). EDX spectrum collected from the edge of the nanowire[59].

2.1.4 Fundamental Thermodynamics of Corrosion

Corrosion is generally defined as the deterioration of metals or the release of metal ions when they react with their environment. For decades, there has been considerable interest in understanding the electrochemical stability or corrosion behaviour of metallic nanoparticles (NPs) and how this behaviour is different from their bulk analogues. Early works on the size-dependent electrochemical oxidation of metal NPs (*e.g.* the theoretical calculations of Henglein[62] and Plieth[4]) have shown that the standard electrode potential (E°) is size dependent and tends to shift to more negative values as the size of particles decrease. According to Henglein[62],

$$Ag_n \longleftrightarrow Ag_{n-1} + Ag^+ + e^- \quad (2.7)$$

the standard electrode potential for a free single silver atom (n = 1) is -1.8 V and the standard electrode potential of silver trimer (n = 3) is predicted to be - 1.0 V versus a normal hydrogen electrode (NHE), which are shifted negatively when compared to the standard electrode potential of bulk silver (n = ∞) of - 0.799V vs. NHE. This implies that AgNPs could act as stronger oxidising agents than zinc metal, which has standard electrode potential of + 0.76 V vs. NHE.

2.1.3.1 The Redox Potential of Small Metal Cluster on Surfaces

In the following section, the thermodynamic theory behind the redox potential of metal particles shifts negatively with decreasing particle size is explained.

Let us consider an electrochemical cell consisting of two half-cells, one with metal in its bulk state (Me_b) and the other with metal in its dispersed state (Me_d). In order to obtain the equation for the redox potential of metal clusters, the equation can be described as followed [4]:

Half Cells: $$Me_b \rightarrow Me^{z+}{}_{solv} + ze^- \quad (2.8)$$

$$Me^{z+}{}_{solv} + ze^- \rightarrow Me_d \quad (2.9)$$

Overall: $$Me_b \rightarrow Me_d \quad (2.10)$$

where z is the number of electrons and $Me^{z+}{}_{solv}$ is metal cations in the liquid phase.

The overall reaction is the transfer of one mole of bulk metal into its dispersed form. Then, the voltage of the electrochemical cell, $\Delta\varepsilon_D$, can be calculated from the overall Gibbs free energy of the dispersion process, ΔG_D, which is equal to the difference between the free energy of the dispersed species, G_d and free energy of the bulk, G_b, in J mol^{-1}.

$$\Delta G_D = G_d - G_b \quad (2.11)$$

$$\Delta\varepsilon_D = \varepsilon_d - \varepsilon_b = \Delta G_D / zF \quad (2.12)$$

where $\Delta\varepsilon_D$ is the difference in equilibrium oxidation potentials between the dispersed, ε_d and the bulk metal, ε_b in volts.

The change of free energy, ΔG_D can be determined in terms of the change in free energy associated with the change in surface area. Considering the formation of 2D metal clusters on surfaces, the change of free energy is given by the following expression[4]:

$$dG = \delta \, dl \tag{2.13}$$

where δ is the boundary free energy in J $mol^{-1}cm^{-1}$ and l is the boundary length of the two dimensional clusters in cm. Assuming two dimensional clusters are disk - shaped, a change in boundary length of the cluster, dl is related to a change in the differential of the number of moles of metal present as clusters, dn by the relationship:

$$dl = \left(A_M / r\right) dn \tag{2.14}$$

where A_M is the molar area of the cluster forming atoms and r is the mean radius of the cluster disk on the surface.

Substituting equation 2.14 into equation 2.13 and integrating between n = 0 and n = 1 gives the change of free energy, which can be inserted into equation 2.12 to obtain an expression for the redox potential.

$$\Delta\varepsilon_D = \varepsilon_d - \varepsilon_b = -\frac{\delta A_M}{zF}\frac{1}{r} \tag{2.15}$$

Then, the redox potential of metal nanoparticles is predicted to become more positive as the particles grow. If the surface free energy, δ is assumed to be the same for both the small metal particles and the bulk metal surfaces, then the equation (2.15) predicts that the redox potential of the nanoparticles is shifted negatively from the redox potential of the bulk metal[63].

For the electrochemical stability of metal NPs, Ng *et al.* [63] have carried out the first experimental work to test a theoretical prediction made by Plieth and Henglein, who proposed the decreasing stability of NPs with particle sizes. However, the authors observed that the obtained experimental result was different from Plieth and Henglein's theoretical calculations. Fig. 2.2 illustrates that the unexpected persistent behaviour of AgNPs on the highly oriented pyrolytic graphite (HOPG) electrode

surface and their dissolution required more than an hour at an applied potential of +500 mV vs Ag/AgCl. Their analysis showed that a sharp decrease in the oxidation rate was observed when silver particles were reduced in diameter to 0.4 nm - 1 nm.

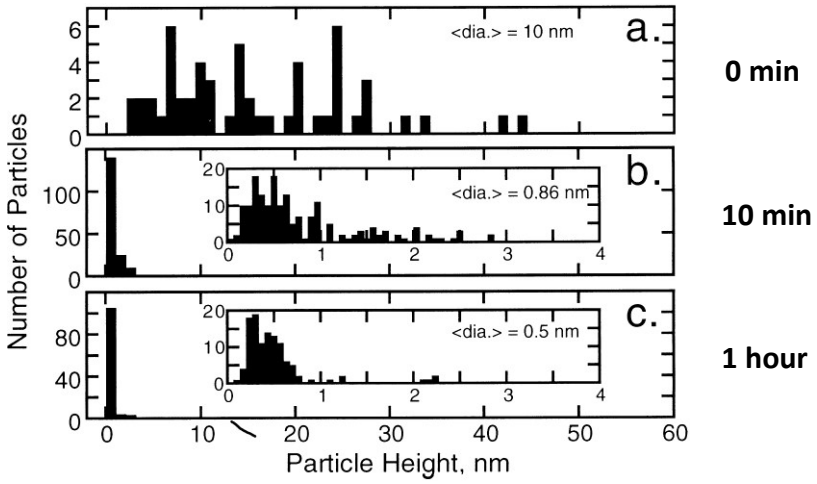

Fig. 2.2: Histogram of the atomic force microscopy (AFM) - measured height of AgNPs following equilibration at +500 mV vs Ag/AgCl for (a) τ_{+500} = 0 min, (b) τ_{+500} = 10 min, (c) τ_{+500} = 1 h[63]. The inserts are the enlarged histogram for particle sizes ranging between 0 and 4 nm.

Similarly, Kolb *et al.* [64, 65] examined the stability of small Cu clusters (typically two to four atomic layers in height) on an Au (111) surface, showing remarkable stability to potentials up to about + 300 mV above the dissolution potential of a bulk Cu electrode. It was suggested that the stability is caused by quantum confinement of electrons in the metal cluster. However, several research groups reported that the spontaneous formation of a copper gold alloy in the cluster may give an alternative explanation for the increased stability of the Cu nanocluster[66-68]. These two metals form stable alloys which are electrochemically more stable than pure Cu.

In another study, the electrochemical stability of single gold nanoparticle was examined by Lakbub *et al*. on a nanometer-sized Pt electrode[69]. The authors reported that it becomes more difficult to oxidise a nanoparticle as the particle radius becomes smaller. Fig. 2.3 demonstrates that the peak potential is directly related to the reciprocal of the radius of gold nanoparticles, which is in disagreement with theories developed by Plieth[4] and Henglein[62, 69].

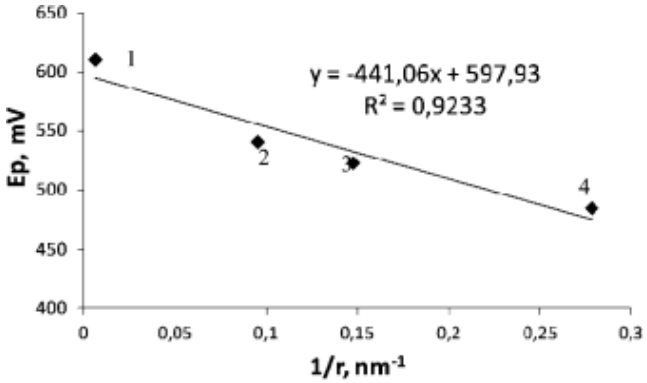

Fig. 2.3: Plot of the potential of gold oxide stripping peak versus the reciprocal of the radius of bulk gold (point 1) or gold nanoparticles (point 2, 3, and 4). The radius and oxide gold stripping peak position for the gold NPs are measured from CV[69].

In contrast, only a small number of experimental studies have been carried out which are aimed at examining the electrochemical stability of isolated metal nanoparticles. For instance, Tang *et al.* directly examined the stability of individual nanoparticles and presented the results of a combined experimental analysis using a first principles study on the electrochemical stability of individual Pt NPs in acidic environments [70]. The dissolution behavior of Pt NPs with diameter between 1.2 to 3.0 nm confirmed the thermodynamic predictions of Plieth and Henglein as shown in Fig 2.4.

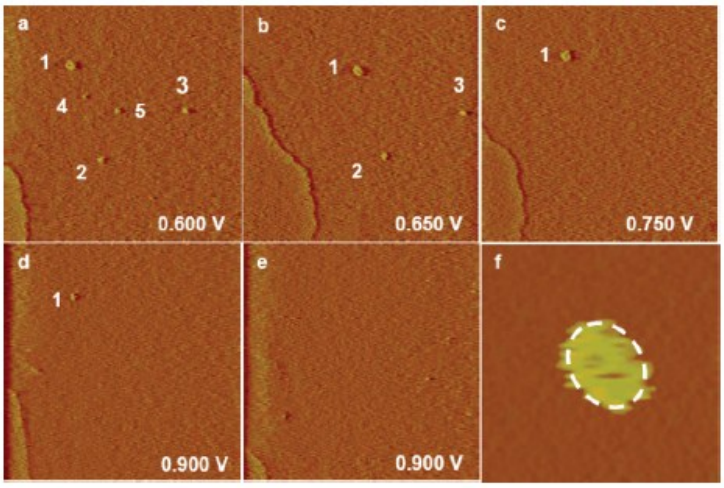

Fig. 2.4: Electrochemical Scanning Tunnelling Microscopy (ECSTM) image of five Pt-black NPs on a gold substrate in 0.1 M H_2SO_4. (a) The initial set of 5 particles at 0.600 V (NHE). (b) Voltage pulsed to 0.650 V showing the dissolution of particles 4 (r_m = 0.58 nm) and 5 (r_m = 0.62 nm). Particles 2 (r_m = 0.83 nm) and 3 (r_m = 0.81 nm) were stable to 0.700 V and dissolved at 0.750 V. (c) Particle 1 (r_m = 1.43 nm) was stable at 0.750 V after 600 s at this potential. (d) Particle 1 remained stable to 0.900 V and (e) dissolved after 300 s at 0.900 V. Scan size 95 × 95 nm. (f) Magnified view of particle 1 showing the individual particle was ellipsoidal. Scan size (a) – (e) 95 x 95 nm and (f) 10 x 10 nm[70].

To construct an *ab-initio* Pourbaix diagram, Tang *et al.* performed computation works using more than 50 Pt nanoparticles of radius 0.25, 0.5 and 1 nm. As shown in Fig. 2.5, the blue and gray areas indicate the region of O_2 and OH^- adsorbed on the particle surface. The red area illustrates the region of stable Pt^{2+} dissolution (assuming $[Pt^{2+}] = 10^{-6}$ M) which is extended as compared to that of bulk Pt (black dashed line). For a 1 nm radius Pt NP, the dissolution boundary occurs at 0.93 V, whereas for 0.5 nm NPs it is predicted to be 0.7 V. Both sets of experimental and calculation data agree well, substantiating the notion that the dissolution potential decreases with decreasing particle size. Furthermore, the author extended his work by investigating the dissolution behaviour of Pt NPs as a function of applied potential over a larger size range of 1 - 10 nm. Generally, the author observed that the particle dissolution rate increased with decreasing particle size for particle smaller than 2 nm, while the larger particles were still found stable after ~ 30 min at 1.2 V.

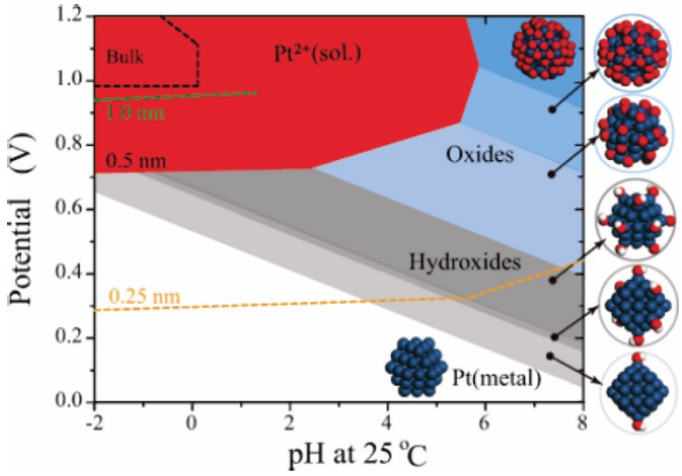

Fig. 2.5: Ab initio calculated Pourbaix diagram for a Pt particle with a radius of 0.5 nm. The stability region of Pt^{2+} in solution is shown in red. The regions of hydroxide and oxygen surface adsorption are, respectively, in grey and blue. The green (orange) dashed line shows the solubility boundary for $[Pt^{2+}] = 10^{-6}$ for a Pt particle with radius 1 nm (0.25 nm)[70].

On the other hand, Holby *et al.*[71] combined both experimental and theoretical techniques to demonstrate the essential role of particle size on the degradation of platinum polymer electrolyte membrane fuel cell (PEMFC) cathodes. The authors found there is a critical enhancement in stability, from a ~2 nm to ~5 nm particle size, due to rapid changes in the Gibbs-Thompson energy (see equation 2.16). Their

model demonstrated that particle size effects play almost no role for ~ 5 nm particles, but dominate degradation for ~ 2 nm particles.

The Gibbs-Thomson (GT) equation yields an estimate of the size dependence of particle stability, and is generally written as a shift of chemical potential (partial molar free energy) of a metal atom in a particle:

$$E_{GT} = \mu(d) - \mu(\infty) = -[4\gamma\Omega/d] \quad (2.16)$$

where d is the particle diameter, γ is the particle surface free energy, and Ω is the molar volume of the particle[72]. This GT equation has been used to study the destabilization of NPs, but it only accounts for isotropic surface tension destabilization and not further destabilization due to corner and edge sites[72].

The description of the GT equation on the stability of NPs is significantly more relevant for particles < 5 nm. This suggests that theoretically derived energy diagrams for a bulk material might not always be accurate for NPs. The existing GT equation may need to consider surface stress and surface energy in the calculation in order to predict electrochemical stability of NPs for their long term applications accurately.

2.1.5 Particle Stability at the Nanoscale

Many studies show that nano-sized particles behave differently from their bulk metals and are actually stabilized by their quantum size effects[3, 63]. There are several reasons to explain why the solubility of smaller-sized particles is different from larger particles. First, smaller particles experience faster dissolution rate kinetics due to their greater surface area to volume ratio. According to the Noyes-Whitney equation, the solubility of particles depends on size as described in equation 2.17[73]:

$$\frac{dm}{dt} = \frac{DA}{h}(c_s - c) \quad (2.17)$$

where $\frac{dm}{dt}$ is the dissolution rate, D is the diffusion coefficient, A is the surface area, and h is the thickness of diffusion layers, c_s is the saturation concentration, and c is the bulk concentration.

Secondly, the increased curvature (i.e., Kelvin effect) of nanoparticles leads to a larger thermodynamic driving force for solubility; *i.e.*, a greater amount of dissolution before the equilibrium solubility is reached. Kwon and Messing[74] and Mihranyan *et al.*[75] studied the effect of particle radius on solubility, S, using the Ostwald-Freundlich equation:

$$S = S_0 \exp(\frac{2\gamma_{sl}V}{RTr})[mol/l] \qquad (2.18)$$

where S_0 is the solubility of a flat plate (equilibrium solubility), γ_{sl} is the solid-liquid interfacial energy, V is the molecular volume of the solid phase, R is the ideal gas constant, and T is the temperature.

As pointed out by Kwon and Messing[74], the particle solubility increases significantly as the particle size decreases, given that all the other conditions are constant. Similarly, Mihranyan *et al*.[75] discussed the relationship between the solubility of a material and the particle size as shown in Fig. 2.6. In this study, they consider the dissolution of hypothetical particles of molecular weight, V_m of 700 g/mol, with a surface tension of 100 dyn/cm, a surface charge of 200e (e being the unit charge equal to 1.6 x 10^{-19} C), a dielectric constant of $10\varepsilon_0$ (ε_0 being the permittivity of free space equal to 8.85 x 10^{-14} F/cm). The author confirmed that the increase in solubility of particles depends crucially on particle sizes. Surface properties become increasingly important for the solubility of solids, as the specific surface area is increased with the decreasing of particle size. Fig. 2.6 demonstrated that the solubility of the examined material reaches its maximum when the critical particle radius r* is approximately 21 nm.

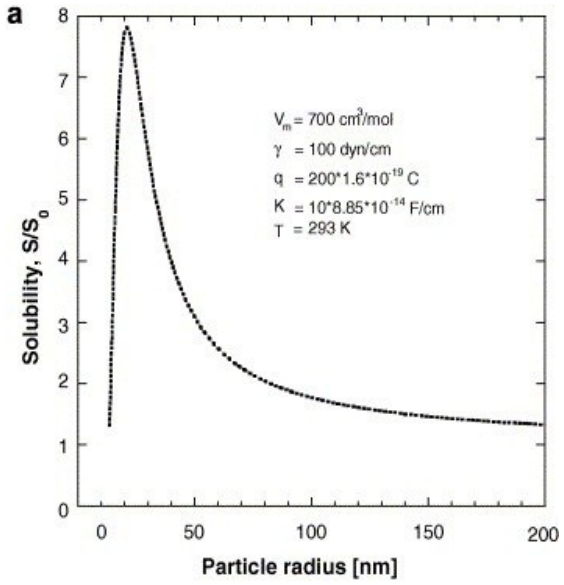

Fig. 2.6: Particle size effect on the solubility of a material with the different physical characteristics[75].

Thirdly, if the detailed structure of the particle is considered, smaller diameter nanoparticles have a much larger fraction of surface atoms. Such materials exhibit physical and chemical properties characteristics of neither the isolated atoms nor the bulk material. As a particle size shrinks to approximately 4 nm – 8 nm, a significant increasing fraction of atoms (≈ 50%) are exposed on surfaces rather than contained in the bulk, as shown in Fig. 2.7.

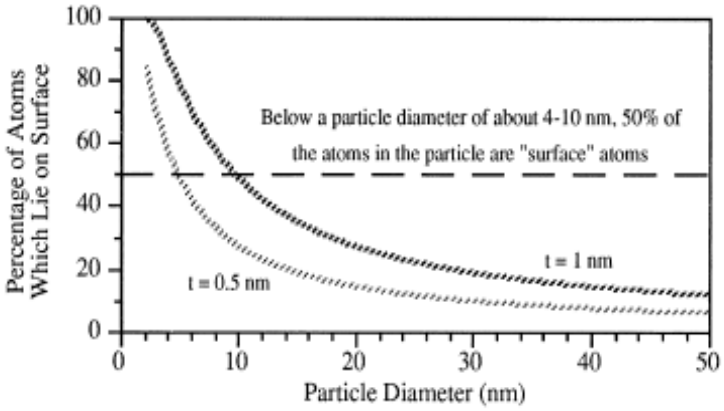

Fig. 2.7: Fraction of atoms in a particle which are surface atoms, for different presumed thicknesses, t, of the surface layer[75].

Furthermore, passivation effects on the surface of NPs are more reactive than their bulk materials[76]. Therefore, nanoparticles become passivated more rapidly with the passivating agents in solutions, for instances oxygen, protons, or hydroxyl groups

due to their higher surface energy[77]. This adsorption may change the surface chemistry of the particles and the dissolution mechanism. The stability of nanoparticles is an area of active fundamental research which is expected to lead engineered nanomaterials (ENMs) with novel properties for industrial application. Therefore, an improved understanding of the parameters which control dissolution is very important to design materials that can be used commercially.

2.2 Health Exposure Concerns of Nanomaterials

The large production volume of manufactured ENMs raises concerns of their environmental, occupational health and safety[36, 78, 79]. An increase in the number and production volume of products containing ENMs, however, will inevitably lead to a greater release of these materials into the environment[7]. In addition, occupational health risks to workers will increase as significant amount of ENMs have been released during both wet and dry production processes[80, 81]. Therefore, there is a growing concern about the potential adverse effects on human health upon exposure to ENMs, which must be assessed to enable the responsible development of nanoscale materials.

According to statistical studies, most consumers are unaware whether their purchased items contain NPs[82]. Similarly, employees in manufacturing plants may not be advised to wear personal protective equipment (PPE) when they handle NPs, to prevent inhalations of the fine particles. As reported by NIOSH, seven workers had been found to have hypoxemia and to have developed severe lung disease after working with a chemical paste comprising of a mixture of undefined NPs. In terms of occupational health exposure risk, data have emerged providing evidence that welders exposed to fumes containing Mg NPs may show an early onset of neurodegenerative disease[83, 84].

From a historical perspective, the rapid progress and use of asbestos was seen as a breakthrough and widely utilised in various industrial applications before the health risks of this material were properly investigated. Their potential risks were ignored and the governments failed to create legislation for over two decades, even after clear proof of the damaging nature of asbestos to respiratory health. The respiratory effects of inhaled asbestos-fibres cause severe diseases such as lung cancer and asbestosis[85-87]. The latest surveys have shown that the cost of health care for

mesothelioma patients are still increasing, for instance, more than 24,000 patients are still receiving treatment today, even after its prohibition 24 years ago. Furthermore, buildings containing asbestos such as the 'Tour Montparnasse' in Paris have to be decontaminated with costs of over 250 million euros. A lack of consideration of health and environmental risks of nanomaterials in the early stages of nanotechnology development would repeat these failures, and could trigger huge future social, health and economic repercussions.

2.2.1 Portals of Entry of Nanomaterials

Routes by which substances can enter the human body include ingestion, inhalation, injection, and permeation through the skin. The potential of NMs to exhibit toxicity at the primary exposure site, namely skin, lungs and gastrointestinal tract (GIT), is of great relevance. However, the NMs localisation is not restricted to their portal of entry as they are distributed to a number of secondary targets (including the kidneys, liver, brain and spleen) which also need to be considered when evaluating the toxicity of NMs to human health. A detailed diagram of routes of exposure, translocation and potential fates of NMs within the human body is schematised in Fig. 2.8.

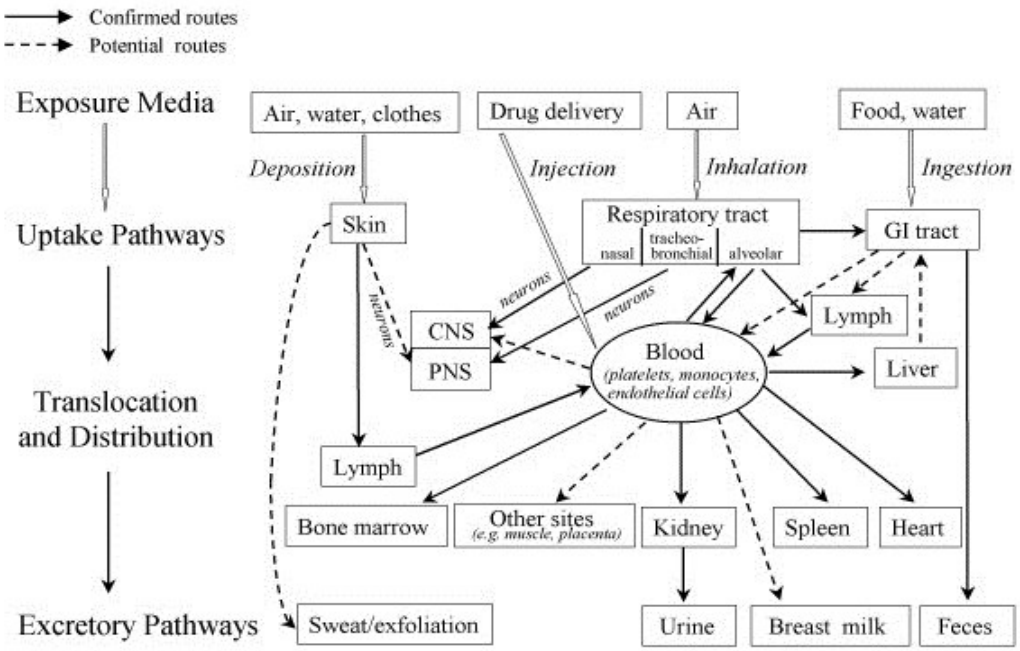

*CNS : Central nervous system; PNS: Peripheral nervous system.

Fig. 2.8: Potential routes of exposure, translocation and deposition of NMs[12].

2.2.1.1 Inhalation

Inhalation is widely accepted as the main unintentional route of exposure of ENMs. The respiratory tract is the portal of entry for the air we breathe, as such lungs will be the first point of contact of airborne particles that enter the body. For particulates, size is the main factor that influences deposition in the respiratory system. Fig. 2.8 illustrates the fractional deposition of inhaled particles in the three regions of the respiratory tract (including the nasopharyngeal, tracheobronchial and alveolar regions) during breathing. Generally, inhaled gas will pass through the nose, pharynx, larynx, trachea, and bronchi prior to entering the lungs. Large particles are likely to impact on the walls of the nasal cavity or pharynx during respiration, while smaller particles typically move by diffusion into the alveoli[11, 88].

Fig. 2.9 shows that most inhaled NPs (> 1 μm) have the highest deposition efficiency in the nasopharyngeal compartment, whereas most 20 nm NPs (~ 50 %) are deposited in the alveolar region. Oberdorster *et al.*[12] demonstrated that the size distribution of NPs influences the target deposition in the respiratory tract. In the upper airways, particles are efficiently expelled by the mucociliary escalator system[89]. On the other hand, smaller-sized NPs are able to penetrate the alveoli[90, 91]. The average diameters of human and rat alveolar macrophages is between 14 and 21 μm and 10.5 and 13 μm, respectively[92]. Macrophages will engulf particles having a diameter of > 1 μm but less effective in recognising particles < 0.5 μm in diameter[93]. In some cases, depending on the physicochemistry of particles, NPs can impair the alveolar macrophages phagocytosis, enter pulmonary interstitial sites, translocate across the lung-epithelial barrier into the circulatory and lymphatic systems and eventually distribute to different organs (*e.g.* kidneys, spleen, heart and brain)[90, 94, 95].

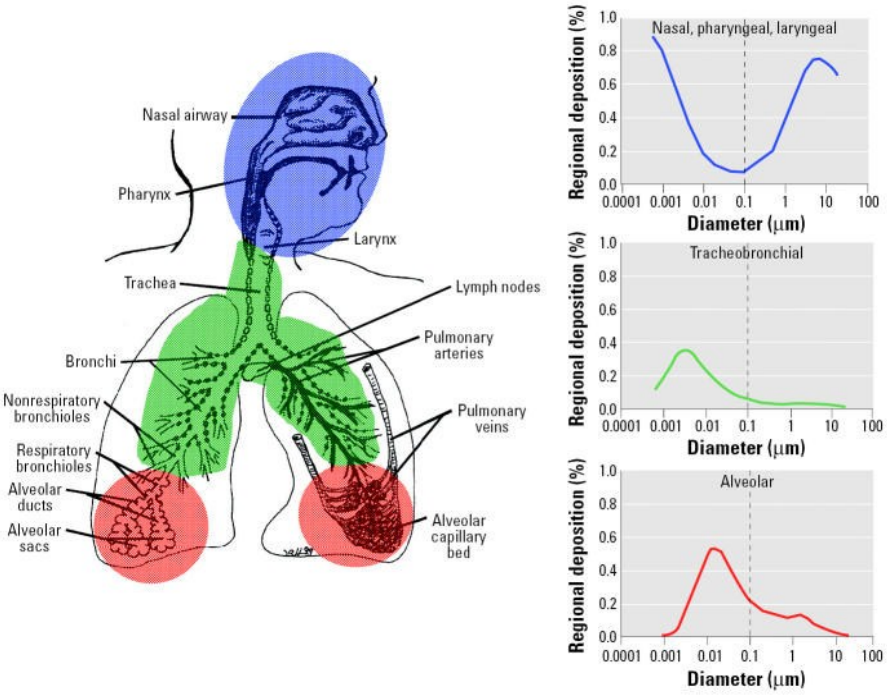

Fig. 2.9: The fractional deposition of inhaled particles in the nasopharyngeal, tracheobronchial, and alveolar regions of the human respiratory tract under conditions of nasal breathing, based on a predictive mathematical data from the International Commission on Radiological Protection[95].

In addition, insoluble particles in the lung will accumulate rapidly upon continued exposure as shown in Fig. 2.10, for carbon black, asbestos, multi-walled carbon nanotubes (MWCNTs) and grounded CNTs. The lung defence mechanisms will become overwhelmed when the macrophage clearance capacity is exceeded, resulting in lung tissue injury. Muller *et al.*[96] reported that MWCNTs were bio-persistent in the lung when 81% remained in the lung after 60 days. The pulmonary persistence and increased accumulation of certain classes of inhaled NPs may induce lung inflammation, fibrosis and lung cancer[96, 97].

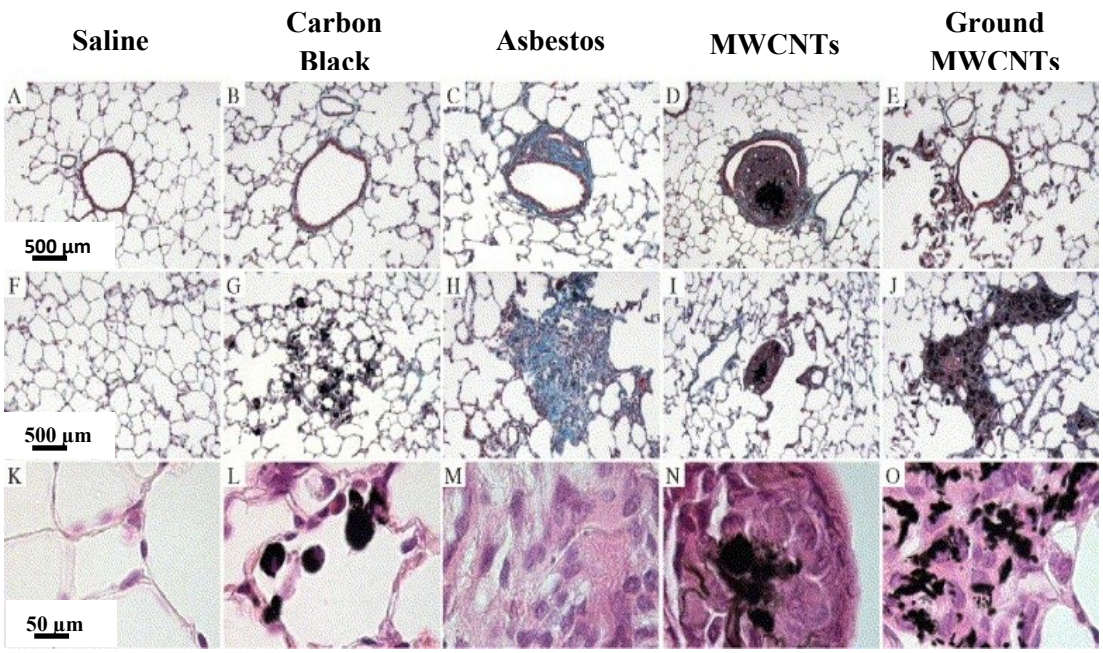

Fig. 2.10: Rat lung lesions induced by (A, F, K) carbon black, (B, G, I; 2mg/rat) asbestos, (D, I, N; 2mg/rat) multiwalled carbon nanotubes (MWCNT), and (F, J, O; 2mg/rat) ground MWCNT compared to (A, F, K) saline solution after 60 days instillation[96].

2.2.1.2 Skin / Dermal Absorption

As shown in Fig. 2.11, the skin is composed of three layers, namely epidermis, dermis and hypodermis. The outer layer of the epidermis is called stratum corneum, which is a 10 µm thick keratinised layer of dead cells, preventing the penetration of foreign particles effectively. To date, dermal penetration of NPs is still controversial[98]. Several studies showed that NPs are able to penetrate the stratum corneum[98-101]. The general consensus is that NMs are more likely to penetrate through the skin at cracks, creases, or hair follicles and enter tissue more effectively in a region of a damaged or broken skin[58, 100].

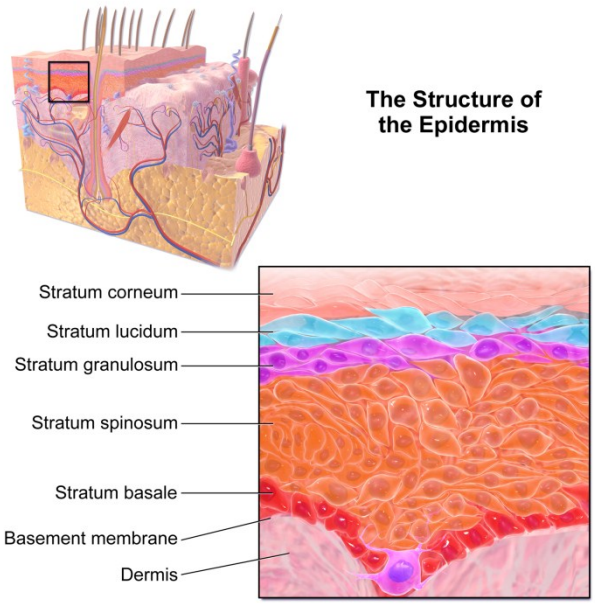

Fig. 2.11: 3D representative of the skin layers and components[102].

According to Toll *et al.*[101], spherical particles with diameter between 0.75 and 6 µm are able to penetrate the skin at hair follicles up to a penetration depth of > 2.3 mm. Broken skin facilitates the penetration of larger particles with diameter (0.5 - 7 µm)[95] . Current *in vitro* studies have shown that less than 1% of the total amount of applied sunscreen is found in a given hair follicle; some reports state that no penetration of NPs is observed and TiO_2 NMs based sunscreens are safe to use[102, 103]. The reason why skin is difficult to penetrate is due to a 10 µm thick barrier of strongly keratinised stratum corneum. Apart from metal oxide NPs, other metal NPs such as AgNPs (70 µg/cm^2) exposed to intact *vs.* damaged human skin have shown very low skin penetration, suggesting their safe application on intact skin or wound dressings on damaged skin[104].

2.2.1.3 Ingestion

Nanoparticles used as dietary supplements, food additives and drugs are likely to transport through gastro-intestinal (GI) tract[105, 106]. Ingested NMs will be expelled if they are unstable in the extreme conditions of the GI tract. Highly acidic conditions may trigger NMs to agglomerate inside the intestinal tract, resulting in obstruction of GI tract, causing death. In comparison, small agglomerates will be removed through the faeces with little absorption. This process was demonstrated by

Wang *et al.*: mice fed with zinc NPs (5 g/kg body weight) developed severe diarrhoea, vomiting and anorexia followed by death[107]. Autopsy results revealed clumps of NPs blocked in the intestine.

Several studies have claimed that ingested NPs are eliminated rapidly where 98 % are removed in the faeces within 48 h, whereas most of the remainder was cleared in the urine and the rest was translocated into the blood circulation[95]. However, some studies indicate that NPs can penetrate the GI tract and translocate to organs[108]. Oral uptake of 25 nm and 80 nm of TiO_2 NPs (5 g/kg body weight) induced more severe lesions of liver and kidneys than fine particles (155 nm) in mice after 2 weeks exposure[109, 110].

2.2.1.4 Translocation to Distant Organs

The physicochemical properties of NPs (*e.g.* surface charge, size, surface coating or attachment of ligands) affect the site-specific targeting of different regions of the GI tract. Studies have shown that NPs can translocate to the liver, bone marrow, blood, lymph nodes, kidneys, brain and lung[58, 111]. Jani *et al.* showed that polystyrene microspheres larger than 100 nm were absent from bone marrow, while particles larger than 300 nm were not found in the blood[111].

Besides, Choi *et al*. investigated the translocation of a series of near –infrared (NIR) fluorescent NPs with different chemical composition, size, shape and surface charge from the lung airspaces to the body[112]. The authors demonstrated that non-cationic NPs with hydrodynamic diameter (HD) $\leq$ 34 nm can translocate across the epithelial barrier, and enter regional lymph nodes. Once lodged in lymph nodes, non-cationic NPs (6 nm $\leq$ HD $\leq$ 34 nm) could cause inflammation and could contribute to carcinogenesis. Nevertheless, when the surface charge on the particle is zwitterionic and HD < 6nm, NPs are able to enter the bloodstream rapidly from the alveolar spaces and then permit renal clearance of a drug not bound to its target. NPs $\approx$ 5 nm able to traverse from the lung to the blood stream and then reach tissues and organs [113]. However, the effect of long-term deposition in organs is still unknown.

2.2.2 Excretion of Nanomaterials

Nanoparticles can be expelled through sweat, breast milk, saliva, faeces and kidneys, but *in vivo* experiments have only proved excretion *via* urine[114] and faeces[115]. There is a consensus that the size of particles and adsorption of biomolecules onto

particles are related to the ability to clear the particles from the body effectively *via* renal filtration and urinary excretion. Both factors are the key design parameter in developing therapeutic and diagnostic agents.

Choi *et al.*[116] proposed that the major excretion route of NPs, which do not biodegrade into biologically benign components, from the human body is through liver, into bile and faeces. However, the liver is designed to excrete NPs > ~ 10 - 20 nm in hydrodynamic diameter and the elimination of NPs into bile is an extremely slow process. Moreover, the long-term retention of NPs in the reticuloendothelial system (*e.g.* liver, spleen and bone marrow) enhances the toxicity[116]. Several studies have suggested that NMs alter metabolic functions in the kidney, damage the excretory systems, leading to NPs retention, nephrotoxicity and organ failure[117, 118].

To date, there is ample evidence that physicochemical properties (*e.g.* surface chemistry, size and shape) influence the biodistribution, clearance and biocompatibility of NPs *in vivo*. It is well established that rod-shaped (non-spherical) and negatively charged particles show a longer retention time in the blood stream [119, 120]. For instance, Huang *et al.* studied the effect of fluorescent mesoporous silica NPs (MSNs) on their excretion rate and organ distributions[119]. Short-rod MSNs were found to trap in the liver, whereas long-rod MSNs were distributed in the spleen. Moreover, short-rod MSNs have a higher clearance rate *via* urine and faeces than long-rod MSNs. The phagocytic activity of macrophages being less stimulated by rod-shaped particles compared to spherical ones[121]. In addition, neutral or negatively charged NPs have a low rate of nonspecific cellular uptake and a marked reduction in the plasma protein adsorption, decreasing early clearance from the body, minimising side effects and reducing the total dose required[120]. Therefore, targeted NPs functionalised with ligands by modifying physicochemical properties of NPs, have been shown to increase their long circulating drug delivery system.

2.2.3 Pulmonary Toxicity of Nanomaterials

Several studies have compared the colloidal stability of NPs in different suspension media, including rat bronchoalveolar lavage (BAL)[122]; phosphate buffered saline (BAL fluid mimic containing bovine serum albumin (BSA) and

dipalmitoylphosphatidylcholine (DPPC))[18, 123]; semisynthetic lung fluid (DPPC/palmitoyl-oleoyl-phosphatidylglycerol/ surfactant protein B (SP-B); 70:30:1 wt %)[124]. These studies found that NPs were well-dispersed in the presence of DPPC and protein and the synthetic lung fluid was as effective as BAL in dispersing the NPs.

It is imperative to emphasize that DPPC-NPs interactions depend on several factors, such as particle size[125], surface charge[126] and particle nature (hydrophilic or hydrophobic)[127]. Interactions occurring between the biological media and NPs are expected to govern the subsequent biological effects of the particles. In the context of respirable NPs, the interactions with both lung lining fluid components and local cell populations will determine the effects on cell metabolism and lung function[128]. The effects of the lung lining fluid on the aggregation state of NPs will play an important role in determining the interaction of particles with proteins, cells and tissues[129]. An altered aggregation state of the particles will modify particle transport, the amount of Ag particles internalised by cells and their subsequent interactions within cells[130]. The aggregation state of the particles can also alter the surface tension of the lung lining fluid and thus subsequently affect innate immune responses by sequestering lipids or proteins[131]. These factors may eventually alter the bioavailability of AgNPs, cellular toxicity and even lung function[132].

The phospholipids coating of AgNPs could lead to serious pulmonary homeostasis by interfering with biophysical surfactant function. The detailed mechanisms by which AgNPs damage cells and tissues is not fully understood; however, as described in section 2.1.1, recent studies have indicated that Ag^+ ion release is a major pathway underlying the biological reactivity and toxicity of AgNPs[133, 134]. Ionic silver (Ag^+) is a well-known oxidation catalyst that has been implicated in protein damage by desulphurisation and generation of reactive oxygen species (ROS)[135]. In addition, Ag^+ ions may interfere with NO redox equilibria in the lung and in the generation of ROS[10]. This oxidative potential may increase the permeability of the lung epithelium to AgNPs resulting also in DNA damage, lipid membrane damage, chromosomal aberrations, and cell cycle arrest[11, 36]. Through these biochemical pathways, release of Ag^+ ions is a critical process that will

determine the downstream effects of AgNPs on human health[136, 137]. Currently, the importance of the AgNP-surfactant interaction and the effect of bound surfactant components on the intracellular response of AgNPs have been neglected in the literature. For this reason, it is critically important to understand how the interaction between lung surfactant components and AgNPs will affect their stability in biological media, and ultimately any downstream effects of the particles can be predicted.

2.2.3.1 Pulmonary Surfactant

The deep lung consists of a layer of lung lining fluid, pulmonary surfactant that is composed of 90% phospholipids and 10 % surfactant proteins[138]. The most abundant phospholipids are based on phosphatidylcholine (PC) with DPPC predominant, making up 41 – 70 % of the PC component. The lung lining fluid plays an important role in regulating the innate immunity of the lung[139, 140], and DPPC is mainly responsible for reducing surface tension at the alveolar surface[141]. It is generally believed that a DPPC enriched monolayer is able to produce the near-zero surface tension at the end of exhalation, easing the work of breathing and preventing the alveoli from collapsing[142].

There are four lamellar phases recognised in saturated phosphatidylcholines (*e.g.* DPPC): a liquid-crystalline phase (L_α) and phases with ordered hydrocarbon chain arrangements, namely sub-gel or crystal phase (L_c), gel phase (L_β) and ripple phase (P_β)[143]. The pre-transition temperature associated with lamellar gel phase (L_β) to ripple phase (P_β) in aqueous dispersion of DPPC in bilayer is approximately 35 ºC. Whereas, the main transition temperature of the gel-to-fluid phase (T_c) is observed at 42 ºC[144, 145]. Below this transition or melting temperature (T_c), hydrated DPPC molecules may be less mobile but may rotate occasionally. At ambient temperature or 37 ºC, DPPC monolayers are rigid enough to be compressed to a high surface pressure ($\pi > 50$ mN/m) or a low surface tension ($\gamma = 0$ mN/m) and can be sustained at these low values of surface tension for a considerable amount of time, without collapsing[146, 147]. Lung surfactant deficiency and dysfunction may lead to the severe pulmonary disorders such as acute respiratory distress syndrome (RSD)[148].

It is well established that lipid vesicles do not rupture to form a bilayer on metal surface[149]. To confirm the formation of lipid bilayer on citrate coated AgNPs,

McConnell's group[150] created supported lipid bilayers by spreading the lipid vesicles on hydrophilic supports. Sachan *et al.* visualised the topology of a hydrophobic polyorganosiloxane (AmOrSil20) NPs and characterized their localization within the compressed pulmonary surfactant film using scanning force microscopic and electron microscopy techniques[151]. The authors demonstrated that hydrophobic AmOrSil20 NPs neither significantly destabilize the film at the interface nor compromise the functioning of the film. In addition, TiO_2 NPs have been shown to interact with pulmonary surfactant directly, inducing dysfunction of the biophysical surfactant or altered toxic particle effects[88]. However, to date, high resolution imaging of the lipid-NPs interactions is still scant in the literature. To study the detailed morphology of the DPPC layer(s) bound to the NPs surface, uranyl acetate negative staining technique was used.

2.2.3.2 The bio-nano Interface (Protein/ Lung lining fluid)

Recent nanomedicine research has been undertaken to develop NPs as potential drug candidates due to their size-related properties, making them ideally used for a specific pathway. In the biological environment, NPs are immediately entrapped by proteins, leading to the formation of a 'protein corona' surrounding and hiding the surface of the NPs. Thus, the NPs will not remain as an inert object but form hybrid bio-nanomaterials with different physicochemical properties, including changes of aggregation state, effective size and surface charge [152-154]. The interaction of NPs with plasma proteins is one of the most prominent factors that should be considered to address nanotoxicology issues of NMs and take their medical applications into the next level.

There are several factors (*e.g.* surface charge, hydrophobicity, particle size and surface curvature) that play a role in influencing NPs - protein interactions, thus the kinetics of protein binding can be manipulated by these factors to increase the retention and circulation time of NPs in the body[155-157]. Neutrally - charged particles have been shown to have a reduced opsonisation rate in comparison with charged particles[157, 158]. Besides, the hydrophobicity of NPs also affects the amounts of protein adsorption to their surface. Generally, hydrophobic NPs have a higher opsonisation rate than hydrophilic NPs, leading to a large uptake by the liver and spleen[159, 160].

Apart from surface chemistry, Roiter *et al.*[125] demonstrated that nearly all smaller NPs (< 22 nm) were not covered by the lipid bilayer due to their higher surface curvature. The high curvature could not be confirmed by the bending energy of the lipid membrane compared to the attractive force pulling the membrane to the surface as shown in Fig. 2.12 c. In contrast, their larger counterparts were nearly covered with lipid bilayers but holes remained only around smaller-sized NPs as shown in the image of the lipid bilayer after subtraction of the particles and the substrate (Fig. 2.12h). On the other hand, Cedervall *et al.*[161] have shown that the size and the surface curvature of NPs play a main role in determining the amount of bound proteins but do not influence identity of bound proteins.

There are some arguments on the advantages and disadvantages of protein binding[162]. Exploiting protein binding can be useful to target the NPs to a specific area of the body[163-165]. For instance, polysorbate 80-coated polybutylcyanoacrylate (PBCA) - NPs preferentially adsorb apolipoprotein E (apoE) on their surface, prolonging their circulation in the blood due to the creation of hydrophilic surfaces and increasing their ability to deliver various drugs to the brain[166]. Nevertheless, binding of these specific proteins has been shown to enhance uptake of the coated NPs by cells of the reticuloendothelial system (RES) and affect the route of particle internalisation and their eventual fate in the body (*e.g.* rate of clearance from the blood stream and organ disposition)[166, 167]. The addition of poly (ethylene glycol) (PEG) has been shown to 'mask' NPs from RES recognition and prolong blood circulation[168-170]. PEG coated – gold NPs were shown to be targeted and accumulated in the tumor in a tumor-burden mouse model. In contrast, colloidal gold NPs (without PEGylation) accumulated in the liver and spleen rapidly and did not dissipate out of these organs after 3 months[171].

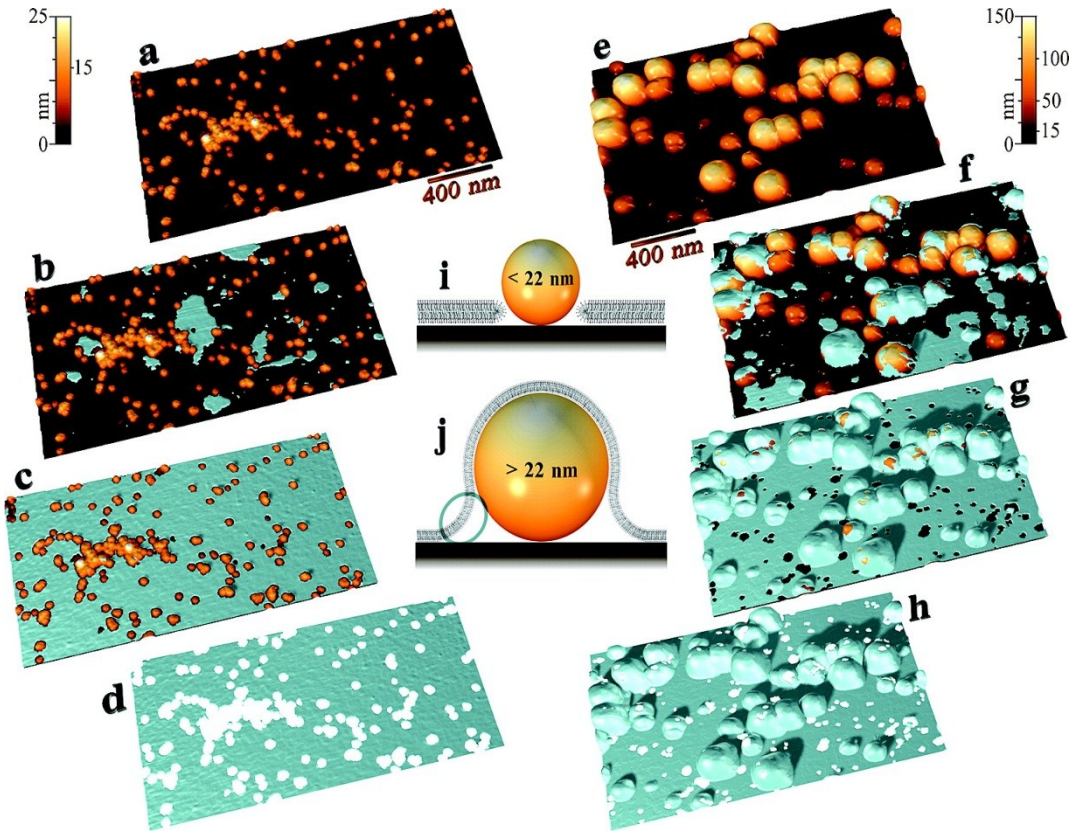

Fig. 2.12: Lipid bilayer formation in the presence of particles larger than the lipid bilayer thickness (~5 nm, including the interfacial layer of water). AFM images of lipid bilayer formation over a surface with (left; a-d) 5 - 20 nm silica NPs and (right; e-h) mixed 5 - 140 nm silica NPs: (a, e) substrate with particles and no lipid, (b, f) partial coverage of the surface by lipid bilayer (shown in silver colour), (c, g) lipid bilayer formed on the substrate, and (d , h) image of the lipid bilayer after "subtraction" of the particles and the substrate. Schematics in the center illustrate how the lipid bilayer forms a pore around particles smaller than 22 nm (i) and how it may envelope the larger particles (j). The structure of bilayer area encircled in (j) is speculative because it cannot be resolved or assumed from AFM experiments[125].

Numerous studies have also shown that protein adsorption decreases with increasing molecular weight of a PEG coating, subsequently reducing cellular uptake and enhancing the particle's blood circulation half-life[157, 169, 172]. Generally, PEG is not the only polysaccharide that can be bound to the NPs surface to affect the protein binding or to avoid the immune recognition. Apart from PEG, various other polysaccharides and polymers have also been used to achieve the desired targeting effect for a particular medical function. A detailed understanding of the NPs - protein interactions will help in improving the delivery and the biodistribution of

nanomedicines within a biological system and also in increasing the bio-safety of NMs.

2.2.4 Central Nervous System (CNS) Toxicity

Neurological diseases affect 24.3 million people worldwide and are one of the most severe medical burdens. NPs have been widely exploited for controlled and site-specific delivery of drugs, which have shown promising results for the treatment of various diseases including Alzheimer's disease (AD) and Parkinson's disease (PD) [173, 174]. Over the past few years, several studies have suggested that AgNPs can localise inside the brain and may cause brain diseases (including Alzheimer's and Parkinson's diseases), if the particles are accidentally inhaled through the nose. Hadrup *et al.*[20] compared the neurotoxic effects of 14 nm AgNPs and ionic Ag *in vivo* and *in vitro.* The authors found that both the AgNPs and ionic Ag^+ increased dopamine concentrations in the brain following oral administration. Furthermore, exposure of PC12 neuronal cells to AgNPs and Ag^+ ions caused apoptosis which was linked to induction of the mitochondrial and death receptor pathways[20].

A number of *in vitro* studies have shown that the release of Ag^+ ions from the NPs might cause oxidative stress, damage cellular constituents, and affect DNA replication, resulting in cell apoptosis[175-178]. The interaction of Ag^+ with thiol groups of proteins or enzymes may cause interruption of normal cell or enzymatic activities, interfere with NO redox equilibria in the lung and trigger the generation of reactive oxygen species (ROS)[135]. Moreover, Ag^+ might perturb mitochondrial function through interaction with thiol groups of the mitochondrial inner membrane, causing oxidative damage[179-181]. For over a decade, researchers have debated the main mechanism of AgNPs toxicity, whether the particles exert direct, particle-specific biological effects or whether their effects are due to the release of Ag ionic species, or a combination of both. Although these particle-specific mechanisms are highly debated, there is a consensus that Ag^+ ion release is responsible for biological actions; consequently AgNPs toxicity is mainly elucidated by exposing cells to Ag ions (Ag^+).

Recent reports have shown potential neuronal uptake and translocation of inhaled particles and pathogens to the brain *via* the olfactory nerve[182-185]. Both *in vivo* and *in vitro* studies have reported that AgNPs can translocate from entry portals

(*e.g.* human skins, lungs and the gastro-intestinal tract) through epithelial and endothelial cells into blood circulation, accumulating in various tissues or organs, including bone marrow, liver, spleen, lymph and heart[186]. Spherical AgNPs (Sigma –Aldrich) with a 70 nm ± 20 nm particle diameter, have the ability to cross or damage the blood brain barrier (BBB) and reach the central nervous system (CNS)[187, 188]. Trickler *et al.*[187] examined the molecular mechanisms and integrity of the BBB *in vitro* following with the interactions of AgNPs with the cerebral microvasculature. The author suggested that cerebral microvascular damage and dysfunction were dependent on the size of the NPs, with smaller AgNPs much more profound in producing inflammatory responses. Tang *et al.*[189] also confirmed that pure AgNPs (Sigma-Aldrich) with a 50 -100 nm particle diameter could cross the BBB and accumulate in the brain *in vivo*, resulting in BBB destruction and astrocyte swelling, inducing neuronal apoptosis. Moreover, a two week inhalation exposure of mice to AgNPs has been shown to affect brain gene expression associated with motor neuron disorder and immune cell function[19].

To the best of my knowledge, most of the attempts to study the neurotoxicity of NMs have focused on the ability of AgNMs to cross the BBB and the brain tissues uptake of NPs. However, the possible interaction of Ag^{+} ions with thiol groups of proteins and their effect on the upregulation of enzymes have not been investigated thoroughly in the brain. Considering the existing problems, it is crucial to understand how the transformation of Ag will impact their neurotoxicity, and subsequently activate the production of enzymes to achieve the chemical equilibrium in a biological system. Here, the interactions of Ag^{+} with thiol groups of proteins, and the downstream bioactive effects of transformed AgNPs were discussed in the study.

2.3 Biological - Nanomaterials Interaction

2.3.1 Cellular Uptake

Nanomaterials are able to enter into the cells and various cellular compartments, including the nucleus, cytoplasmic vacuole and mitochondria. The pathway of cellular internalisation, subcellular localisation and ability of catalysed oxidative products are highly dependent on the physicochemistry of particles [172, 190-193]. Upon non-phagocytic uptake, NPs can be found in various locations inside cells. NPs can be internalised, not only by professional phagocytes, such as alveolar

macrophages but also by various cells, such as red blood cells[90], pulmonary epithelium[194, 195], endothelial cells[196, 197], intestinal epithelium[198, 199], and neuronal cells [200].

Ayush *et al.*[201] suggested that positively-charged NPs more readily cross cell-membrane barriers than neutral and negatively charged particles, which may increase the toxicity. In contrast to the high level of cell interaction and internalisation by positively-charged particles, NPs with neutral or negative surface coating (*e.g.* PEG) resist interactions with negatively charged cell-membrane surfaces and display minimal internalisation[201]. Liu *et al.*[202]examined the influence of surface and size on the uptake of gold (Au) NPs by both phagocytic and nonphagocytic cells. The authors showed that positively-charged AuNPs were internalised more readily than those with a negative surface charge, in nonphagocytic HepG2 cells and the majority of AuNPs were localised in lysosomes. In contrast, for a phagocytic macrophage cell line (RAW 264.7), internalisation was more efficient for negatively-charged AuNPs, where most of them were mainly found in phagosomes. This study suggested that the cell interaction with NPs is not only affected by NPs' physicochemical properties but also depended on cell types. There is a consensus that phagocytosis of particles is most efficient when particles have dimensions in the range between 1 and 2 μm[190, 193, 203].

Recent studies of the particle shape effect on cellular uptake of NPs suggest that the morphological features of NPs play a more dominant role than particle size, surface chemistry, and chemical composition in determining the NPs' cellular translocation and their excretion rate[192, 204]. Huang *et al.*[205] investigated the effects of the shape of mesoporous silica NPs with three different aspect ratios on cellular uptake. Particles with higher aspect ratios, regardless of their surface charge, particle diameter and chemical composition, showed a greater impact on cellular responses such as cell proliferation, apoptosis, adhesion and migration and cytoskeleton formation. On the other hand, Chu *et al.*[204] observed the role of morphological features in determining their cellular fate (Fig. 2.13). NPs with sharp corners or edges were found to penetrate the endosomal membranes easily and remain in cytoplasm for a long period of time, decreasing the cellular excretion rate of NPs significantly. In contrast, spherical NPs (low sharpness) remained stable in endosomes after endocytosis and were involved with endosome maturation and

accelerated lysosomal exocytosis[206]. Therefore, the discovery of the role of morphology on NPs' cellular fate is vital for manipulating NPs - cell interaction for various applications, including bio-imaging, bio-sensing, drug delivery and *etc*..

Endocytosis has been proposed as a mechanism by which AgNPs (≤ 100 nm in size) might enter cells[207]. During endocytosis, the cell membrane forms a saclike vesicle, or endosome, to engulf NPs into the cell. There are two kinds of endocytosis: phagocytosis and pinocytosis. Phagocytosis is conducted by specialised cells in the immune system (*e.g.* microglial cells or macrophages) by which the membrane seal around NPs, forming a phagosome or "food vacuole". In pinocytosis, an infolding of the cell surface or plasma membrane engulfs fluid phase and single molecules into large endocytic vesicles, known as macropinosomes[208].

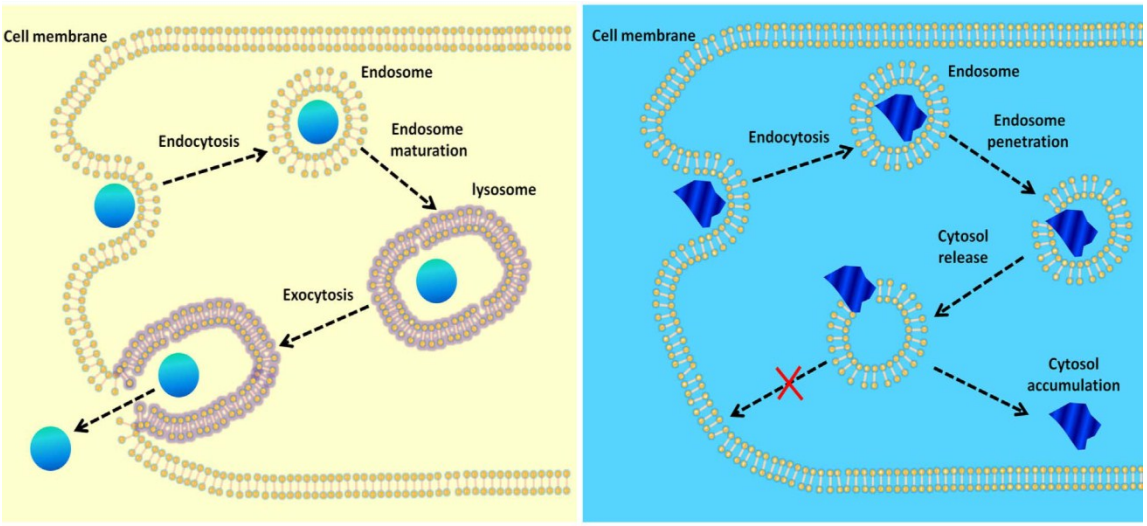

Fig. 2.13: Schematics showing intracellular trafficking of NPs with different morphological features. Left: Spherical NPs with low sharpness reside in the endosome after endocytosis, then evolve into the lysosome by endosomal maturation, and easily excreted *via* exocytosis with the lysosome as the vehicle. Right: NPs with sharp shapes or edges could pierce the membranes of endosomes before the lysosome is formed. NPs has very low excretion rate and will stay in the cytoplasm for a long time without a lysosome as the vehicle[204].

For cellular uptake of NWs, Chen *et al.*[21] showed that AgNWs could translocate across the plasma membrane by "needle-like" mechanism of insertion into cells as previously reported for functionalised carbon nanotubes[209]. The uptake mechanism of NMs must be known in order to understand the behaviour of NPs in biosystems. However, current research does not provide sufficient information to

drawing conclusions on the mechanism of internalisation of AgNWs and their uptake kinetics. Here, we have undertaken investigations to determine the cellular uptake of AgNPs and AgNWs in the central nervous system which are critical in understanding the adverse effects as well as the mechanism of action of the NMs.

2.3.2 Oxidative Stress and Inflammation

To date, the exact mechanism underlying nanotoxicity is not known; it has been suggested that the overproduction of reactive oxygen species (ROS) induce pro-inflammatory effects, thereby damaging cells by interfering with cell signalling, altering proteins, disrupting DNA and leading to changes in cell motility and apoptosis[210, 211]. Nevertheless, there is a consensus that ROS production is a 'double edged sword' in disease prevention and promotion. Studies have shown that ROS play beneficial physiological roles in cellular signalling systems, response to growth factors and induction of mitogenic responses[212, 213]. During normal physiological processes, ROS (*e.g.* hydrogen peroxide (H_2O_2), superoxide ions (O_2^-), and hydroxide radicals (OH^-)) are by-products of cellular oxidative mechanism. The overproduction of these compounds is able to damage cellular proteins and lipids, developing cancer and cardiovascular disease[210]. The oxidative stress induced by NPs can be affected by several critical determinants, including NPs size, shape, surface chemistry, dissolution or aggregation of NPs and medium pH[214-216].

Nanoparticle – induced oxidative stress may have several sources which relate to the chemistry of the particles, cellular type, and the intracellular fate of the NPs:

(i) Transition metals such as copper, chromium, iron, vanadium can act as catalysts by participating in one-electron oxidation-reduction reactions (Fenton type reactions), leading to the formation of ROS[217]. For instance, the reduction of hydrogen peroxide (H_2O_2) with transition metal ions (M^{n+}) results in the formation of hydroxyl radicals ($^{\bullet}OH$) which is highly reactive in attacking biological macromolecules (*e.g.* lipids, amino acids and nucleic acids[218].

$$M^{*+} + H_2O_2 \longrightarrow M^{*++} + {}^{\bullet}OH + OH^- \qquad (2.19)$$

(ii) Activation of inflammatory cells (*e.g.* neutrophils and alveolar macrophages) generates ROS and reactive nitrogen species[219]. The effect of exposing human lung submucosal cells to the amorphous nano-SiO_2 was investigated by McCarthy *et al.*[220]. SiO_2 NPs have been shown to induce inflammatory effects in submucosal cells, and generate ROS, leading to apoptosis and decreased cell survival.

(iii) NPs are able to enter mitochondria and alter their functions [221] [222]. The effects of PVP-coated AgNPs and Ag^+ ions in the human alveolar cell line A549 were investigated by Foldjerg *et al.*[223]. A strong correlation between mitochondria damage and the ROS production was observed. Mitochodria damage severely affects the flow of electrons through the electron-transport chain, inducing leakage of electrons and an increase in the amount of ROS production[224].

(iv) When both oxidants and free radicals piggy-back the NPs surfaces, ROS can be generated from their surfaces, leading to oxidative damage (*e.g.* NO_2 and O_3).

Oxidative stress and ROS have also been linked to many age-related degenerative diseases, such as inflammation, Parkinson's disease, Alzheimer's disease, arthritis, cardiovascular disease and *etc.*[225-227]. It has been reported that antioxidants, anti-inflammatory and metal chelators show promising therapy in treating the adverse health effects caused by the cytotoxicity of NPs[228, 229]. Antioxidant therapy has been shown to offer neuro-protection and to minimise the development of cardiomyopathies, coronary heart disease, hypertension, and congestive heart failure[228].

2.3.3 Genotoxicity

As discussed earlier, NPs are able to generate ROS on their surface or by activation of inflammatory cells. The increase of oxidative species may cause mitochondrial dysregulation, chromosomal aberrations and DNA damage, which are known to be the main factors resulting in cell cycle arrest[177]. Asharani *et al.*[177] investigated the biokinetics of NPs on their toxicity in human cells. AgNPs disrupted the mitochondria respiratory chain, causing interruption of ATP synthesis and production of ROS, leading to DNA damage. Hackenberg *et al.*[230] also found that

AgNPs, at a high exposure concentration (10 μg/ml), may lead to geno- and cytotoxic effects in human mesenchymal stem cells, but the migration activity was not affected by AgNPs at non-toxic levels. Taken together, all these studies suggested that the interaction of NPs with cells could be associated with increased cell injury, genotoxicity and diseases[231, 232].

2.4 Production and Physiology Effects of Hydrogen Sulfide (H_2S)

2.4.1 Emerging Roles of H_2S in Health and Disease

Studies in biological mammalian systems have shown that H_2S equilibrates with aqueous sulphides (HS^- and S_2^-) and plays vital roles in diverse physiological and pathological processes, such as angiogenesis, inflammation, regulation of blood pressure, vasorelaxation, metabolic disorders, energy production in mitochondria and insulin signalling inhibition[233, 234]. Studies have also demonstrated H_2S is an universal cytoprotective defence mechanism for biological organisms and a defect in its production may be related to a number of diseases, including Alzheimer's disease[235], hyperglycaemia[236], Down's syndrome[237] and ischaemia[238]. Shiau *et al*.[239] showed that decreasing endogenous H_2S levels will significantly lower intracellular calcium concentrations, which is an essential element for normal cellular functions, suggesting that endogenous H_2S may regulate calcium homeostasis. These observations suggested H_2S may function as a neuromodulator in mediating signalling between neurons and microglial cells in the brain.

2.4.2 H_2S Producing Enzymes

Hydrogen sulphide (H_2S), which is generally considered as a toxic gas, has been found endogenously produced mainly by the pyridoxal-5'-phosphate (PLP) - dependent enzymes, cystathionine β-synthase (CBS) and cystathionine γ-lyase (CSE) *via* homocysteine, amino acids cysteine and cystathionine. Recent studies have revealed a third potential enzymatic mode of H_2S production by 3-mercaptopyruvate sulfurtransferase (MPST) *via* the cysteine catabolic pathway in the presence of reducing substances such as dithiothreitol (DTT)[240]. Recent accumulating evidence suggested that H_2S serves as an important endogeneous neuromodulator and vasodilator. However, the evidence of its involvement in H_2S biosynthesis in rodents or humans is still poor.

It has been widely suggested that the expression of enzymes in mammals is tissue specific. The current consensus in the literature is that CBS is highly expressed in the central and peripheral nervous system, while CSE is the predominant source of H_2S in the vasculature (*e.g.* smooth muscle and endothelium), heart, kidney and liver; MPST can be found in the brain and vasculature[239]. Fig. 2.14 summarises the H_2S generation and H_2S-generating reactions catalysed by CBS, CSE and MPST. Despite the evidence suggesting that AgNPs may led to neuroinflammation as shown in section 2.2.4, much less is known about their interaction with proteins that might affect their impacts on neurotoxicity. Therefore, a link between the effect of inhaled AgNPs and the endogeneous production of H_2S is vital in understanding the response of sulfur metabolism enzymes to NMs in central nervous system.

So far, there is a lack of research which elucidates cellular uptake of AgNMs and any transformation of these materials inside the brain cells. A link between their interactions with H_2S producing enzymes causing a reduction in H_2S production in the brain cells remains to be shown. Therefore, the aims of this study are to investigate uptake of AgNMs (particles and wires) by microglia cells and their transformation inside cells. Regulations and colocalisation of the H_2S producing enzymes (CBS, CSE and MPST) were monitored using confocal microscopy of cells exposed to the NMs. There is a paucity of research which correlates transformation of AgNMs to cell viability and oxidative stress, following uptake by microglial cells related to expression or the activity of H_2S producing enzymes in the brain. Microglial cells have been chosen as these are the primary immune cells in the brain and play a central role in inducing oxidative stress response. Microglia primarily involved in the macrophagy, surveillance, production of pro-inflammatory signals (i.e. cytokines and chemokines) in the brain.

2.5 Future Direction of Nanotechnology: Applications or Hazards?

According to the report entitled 'Nanoparticles in Biotechnology, Drug development and Drug Delivery' by the BCC research team in USA, the global market for NPs in biotechnology and pharmaceuticals has been increased from approximately $ 25 billion in 2013 to $ 29.6 billion in 2014[241]. This market is projected to grow and reach $ 79.8 billion in 2019. The novel features of the NMs offer enormous potential for technological progress in the twenty-first century. Currently, NMs are increasingly incorporated into various consumer products as discussed in section 2.1.

To date, the exponential growth of nanotechnology has not been matched by investigations of their potential hazards and the risks of these new materials. Recently, industries have faced difficulties in assessing and quantifying the safety of ENMs during their production. The development of advanced nanometrology protocols and the use of a combination of characterisation techniques are crucial to elucidate the consequences on the bioreactivity of inhaled AgNMs. Moreover, the approach of assessing the toxicity of ENMs with different physicochemical properties (*e.g.* size, shape and surface chemistry) and understanding their possible benefit or adverse effects on environment and human health are also crucial to minimise their risks and hazards.

Krug *et al.*[242] proposed there are contradictions or inconsistencies in toxicity data possibly due to a methodology effect, different experimental conditions or the use of a completely new material. Furthermore, adequate physicochemical characterisation of AgNMs prior to the toxicity assessment and selection of appropriate doses in toxicological studies are paramount to correlate biological action with NPs properties. Furthermore, regulatory bodies such as the United States environmental Protection Agency or the Food Standards Agency (FSA) should consider the life cycle of ENMs, whether the physicochemistry of ENMs changes during their life cycle, and also identify the likely exposure pathways as well as the sustainability of the product before approval[243].

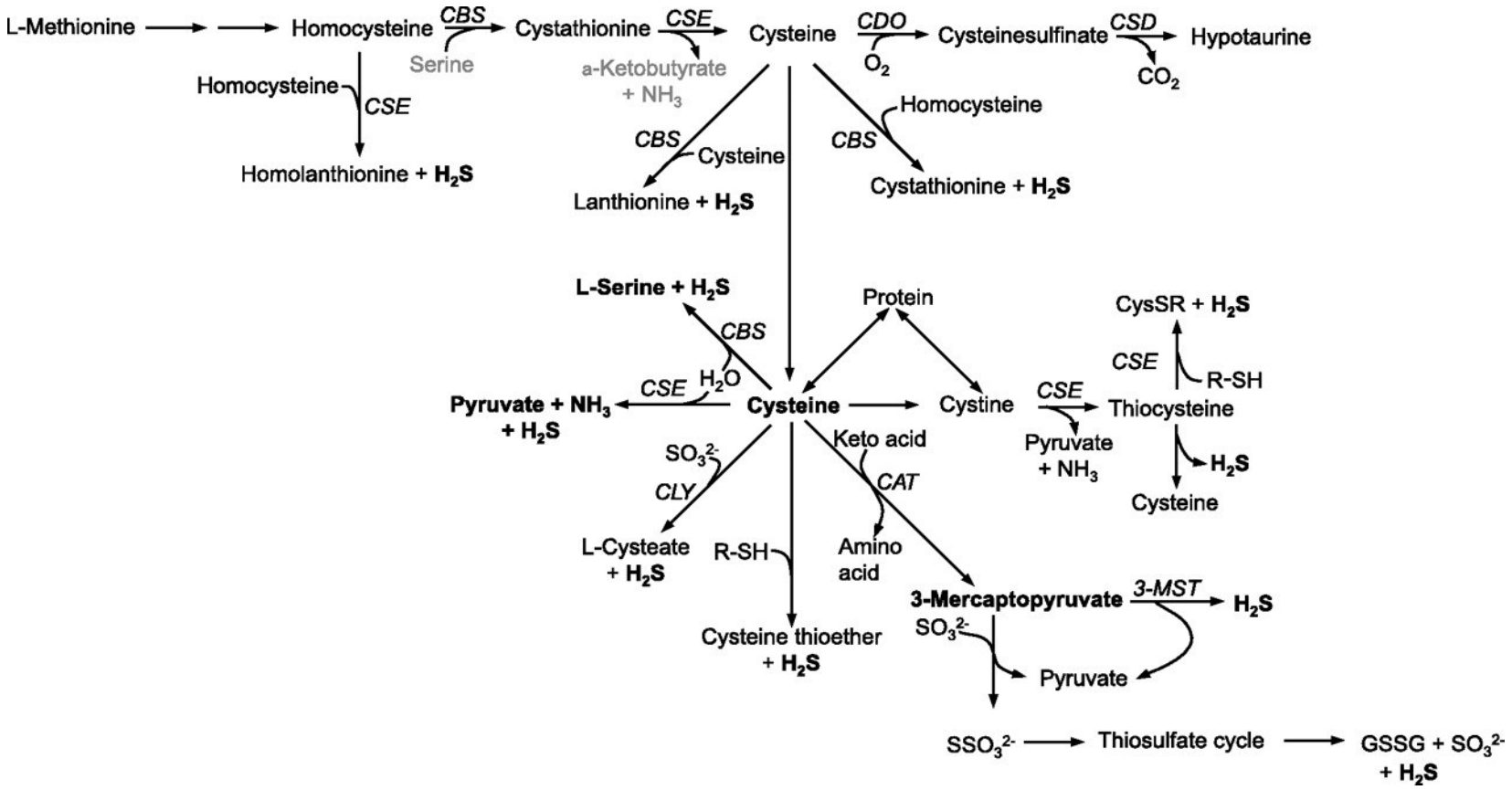

Fig. 2.14: Schematic of H_2S production and metabolism. CAT, cysteine aminotransferase; CBS, cystathionine β-synthase; CDO, cysteine dioxygenase; CLY, cysteine lyase; CSD, cysteine sulfinate decarboxylase; CSE, cystathionine γ-ligase; MPST, 3-mercaptopyruvate sulfurtransferase; R-SH, thiol[244].

3.0 Size – Dependent Electrochemical Stability of Silver Nanoparticles

3.1 Aims and Overview

Silver nanoparticles (AgNPs) have attracted much interest in electrochemical based applications, such as fuel cells[245, 246], catalysis[247], sensing[248, 249] and the reduction of organic halides[250, 251]. Therefore, stability against oxidation or loss of effective surface area is necessary for metallic nanoparticles (NPs) to retain their useful properties in long-term applications and to minimise their harmful effects on organisms and the environment. According to the literature, findings related to the electrochemical stability of nanoparticles have shown contradictory conclusions (See Sec. 2.1.3). For instance, Ng *et al.* investigated the anodic dissolution of silver nanoparticles (AgNPs), with dimensions of 1 nm, on highly oriented pyrolytic graphite (HOPG) electrode surfaces *via ex-situ* scanning electron microscopy (SEM) [63]. SEM images showed that they were stable at a potential of +500 mV greater than the reversible potential of bulk silver. Contrary to this, opposing conclusions on the electrochemical stability of nanoparticles suggesting a dissolution potential decreases with particle size can also be found (detail see 2.1.3)[4, 252].

To investigate the electrochemical stability of silver nanoparticles (AgNPs) as a function of applied potential, pH and particle size, electrochemistry techniques have been proven as a particularly useful approach for detecting and quantifying AgNPs, especially in the liquid phase[253]. Since a large variety of electrochemical processes involve the use of Ag as catalysts, nanosensors or the reactive species in various applications, the basic issues around their electrochemical stability need to be addressed. So far, only a small number of studies have reported an investigation of the electrochemical stability of Ag as a function of size, pH and potential. The lack of individualised AgNPs with a well-controlled size distribution has also resulted in inaccurate predictions on the dissolution behaviour of NPs in solution. In this work, assessment of available NPs deposition methods (namely electrodeposition, e-beam evaporation and magnetron sputtering) was done to prepare individualised AgNPs with a homogenous distribution. Among these methods, magnetron sputtering with a filtered capability proved the best method in preparing well-distributed AgNPs. A magnetron sputtering system NanoSys 500 (Mantis Deposition Ltd) was used to deposit pristine AgNPs without a stabiliser/surface coating on boron-doped diamond (BDD) substrates. The stability,

passivation and dissolution behaviour of AgNPs were determined by combining experimental studies with thermodynamic calculations.

3.2 Experimental Methods

3.2.1 AgNPs Sample Preparation

Individualised AgNPs were prepared either using electrodeposition methods (*e.g.* potentiostatic step deposition[254] and pulsed galvanostatics methods)[255] or non-electrochemical methods (*e.g.* physical vapour deposition - PVD[256] and chemical vapour deposition - CVD[257]) . Ideally, well-dispersed and homogeneous NPs distributions are favoured in order to improve the electrochemical performance of AgNPs on boron-doped diamond (BDD) electrodes. In this study, BDD electrodes were chosen as working electrodes due to their desirable electrochemical properties, such as a wide potential window, a low signal to background current ratio and a robust nature. Furthermore, they are also useful for fundamental chemical studies of electrocatalysis since they do not corrode or oxidise, but demonstrate superior chemical resistance and bio-compatibility[258]. Besides, BDD electrodes have been extensively employed as NPs supports since they do not catalyse the studied reactions. Various deposition methods (*i.e.* electrodeposition, e-beam evaporation and magnetron sputtering) were compared in order to optimise the size distribution of AgNPs on BDD working electrodes.

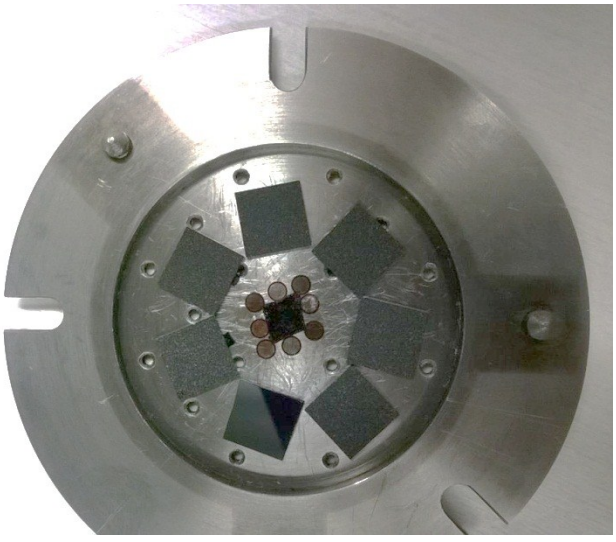

Fig. 3.1: BDD substrates and carbon-coated Cu grids (TEM) on the substrate sample holder for magnetron sputtering deposition of AgNPs.

3.2.1.1 Electrodeposition

Electrochemical deposition is one of the most attractive methods for the deposition of metal NPs. It is a simple, fast and economic method in which metal cations (i.e. Ag^{+}) from the electrolyte salt are reduced at the working electrode by applying a specific potential. The deposition of NPs can be controlled by different deposition conditions, including the deposition time, applied potential, scan rate, electrochemical method and metal ion concentration[259]. For example, there is a consensus that the deposition time is proportional to the mass loading of NPs[260]. The classical deposition technique from solutions is not practical as it results in an inhomogeneous NPs distribution. A better technique is a potentiostatic double-pulse technique, introduced by Schedule and Todorova, which can control monodispersity of NPs[261].

In this work, the double – pulse technique was used for depositing AgNPs on BDD in a 0.1 M KNO_3 solution containing 1.0 mM $AgNO_3$. The procedure was adapted from Afsaneh *et al.* to prepare individualised AgNPs (1- 10 nm in diameter), with controlled dimensions[254]. The working electrode was a boron - doped diamond substrate (BDD, Element Six Group) with a surface area of 1 cm^2. A saturated Ag/AgCl and a platinum wire served as a reference electrode and a counter electrode, respectively. The details of experimental set up were shown in Fig. 3.2. The current-time setting was done using IviumSoft^{TM} Electrochemistry Software by computer control. The detailed optimised pulse parameters were outlined as follows:

Nucleation pulse: E_1 = 130 mV vs. Ag/AgCl; t_1 = 10 ms

Growth pulse: E_2 = 240 mV vs. Ag/AgCl; t_2 = 50 s, 250 s and 500 s

The AgNPs-modified working electrodes were washed with distilled water and dried with N_2 gas after the deposition.

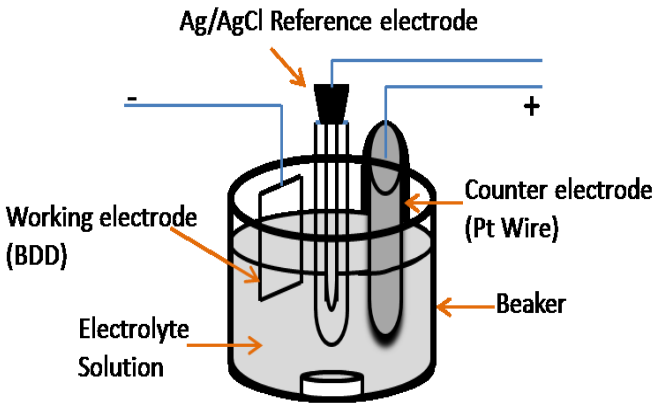

Fig. 3.2: Experimental set up of electrodeposition of AgNPs on BDD substrates.

3.2.1.2 E-beam Evaporation

E-beam evaporation is a physical vapour deposition (PVD) process in which a source material is bombarded by an electron beam drawn from a tungsten filament under ultra-high vacuum. The focused electron beam is swept across the surface of the target material and causes atoms to vaporise into the chamber. Upon impact, the high kinetic energy is converted into thermal energy, causing the evaporation of the target material (source). Therefore, these atoms condense on the substrate surfaces with a thin layer of the coating or film[262]. The basic principle of the E-beam evaporation method is described in Fig. 3.3 (a). In order to get individualised NPs on substrates, an annealing treatment is needed to initiate the de-wetting process of the thin film as shown in Fig. 3.3 (b). The E-beam evaporation process was carried out using a Mantis QPrep Deposition system with the parameters as shown in Table 3.1.

Table 3.1: The parameters used in the E-beam evaporation method.

Tooling factor (TF)	175%
Evaporation rate	0.2 A/s
HV voltage	2 V
Substrate Temperature	21 ºC
Effective mass thickness	8 nm
Current power	45 kV
Pressure	5.0×10^{-7} mbar
Thermal annealing	250, 300, 400 ºC
Annealing time	10 min

(a)

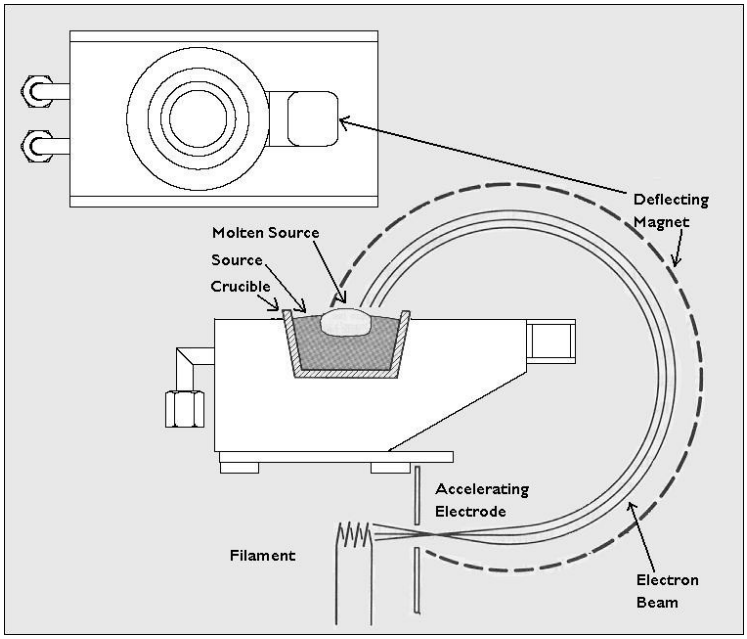

(b)

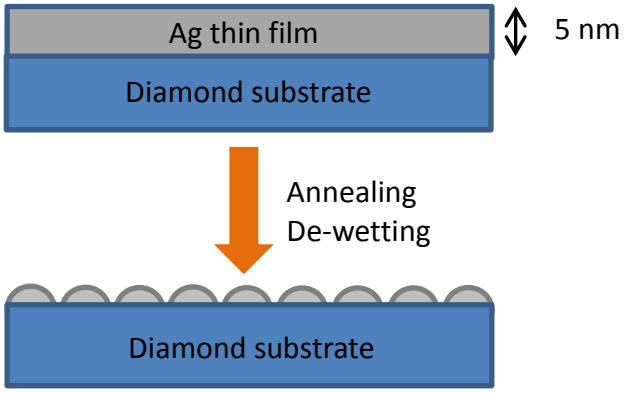

Fig. 3.3: (a) The working principle of E-beam evaporation of a Ag thin film[276]; (b) a schematic diagram of annealing treatment and de-wetting of Ag thin films, forming individual Ag islands.

3.2.1.3 Magnetron Sputtering with Size Filtering Capability

Magnetron sputtering is a plasma coating process whereby a plasma is generated and positively charged Ar^+ ions from the plasma are accelerated into the negatively charged electrode striking the target surface, resulting a layer of sputtered coating on the substrates in front of the target. The main difference between this technique and the basic Direct Current (DC) sputtering is the addition of magnetic field near the target to trap electrons, enhancing the efficiency of the initial ionisation process and allowing plasma to be generated at lower pressures. The advantage of the magnetron sputtering technique is that magnetic field causes electrons to travel for a longer

distance (spiral along the magnetic flux lines), significantly increasing the probability of further ionisation.

AgNPs with a controlled size and size distribution were deposited onto BDD electrodes with a sputtering system NanoSys 500 (Mantis Deposition Ltd, UK). The AgNPs are formed by gas-phase condensation from a flux of Ag atoms sputtered from a 99.99% purity Ag target. As suggested by Haberland *et al.*[263], the initial step of cluster formation involves three-body collisions: two hot metal atoms and a cold argon atom. The small clusters will continue to grow by inter-cluster collisions or by sticking addition Ag atoms onto the cluster as they travel through the aggregation zone. The size distribution of nano-cluster can be controlled by determining their residence time within the aggregation zone. By controlling key parameters such as sputtering power, the aggregation length and the Ar gas flow, it is possible to tune the NPs size by controlling their residence time in the aggregation zone. After the particles are formed, they enter a quadrupole mass filter (MesoQ) which is located between the NPs source and the main deposition chamber. The mass selected particle production can be monitored by a quartz crystal microbalance (QCM). The MesoQ is used to filter charged NPs of a particular size (2nm, 5nm and 12nm) selected from their wide size distribution in the aggregation region, according to their mass-to charge ratio.

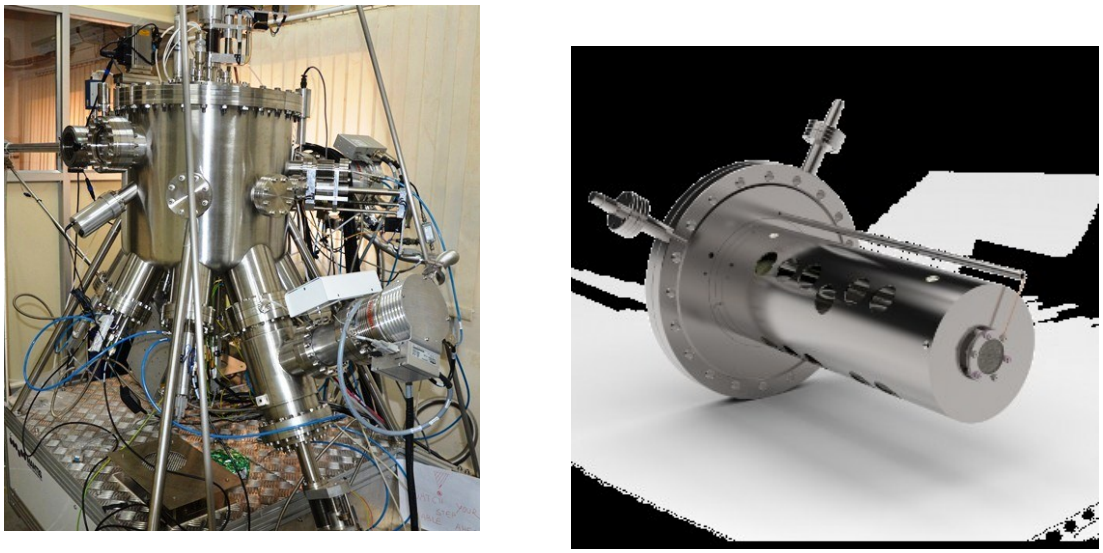

Fig. 3.4: Picture of the NanoSys 500 sputtering unit and a quadrupole mass filter (MesoQ) used in the magnetron sputtering system.

3.2.2 Sample Characterisation

The morphology, purity and size distribution of NPs prepared by these three different methods were further characterised by scanning electron microscopy (SEM) or transmission electron microscope (TEM). The afore-mentioned methods can be used to prepare individualised AgNPs with controlled size distribution, which is important in fundamental studies. Then, these samples will be further characterised using Bruker Innova Atomic Force Microscope (AFM,) to study their height profile. The crystalline structure of AgNPs was confirmed using X-ray diffraction (XRD).

SEM images were obtained using a field emission scanning electron microscopy (AURIGA40) at an accelerating voltage of 20 kV. The AgNPs has been deposited on a carbon carbon coated Copper grid and TEM images were obtained using high resolution FETEM (JEOL, JEM 2100F) at an accelerating voltage of 200 kV. The XRD pattern was recorded by X-ray diffractometer (2 PANalytical X'pert) equipped with Ni filter and CuKα (λ = 1.54 Å) radiation source.

3.2.3 Electrochemical Response of AgNPs

Electrochemical studies were performed and linear sweep (LSW) curves were recorded using an Autolab II (Ivium system, UK) unit in a Faraday cage. Each scan was performed at 100 mV/s. The potential limits for the LSW were established by scanning first from 0 to 1.2 V to determine the oxidation potential of AgNPs at pH 2, 5, 7, 10 and 12. All solutions were purged with nitrogen gas for 10 min prior to the LSW experimentation. Noninteracting perchlorate buffer was used to minimise the interaction of anions with the Ag cations and also to avoid the Ag-salts precipitation. The pH was adjusted using either 0.1 M perchloric acid ($HClO_4$) or sodium perchlorate ($NaClO_4$) solutions.

In the electrochemistry experiment, a three-electrode cell was employed consisting of a Ag/AgCl reference electrode (1M KCl, 0.175 Vvs. NHE), AgNPs on a diamond substrate as a working electrode and a Pt wire that acted as a counter electrode. Before each deposition, the working electrode was polished with alumina micropolish II (Buehler, UK) of decreasing particle size (1 - 0.1 μm) and ultrasonically cleaned in water and acetone for 5 min each. Then, each working electrode was scanned in 0.1 M nitric acid (HNO_3) solution to ensure its surface was

cleaned from impurities. Thus, these BDD substrates can be re-used by cleaning their surfaces after each CV run.

3.2.4 X-ray Photoelectron Spectroscopy (XPS)

XPS is an ultra-high vacuum (UHV) surface analysis technique and it is based on the photoelectric effect, whereby the ejection of the core electrons from the atoms is a consequence of the adsorption of the X-ray photon energy. The emitted electron with kinetic energy (E_k) is referred to as a photoelectron. The binding energy (E_b) of the electron represents the energy required to eject a photoelectron from its core orbital to a position at the Fermi level. The binding energy of the core electron relative to the Fermi level of the sample is determined by the following Einstein equation:

$$h\nu = E_b + E_k + \phi \tag{3.1}$$

$$E_b = h\nu - E_k - \phi \tag{3.2}$$

Where $h\nu$ is the photon energy of soft X-rays such as Al Kα (1486.7 eV) or Mg Kα (1253.6 eV); E_k is the kinetic energy of the emitted electron, which can be measured by the energy analyser; and the ϕ is the work function of the analyser/spectrometer (~ 4 – 5 eV). The work function is the energy required to eject the photoelectron from the Fermi level into vacuum. In order to minimise radiation damage to non-metallic surfaces, soft X-rays are used instead of hard X-rays (*i.e.* Mo Kα at 17.5 keV) (see Fig. 3.5).

X-rays can penetrate up to the depth of 10 μm from the surface to excite electrons and generate photoelectrons, but only those electrons within ~ 5 - 10 nm from the surface are detected. This is because when photoelectrons travel through the solid, they will interact with other electrons in the sample, thus losing some of their energy due to inelastic scattering, contributing to the substantial background as seen in XPS spectra. Fig 3.6 shows a typical XPS spectrum in which intense and narrow peaks can be seen, which are associated with photoelectrons ejected from a core orbital. The presence of peaks at particular energies indicates the existence of the specific elements in the sample. Moreover, the intensity of the peaks is correlated to the concentration of the element within the sample region. Therefore, XPS provides quantitative and chemical states analysis of the surface composition. Although peaks

from other processes (*e.g.* Auger) can be seen in the XPS spectrum, they are not the focus of this study.

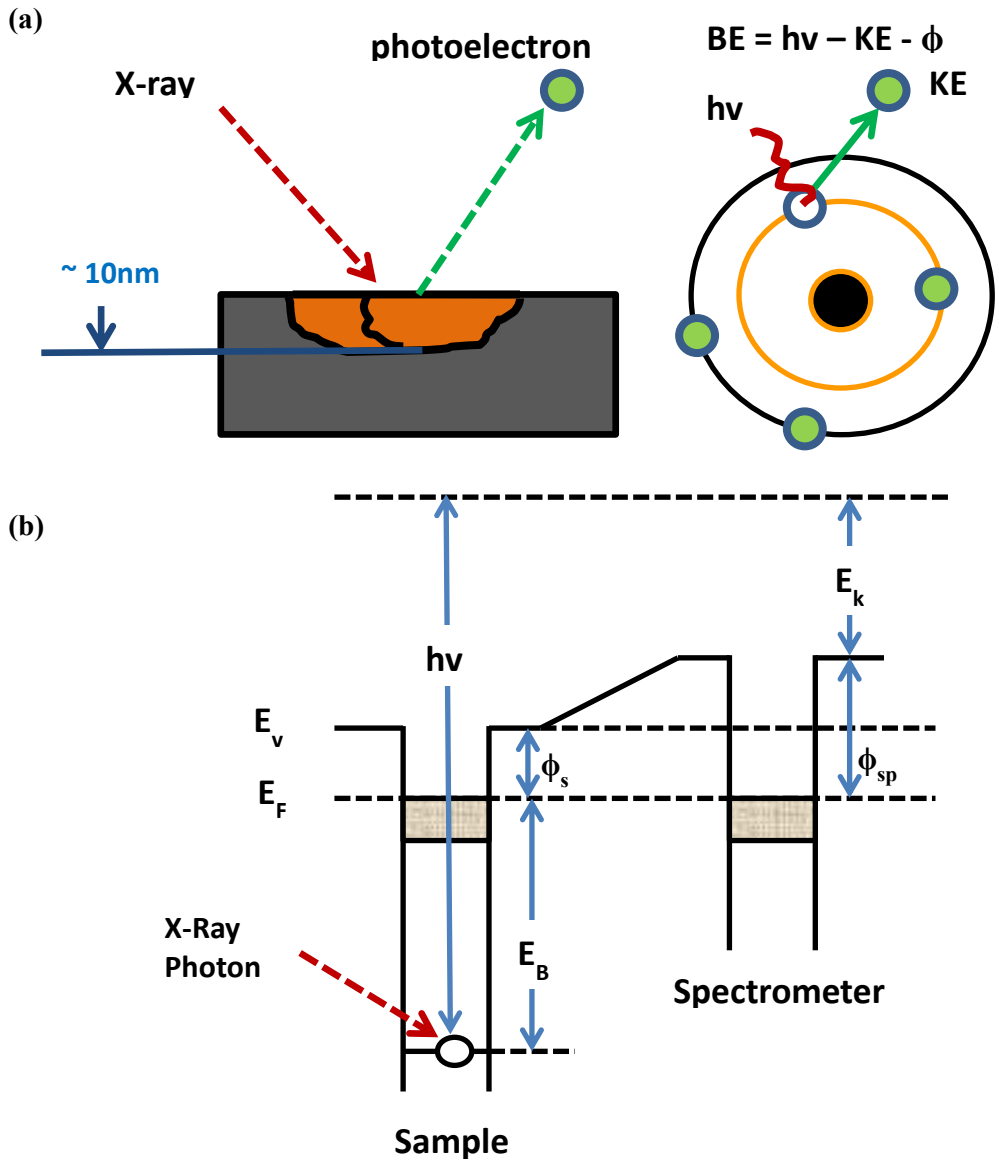

Fig. 3.5: A schematic diagram showing the basic principle of XPS emission process as a sample is irradiated with photons of energy hv and atoms on the surface emit electrons after direct transfer of energy from the photons to the core-level electron; (b) Energy levels of core orbitals and spectrometer. Subscripts s and sp refer to sample and spectrometer, respectively.

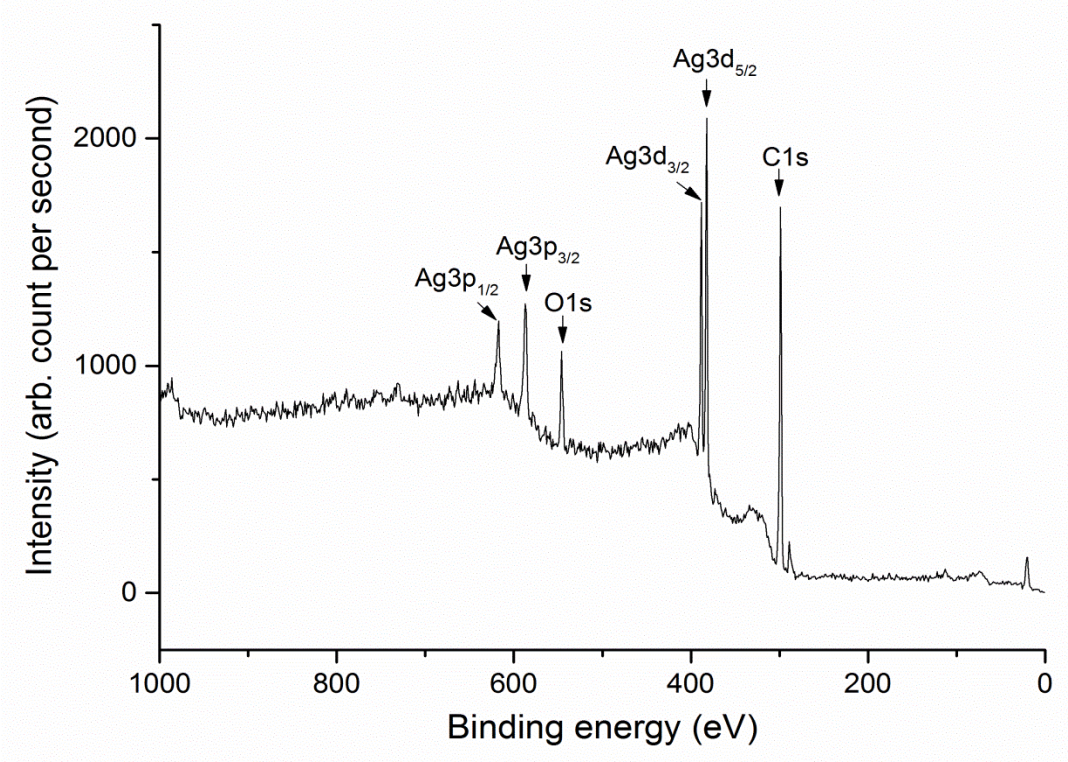

Fig. 3.6: A typical XPS survey spectrum taken from a 5.2 ± 2.5 nm AgNPs on BDD sample.

In the experiment, the surface composition of the AgNPs sample (approximately the top of 4 nm) was analysed using a X-ray photoelectron spectrometer, maintained at a pressure in the 10^{-9} Torr range. The curve fitting was done using XPSpeak41 software. A Shirley background correction was applied when the background at lower BE was larger than at higher BE, with a range of 10 eV or less. In the rare case where the assumptions of the Shirley method were not met, a linear background was used. Then, each of the characteristic peaks was fitted using a mixture of Gaussian and Lorentzian functions. In most peak fitting, constraints were avoided to allow the software to fit peaks automatically, but sometimes they were necessary (*e.g.* spin states). XPS peaks were calibrated to the position of C1s (285 eV). Peaks intensities were normalised to that of the F1s photoelectron peak by 'atomic sensitivity factors' (ASF)[264].

*The XPS testing was carried out by Geoff Nelson at Oxford University, except the data analysis.

3.2.5 E-pH Theoretical Calculations

Studying the stability of AgNPs is highly interesting from a fundamental point of view. Generally, metal NPs are known to transform quickly into metal ions or

oxides, depending on the environment condition (*e.g.* ion concentration and solution pH). Pourbaix diagrams can be used to predict the most stable state of a material in aqueous environments as a function of pH and potential. Fig. 3.7 shows the potential-pH equilibrium diagram for the silver-water, at 25°C.

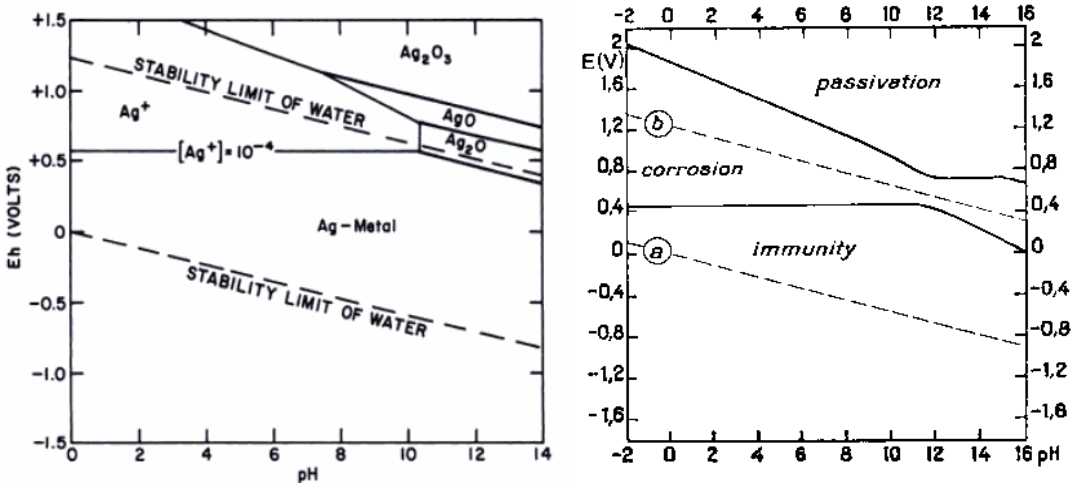

Fig. 3.7: (a) The Ag Pourbaix diagram for the system silver-oxygen-hydrogen (Ag-O-H) and (b) the theoretical domains of corrosion, immunity and passivation of silver, at 298K (25°C). The dotted line (a) and (b) correspond to redox potentials determined by hydrogen and oxygen saturation at one standard atmosphere, respectively[265].

The thermodynamic information in aqueous corrosion is normally summarised for practical purposes in Pourbaix diagram. These diagrams are constructed from the standard electrode potential and equilibrium constant for a given metal as a function of redox potential and pH, distinguishing the boundary positions between the corrosion, passivation and immunity zones[265]. Fig. 3.7 (b) deduces from the Fig. 3.7 (a), summarising the stability boundaries of the silver-water system. The observed two parallel dashed lines indicate the upper and lower stability limits for liquid water at 25 °C.

Let us consider reactions between Ag, H and O and discuss their relationship as shown in Fig. 3.7[2]:

$$Ag \rightarrow Ag^{+} + e^{-} \tag{3.3}$$

$$Ag + \frac{1}{2} H_2O \rightarrow \frac{1}{2} Ag_2O + H^{+} + e^{-} \tag{3.4}$$

$$Ag + H_2O \rightarrow \frac{1}{2} Ag_2O_2 + 2H^{+} + 2e^{-} \tag{3.5}$$

$$Ag + \frac{3}{2}H_2O \rightarrow \frac{1}{2}Ag_2O_3 + 3H^+ + 3e^- \quad (3.6)$$

$$Ag + 2H_2O \rightarrow Ag(OH)_2^- + 2H^+ + e^- \quad (3.7)$$

It is well known that silver resides high on the electromotive series, thus it occupies much of the stable region as shown in the Pourbaix diagram (Fig. 3.7). In acid solutions, Ag dissolves directly to form monovalent silver ions in solution. The presented diagram uses 10^{-6} M as the standard concentration to define regions of stability. Generally, Ag is stable in alkaline solutions. The oxides are the only stable solids in contact with aqueous solutions at high pH. The stability field for silver oxide (Ag_2O) lies just within the corrosion boundaries at pH 12. The other silver oxides, such as Ag_2O_2 and Ag_2O_3 exist in the passivation region of the diagram, but these are all relatively unstable at room temperature and standard pressure. In addition, anion such as Cl^- and S^{2-} are not included in the E-pH diagram.

Corrosion processes involve mixed potential systems where the anodic reaction occurs at the anode ($M \Rightarrow M^{n+} + ne^-$) and reduction reactions occur at the cathode. The most significant reduction reactions which occur during aqueous corrosion are the oxygen reduction and hydrogen reduction reactions:

Oxygen reduction: $O_2 + 2H_2O + 4e^- \rightarrow 4OH^-$ (3.8)

Hydrogen reduction (evolution): $2H^+ + 2e^- \rightarrow H_2$ (3.9)

These cathodic reactions will increase the local pH at the cathode site. As mentioned earlier, Pourbaix diagrams are potential-pH diagrams illustrating those domains in which a metal is immune and protected from corrosion, the area in which corrosion occurs, and also the area in which a protective passivating oxide layer could form on the metal. Pourbaix or potential-pH diagrams are constructed using the relevant Nerst Equations as shown below[252]:

(i) Direct electrodissolution: $M^{n+} + ne^- \leftrightarrow M$ (3.10)

$$E_{M/M^{n+}} = E^{o}_{M/M^{n+}} + \frac{2.303\,RT}{nF}\log(M^{n+}) \quad (3.11)$$

(ii) Oxide formation: $M_aO_n + 2nH^+ + 2ne^- \leftrightarrow aM + nH_2O$ (3.12)

$$E_{M/M_aO_n} = E^{o}_{M/M_aO_n} + \frac{2.303\,RT}{F}\,pH \qquad (3.13)$$

(iii) Chemical dissolution of the oxide:

$$M_aO_n + 2nH^+ \leftrightarrow aM^{n+} + nH_2O \qquad (3.14)$$

$$\log K = -\,2n\,pH - a\log(M^{n+}) \qquad (3.15)$$

The Nernst equation is derived entirely from thermodynamics, the Pourbaix diagram can be used to determine which species is thermodynamically stable at a specific potential, E and pH, which is valid for the bulk material. However, it provides no information about the kinetics of the oxidation process by which surface energy (ϒ) term is not included in the classic model. Since metal nanoparticles behave differently from their bulk metal due to their high surface energy and larger fraction of atoms at the vertex and edge, their interfacial free energy and surface stress become increasingly important and should be included in the thermodynamic calculations.

Assuming isotropic surface stress and surface energy, the Gibb-Thomson relation of each of these electrochemical and chemical equilibria for spherical NPs can be developed. Considering a reaction involves the reversible electro-dissolution and deposition of metal M, the chemical potential (μ) of the metal cation in the liquid phase at concentration M^{n+} surrounding a finite size particle is[252]:

$$\mu_l = \bar{\mu}_l(\bar{M}^{n+}) + RT\ln(M^{n+}/\bar{M}^{n+}) \qquad (3.16)$$

where $\bar{M}^{n+}$ = saturation concentration for a planar surface

The chemical potential of the metal in the NPs is:

$$\mu_s = \bar{\mu}_l(\bar{M}^{n+}) + f_M\Omega_M(2/r) \qquad (3.17)$$

where f=surface stress; Ω = molar volume of the solid and r is radius of NPs.

By applying the equilibrium condition, the chemical potential of metal cation in the liquid phase ($\bar{\mu}_l(\bar{M}^{n+})$) in equilibrium with the planar solid surface ($\bar{\mu}_s(\bar{M})$):

$$\bar{\mu}_s(\bar{M}) = \bar{\mu}_l(\bar{M}^{n+}) \qquad (3.18)$$

For a finite-size solid immersed in a fluid containing a single soluble component of the solid, there is a difference in the Laplace pressure for a finite-size solid and a liquid, thus the chemical potential of the component in the solid and fluid phases:

$$\mu_s - \mu_l = (f - \gamma)\Omega(2/r) \tag{3.19}$$

Subtracting Eqn (3.17) from Eqn (3.16):

$$\bar{\mu_l}(\bar{M}^{n+}) + f_M\Omega_M(2/r) - \bar{\mu_l}(\bar{M}^{n+}) - RT\ln(M^{n+}/\bar{M}^{n+})$$

$$= f_M\Omega_M(2/r) \quad - \gamma_M\Omega_M(2/r) \tag{3.20}$$

Therefore,

$$RT\ln(M^{n+}/\bar{M}^{n+}) = \gamma_M\Omega_M(2/r) \tag{3.21}$$

Since $\Delta G = - nFE_{cell}$ and the $\Delta G = \Delta G° + RT \ln (Q)$

$$E_{M/M^{n+}}(r) - E_{M/M^{n+}} = -\frac{\gamma_M\Omega_M}{nF}(2/r) \tag{3.22}$$

Thus, eq (3.22) gives the surface energy corrected form of potential, E. By using the equation, the potential at which AgNPs oxidise and dissolve into Ag^+ ions can be determined (assuming accurate values of γ_M and Ω_M can be found).

3.3 Results and Discussions

3.3.1 Characterisation of As-prepared AgNPs

Individual AgNPs (without surface coatings) were prepared using three different techniques, namely electrodeposition, e-beam evaporation and magnetron sputtering with size filtering capability. After sample preparation, the morphology of the NPs was observed using either the JEOL2000 TEM or the Auriga40 SEM. The method able to produce individualised spherical AgNPs with the best homogeneity was chosen for size - dependent electrochemical studies. The results obtained from these three different methods are shown in sub-section 3.3.1 and the comparison of the techniques is summarised in Table 3.2.

3.3.1.1 Electrodeposition

The electrodeposition method has been reported as an extremely powerful technique in the development of macroelectronics devices such as photovoltaic (PV) solar panels and also produces excellent quality thin film devices. It has been cited with

advantages such as ease of implementation, low energy consumption, little capital investment and ability to achieve conformal coverage of complex surfaces.

In order to deposit small electroactive NPs of Ag on diamond with a homogeneous size distribution, the potentiostatic double pulsed method was chosen. This double pulse technique is a simple and fast method for controlling the size of AgNPs electrodeposited on BDD surface. This technique was introduced by Scheludko and Todorova [266] based on an extremely short first pulse, which is more negative than the critical potential for nucleation (E_{crit}), to initiate nucleation at the high cathodic polarisation, followed by a much longer second pulse at a lower overpotential to inhibit the generation of new nuclei and promote the growth of existing nuclei [261, 267]. The ideal situation is where nucleation only occurs in the first pulse and the growth of nuclei is controlled by the second pulse, having a potential more positive than E_{crit} but more negative than the reduction potential[268].

Fig. 3.8 illustrates the cyclic voltammograms of $AgNO_3$ in 0.1 M KNO_3 when the potential was swept from +0.7 V to -0.2 V and then back to +0.7 V versus Ag/AgCl. This set up is a general phenomenon to electrodeposit and strip a metal from a graphite electrode, modified from the work published by Afsaneh *et al.* [254].

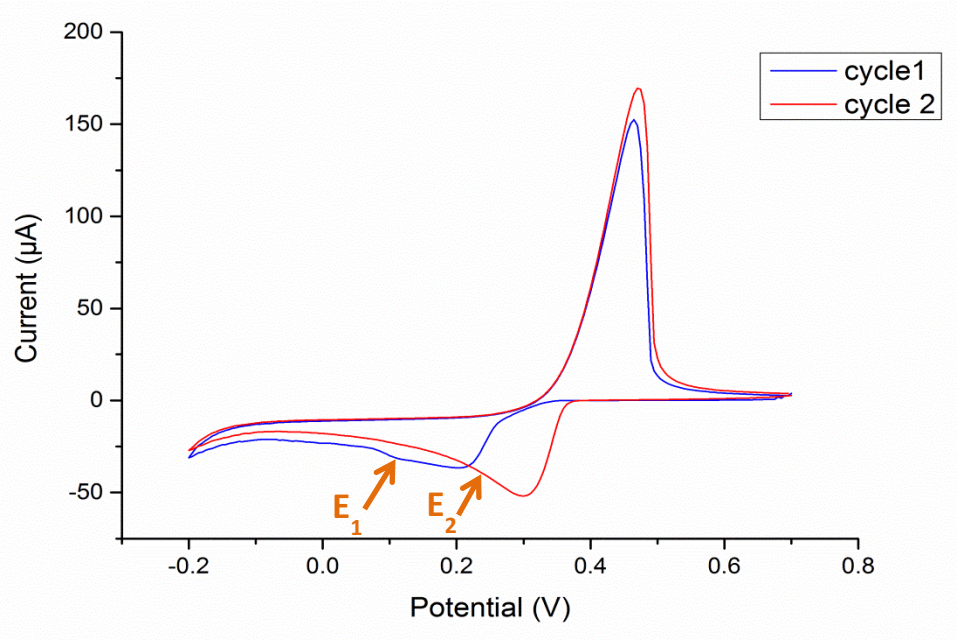

Fig. 3.8: Cyclic voltammograms of 1.0 mM $AgNO_3$ in 0.1M KNO_3 on BBD surface. Scan rate 0.1 V/s.

Cyclic voltammetry (CV) was used to characterise the system and the appropriate deposition potentials were chosen for the nucleation and growth of NPs. As seen in Fig. 3.8, the cyclic voltammogram of $AgNO_3$ showed a reduction peak at 0.2 V (vs. Ag/AgCl), consistent with Ag^+ ions being reduced and deposited onto the electrode surface[254]. In the first cycle (blue line), the oxidation of Ag^0 at the surface of the BDD substrate to Ag^+ occurred at 0.45 V. The second cycle (red) shows a cathodic peak at *ca*. + 0.32 V which is different from the first cycle, suggesting that not all Ag^0 was stripped at the first cycle and that deposition of Ag^+ on pre-existing Ag^0 nuclei occurred at the second cycle[63]. This is due to the activation overpotential of Ag for diamond. Therefore, to deposit Ag, a nucleation pulse of 0.13 V (vs. Ag/AgCl) with a duration time of 10 ms was applied to initiate nucleation of Ag on BDD. Then, the growth of Ag nuclei was promoted by holding the potential at 0.28 V (vs. Ag/AgCl) for varying deposition time (50s, 250s and 500s). These three steps are summarised as below:

Mode (1): E=0.130V for 0.01s
Mode (2): Potential held for 5 s
Mode (3): E=0.280 V for 50 s to 500 s

After the electrodeposition process, the samples were dried in a desiccator and then were analysed by the SEM.

Figure 3.9 shows SEM images of AgNPs on BDD electrode surfaces following the cyclic voltametry experiments either aerated or non-aerated by N_2 gas prior to analysis. By using an aerated electrolyte solution, CV curves were produced that followed the pattern with clear redox couple for $Ag \longrightarrow Ag^+ + e^-$ as seen in Fig. 3.9(c). Nevertheless, unexpected behaviour was observed for samples with de-aerated electrolyte solutions. As shown in Fig. 3.9 (d), peak A and peak B reduce intensities, with a new peak (peak C) on the second scan growing during the subsequent scans. This might be due to the role of O_2 in the non-aerated solution which seems to alter the growth of particles on BDD. Thus, each system was thoroughly de-gassed with N_2 gas for 10 min prior to the deposition process to minimise the agglomeration of the NPs.

As shown in Fig. 3.10, an increasing of growth time influences the structure of the AgNPs and leads to NPs aggregation. Electrodeposition of NPs was taken at

different pulses and the narrower NPs distribution was found under the optimum nucleation pulse (E=0.130 V for 0.01 s) and followed with growth pulse at E=0.280 V for 250 s. However, irregular shaped and larger-sized of NPs were found at growth time 500 s.

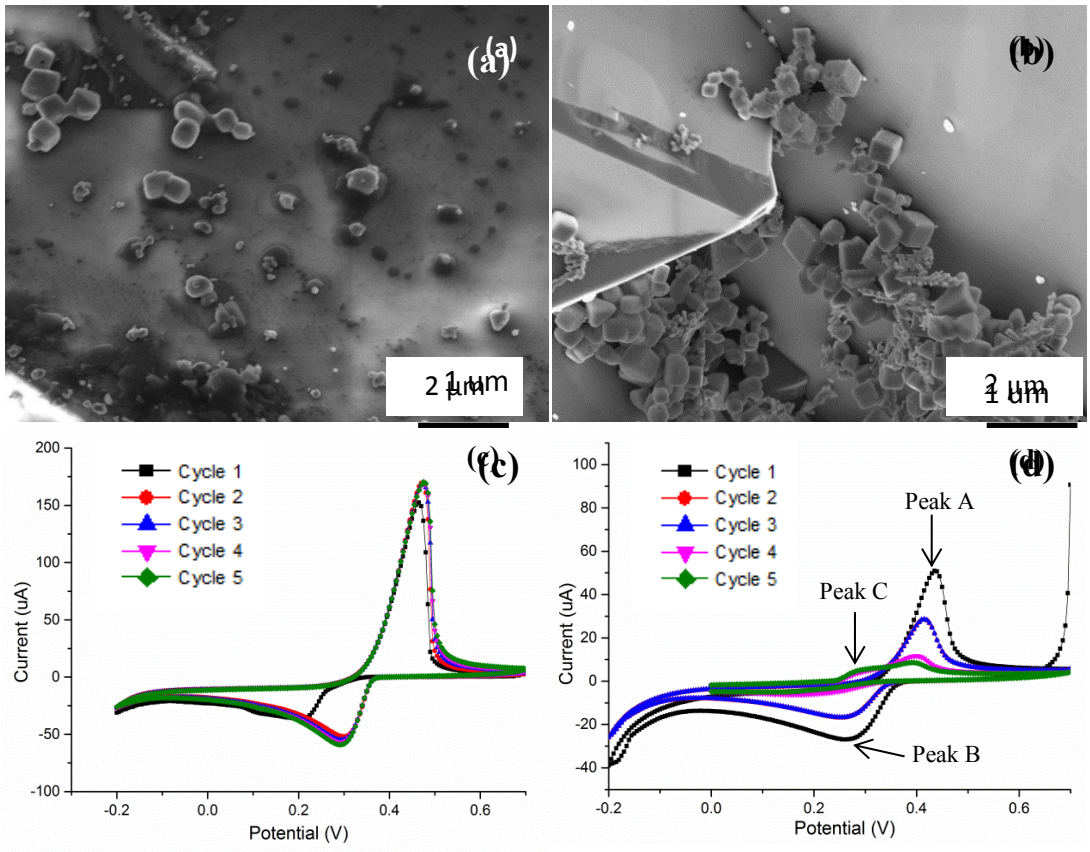

Fig. 3.9: SEM morphologies of AgNPs on BDD after cyclic voltammetry (CV) experiments at which (a) the system was throughly degassed with N_2 gas for (a) 10 min and (b) 0 min prior to analysis. Their cyclic voltammograms (5 cycles) in 1mM $AgNO_3$ in 0.1M KNO_3 at a scan rate of 10 $mV.s^{-1}$ are shown in (c) and (d), respectively.

To obtain the average diameter of the NPs at different growth time, 300 particles were randomly selected from SEM images and measured using *Image J* software. The average size of the NPs was affected by growth time, increasing from 28.9 nm to 98.1 nm as the growth time rose from 50 s to 500 s. The observed agglomeration of NPs might be due to the re-deposition of Ag ions onto the nuclei or particles on the substrate in order to reduce the total energy in a system. Cluster aggregation increased with the increasing of growth time. Moreover, a large amount of AgNPs were deposited on grain boundaries with a non-uniform size distribution as shown in Fig. 3.10

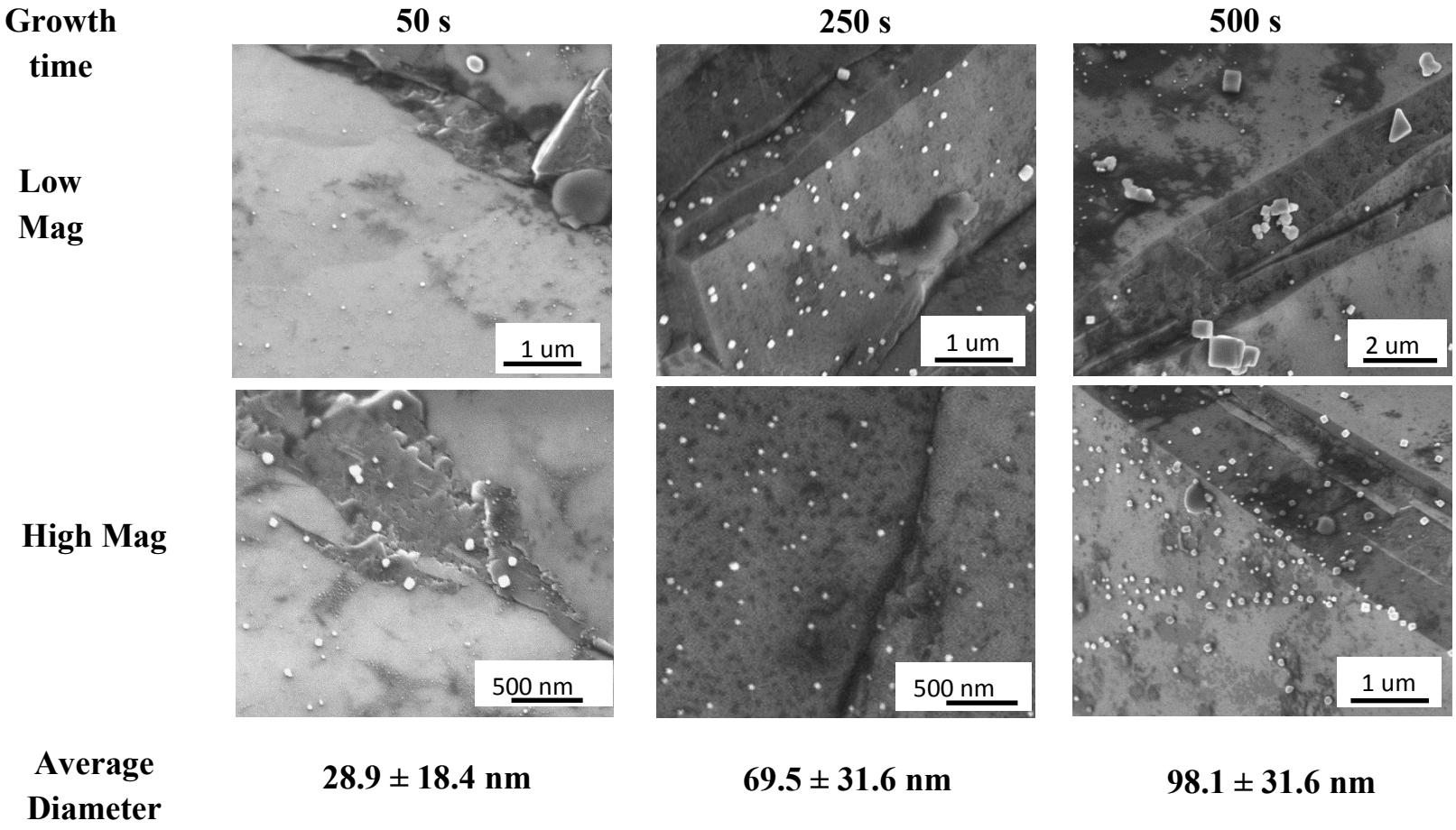

Fig. 3.10: SEM images of AgNPs on BDD at different deposition conditions: E_1= 0.13V vs. Ag/AgCl, t_1= 10 ms; E_2= 0.24 V vs. Ag/AgCl, t_2= 50 s, 250 s, 500 s.

Regarding the deposition of NPs, most of them were deposited as spheres or nanocubes with an average size larger than 50 nm. Non-spherical or irregularly shaped NPs and the difficulties in depositing smaller-sized NPs (*e.g.* diameter of NPs < 10 nm) mean this method is less suitable for fundamental electrochemical studies, such as size-dependent redox potential of elemental NPs which is of major interest in this study. Moreover, boron sites on diamond substrates are electroactive and also their grain boundaries may affect the homogenous distribution of NPs.

3.3.1.2 E-beam Evaporation

E-beam evaporation is a popular method to deposit metal NPs on a diamond surface. Uniform NPs deposition can often be obtained by E-beam evaporation followed with heat treatment, as the deposition is unaffected by inhomogeneous distribution of boron at BDD or by the grain boundary. In this experiment, AgNPs were deposited as a thin layer by thermal evaporation and then annealed. Annealing is needed to initiate the de-wetting of the thin film in order to get individualised NPs.

In this work, the size of the NPs was tuned by thermal annealing at temperature from 150 °C to 400 °C, well below the melting point of Ag. During annealing, the particles merged together to form islands due to their surface tension. In this technique, NPs were distributed evenly with more homogeneous NPs size distributions as compared to the afore-mentioned electrodeposition method. To investigate the morphological variation of Ag islands, 200 NPs were randomly chosen from SEM images and their diameters were analysed using *Image J* processing software. As seen in the size distribution histogram (Fig. 3.11), the average NP size was found to increase from 8 nm to 14.2 nm when the annealing temperature increased from 150 ºC to 400 ºC. Uniformly distributed spherical AgNPs were deposited on BDD with no distribution of NPs at grain boundaries.

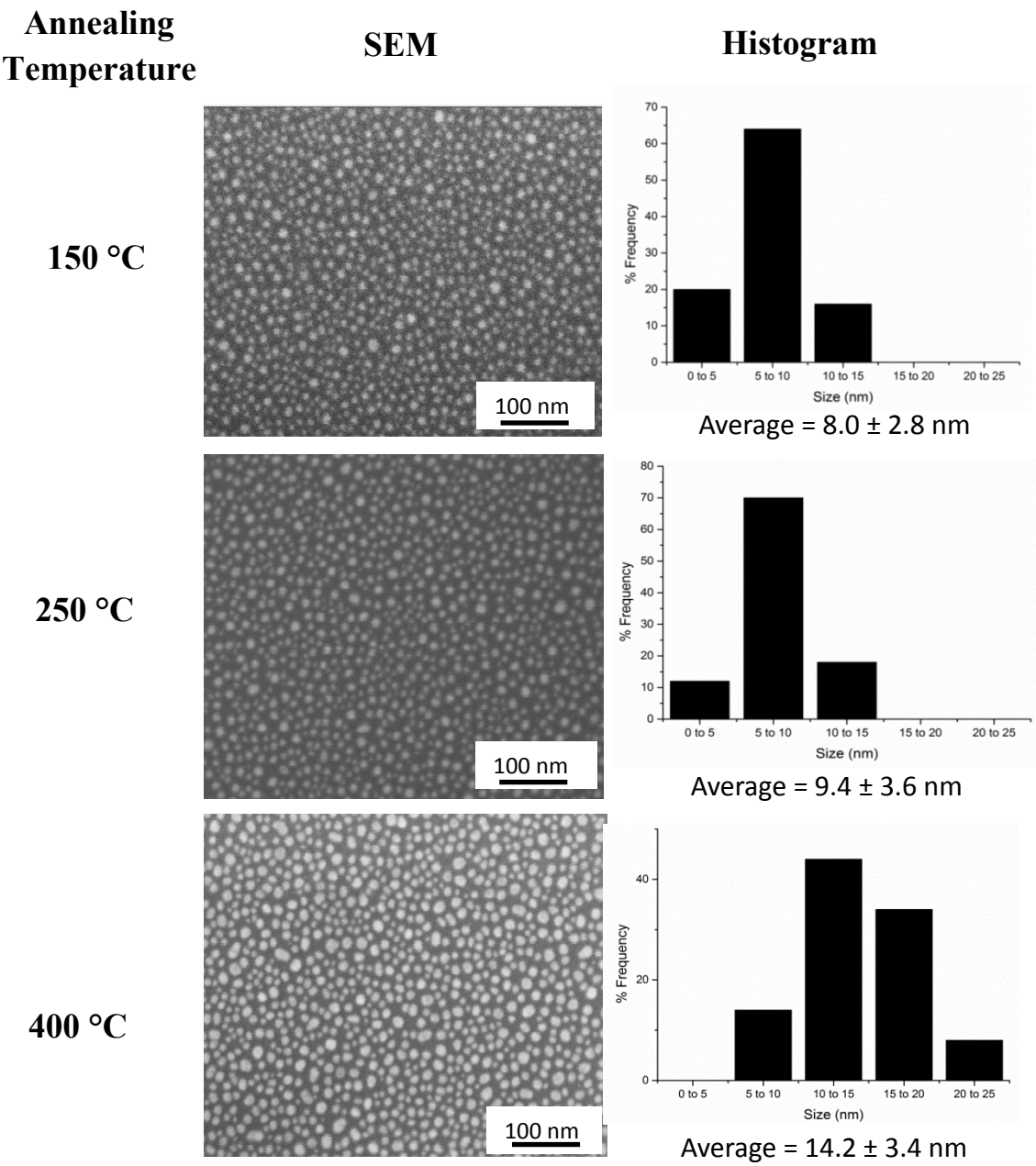

Fig. 3.11: SEM images of AgNPs on BDD resulting from annealing of Ag thin films as a function of annealing temperature for 10 min and their size distribution histograms.

The greatest advantage of the application of an ultra-high vacuum condition in sample preparation chamber is to reduce unwanted physicochemical effects, such as water, oxidation on NPs due to ambient or solution conditions. However, NPs with an average size < 5 nm were difficult to obtain because of the annealing treatment process, which reduced its application to nanosized electrochemical studies.

3.3.1.3 Magnetron Sputtering with Size Filtering Capability

A new generation of a Mantis Deposition System (Nanosys500) has been developed which allows deposition of NPs with a controlled size ranging from 20 atoms up to 20 nm[269]. It also enables stoichiometric NPs with controlled shapes and sizes to be obtained. In this work, NPs with a narrow size distribution were successively prepared by magnetron sputtering with size filtering capability (Nanoparticle High-Mass Filter MesoQ). Fig. 3.12 shows the TEM images of AgNPs and their size distribution histogram. The average NPs sizes were larger than the selected mass from the quadrupole mass filter as seen from the histogram. For instance, NPs as large as 15 nm could be found on the substrate with a 2 nm-sized filter used in the magnetron sputtering process. This might be due to the diffusion of NPs which have a high reactive surface energy when they travel along the aggregation zone before reaching the diamond substrate during the sputtering process. Generally, naked metallic NPs without an organic stabiliser tend to form agglomerates to reduce the energy associated with their high surface area to volume ratio. Moreover, a fraction of the particles produced may have neutral charges that cannot be filtered by the quadrupole. However, this fraction will decrease significantly when they pass through the mass filter and the einzel lens, due to the focusing of charged particles before entering the sample preparation chamber. Therefore, the very large particles observed on BDD are believed to be neutral particles that may have reached the substrates.

From Fig. 3.13, SEM images demonstrated that the measured average size of NPs was not significantly different from the TEM measurement when the samples with the same filter size (*e.g.* 2 nm) were compared. SEM images (Fig. 3.14 (c)) also showed that the NPs were distributed evenly on BDD surfaces with a homogeneous distribution. However, more aggregation of NPs was observed when a larger filter size was used (*e.g.*MesoQ filter at 12 nm). Therefore, larger mass filters are unsuitable for the controlled NP deposition of < 10 nm size. For a size filter < 12 nm, the magnetron sputtering deposition method is ideal to prepare pristine NPs with an average size smaller than 10 nm with controlled size distribution.

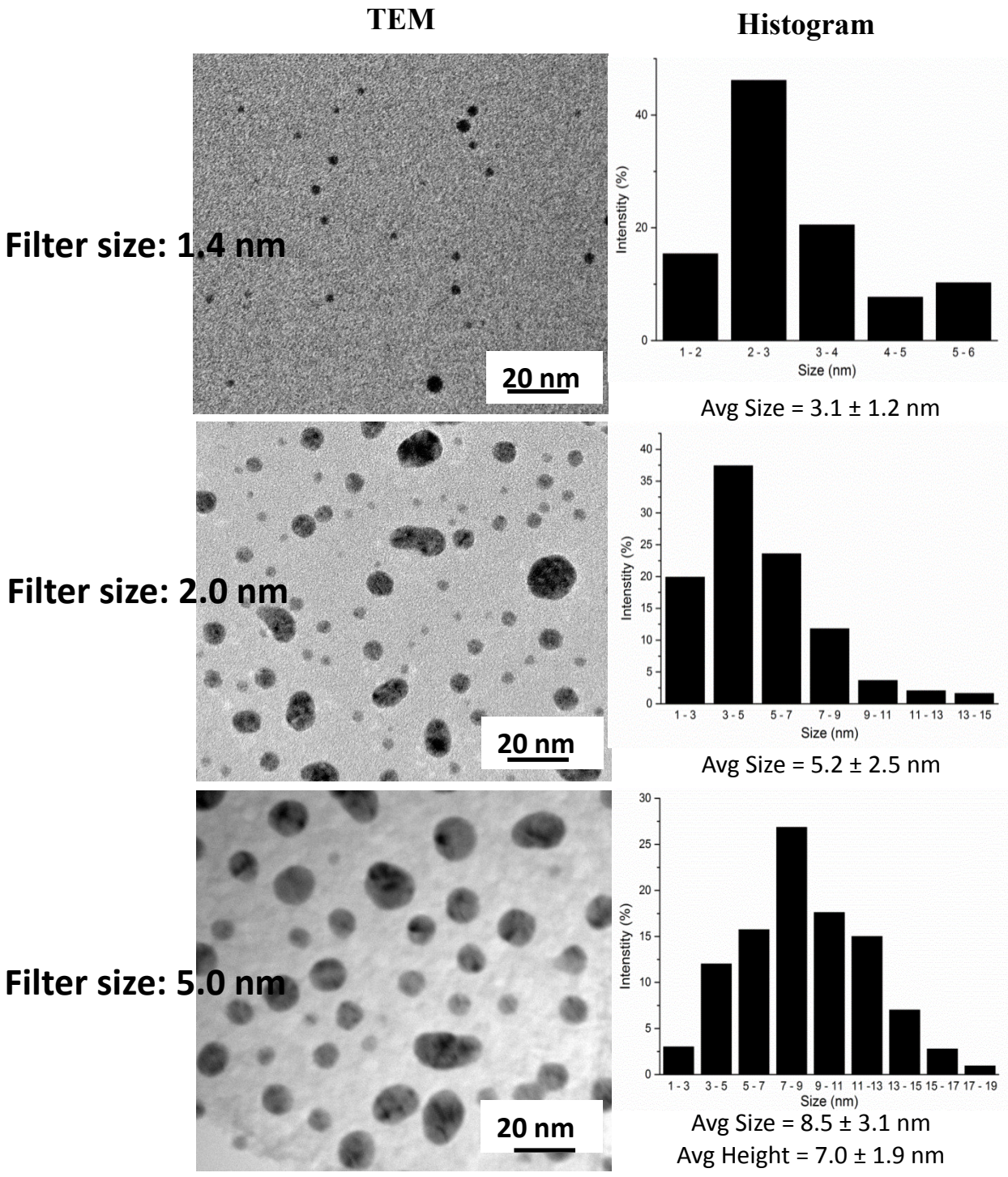

Fig. 3.12: TEM images of AgNPs deposited on BDD *via* the magnetron sputtering method with different filter sizes and their size distribution histograms.

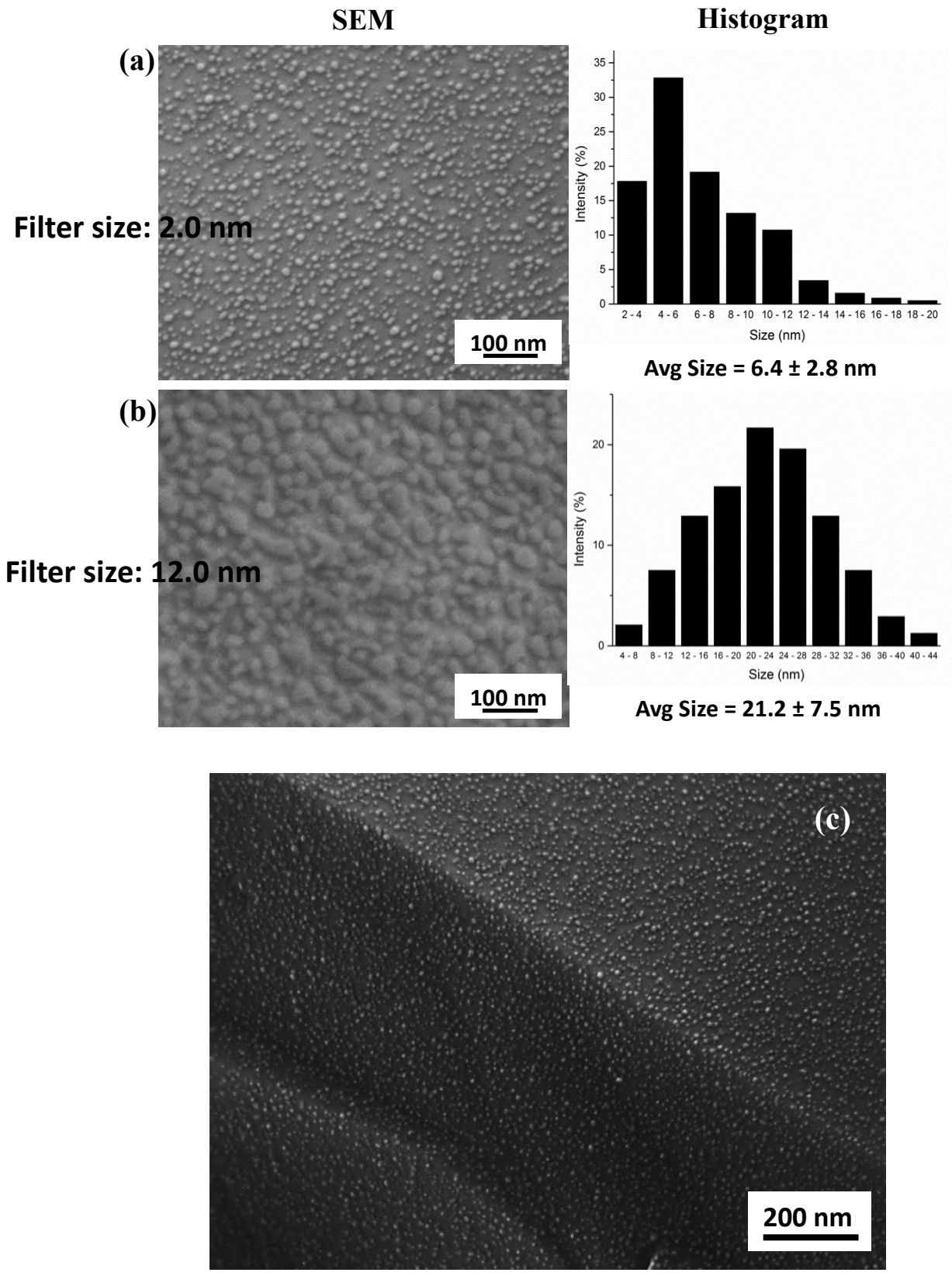

Fig. 3.13: SEM images and size distribution histograms of AgNPs deposited on BDD *via* magnetron sputtering method with different filter sizes (a) 2 nm and (b) 12 nm. (c) AgNPs were distributed on the BDD surface homogenously.

3.3.1.4 Comparison of Deposition Methods

Production of AgNPs with a homogenous size distribution is a key factor in studying the fundamental electrochemistry of NPs. As described earlier, AgNPs were prepared using different deposition methods and these sample preparation techniques are summarised in Table 3.2. Among these techniques, magnetron sputtering with a size filtering capability was chosen as the most ideal sample preparation method since the controlled size distribution of NPs with an average size < 10 nm were required for the subsequent electrochemical studies. Therefore, samples prepared by magnetron sputtering method were further characterised using XRD and AFM prior to the E-pH studies.

Table 3.2: Sample preparation techniques of AgNPs on BDD for E-pH studies.

Electrodeposition	E-beam Evaporation	Magnetron Sputtering
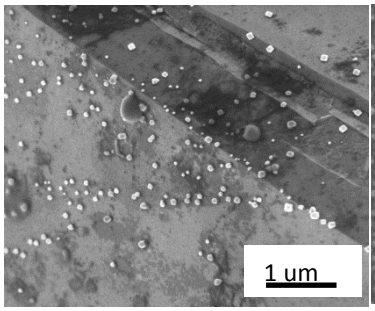	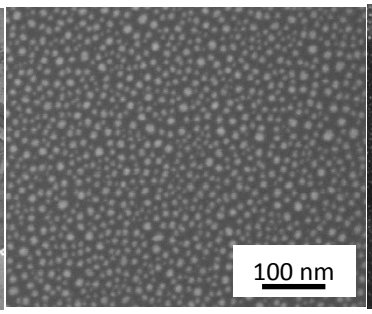	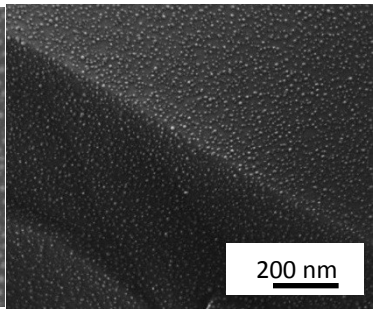
• NPs were found in spherical form and as nanocubes • Inhomogeneous distribution • NPs > 50 nm • Lower cost • Less complex	• Uniform distribution • Homogeneous distribution • Not ideal for NPs < 5 nm due to annealing treatment.	• Uniform distribution • Homogeneous distribution • Not ideal to deposit larger-sized NPs • Ideally used to prepare NPs < 10nm.

3.3.1.4 XRD

Fig. 3.14 showed the XRD pattern of as-prepared AgNPs *via* the magnetron sputtering method. The XRD peaks were dominated by a diamond layer but the inset showed the small Ag peak, consistent with FCC crystal structure of Ag (111) plane. For noble metal as Ag, the (111) facets have the lowest energies and thus dominate the surface area of NPs[270]. The height of the NPs was measured by AFM but this technique was not ideal for smaller-sizes of NPs (< 5 nm) especially on the rough surface of BDD. AFM is prone to overestimate the NPs diameter due to its tip-convolution effects but it provides a good estimation of the NPs height. The average height of NPs for the MesoQ filter size 5 nm is 7.0 ± 1.9 nm, showing that the NPs were not in a perfect spherical shape as first noted from SEM/TEM evidence but rather that some of them had the shape of an ellipse (see Fig. S1).

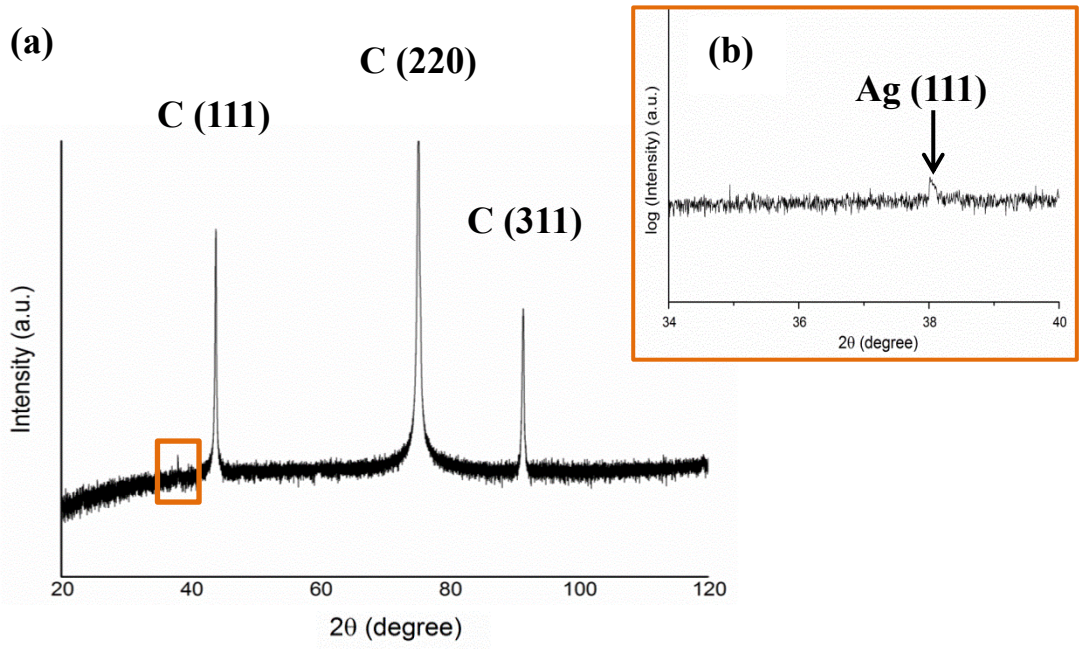

Fig. 3.14: (a) XRD peaks of the carbon substrate and (b) the insert shows the XRD pattern of AgNPs on a diamond substrate.

3.3.2 Electrochemical Response of AgNPs (Linear Sweep)

Individualised AgNPs were successively prepared by the magnetron sputtering deposition process and then samples were characterised as shown in 3.3.1. To investigate the electrochemical stability of AgNPs as a function of size and pH, anodic potentials of NPs were determined by the linear polarisation sweep technique. Fig. 3.15 shows a familiar phenomenon associated with the stripping of 5.2 nm AgNPs from BDD electrode surface by linear sweep voltammetry. The potential was swept from open circuit potential (OCP) to 1.0 V vs. Ag/AgCl at different pH. The data in Fig. 3.15 suggested that the oxidation potential of the Ag was influenced by the solutions pH. An anodic peak of Ag was observed for all pH solutions where the $Ag \rightarrow Ag^{+} + e^{-}$ reaction taken place, except pH 12 buffer solution. There were two anodic peaks observed at pH 12 solutions, which might be due to the oxidation of Ag and further oxidation of Ag^{+}. At the highly alkaline pH 12 buffers, the overpotential (at ≈ 0.85 V) was high enough to oxidise Ag^{+} to form Ag^{2+}. As seen in Fig. 3.16, the current density (y-axis) was obtained by normalising the current with the surface area of the particles involved in the anodic reaction as determined by use of TEM images.

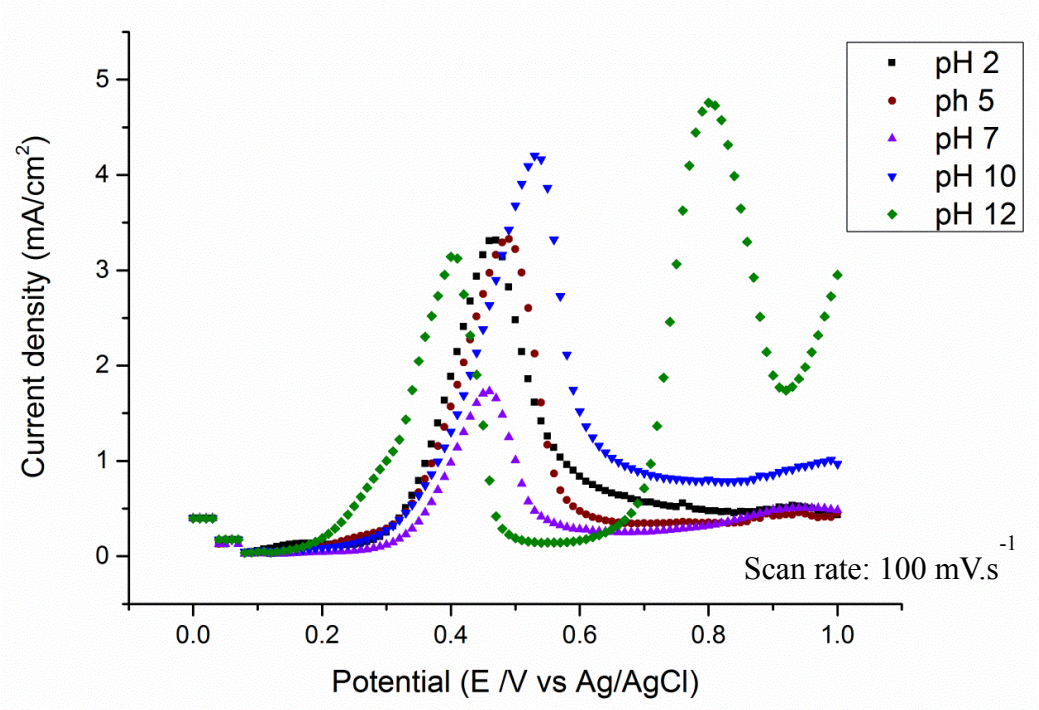

Fig. 3.15: Anodic linear polarisation sweep of AgNPs on BDD substrates in perchlorate buffer solutions as a function of pH at a scan rate of 100 mV s^{-1}.

Note that the intensity of the oxidation peak is dependent on the total electroactive surface area of the NPs found within the O-ring in the LSW experiment. The real surface area can be calculated as shown below:

From the TEM images, the number of particles (n) can be found in a 1 x 10^{-10} cm^2 (= 100 nm * 100 nm) area, a. Thus the surface density (ρ_A) = $\frac{n}{a}$ particles/cm^2

The radius of the O-ring (r) is 0.149cm, therefore the surface area of the electrode (A) is:

$$A = \pi r^2 \qquad (3.23)$$

Thus, the number of particles involved in the redox reaction is:

$$N = \rho_A * A \qquad (3.24)$$

and the electroactive surface area (A_E) is:

$$A_E = N * 4 \pi r_{avg}^2 \qquad (3.25)$$

where r_{avg} is the average particle radius obtained from TEM particle size distribution studies.

In applying the equation to these results, several assumptions need to be included:

- NPs are spherical and whole NP surface areas are electrochemically active in the reaction.
- NPs have ideally smooth surfaces with no defects.
- NPs are monodisperse with a uniform size.

Table 3.3: Electroactive surface area of NPs involved in the anodic reaction for different filter sizes.

Average Diameter of NPs (nm)	**Surface area in Echem experiment (TEM), A_E (cm^2)**
3.1	0.0101
5.2	0.0326
8.5	0.0397
12.8	0.0431
21.2	0.0879

The electroactive surface area of NPs on BDD substrates can be calculated from the integration of CV experimental curves and this area gives the charge (Q). Dividing by the number of electrons (per atoms) involved in the redox reaction gives the number of metal atoms, each of which is assumed to be an electroactive adsorption site:

$$\frac{Q}{e} = \text{number of Ag atoms involved in reaction}$$

Table 3.4 summarised the results of the number of Ag atoms involved in the reaction as a function of pH and NPs size. For smaller - sized NPs, the surface loading of the NPs in acidic solutions was found to be higher compared to basic solutions, suggesting that NPs have a higher tendency to oxidise to Ag^+ ions in a lower pH environment. However, larger-sized of NPs (*e.g.* average diameter = 11.2 nm) at pH 10 and 12 did not follow the mentioned trend. This may be due to the nonhomogeneous distribution of NPs especially at grain boundaries of BDD. Moreover, Toh *et al.*[271] suggested that the diffusion layers of the formed Ag^+ ions of individual AgNPs will strongly overlap at a high surface coverage. In contrast, at a relatively lower surface coverage, the diffusion layers of the neighbouring NPs do not overlap and their peak potentials become relatively insensitive to the surface coverage being governed by radial diffusion, which is dependent upon the size of NPs. In this work, the active surface area of larger-sized NPs might be influenced by the surface coverage of the samples, resulting in a higher area at pH 12 compared to pH 2.

Table 3.4: Surface loading of AgNPs on BDD substrate as a function of pH and sizes.

Average diameter of NPs (nm)	pH	Charge, Q (μC)	$N_{(Ag)}$, (x 10^{13} atoms)
D= 5.2 nm	2	14.2	8.90
	5	14.3	8.94
	7	12.2	7.62
	10	16.7	10.41
	12	12.5	7.79
D= 8.6 nm	2	24.5	15.30
	5	23.8	14.93
	7	8.8	5.51
	10	14.1	8.82
	12	8.4	5.26
D= 11.2 nm	2	13.6	8.48
	5	16.2	10.10
	7	17.6	11.01
	10	12.0	7.48
	12	20.1	12.64

3.3.3 Potential – pH Relationship

The potential *vs.* pH diagrams are useful tools for materials selection, which can be used to predict conditions under which corrosion will be thermodynamically possible so that it is possible to control or prevent corrosion by adjusting the parameters (i.e. potential or pH). In this work, the stability of the NPs can be studied by determining the anodic potential of NPs in an aqueous environment as a function of particle sizes and solution pH. As shown by the current vs. potential plot (*e.g.* Fig. 3.15), the definition of anodic potential for the E-pH studies is somewhat ambiguous. Here, both the potential at anodic peak maxima (E_{max}) and the onset anodic potential were compared and tested to identify the ideal anodic potential used for the further studies.

Fig. 3.16 demonstrates the influence of particle sizes and pH on the dissolution potential at anodic peak maximum, E_{max}. By comparing Fig. 3.16 and Fig. 3.18, a specific trend on the relationship between E_{max} and pH is difficult to identify. E_{max} is

not ideally used as a redox potential in the E-pH fundamental study because a redox reaction might be taken place or in the middle of a redox reaction. By contrast, the onset anodic potential can be defined as the potential where the NPs begin to oxidise or dissolve into ions. Fig. 3.18 showed the size dependent anodic potential of NPs in different solution pH and the measurements were more sensible than Fig. 3.16, showing the expected dependence of E on pH and particle sizes.

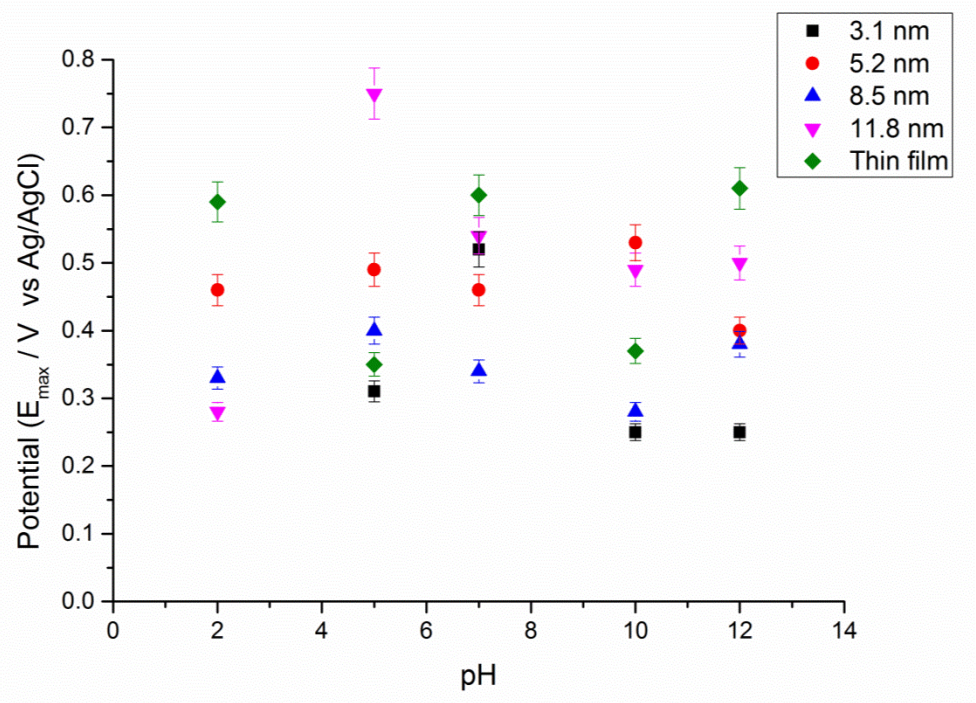

Fig. 3.16: Potential at oxidation peak maximum (E_{max}) – pH curve for AgNPs with different sizes.

From the current density - potential curve (Fig. 3.15), the onset anodic potential can be determined from the intersection of the tangent between the baseline and the signal current as shown in Fig. 3.17. We chose to define the potential at the intersection point of two tangents drawn to the linear parts of the curve. Using the definition of onset potential in Fig. 3.17, potential (E) vs. pH diagram of AgNPs as a function of particle sizes can be plotted as shown in Fig. 3.18.

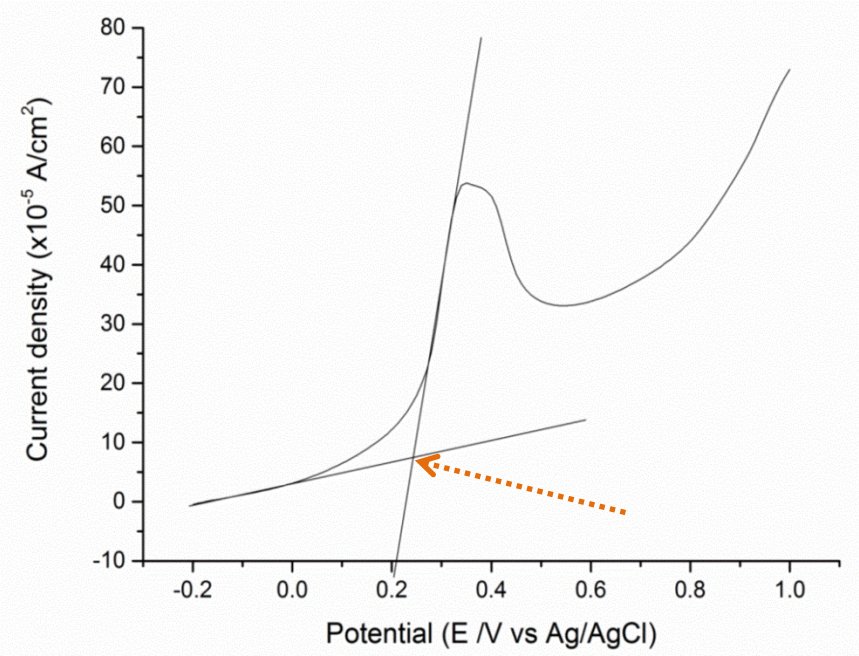

Fig. 3.17: The onset potential of oxidation was determined from the intersection of the tangent between the baseline and the signal current. The arrow represents the onset oxidation potential.

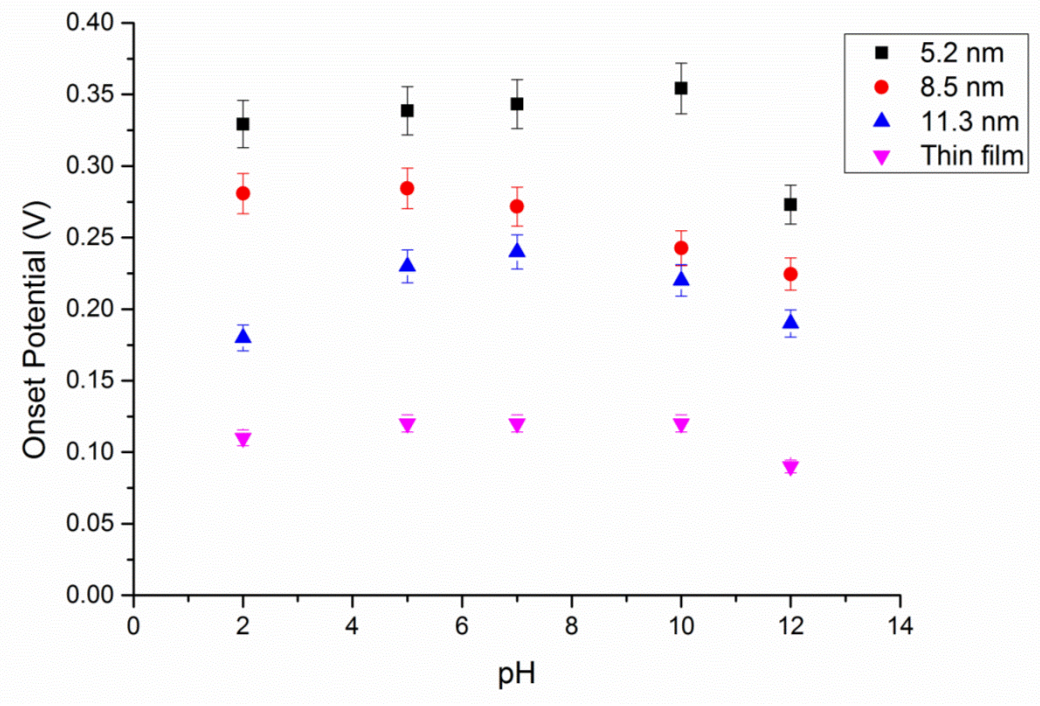

Fig. 3.18: Onset anodic potential (E_{onset}) vs. pH curve for different sizes of AgNPs on BDD substrate.

As seen in Fig 3.18, the E_{onset} increased with the reduction of the NPs sizes, suggesting that larger-sized of particles have a higher tendency to dissolve compared

to smaller particles. This finding agreed with Lakbub *et al.*[69] and Kolb *et al.*[64, 65]. In Fig. 3.18, smaller-sized of NPs (D= 5.2.nm) followed the Pourbaix diagrams for bulk Ag suggesting the equilibrium condition is not pH-dependent in acidic conditions. Nevertheless, larger NPs showed the shift in anodic potentials when the solution pH increased. For the relationship between potential and pH at higher pH (≥ 10), all particles follow that of bulk Ag for alkaline solutions (i.e. onset at lower overpotential).

In addition to Fig. 3.18, the onset anodic potential of the smallest NPs with average diameter of 3.1 nm was examined in different solution pH to compare with other NPs sizes. In the E-pH studies, the smallest-sized of AgNPs demonstrated a sharp drop of E when the pH increased from 7 to 12 or decreased from 7 to 5. The extremely high surface energy of these NPs could cause them instability especially in the highly acidic or basic solutions. Moreover, no oxidation peak of these smaller sized of NPs (3.1 nm) was observed at pH < 4, suggesting their oxidation reaction was too quick to be observed or these NPs were oxidised during the sample preparation process. Besides, electrochemistry errors with respect to the onset potential may occur while determining the potential from the I-E graphs.

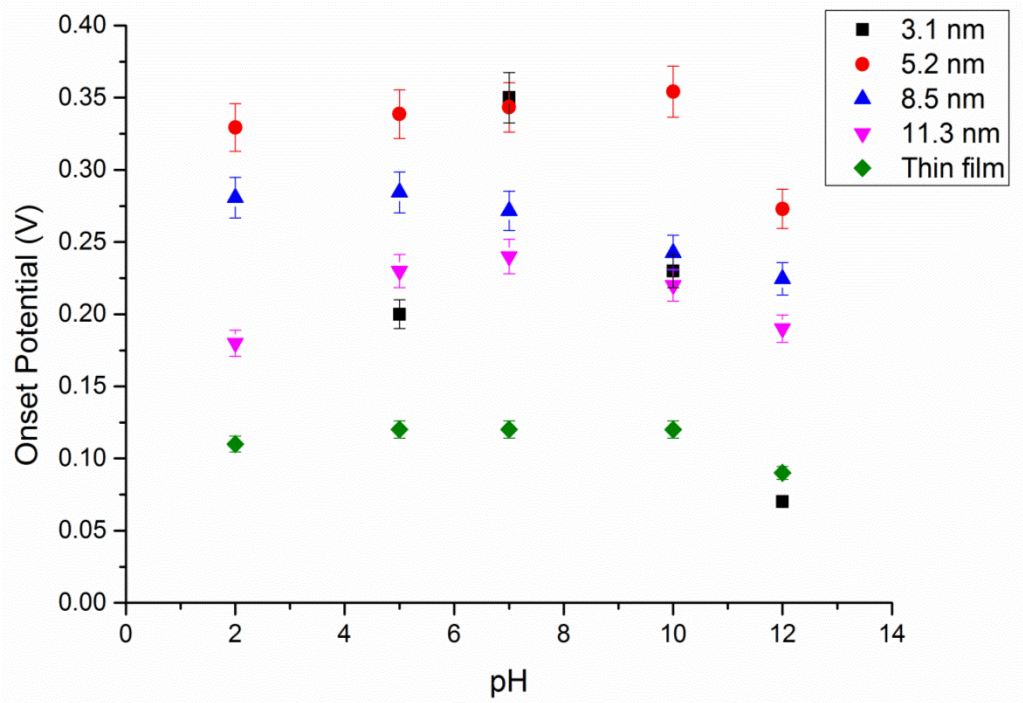

Fig. 3.19: Onset anodic potential vs. pH curve of AgNps as a function of particle size. Smallest NPs with an average size of 3.1 nm showed different E-pH trend compared to other NPs sizes.

Liu *et al.* found that dissolution of Ag is a cooperative effect of both dissolved oxygen and protons[49]. The Pourbaix diagram for bulk Ag suggests that the anodic potential of Ag is not affected by pH in acidic conditions, however it is clear from these data that the kinetic of oxidation is effected by pH. Protons in the fluid phase serves as a mediator and dissolution of NPs increases with higher [H^+], agreeing the surface loading data as shown in Table 3.4. In basic solutions, smaller particles are more reactive than larger particles, thus they will compensate their additional energy by bonding strongly with the passivating agents. This suggests a mechanism by which smaller particles are actually stabilised more than larger-sized particles.

3.3.4 Thermodynamic Theoretical Calculations

Thermodynamic analysis was used to predict the electrochemical stability of elemental AgNPs as a function of potential and pH. The analogues of equation (i) - (iii) for the case of bulk Ag are derived in this work:

(i) Direct electrodissolution: $Ag^+ + e^- \leftrightarrow Ag$ (3.26)

$$E(Ag/Ag^+) = 0.6 + 0.0591 \log [Ag^+] \quad (3.27)$$

(ii) Oxide formation: $Ag_2O + 2H^+ + 2e^- \leftrightarrow 2Ag + H_2O$ (3.28)

$$E\ (Ag/Ag_2O) = 1.173 - 0.0591\ pH \quad (3.29)$$

(iii) Chemical dissolution of the oxide: $Ag_2O + 2H^+ \leftrightarrow 2Ag^+ + H_2O$ (3.30)

$$\log K = -\ 2n\ pH - a \log [M^{n+}] \quad (3.31)$$

A Pourbaix diagram (E-pH) of bulk Ag can be plotted by using the above Nerst and equilibrium constant equations. However, theoretically derived energy diagrams for a bulk material might not always be accurate for NPs since surface stress and surface energy are absent in the classical thermodynamic equations. By applying the equilibrium condition as shown in methodology[252]:

$$RT \ln(M^{n+}/\bar{M}^{n+}) = \gamma_M \Omega_M (2/r) \quad (3.32)$$

Thus, cell potential of AgNPs is:

$$E_{Ag/Ag^+} - E^{\circ}{}_{Ag/Ag^+} = -\frac{\gamma_M \Omega_M}{nF}(2/r) \quad (3.33)$$

Assume the interfacial free energy of the liquid vapour, $\gamma_M = \gamma_{sv}$ = 1.14 J m^{-2} and substituting the molar volume of the solid, Ω_M = 10.27 cm^3/mol = 10.27 * 10^{-6} m^3 mol^{-1}; Faraday constant, F= 96485.3 sA mol^{-1} and the number of electrons involved in the reaction, n =1. Assuming the NPs have the equilibrium shape, the particle-size-dependence anodic potential of Ag is:

$$E_{Ag/Ag^+} = 246 - \frac{(1.14)(10.27*10^{-6})}{(1)(96485.3)}(2/r) \quad (3.34)$$

$$E_{Ag/Ag^+} = 246 - 121\,(2/r) \quad (3.35)$$

where r = radius of particles

If we consider the thin film as a bulk metal and assume $[Ag^+] = 10^{-6}$, the anodic potential of bulk Ag is:

$$E_{Ag/Ag^+} = 0.6 + 0.0591 \log [Ag^+] \quad (3.36)$$

The thermodynamic theoretical calculation of AgNPs as a function of particle size and pH is summarised in Table 3.5 and is plotted in Fig. 3.21.

Table 3.5: Theoretical calculations of anodic potential of AgNPs with different sizes.

Average diameter of NPs (nm)	Anodic potential of Ag (V)
5.2	0.15
8.5	0.19
22.6	0.23
Thin film	0.25

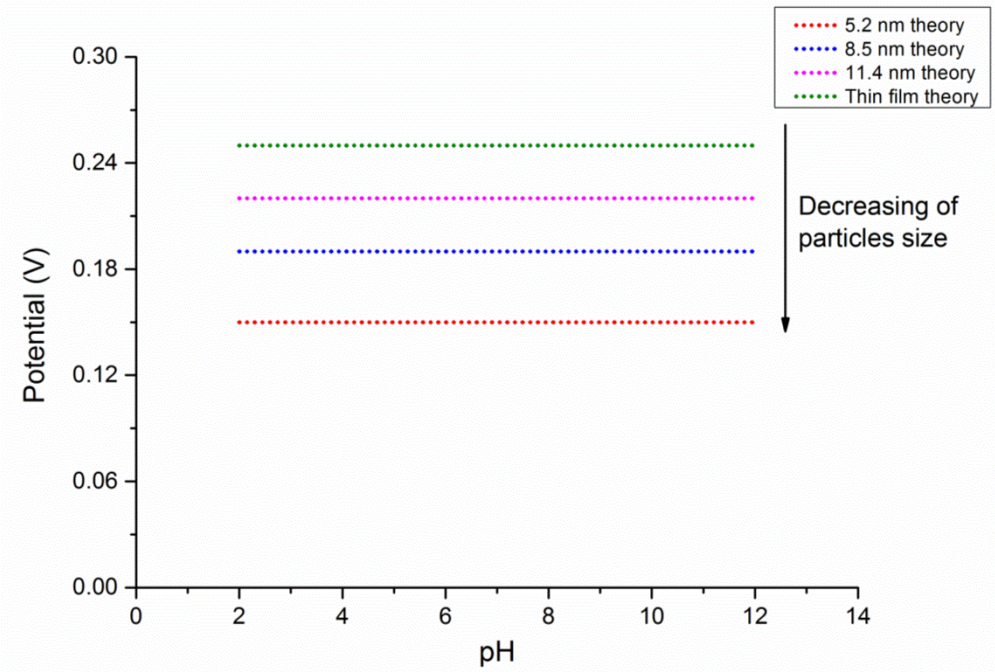

Fig. 3.20: E – pH of AgNPs as a function of particle size plots based on thermodynamic theoretical calculation.

As seen in Fig. 3.20, E-pH data showed that the anodic potential is predicted to increase with particle size, demonstrating that the smaller-sized NPs are less stable. This would suggest they tend to dissolve with a higher dissolution rate compared to larger particles. This theoretical finding showed a specific size dependent behaviour which opposed the experimental results as discussed in previous section. As mentioned, information on the reaction rate, passivation effect of NPs and their interactions with diamond substrates were not considered in the theoretical analysis.

According to the Butler-Volmer equation, overpotentials are exponentially dependent on the current density:

$$i = i_0\left[\exp\left(\frac{\alpha_A nF}{RT}\eta\right) - \exp\left(-\frac{\alpha_C nF}{RT}\eta\right)\right] \qquad (3.37)$$

where net current at the electrode, i, is the sum of the exchange current densities (i_o) for the anodic and cathodic reactions, α is the symmetry factor or charge transfer coefficient dimensionless, n is the number of electrons involved in the electrode reaction, F is the Faraday constant, R is the universal constant, T is the absolute temperature, K and η is the overpotential. Passivation of the NPs by passivating agents (*e.g.* oxygen, proton or hydroxyl groups) will affect the electrode kinetics and

is detrimental to performance as it causes additional resistances to a reaction. Therefore, a higher overpotential is required to increase currents moving across the interface when the exchange current density is really low.

3.3.5 Theoretical Calculations vs. Experimental Results

By comparing the theoretical calculation data and experimental results as shown in Fig. 3.22, theoretically calculated onset potentials are lower compared to most NPs systems, except for thin films. Moreover, anodic potentials from both theoretical and experimental techniques show a similar magnitude. However, the experimental data were found to be opposite to the computation calculations, suggesting that the electrochemical stability of the NPs increased with the decreasing of particle size. This is mainly due to the enhanced stability of smaller - sized NPs, which may interact more strongly with the diamond substrate. In addition, there are several factors that may also contribute to the findings:

- In the theoretical calculation, several assumptions were proposed such as equilibrium shape of NPs which may rarely take place on real particles.
- The potential-pH diagrams plotted using the thermodynamic theoretical calculations provide no kinetic information.
- Since NPs have a higher surface energy, they may compensate their additional energy by bonding strongly with passivating agents in solutions. However, passivation effects on the surface of NPs may be neglected by the theoretical analysis.
- Divergent concentrations of boron at different sites of diamond or diamond structure (*i.e.* grain boundary). Also, only electroactive AgNPs participate in the reactions (i.e. not all particles).
- Apart from the NPs size, the voltammetry stripping behaviour of NPs is also sensitive to the surface coverage of the electrode. As mentioned in section 3.3.2, surface loading of NPs could be affected by the higher surface coverage due to the overlapping diffusion layers of each NPs. Similarly, the variation in the surface coverage of the metal NPs may also influence the shifting of the anodic stripping potential[271]. Thus, the observed ‘size effect’ upon the anodic stripping potential maybe due to the surface coverage of the metal NPs instead of their altered nanoscale thermodynamics.

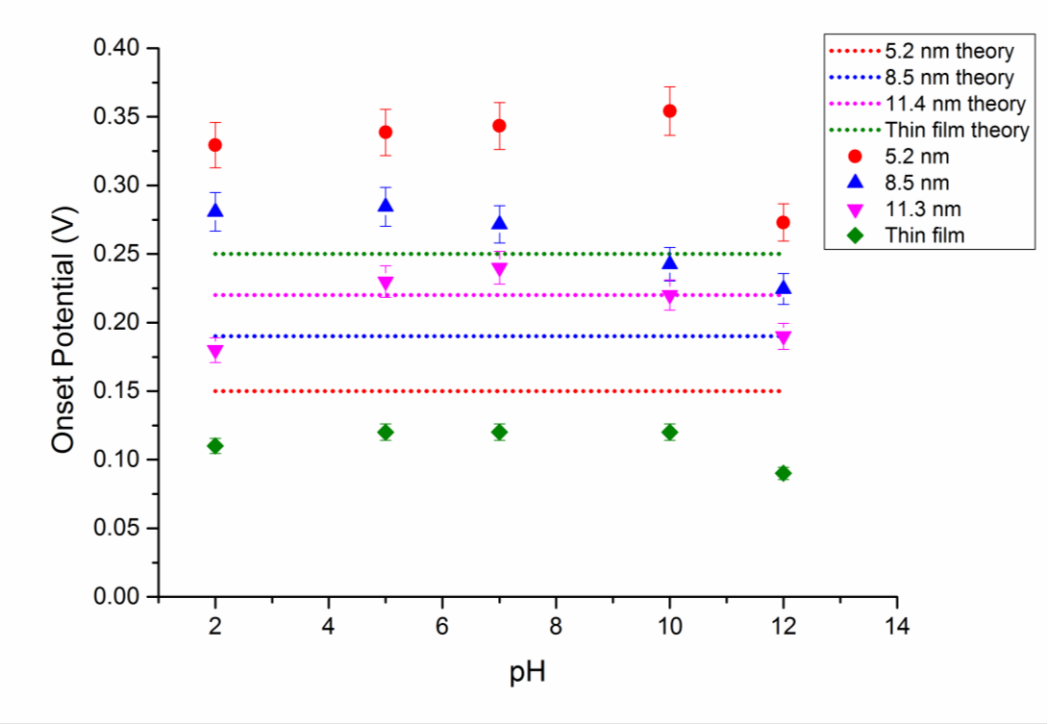

Fig. 3.21: Combined experimental and thermodynamic theoretical calculations of the electrochemical stability of AgNPs as a function of NPs size, potential and solution pH.

3.3.6 XPS Analysis of AgNPs as a function of Size and pH

By analysing the surface chemistry of AgNPs after electrochemistry (LSW), the chemical changes at the interface of the NPs caused by the anodic reaction can be inferred. The focus of the XPS analysis is to monitor the effect of solution pH on surface chemistry of AgNPs after anodic polarisation sweeps in aqueous environments. The comparison of the Ag3d and the O1s XPS spectra between 5.2 nm and 21.2 nm AgNPs is shown in sections *3.3.6.1* and *3.3.6.2*, respectively.

3.3.6.1 Ag3d – 5.2nm vs. 21.2 nm AgNPs

Fig. 3.24 shows the XPS spectra of the $Ag3d_{5/2}$ region for 5.2 nm vs. 21.2 nm AgNPs in different pH solutions. As shown in the XPS spectrum, the core level of each element has a unique binding energy (BE) from which each photoelectron is generated, thus the changes of surface chemistry of elements of interest can be identified.

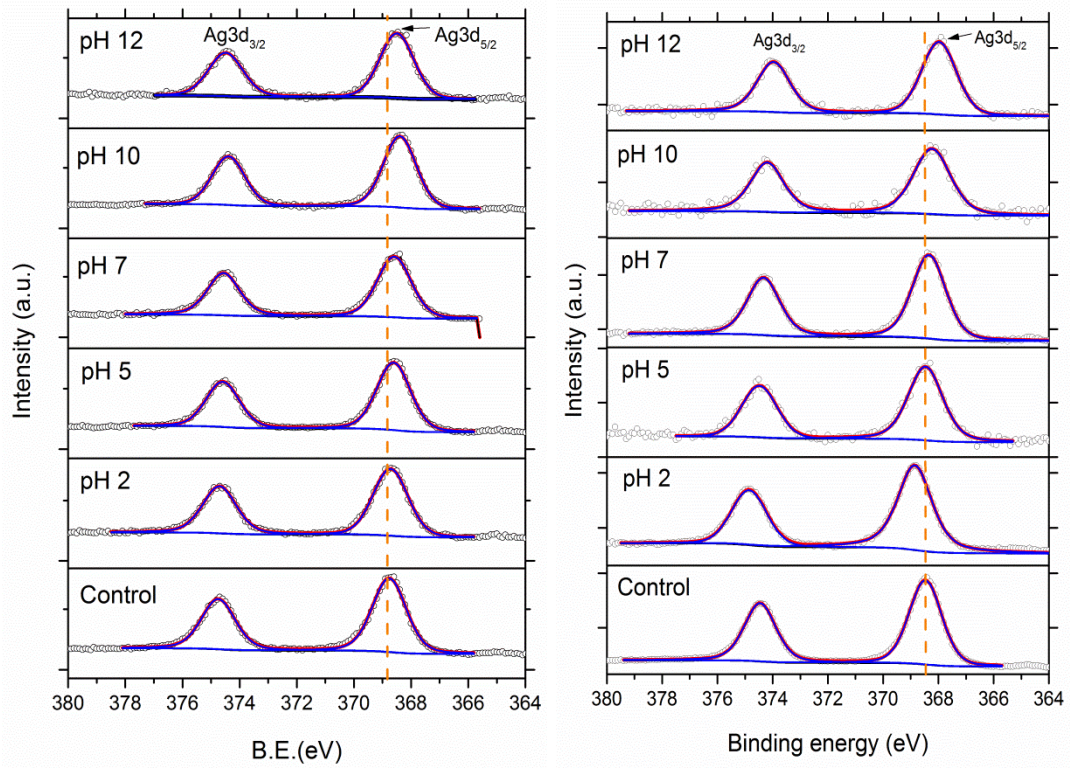

(a) 5.2 nm AgNPs (b) 21.2 nm AgNPs

Fig. 3.22: High resolution XPS data of the Ag3d5/2 region (symbols) for AgNPs with (a) 2 nm and (b) 12 nm sized filters in different pH solutions. Fitted peaks (Lorentzian-Gaussian functions) are shown as think solid blue lines; the fitted peak sums are shown as thick red lines.

Fig. 3.22 shows the XPS spectra after correcting the peak position by calibrating spectra using the adventitious Cls peak (the internal standard is the C1s photoelectron peaks at 285 eV). This is because photoelectron peaks normally shift to a higher BE due to positive surface charge, causing outgoing photoelectron to lose kinetic energy. The chemical shifting of a photoelectron peak from its expected BE may also be caused by the post-photoemission processes or the chemical environment of the element. Higher oxidation states or an increased number of electronegative or positive neighbouring atoms may shift photoelectron peaks to higher BE, and *vice versa*. Tables of the BE of each elements can be found in XPS handbooks, manuals and the National Institute of Standard Databases (NIST)[272-274].

For NPs with average size of 5.2 nm, the binding energy (BE) of Ag $3d_{5/2}$ was to shifted to lower BE as pH increased from 2 to 10, indicating changes of the Ag oxidation state from 0 to +1 (Ag_2O). Larger-sized of NPs with average diameter 21.2 nm showed similar trend as 5.2 nm AgNPs, where BE decreased with increasing of pH (except for pH 2). At highly acidic solutions, dissolution of AgNPs occurs *via* direct electro-oxidation to Ag^+ ions where the oxidation strength of the solutions are not strong enough to form surface oxides or hydroxides, and no passivation is achieved. Therefore, the photoelectron peak of Ag did not shift to the lower BE.

Table 3.6 summarised the BE of $Ag3d_{5/2}$ peak position and $Ag3d_{5/2}$ / C1s ratio as a function of solution pH and NPs size. $Ag3d_{5/2}$ / C1s ratio in acidic solutions was found to be higher than the basic solutions, suggesting that direct dissolution of Ag to Ag^+ occurred in the acidic solution. Whereas, oxygen or hydroxyl covering the surface layer of AgNPs may cause the shifting of photoemission peaks and the varying data of surface loading as a function of pH (Table 3.3).

Table 3.6: $Ag3d_{5/2}$ peak position and $Ag3d_{5/2}$ / C1s ratio as a function of pH for 5.2 nm and 21.2 nm AgNPs.

	5.2 nm AgNPs		**21.2 nm AgNPs**	
	$Ag3d_{5/2}$ peak	**$Ag3d_{5/2}$/C1s ratio**	**$Ag3d_{5/2}$ peak**	**$Ag3d_{5/2}$/C1s ratio**
Control	368.8	0.071	368.5	0.115
pH 2	368.7	0.027	368.9	0.012
pH 5	368.6	0.043	368.5	0.042
pH 7	368.6	0.076	368.3	0.068
pH 10	368.4	0.078	368.2	0.052
pH 12	368.5	0.075	368.0	0.103

3.3.6.2 O1s - 2nm vs. 12 nm AgNPs

To identify the surface chemistry changes of AgNPs after the stripping process at different solution pH, XPS data of the O1s region for oxidised 5.2 nm *vs.* 21.2 nm AgNPs was plotted as shown in Fig. 3.23. The binding energy (BE) of the O1s peak from Ag (I) was found to be 531.7 eV[272-274]. Fig. 3.23 shows that the integrated intensity of the area underneath the Ag_2O peak was increased with pH for both 5.2 nm and 21.2 nm AgNPs.

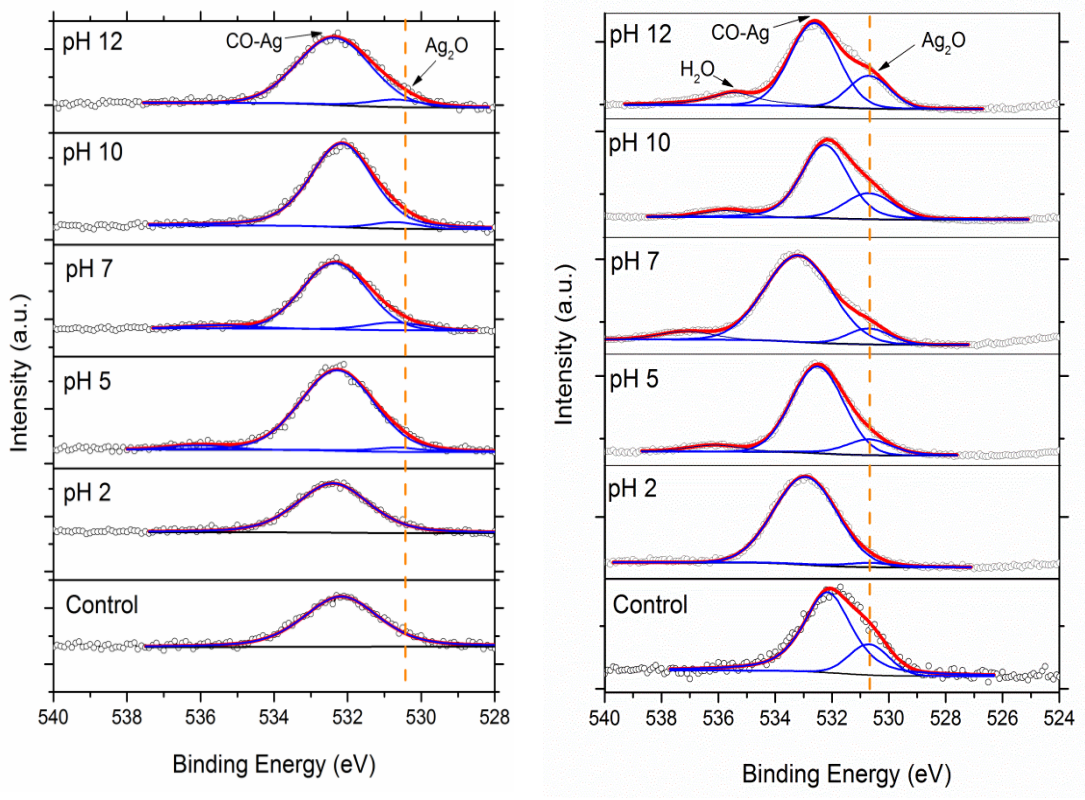

(a) 5.2 nm AgNPs (b) 21.2 nm AgNPs

Fig. 3.23: High resolution XPS data of the O 1s region (symbols) for oxidised AgNPs (a) 5.2 nm and (b) 21.2 nm in different pH solutions. Fitted peaks (Lorentzian-Gaussian functions) are shown as thick solid blue lines; the fitted peak sums are shown as thick red lines.

As summarised in Table 3.7, the O1s (Ag) / C1s ratio increased with pH, suggesting that AgNPs have a higher concentration of oxide layer on the AgNPs surface in basic solution. As shown in the XPS spectra (Fig. 3.23), another two O1s peaks were due to oxide layers (i.e. C-O-Ag and H_2O). For 21.2 nm AgNPs, the O1s peak was found from the control sample, meaning that the oxidation of Ag may occur in ambient air during the transportation of sample for XPS analysis. If AgNPs were oxidised before

the LSW experiment, no reduction or oxidation peaks could be observed in the LSW spectra (Fig. 3.15) due to the thick oxide layer that might hinder the redox reaction. However, the O1s (Ag) / C1s ratio was found to be diminished in an acidic solution and it then increased gradually with pH as shown in Table 3.7. The ratio of O1s (Ag)/ C1s showed the expected oxidation trend of AgNPs where they tend to oxidise and form Ag_2O at a higher pH.

Table 3.7: O1s (Ag)/ C1s ratio for 21.2 nm AgNPs on BDD as a function of pH.

	5.2 nm AgNPs	**21.2 nm AgNPs**
	O1s (Ag) / C1s ratio	**O1s (Ag) / C1s ratio**
Control	0.001	0.040
pH 2	0.005	0.032
pH 5	0.029	0.067
pH 7	0.035	0.086
pH 10	0.033	0.113
pH 12	0.050	0.109

Collectively, XPS analyses suggest the changes of NPs surface chemistry by showing the shifting of a photoelectron peak from its expected BE. The Ag3d XPS spectra indicate the changes of the Ag oxidation state from 0 to +1 as the pH increased from 2 to 12. This observation was consistent with the O1s XPS data, confirming an increased density of oxygen at NPs surface at higher pH.

3.3.7 SEM Observation of NPs Stability

To examine the effect of the redox reaction on the morphology of the NPs, the stability of NPs in water and after CV analysis was examined by SEM characterisation. As observed in Fig. 3.24, AgNPs were stable in DI water and no aggregation of NPs was found after 30 mins. Fig. 3.24 (c) demonstrated that as-prepared AgNPs were well-distributed at all surfaces of BDD. However, NPs tend to diffuse in solutions or dissolve followed with re-precipitation to form larger aggregates after CV run (3 cycles) at pH 5 perchlorate buffer solutions, as shown in schematic Fig. 3.24 (e). AgNPs were no longer maintained as single or individualised particles.

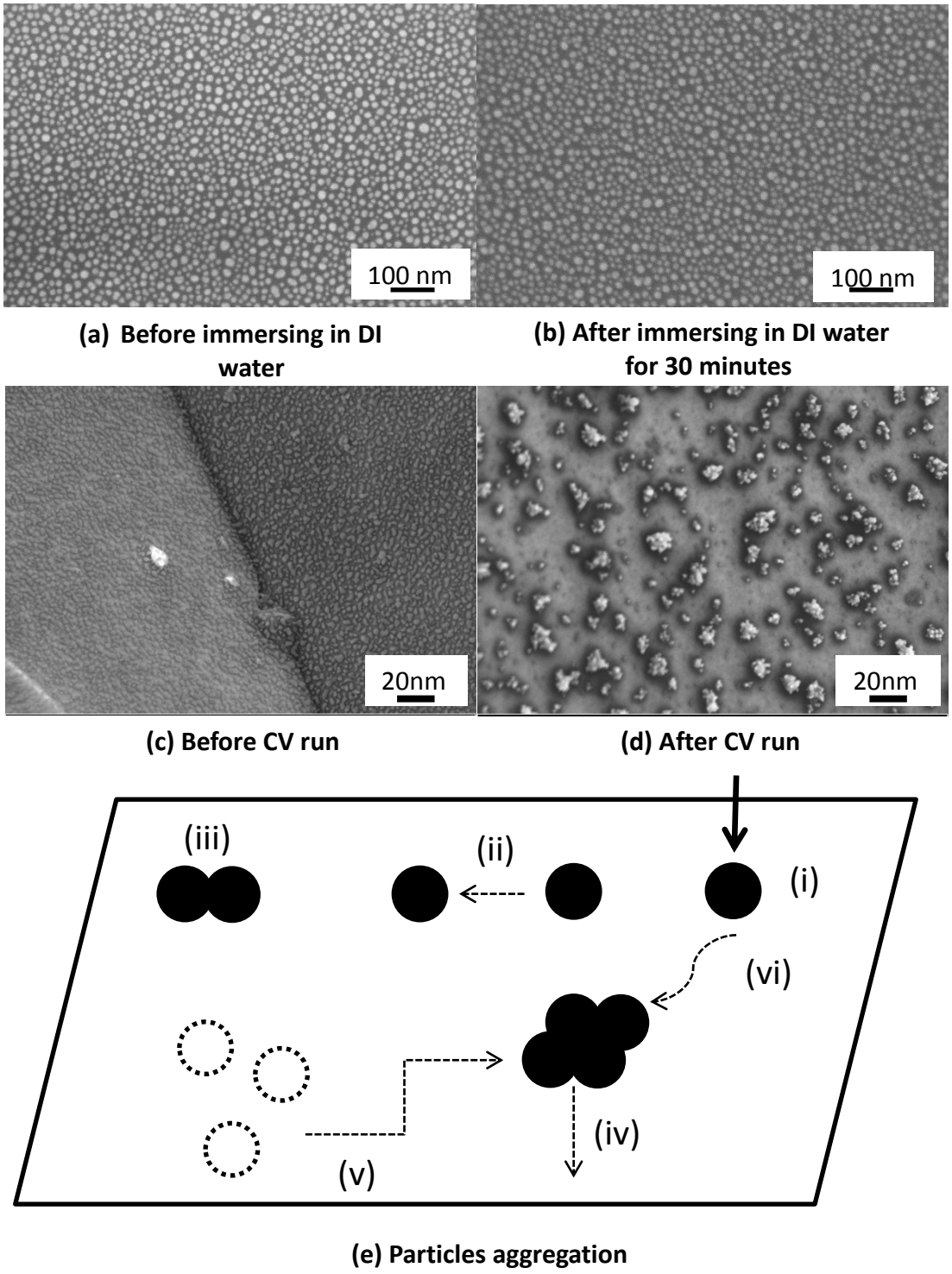

Fig. 3.24: SEM images of (a) as-prepared AgNPs, (b) their stability in DI water, (c) before and (d) after cyclic voltammetry (CV) run at pH 5 (3 cycles) perchlorate buffer solutions; (e) Schematic representation of the diffusion and aggregation of particles on the substrate: (i) deposition, (ii) diffusion, (iii) aggregation, (iv) island diffusion and (v) dissolution – precipitation, (vi) diffuse to an existing island.

These results might be useful to predict the decreasing efficiency of catalysts or fuel cells/battery due to the reduced active surface area of NPs over the long term during applications. These SEM results suggested that NPs may tend to diffuse to form larger-sized aggregates in solutions with the applied potential, leading to inconsistency of experimental results compared with theoretical calculations. For a better understanding of the electrochemical stability of NPs, further SEM studies are required by analysing the morphology of NPs after the reduction or oxidation process.

3.4 Summary

In the 21st century, technology incorporates nanomaterials in a variety of applications, such as nanoscale sensors, inter-connects and coatings. The recent development of electrodes has focused on various nanoscale objects, including nanodots, nanotubes, and in particular nanoparticles[275]. The intense interest on AgNPs is due to their unique electronic, chemical and optical properties, which differ greatly from the bulk metal[276]. Nanoparticles normally produce a higher signal-to-noise ratio due to their larger effective surface area. Therefore, the cost of producing an expensive metal electrode can be reduced. The aim of this work is to examine the electrochemical stability of AgNPs as a function of applied potential, particle size and solution pH. Here, AgNPs with controlled size and size distribution were deposited on to boron-doped diamond electrodes *via* magnetron sputtering, with size-filtering capability. The magnetron sputtering method was chosen after comparing it to other methods carefully. The anodic behavior of AgNPs in perchlorate buffer pH solutions (ranging from pH 2-12) were examined by linear sweep voltammetry. The surface chemistry and oxidation state of Ag after each treatment were characterized using X-ray photoelectron spectroscopy (XPS). The size distribution of AgNPs in response to electrochemical polarization was examined using atomic force microscopy (AFM). Pourbaix diagrams for bulk Ag suggest that their electrochemical stability is not pH-dependent in acidic conditions. However, we observe that, for nanoparticles with the average size of 5.2 ± 2.5 nm, the oxidation potential deviates from that expected in acidic conditions by approximately 0.015 V / pH**.** By contrast, the relationship between the potential and the pH follows that of bulk Ag for alkaline solutions. XPS confirmed the expected electrochemical changes in the surface chemistry, with binding energy (BE) of $Ag3d_{5/2}$ photoelectron signal

and O1s/C1s ratio correlating with the observed changes in the silver oxidation state. These direct voltammetric measurements of the Ag oxidation potential, as a function of size and pH, indicate that the electrochemical stability of NPs is different from their bulk metal. Theoretically derived energy diagrams for a bulk material might not always be accurate for NPs, especially AgNPs as has been shown in the study and reasons why this may be the case were discussed.

4.0 The Stability of AgNPs in Pulmonary Surfactants

4.1 Aims and Overview

The large production volume of manufactured silver nanoparticles (AgNPs) has raised concerns of the increasing exposure toxicology and environmental issues. Inhalation of airborne NPs is one of the main exposure routes by which NPs can enter the human body. After inhalation, relatively large particles or agglomerates (diameter > 1 μm) are likely trapped in the mucus of the upper airways and are removed by the mucociliary escalator. However, NPs with a diameter < 20 nm are likely to escape the mucus trapping and enter the deepest zone of lung: the alveolar region[6, 186]. The deep lung is comprised of a monolayer of type I and type II epithelial cells which allow gas exchange and also directed transmigration of cells such as macrophages that form part of the lung's immune system. Lung lining fluid (LLF) is the first line of alveolar defence towards inhaled nanomaterials and has not been well investigated. In the context of respirable NPs, the interactions with both LLF components and local cell populations will determine the effects on cell metabolism and lung function. For this reason, it is critically important to understand how the particles behave in different biological media to predict any downstream effects of the particles.

The objective of this study is to investigate the impact of dipalmitoylphosphatidylcholine (DPPC), the main component of pulmonary surfactant, on the stability of AgNPs, with well-controlled physicochemical properties. Here, how the characteristic of size and surface functionalization of AgNPs affect their interaction with pulmonary surfactants were also investigated. The influence of phospholipids on the aggregation state and release of Ag^+ ions at various pH conditions, representative of environments found in the lung, have been investigated. Under *in vivo* conditions, AgNP dissolution has the potential to cause mitochondrial damage and ROS-induced lipid peroxidation and DNA oxidation[177]. Thus, consideration of any feedback processes (*i.e.* how components of the LLF affect the physicochemical properties and reactivity of NPs) in such systems is an important aspect of understanding the impact of engineered nanomaterials on cell toxicity.

4.2 Experimental Methods

4.2.1 Synthesis of AgNPs Suspension

AgNPs were synthesised by chemical bath reduction process using sodium borohydride as the reductant and citrate as the stabiliser. [277] Briefly, $AgNO_3$ (~ 1.0 x 10^{-3} M) solution and $Na_3C_6H_5O_7$ (~ 1.0 x 10^{-3} M) solution were added to boiling water (250 mL). Then, $NaBH_4$ solution (~ 1.0 x 10^{-3} M) was added drop-wise to the mixture over a period of 10 seconds. The colour of the suspension immediately turned to yellow, indicating the formation of silver nanoparticles. Heating was continued for an additional 30 min, and then the solution was cooled to room temperature. The AgNPs suspensions were washed with DI water and centrifuged at a relative centrifugal force maximum value (RCF_{max}) of 13,000 x g. The washing process was repeated three times to remove impurities and unbound citrate. The final silver concentration after three times washing with DI water was 23.5 ppm and all citrate was expected has been removed by the washing process. Then, these purified particles were sealed, stored in the dark and kept in a refrigerator. They were used within two weeks of sample preparation before diluting to 25 mg/L in the DPPC pH solutions. The batch to batch variability of the AgNPs systhesis products was very low and all batches were routinely tested using TEM and UV-vis measurements. The cleanliness of synthesised particles was confirmed with EDS to ensure that sulphidation of AgNPs had not occurred[278] and impurities, such as Na^+, Cl^- were removed by washing.

4.2.2 Effect of pH and DPPC on the Stability of AgNPs

DPPC was purchased from Sigma Aldrich, UK (catalogue number P0763). The effect of pH on the stability of AgNPs (25 mg L^{-1}) was studied for 0 and 100 mg L^{-1} DPPC, in perchlorate acid solutions (pH 3, 5 and 7) by bath sonication for 10 minutes. Samples were incubated at 37°C with reaction times between 1 and 336 hours (2 weeks) in a dri-block heater.

To minimise the impact of anions on the stability of the AgNPs, non-interacting buffers were used and perchloric acid (Sigma-Aldrich), was used to adjust the pH. The pH was adjusted using either 0.1 M sodium perchlorate ($NaClO_4$) or perchloric acid ($HClO_4$) solutions. pH 5 and 7 were chosen to correspond approximately to lysosomal and extracellular media pH, respectively; pH 3 was chosen as a positive control.

4.2.2.1 TEM and SAXS

TEM was performed using a JEOL 2010 instrument operated at an accelerating voltage of 200 kV. The morphology and size distribution of AgNPs were characterised by bright field TEM. At least 200 particles were counted and measured to determine the size distribution (using Image J software). Two axes of particles (x and y) were calculated using Image J software as shown in Fig. 4.1. The particle size reported was estimated by averaging the shortest (x) and longest (y) dimension of 200 particles, *i.e.* $\left[\frac{x_k+y_k}{2}\right]$, $k = 0$ to 200. TEM samples were prepared by depositing a single drop of the suspension on to a 300 Cu Mesh holey support film and were left to dry at room temperature and stored under vacuum. To assess the effects of DPPC on the stability of the NPs, the samples were washed three times to remove excess organic surfactant, prior to TEM analysis. The samples were then negatively stained using 1% uranyl acetate in DI water to identify the phospholipid layer around AgNPs [279].

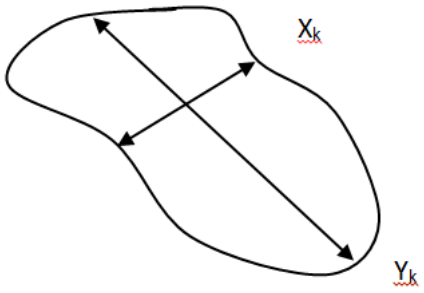

Fig. 4.1: Schematic diagram showing the procedure used to measuring the particle size. The particle size reported was estimated by averaging the shortest (X) and longest (Y) dimension of 200 selected particles, i.e. $\left[\frac{x_k+y_k}{2}\right]$, k=1 to 200.

4.2.2.2 SAXS

Small Angle X-ray Scattering (SAXS) was performed on the I22 beamline at the Diamond Light Source to provide an in-situ correlative measure of particle size and aggregation state. SAXS measurements were performed on the I22 beamline at the Diamond Light Source. A beam energy of 13 keV and a low noise Pilatus 2M detector were used. A camera length of 4.3 m gave an accessible q-range of 0.0437 to 0.3913 Å. The scattering vector q describes the difference between the wavevectors of the incident and diffracted beams. The detector was calibrated using Silver Behenate before the 2D detector image was integrated over 360^o with a fixed

radius and then normalised to give 1D data which were then adjusted for background scattering. Data reduction was performed using the Non-Crystalline Diffraction toolbox within Dawn Science (*Dawn Science, http://www.dawnscience.org)*. Data modelling and fitting was carried out using SasView (ref. *SasView,* http://www.sasview.org). Data were fitted using a unified Guinier-Porod fit allowing the radius of gyration (R_g) to be extracted as well as information about the particle dimensionality[280]. Fits with a dimension < 0.25 were assumed to be spherical and the particle diameter was calculated using the equation:

$$D = 2R_g \left(\frac{3}{5}\right)^{-\frac{1}{2}} \qquad (4.1)$$

AgNP were diluted to a concentration of 10 μg/ml. As-prepared NPs were measured in 1 mm quartz capillaries using a 120 s exposure time. DPPC at 10 μg/ml was added to each pH solution. Samples were then incubated in a water bath at 37 ^{o}C for 560 minutes (~9.5 hours) before being measured in the X-ray beam.

4.2.2.3 SAED and EDS

The crystallinity of particles in different media was studied using selected area electron diffraction (SAED), in order to determine which phases were produced. In particular the possible presence of Ag, AgCl, Ag_2O or Ag_2S were determined by calculating the (111), (200) and (220) interplanar lattices and by comparing these to standard reference structures (Ag: Ref. # 01-087-0597; AgCl: Ref. # 00-031-1238; Ag_2O: Ref. # 00-041-1104; Ag_2S: Ref. # 00-014-0072).

The presence of DPPC was examined using energy dispersive X-ray Spectroscopy (EDX) in the JEOL 2010. The cleanliness of synthesised particles was also confirmed with EDX to ensure that sulfidation of AgNPs had not occurred[278] and all impurities, such as Na^+, Cl^- were removed after the washing process.

4.2.2.4 ICP-OES

ICP-OES was used to determine the amount of dissolved Ag in the presence, or absence, of lung surfactant (DPPC) at different pHs (3, 5 and 7). Each AgNP suspension (pH 3, 5, 7) was incubated in a temperature controller at 37 °C and then centrifuged at high speed (13,000 rpm) with 2 kDa (< 4 nm) filter tubes (Sartorius Stedim VIVACON 500) to separate the NPs from the solution. The concentration of released Ag^+ ions was measured after the particles had been removed at different

time intervals of 1, 6, 24, 72, 168 and 336 hours (n = 3). For the control experiment, clean water (no AgNPs) and supernatant from which the AgNPs had been removed were analysed to ensure that any residual AgNPs were removed by centrifugation and filtering.

4.2.2.5 Zeta potential ξ measurements

The surface charge (zeta potential) of AgNPs/citrate and AgNPs/citrate wrapped with a DPPC lipid layer were characterised with a ZetaPALS (Brookhaven Instruments Corporation, USA) as a function of pH and at 25 ºC. The zeta potential measurements were calculated based on the electrophoretic mobility of charged particles in the dispersion (μ), viscosity (η) and permittivity (ε) of the solvent using the Smoluchowski equation: $\zeta = \frac{\mu\eta}{\varepsilon}$, which determines the magnitude of the electrostatic repulsive force. The pH of the suspension was adjusted to the required value. The samples were sonicated for 2 minutes before making a measurement. The measurement was made in triplicate and the arithmetic mean reported.

4.2.3 Effect of Size and Surface Functionalisation of AgNPs on the Colloidal Stability in Lung Lining Fluid.

Four different types of AgNPs with combinations of two diameters (20 nm vs. 110 nm) and two capping agents (citrate and PVP) were manufactured by nanoComposix, Inc (San Diego, CA) *via* base-catalyzed reduction of silver nitrate using 5-7 nm gold seed as nucleation centers (i.e. the resultant particles have a small Au core). The particles were characterized using transmission electron microscopy (TEM), energy dispersive X-ray spectroscopy (EDX) and zeta potential ζ measurements. 110 nm Ag particles were further characterized using high angle annular dark field scanning transmission electron microscopy (HAADF-STEM). HAADF-STEM combined with EDX analysis were carried out using an FEI Titan 80/300 fitted with a Cs (image) corrector, monochromator and EDX detector (EDAX, Leicester UK) operated at an accelerating voltage of 80 kV. For STEM experiments, a convergence semi-angle of 14 mrad was used, with an inner and outer HAADF collection angle of 49 and 239 mrad, respectively. The probe diameter was <0.5 nm. The interaction between each type of AgNP and a model surfactant was measured *in vitro,* either using 100 μg/ml DPPC.

4.3 Results and Discussions

4.3.1 Characterisation of As-synthesised AgNPs

A bright-field TEM image of as-prepared AgNPs is shown in Fig. 4.2a. The particles were spherical in morphology with an average diameter of 14 ± 1.6 nm (n=200) as characterized by TEM. SAED patterns (Fig. 4.2c) revealed that as-synthesised NPs have characteristic lattice spacings 0.236 nm, 0.204 nm, and 0.145 nm, corresponding to the (111), (200) and (220) planes of metallic silver (Ref.#01-087-0597). EDS analysis confirmed that sulfidation of AgNPs had not occurred and all impurities had been removed after 3x washing with DI water. The ξ value of the as-synthesised AgNPs/citrate was -17.9 ± 3.0 mV. This negative surface charge is consistent with the electrostatic stabilisation against aggregation.

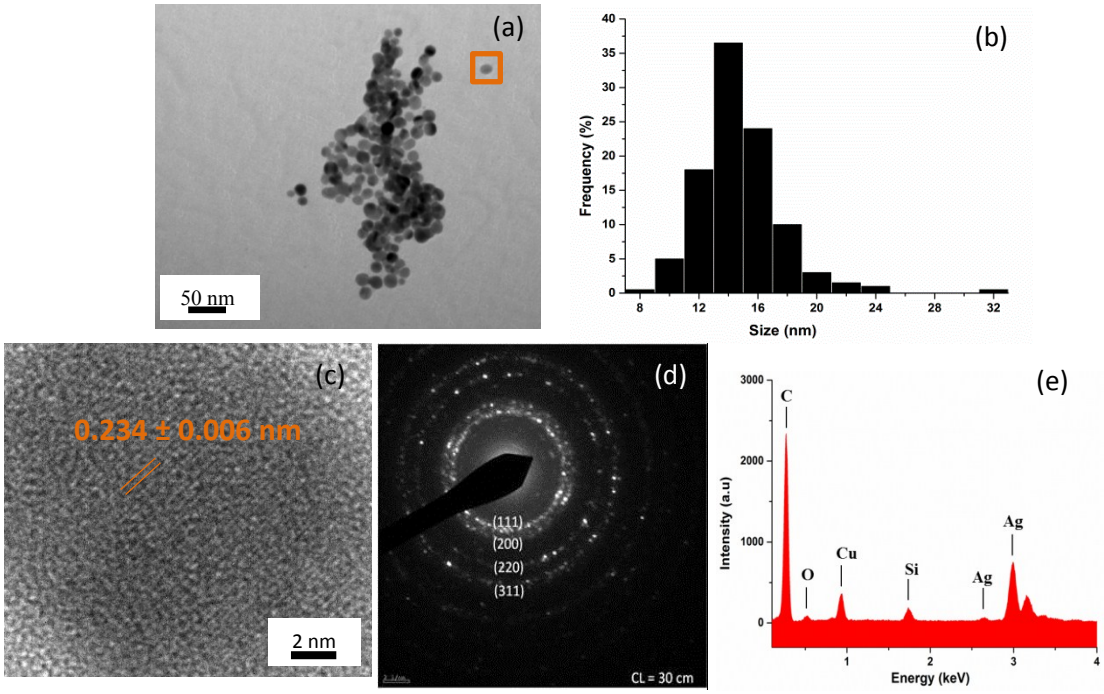

Fig. 4.2: (a) Bright-field TEM image of as-prepared AgNPs and (b) their corresponding size distribution (n=200); (c) HRTEM image of the boxed area in (a), showing a lattice spacing of 0.23 nm (d) SAED pattern (camera length=30 cm) and (e) EDS spectrum taken from AgNPs prepared by $NaBH_4$ reduction.

4.3.2 pH and DPPC: The Effect on Stability of AgNPs

The overall goal of this study was to assess the effect of pH on the stability and aggregation state of AgNPs, and to determine how the presence of DPPC modifies these processes. In the secretory pathway, the pH decreases progressively from the endoplasmic reticulum (ER) lumen, (pH~7.1), early endosomes (pH~6.5) to late endosomes (pH<6.0) and, ultimately, lysosomes (pH<5.5)[281]. A DPPC concentration of 100 $mg.L^{-1}$ was chosen to mimic the concentration range of phospholipid in bronchoalveolar lavage fluid obtained from healthy adults[140]. In this work, we have studied the interaction of AgNPs with DPPC and isolated the effects of DPPC – the majority component of the lung lining fluid. We specifically chose not to include other proteins present in the lung fluid as some of these components (*e.g.* SP-A, SP-B and SP-D) contain sulphur. This may lead to desulfurisation of proteins by AgNPs and formation of Ag_2S particles. The sulfidation process would confound the accuracy analysis of ICP and TEM and make it difficult to draw accurate conclusions about the mechanisms by which the pH affects the stability of the particles.

4.3.2.1 TEM

The stability of AgNPs in the presence, or absence, of DPPC, at pH 3, 5 and 7 was monitored by measuring both the production of Ag^+ ions in solution and by assessing the morphological evolution of the AgNPs as a function of incubation time. The primary particle and aggregate sizes of AgNPs in their dry state were characterized using TEM (Fig. 4.3 (a-n)). The particle size distribution (PSD) became multimodal after t=168 hours, as AgNP dissolution and coarsening occurred (Fig. 4.3 (o-r)).

TEM imaging showed that AgNPs associated more rapidly with decreasing pH. AgNP aggregate sizes in pH 3 were larger than in pH 5 and pH 7 (Fig. 4.3). This implies that the pH will affect the aggregation state of NPs in different cell culture media. Negligible changes in the aggregate sizes were measured at extracellular pH (~7.2) whereas the NPs tended to aggregate in lysosomal pH (~5.5). The PSD histograms (Fig. 4.3(p-r)) illustrate a significant shift in the position of the peak maxima, *i.e.* from 16 nm at pH 7 to 32 nm at pH 5, and 44 nm at pH 3 after 7 days incubation, indicating that the particles aggregated, fused and coarsened significantly at lower pH.

TEM images also show that DPPC addition results in smaller clusters of NPs or isolated primary particles, which are redispersed within the DPPC. In DPPC, NP aggregation was strongly pH-dependent, with the size of aggregates increasing as pH decreases. In particular, Fig. 4.3 (q) and (r) showed a shift in the peak maxima of the PSD to smaller sizes in the presence of DPPC at pH 5 and 3, respectively. After 7 days incubation, the position of peak maxima shifted from 44 nm (without DPPC) to 24 nm (with DPPC) at pH 3, and from 32 nm (without DPPC) to 20 nm (with DPPC) at pH 5. This trend indicates that the phospholipid DPPC provides a more stable barrier between NPs, reducing NP interactions and inhibiting coarsening. At pH 7.0, there is no significant shift in size distribution between the samples with and without DPPC, indicating that DPPC stabilises the NPs dispersion, but does not affect the size distribution at neutral pH. This nano-bio interface is important in shaping the surface properties, charges, resistance to aggregation and hydrodynamic size of NPs.[282]

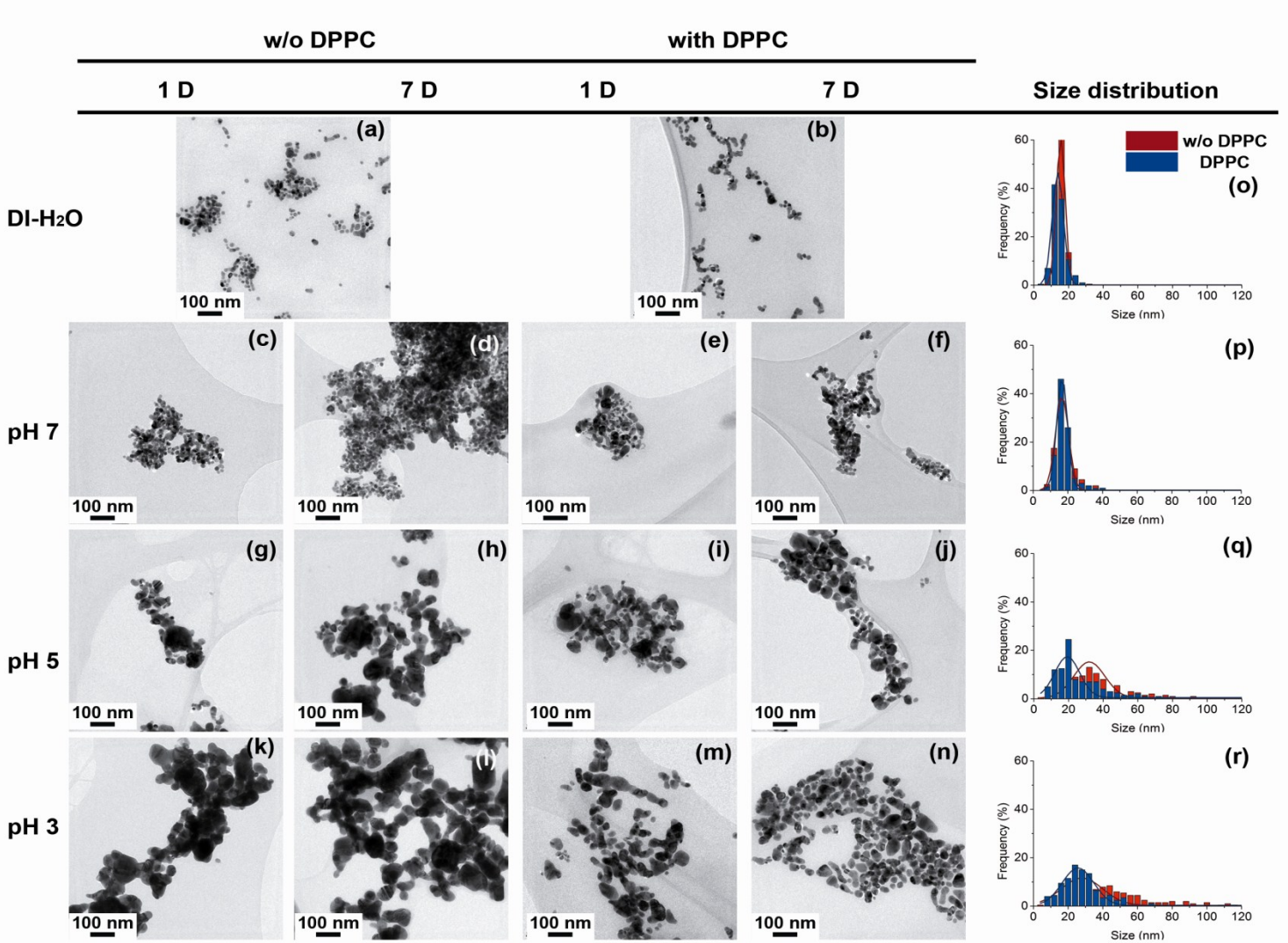

Fig. 4.3: TEM images of AgNPs incubating in water suspension (a-b) and aqueous suspension at pH 7 (c-f), pH 5 (g-j), and pH 3 (k-n) with magnification of 20k and their particle size distribution (N=200) histograms (o-r) were measured from TEM images in the presence, and absence, of DPPC after 7 days incubation.

In order to study further the influence of pH and DPPC on particle aggregation state and morphology, TEM images of AgNPs incubated in solutions in the presence of DPPC were acquired at low (x 50 k) and high (x 100 k) magnification as shown in Fig. 4.4(c) and Fig. 4.4(d), respectively. Fig. 4.4(a) shows the as-prepared citrate - stabilised AgNPs. The NPs were wrapped by a thin layer of stabilising agent (citrate), approximately 1.4 ± 0.3 nm in thickness. By comparison, when NPs were incubated in solutions containing DPPC, there was a significant increase of capping layer thickness, which implies formation of DPPC layer(s) outside AgNPs/citrate, as shown in Fig. 4.4 c-d. The thickness difference of 4.2 ± 1.8 nm is close to a DPPC bilayer thickness of 5.5 nm, as determined by atomic force microscopy (AFM)[283]. Leonenko *et al*. imaged a DPPC-supported bilayer using temperature-controlled AFM and demonstrated that thickness of DPPC bilayer varied as a function of temperature or analysis technique[283].

The detailed morphology of the DPPC layer(s) was further revealed using a uranyl acetate negative staining technique, which takes advantage of the high affinity of electron dense, uranyl ions, to the carboxyl groups of citrate and phosphate groups of DPPC, resulting in dark contrast[284]. The outside layer of NPs, which shows dark contrast, is likely to be the polar groups of the outer DPPC layer facing the aqueous environment (Fig. 4.4e-f). The hydrophilic heads of the inner layer of DPPC likely interact with the citrate layer; however, it is difficult to absolutely define the boundary of the two layers (Fig. 4.4f). The thickness of the bilayer of DPPC hydrocarbon tails, not stained with uranium, show a bright contrast layer in between; this was determined to be 4.3 ± 0.6 nm (Fig. 4.4f), close to the calculated hydrocarbon bilayer thickness of 4.16 nm. The molecular structure of DPPC contains a hydrophilic and a hydrophobic end (Fig. 4.5).

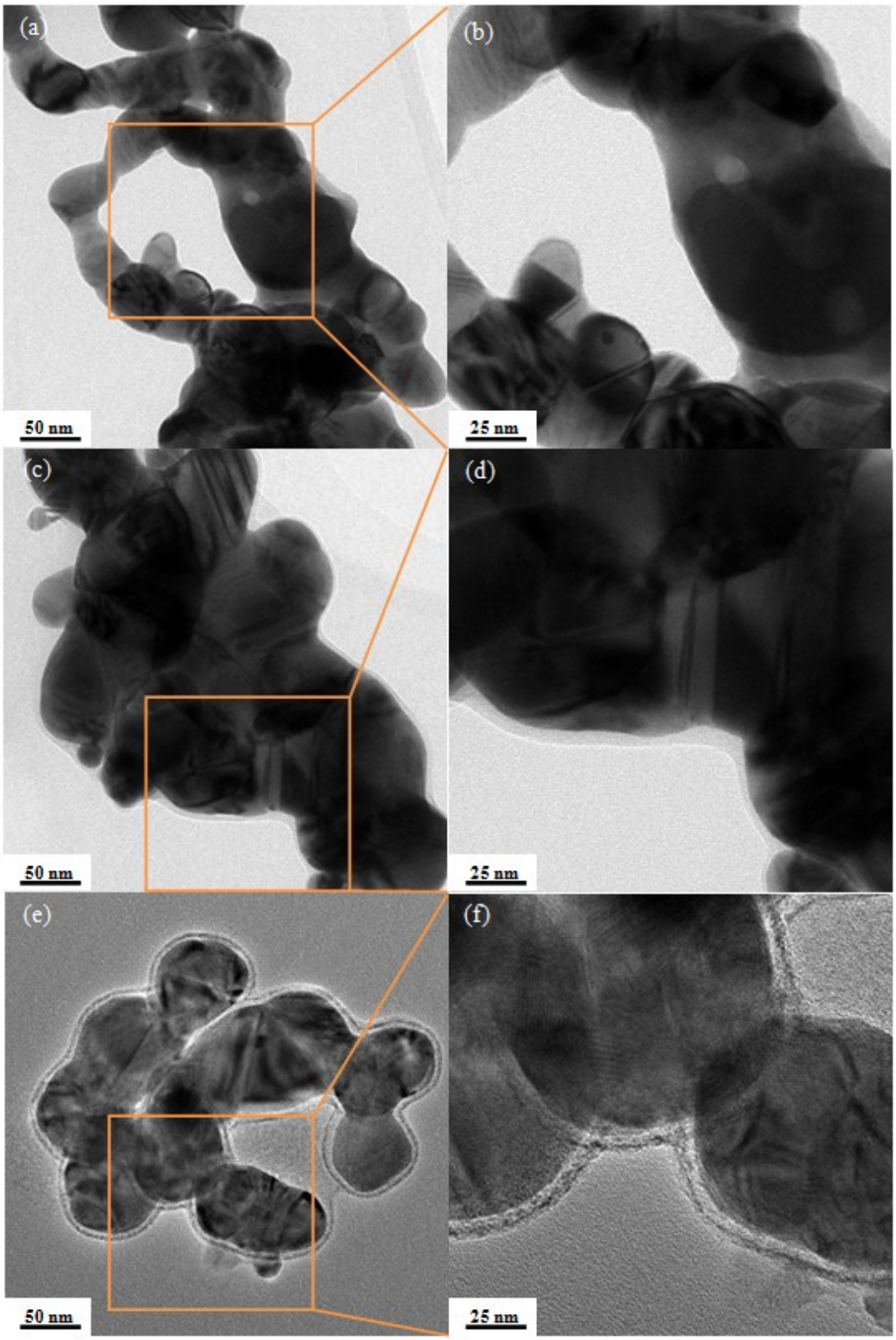

Fig. 4.4: TEM images for AgNPs incubated in pH 3 solution) in the absence (a and b), and in the presence (c and d) of DPPC, for 1 day. Samples negatively stained with uranyl acetate (e and f) to enhance contrast of lipid coating.

A schematic model of the DPPC bilayer structure on AgNPs/citrate is illustrated in Fig. 4.5. The zwitterionic trimethyl ammonium and acidic phosphate head of the molecule is hydrophilic, while the two long chain fatty acid tails esterified to the glycerol are lipophilic and hydrophobic. The formation of hydrogen bonding and electrostatic interactions initiate the interaction between AgNPs/citrate and DPPC lipid. Further evidence for the existence of a lipid layer around AgNPs is provided by EDS analysis which shows the presence of phosphorus in samples immersed in DPPC.

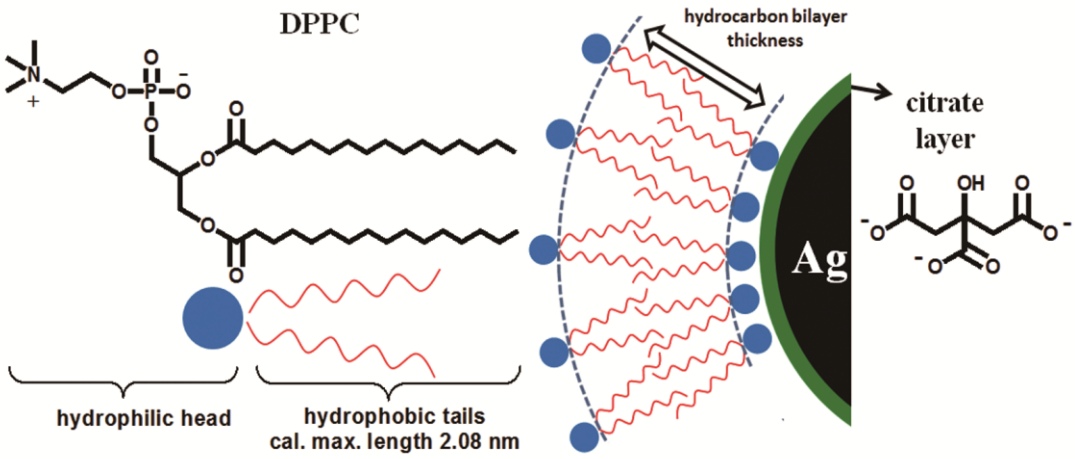

Fig. 4.5: A schematic illustration of a model of DPPC bilayer structure coated outside citrate stabilized AgNPs. The DPPC surfactant molecule consists of a trimethyl ammonium bounded to an acidic phosphate, providing a hydrophilic zwitterionic head group and two hydrophobic fatty acid tails comprised by 16 hydrocarbons. There is likely formation of a lipid bilayer structure on the surface of citrate coated AgNPs, with hydrophobic tails associating with each other, whereas hydrophilic groups of two layers oriented toward to aqueous environment and citrate layer respectively. The hydrocarbon bilayer thickness was determined by TEM analysis through negative staining.

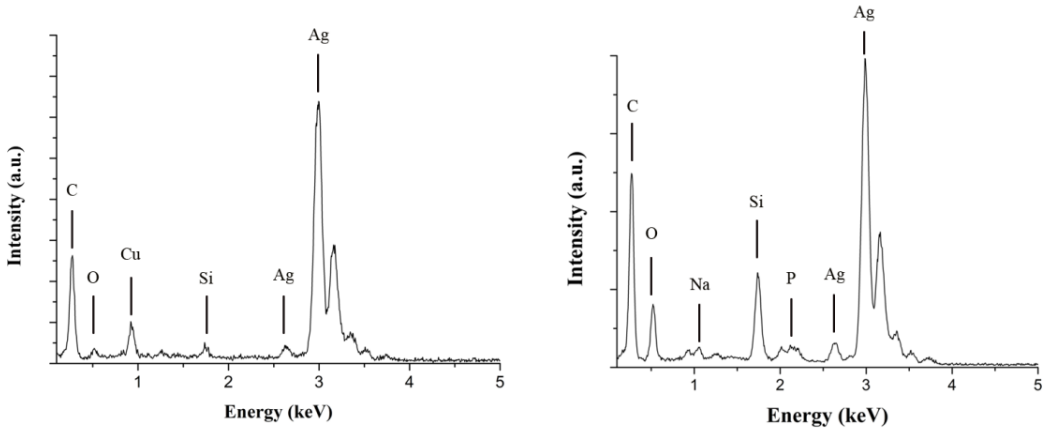

Fig. 4.6: EDS spectra taken from AgNPs incubated in pH 3 solution (a) in the absence, and (b) in the presence of DPPC after 1 week.

The aggregation state of NPs is an important consideration in controlling their reactivity in biological systems. A number of factors, including ionic strength, pH and surface chemistry, control both the propensity of NPs to aggregate and the aggregate size[136], [285]. For any colloidal suspension an equilibrium is set up between the NP and solution, so even a simple Ag colloid will consist of three forms: AgNPs, free Ag^+ (including complexes), and surface-adsorbed silver Ag_{ads}. Here, TEM images show that NPs preferentially aggregate at pH 3 compared to pH 7 (Fig. 4.3). This effect is related to the high $[H^+]$ which causes charge screening (thus reducing electrostatic repulsion), and decreased intramolecular repulsion resulting in molecular shrinkage[286].

TEM analysis showed that the measured size distribution was biased towards small particles with the addition of DPPC, indicating that DPPC improved the stability of the particles. This finding is in agreement with the result reported by Sager[141], who found that diluted alveolar lining fluid obtained through bronchoalveolar lavage improved the dispersion of ultrafine carbon black and TiO_2-NPs. Since the TEM preparation method may cause drying-induced aggregation of the particles; measures have been taken to minimise such effects by placing a small drop of solution on to a Cu grid and drying under vacuum. Moreover, exactly the same protocol was used to dry all the samples, so if observed aggregation was related to such artefacts it would be expected for *all* the conditions studied. This gives confidence that the observed differences can only be attributed to the effects of the environmental test conditions.

Although drying artefacts may create a systematic error, it cannot be disputed that significant differences between the aggregation states of AgNPs +/- DPPC, are observed. Furthermore; the *in-situ* SAXS measurement are consistent with the TEM data suggesting that such an approach (with appropriate care) is valid.

4.3.2.2 ICP-OES

Aliquots of Ag solutions were taken for ICP-OES analysis at various time points from 1 hour up to 14 days (336 hours). Dissolved silver appeared over the course of several hours up to two weeks. In the reaction, the dissolved silver was Ag^+ or Ag^+ complexed with anions (*i.e.* citrate), which can undergo dynamic exchange between surface bound and soluble forms.

Fig. 4.7 shows that the Ag^+ release rate was strongly pH-dependent: increasing ion release rates were observed with decreasing pH. Negligible Ag^+ release (~ 0.4 %) was measured at pH 7, and ~ 2 % Ag^+ was released at pH 5, after 14 days (336 hours) incubation. At pH 3, considerable Ag^+ release was measured initially after 1 hour incubation; ~ 5 % of available Ag^+ ions had dissolved. The dissolution rate of the AgNPs subsequently decreased, and the amount of Ag^+ ions released gradually increased up to ~10 %, at 14 days.

For AgNPs incubated in DPPC, a similar dissolution behaviour was observed compared to those incubated without DPPC (Fig. 4.7). However, the DPPC appears to form a protective membrane, increasing the AgNP chemical stability. At pH 3, < 1 % of AgNPs had dissolved after 1 hour incubation, compared to ~ 5 % released Ag^+ without DPPC. However, after 72 hours incubation at 37 °C (pH 3), the amount of dissolution was not significantly different from the samples without DPPC (Figure 2l and 2n). A similar trend was also observed at pH 5. Overall, DPPC imparted an initial retarding effect on the dissolution of AgNPs but the effect became less significant after two weeks of incubation at a given pH.

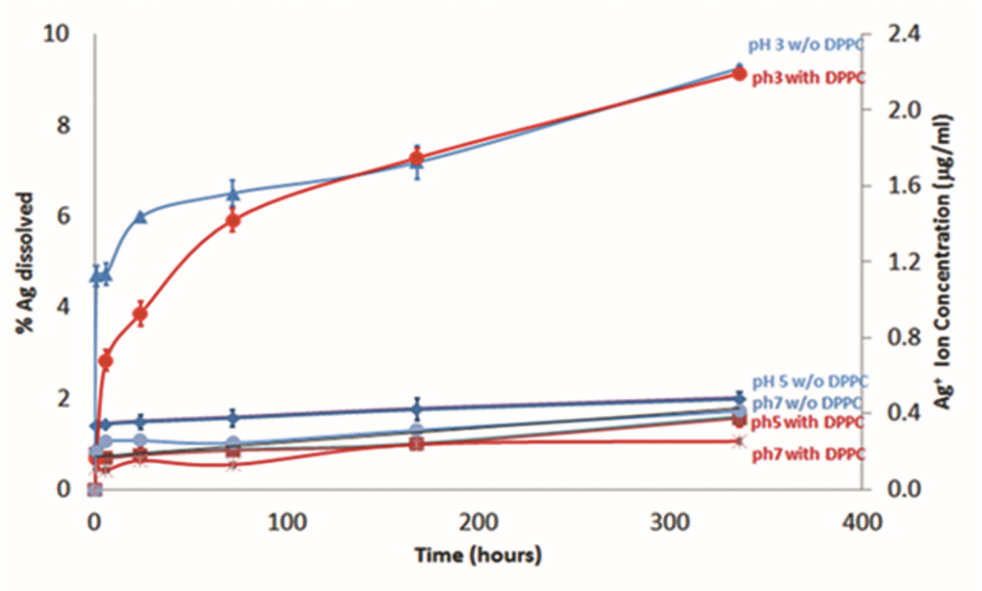

Fig. 4.7: Ag^{+} ion release study of AgNPs incubated in perchlorate acid solutions (pH 3, 5, and 7), in the presence, and absence of DPPC.

In this study, the ICP results (Fig. 4.7) show that NP dissolution rate increases with decreasing pH. Liu[49] found that dissolution of AgNPs is a cooperative effect of both dissolved oxygen and protons. In this study, dissolution was carried out in an ambient atmosphere, and therefore dissolved oxygen was a possible factor in the dissolution of AgNPs. Specifically, in a heterogeneous oxidation reaction, ion release is initiated by oxygen chemisorption accompanied by electron transfer. The Pourbaix diagram for Ag suggests that the equilibrium condition is not pH-dependent for acidic conditions, however it is clear from these data that the kinetics of dissolution are effected[287]. Protons in the fluid phase serve as a mediator and dissolution of NPs increases with higher $[H^{+}]$[49]. The global reaction stoichiometry is:

$$2Ag + ½\ O + 2H^{+} \leftrightarrow 2Ag^{+} + H_2O \qquad (4.2)$$

For surfactant-coated NPs, the DPPC layer may act as a diffusion barrier to molecular oxygen, and thus decreases ion release kinetics and toxicity[288]

4.3.2.3 SAXS

Background-subtracted SAXS data are shown in Fig. 4.8 along with fits to the data and extracted parameters. A good agreement between the data and fit was achieved for all the samples as indicated by the low χ^2 values. The extracted values for diameter D represent the average size of the scattering object: there is a dramatic increase in D for particles suspended in pH 3 and 5 solutions for a period of 9.5 hours: from 18.6 nm to 39.1 nm and 55 nm for pH 5 and 3 respectively. Little change was observed for particles suspended in pH 7 solutions, in agreement with TEM analysis. Addition of DPPC to the solutions reduced the observed changes in D, although measurable differences were seen for both pH 5 and 3 (D = 26.8 nm and 28.0 nm). This suggested that DPPC inhibits particle aggregation and coarsening, but may not fully prevent it. At pH 7, with DPPC there is no change in the SAXS analysis compared to as-prepared samples.

The larger particle size observed at lower pH arises due to increased charge screening, which allows particles to agglomerate and then fuse by diffusion controlled coarsening, forming larger-sized particles. When particles are coated by citrate (pK_{a1}=3.13, pK_{a2}=4.76, pK_{a3}=6.40), they are electrostatically-stabilised by the negatively-charged anions. However, when the pH of the colloidal dispersion is decreased, protonation of citrate anions occurs, and the AgNPs are no longer electrostatically stabilised. Without their negative shell, the particles are not prevented from coming into close proximity, which allows aggregation of the particles. This effect can also be seen in Fig. 4.3 (TEM) and 4.8 (SAXS), where the average particle diameter increases as the pH decreases.

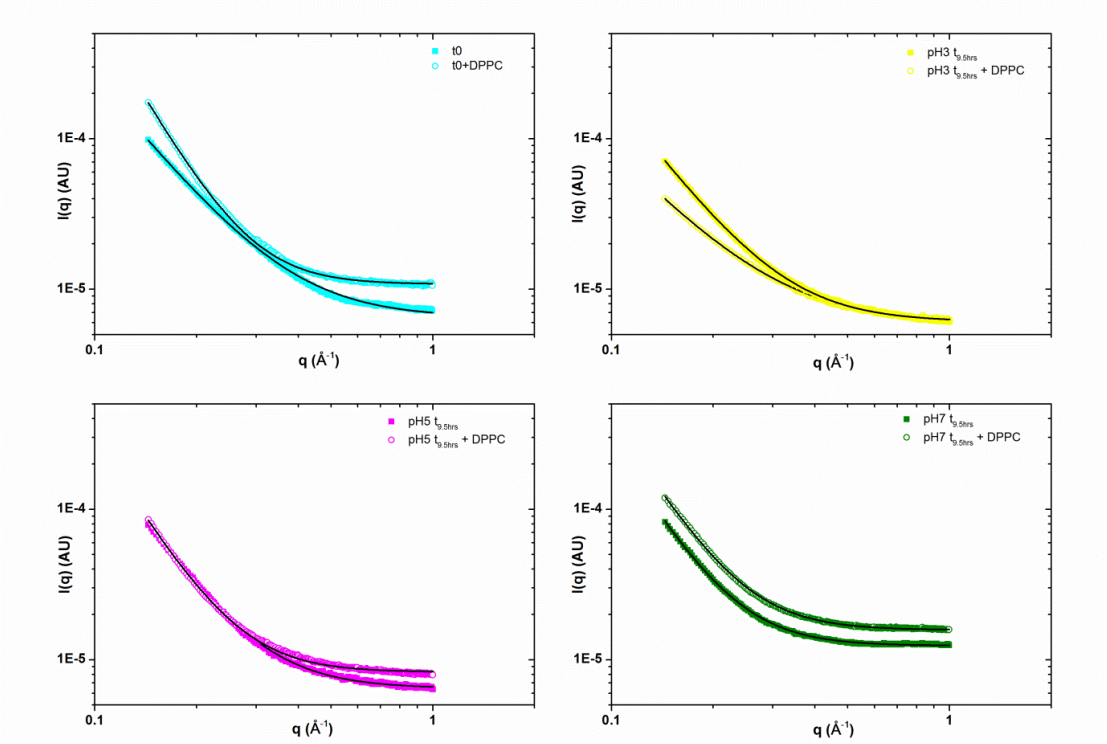

	As made, t=0		pH3, t=9.5 hrs		pH5, t=9.5 hrs		pH7, t=9.5 hrs	
	-DPPC	+DPPC	-DPPC	+DPPC	-DPPC	+DPPC	-DPPC	+DPPC
R_g (nm)	7.1	7.0	21.3	10.9	15.1	10.4	7.7	7.0
D (nm)	18.6	18.0	55.0	28.0	39.1	26.8	19.8	18.8
χ^2 (x 10^{-13})	1.2	2.3	0.5	0.5	1.0	1.3	0.6	1.6

Fig. 4.8: *In-situ* small angle X-ray scattering of NPs suspended in various pH solutions with and without DPPC; data (symbols) and fits (lines) along with extracted data. Y axis shows the total scattered intensity of particles and X-axis refers to the length of the scattering vector, $q = \frac{4\pi}{\lambda} . \sin(\theta)$.

Several reports have indicated that the cytotoxicity of nanosilver is decreased by the aggregation of AgNPs[49, 289]. Generally, NPs tend to aggregate into larger particles, decreasing the available surface area and decreasing reactivity[290]. The present results show that the presence of DPPC maintains dispersion of NPs without significantly increasing the dissolution rates compared to those without DPPC (Fig. 4.7); however DPPC did delay the release of silver ions. In principle, the ion release rate may also be inhibited by an increase in pH, oxygen depletion and high concentrations of free silver and free citrate[291].

This study of the interaction of AgNPs with DPPC has provided an insight into the colloidal stability of these NPs in biologically relevant media under varying pH

conditions. DPPC surfactant is the first line of defence against inhaled particles and helps to maintain homeostasis of the airways. Over the range of pH values investigated, the results indicate that decreasing pH resulted in increased Ag^+ ion release and induced a much greater extent of aggregation and coarsening of the particles. TEM and *in situ* SAXS analysis showed that AgNPs did not aggregate or coarsen at extracellular pH; maintenance of their small size may allow them to enter cells (where NP dissolution and aggregation may subsequently occur). This may lead to a greater formation of ROS within cells, reduced cell viability, and increased DNA damage.

4.3.2.4 SAED and EDS

Comparisons of SAED patterns (Fig. 4.9) in different media identified only the characteristic spacing of metallic silver.

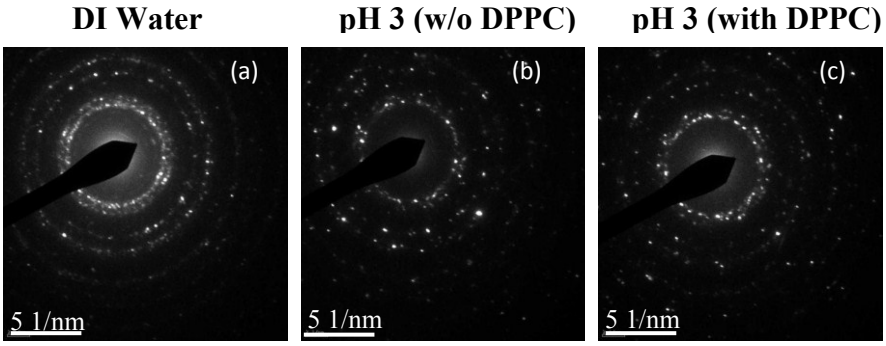

Fig. 4.9: SAED patterns taken from aggregates of AgNPs incubated for 1 week in (a) DI water, (b) pH 3 solution without DPPC, and (c) with DPPC. The selective area aperture size used was 100 nm in diameter. (Indexed patterns are shown in S1, S2 and S3).

Table 4.1: The lattice parameter of samples as a function of pH and incubating medium (with and without DPPC).

	Ag	AgNPs	with DPPC			without DPPC		
h k l	(Standard)	20 nm	pH3	pH5	pH7	pH3	pH5	pH7
1 1 1	0.236	0.230	0.235	0.235	0.231	0.241	0.232	0.234
2 0 0	0.204	0.202	0.199	0.202	0.203	0.208	0.201	0.201
2 2 0	0.145	0.142	0.121	0.143	0.142	0.149	0.143	0.144
Lattice constant (nm)	0.409	0.402	0.402	0.406	0.401	0.410	0.403	0.403

4.3.2.5. Zeta potential ξ measurements

The dispersion surface charge of particles can be altered by changing the solution pH as shown in Fig. 4.10. At the higher pH studied, the AgNPs suspension indicates a high ξ-magnitude of - 32.5 mV, corresponding to a stable suspension. At lower pH, the magnitude decreases to -22.5 and -18.2 mV at pH 5 and 3, respectively, indicating weaker repulsive forces and a less stable suspension.

The ξ of AgNPs/citrate and DPPC-wrapped AgNPs were also investigated at different pH. Fig. 4.10 shows that the ξ of AgNP/DPPC were smaller in magnitude compared to AgNPs without DPPC. ξ continued to decrease with pH, approaching isoelectric point (pI). However, despite the lower surface charge, the NPs are now stabilised by steric factors leading to more stable suspensions. At any given pH, increasing the ionic strength compresses the diffuse layer and decreases ξ of particles (Fig. 4.10), thereby reducing intermolecular repulsion, leading to an increased aggregation (Fig. 4.11)[43, 292, 293].

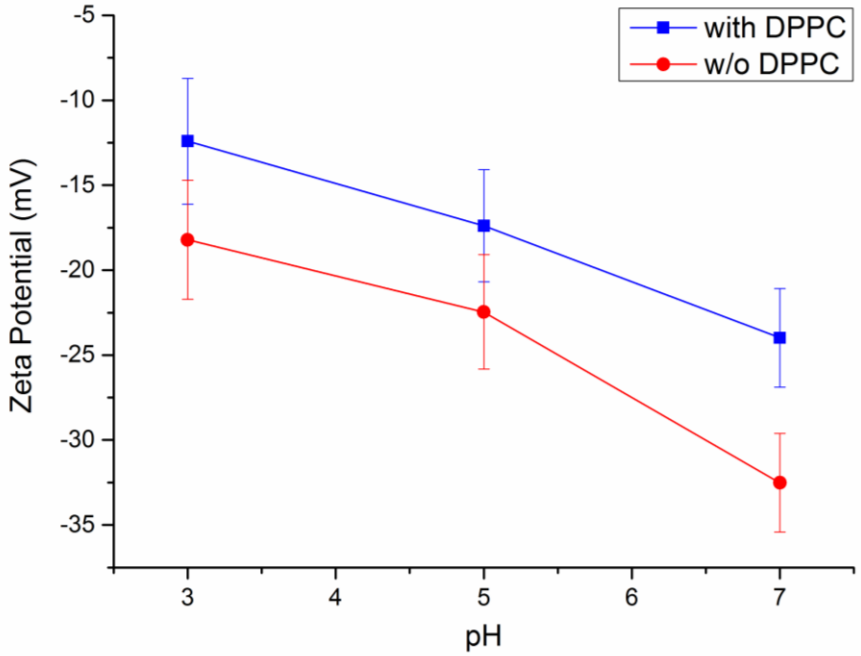

Fig. 4.10: Surface charge of AgNPs incubated in the suspension (with and without DPPC) as a function of pH.

The aggregation of extremely reactive NPs is driven by high surface energy and resultant thermodynamic instability of the NPs surface[294]. In suspension, adsorbates (*e.g.* $Ag_{ads)}$ will tend to diffuse between adjacent adsorption sites on a

surface, forming bonds with nearest-neighbor atoms *via* Brownian diffusion[295]. In this reaction, the coarsening kinetics of the NPs are controlled by surface diffusion. As the system tends to lower its overall energy, smaller-sized particles will first agglomerate, then irreversibly fuse and coarsen to form large particles, decreasing the total energy of the system[296].

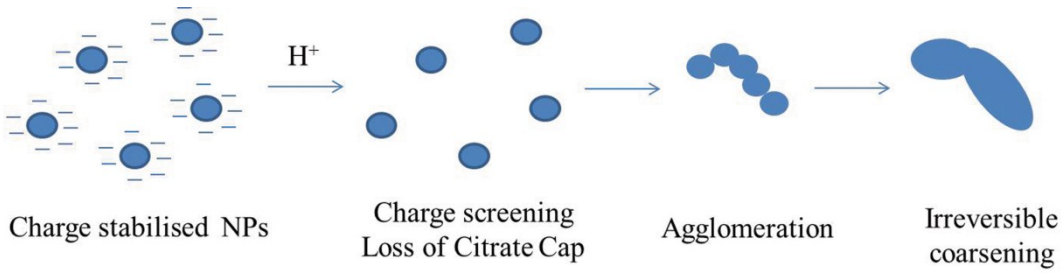

Fig. 4.11: Schematic representation of the aggregation process for citrate-stabilised AgNPs. AgNPs are stabilised by an electrostatic repulsive force between particles. Aggregation occurs with the increasing of pH due to the protonation of citrate anions, which can be elucidated by Derjaguin-Landau-Verwey-Overbeek (DLVO) theory[297, 298].

In contrast, stable NPs dispersion requires a dominant interparticle repulsive force to prevent the adhesion of particles. The decreasing magnitude of ξ with pH agrees well with the effects seen in TEM morphology studies. This supports the suggestion that larger aggregates found at lower pH may be due to the low surface charge and weak repulsive force when pH approaches the isoelectric point (pI)[299]. The 'hard' bonds of aggregates are difficult to break apart with agitation or ultrasonication due to a high energy barrier that hinders the separation of particles. When the pH is far from the pI, the electrostatic repulsive force is high enough to counter the van der Waals force and prevent the aggregation of NPs, and *vice versa*[300, 301].

The ξ of AgNPs/citrate was reduced after lipid adsorption (Fig. 4.10). This may be due to the positive charge of the hydrophilic headgroup of DPPC molecule - $N^{(+)}(CH_3)_3$ interacting with the negatively charged citrate coated AgNPs. Since DPPC is a zwitterion, the positive charge of ammonium group is favourable for electrostatic interaction with the AgNPs/citrate. Therefore, the presence of negative - PO_3^- in the zwitterion may cause the relatively small decrease of surface charge which remains negative[302].

The DPPC hydrophilic head group contains two oppositely charged groups[303]: a positively charged phosphate (P) group (1.8 nm) and a negatively charged choline (N) group (2 nm) as illustrated in Fig. 4.5. The zwitterionic head group of DPPC with neutral charge over a wide pH range approximately from 4 to 10.[304] Despite its neutrality, DPPC carries a significant electric dipole moment and surface potential. Mashaghi[305] reported that the lipid headgroups of DPPC tightly bound to interfacial water molecules facilitates energy transfer across membranes[306]. This might explain the antifouling property of DPPC and the dispersion of NPs in DPPC suspension[306]. Moreover, when NPs interact with DPPC, the hydrophilic trimethyl ammonium and phosphate head group of the molecule is oriented outwards to the surrounding medium; this surface modification of a hydrophilic outer coating also allows the dispersion of the surfactant-coated AgNPs in aqueous media[307].

4.3.3. Effect of Size and Surface Functionalization on the Colloidal Stability of AgNPs

AgNPs (Citrate20, PVP20, Citrate110 and PVP110) were manufactured by nanoComposix, Inc (San Diego, CA) *via* base-catalyzed reduction of silver nitrate using 5 - 7 nm gold seed as nucleation centers (i.e. the resultant particles have a small Au core). The size of the particles was initially characterized by the Nanotechnology Characterization Laboratory, National Cancer Institute at Frederick using TEM and zeta potential ζ measurements. The AgNPs were subsequently provided for study by the Consortium of NIEHS Centers for Nanotechnology Health Implications Research (NCNHIR). The particles were further characterized using transmission electron microscopy (TEM), energy dispersive X-ray spectroscopy (EDX) and used for Ag^+ dissolution studies. 110 nm AgNPs were characterized using high angle annular dark field scanning transmission electron microscopy (HAADF-STEM).

4.3.3.1 Characterisation of the As-received AgNPs

The primary size distribution and aggregation state of the citrate and PVP-stabilized Ag20 and Ag110 in water (Fig. 4.12 (a-d)) and pH 7 solution (Fig. 12 (e-h)) were compared by TEM which confirmed that physicochemical properties of the as - received AgNP (dispersed in DI water) were consistent with specifications from the provider (NCL). After incubation at pH 7 in perchlorate buffer solutions for 24 hours, Ag20-citrate NP formed large aggregates which could not be separated by the

sonication process (Fig. 4.12 (e)). In comparison, the Ag20-PVP NP formed smaller aggregates (Fig. 4.12 (f)) and fused together within the aggregates in some areas (Fig. 4.12 (f)). No significant changes in the aggregation state and morphology of the 110 nm AgNP (either PVP or citrate-capped) before, (Fig. 4.12 (c, d)) and after, the incubation at pH 7 (Fig. 4.12 (g, h)) were noted. As mentioned in section 4.3.2.1, TEM sample preparation may cause drying artefact of NPs. Thus, this technique was used as a comparative method in studying the effect of size and surface coating on the colloidal stability of NPs since exactly the same protocol was used to prepare these samples.

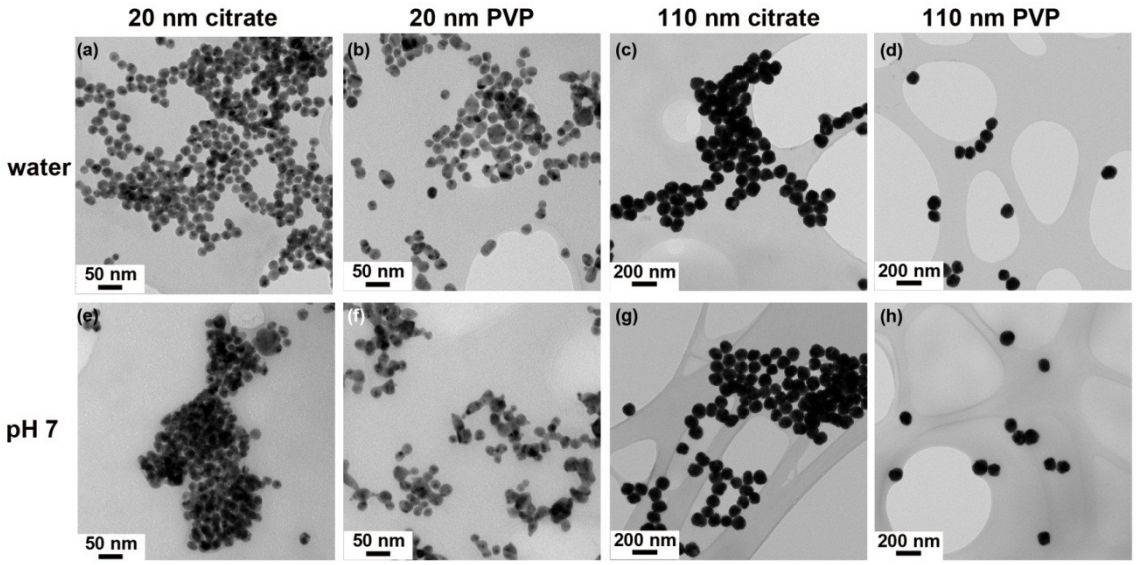

Fig. 4.12: Characterization of AgNP by TEM. Panel (a) Ag20-cit, (b) Ag20-PVP, (c) Ag110-citrate and (d) Ag110-PVP in DI water. Panel (e) Ag20-cit, (f) Ag20-PVP, (g) Ag110-citrate and (h) Ag110-PVP incubated in pH7 solutions (37 ºC) for 1 day.

Table 4.2: Physicochemical Properties of AgNPs in Mili-Q water (~ pH 6.7).

Samples	Primary Diameter (nm)	Zeta potential (mV)
20 nm, Citrate-stabilized Ag	22.2 ± 0.4	-39.4 ± 0.5
20 nm, PVP-stabilized Ag	22.8 ± 0.6	-33.5 ± 0.6
110 nm, Citrate-stabilized Ag	113.1 ± 5.5	-43.7± 0.6
110 nm, PVP-stabilized Ag	127.6 ± 5.6	-28.7± 1.2

In-house characterization analysis confirmed that as-received AgNPs had the physicochemical properties shown in Table 2; the zeta potentials are more similar than would be expected (the citrate capping may have surface-exchanged reducing the effective charge for these particles): all show a negative potential consistent with the manufacturers specification. EDX spectra (Fig. 4.13) showed that consortium particles (20 nm) were gold-silver core-shell NPs. As expected the Au core could not be detected for 110 nm NPs using EDX or high-angle annular dark-field (HAADF) in a scanning transmission electron microscopy (STEM) as it is below the concentration limit for detection, buried in the Ag shell (Fig. 4.14 and 4.15). However, the manufacturers MSDS sheet states that the Au core is present, confirmed by ICP-MS at NCNHIR.

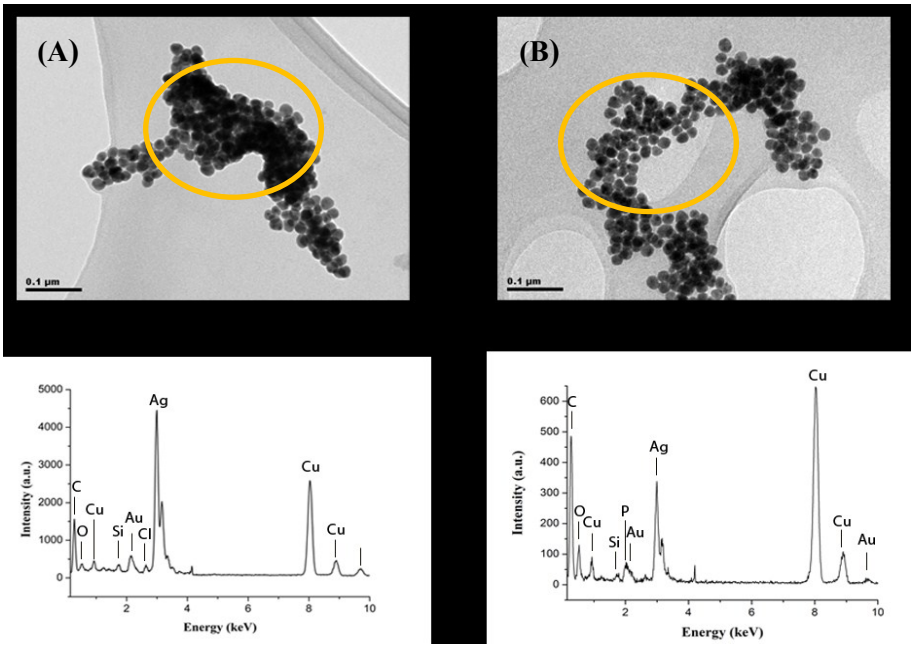

Fig. 4.13: Bright field TEM images and Energy Dispersive X-Ray Spectroscopy (EDX) Particle Analysis: Citrate AgNPs (20nm) incubated in pH 7 (A) without DPPC (B) with DPPC for 24 hours. Au was detected in both the 20 nm citrate and PVP coated AgNPs.

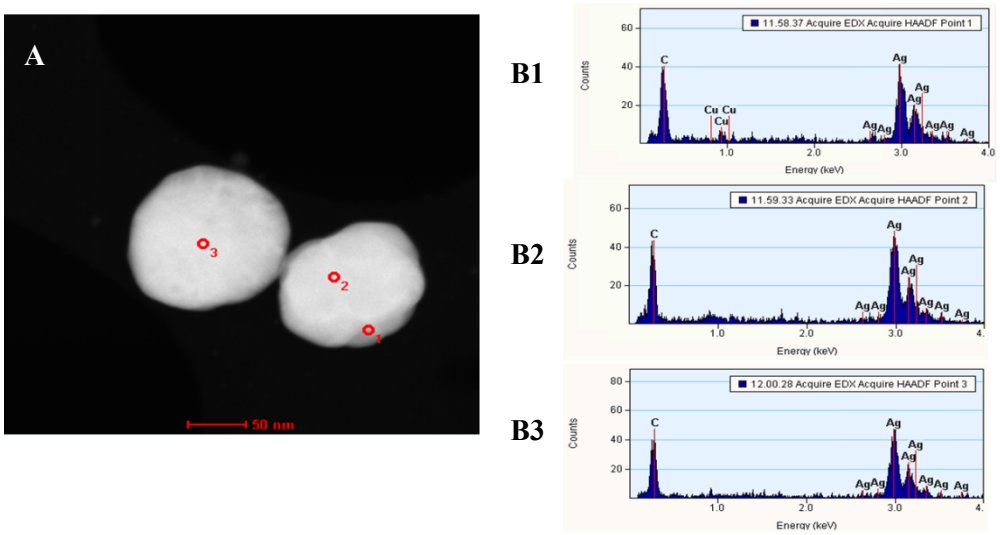

Fig. 4.14: (A) High Angle Annular Dark Field Scanning Transmission Electron Microscopy (HAADF-STEM) images of the citrate coated 110 nm AgNPs and (B1-3) EDX spectra from which only shows the presence of Ag.

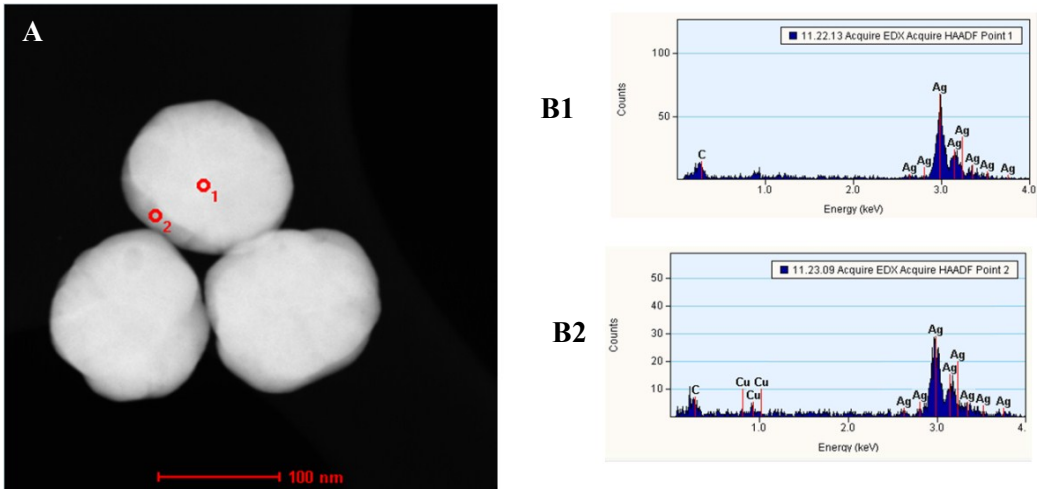

Fig. 4.15: (A) High Angle Annular Dark Field Scanning Transmission Electron Microscopy (HAADF-STEM) image of PVP coated 110 nm AgNPs and (B1-2) EDX spectra taken from region 1 and 2 in (A). Au cannot be detected from the 110 nm AgNPs (both PVP and citrate coating).

4.3.2.2. Effect of size and capping agent on dissolution kinetics and morphology evolution of AgNPs

The dissolution rates of the four types of AgNPs was examined at both pH 5 & 7 (inorganic buffers) by ICP. The dissolution rates were higher at pH 5 than at pH 7

(Fig. 15 and 16). All particles, with the exception of the 20 nm citrate-capped particles, displayed less than 1% total release of silver to the solution over a three-day incubation period (Fig. 4.16 and 4.17). The 20 nm citrate-capped particles displayed greater dissolution than the other particles at both pH 5 & 7; > 4 % Ag was released into the solution after three days of incubation (Fig. 4.16). Both the 110 nm particles (citrate- and PVP-capped Ag 25 µg/mL, pH 7) showed negligible dissolution in H_2O over a 72 hour period (Fig. 4.17), while dissolution of the 20 nm particles was dependent on the type of capping agent and the presence of DPPC. Ag20PVP NPs showed less dissolution than the Ag20citrate NPs with the % of Ag^+ at 72 hours being 1.1 vs 3.9 % for the PVP- and citrate-coated 20 nm NPs respectively. Addition of DPPC lowered the dissolution rate of both citrate and PVP-20nm NPs to 0.05 (PVP) and 1.1 (citrate) % of the total mass of silver.

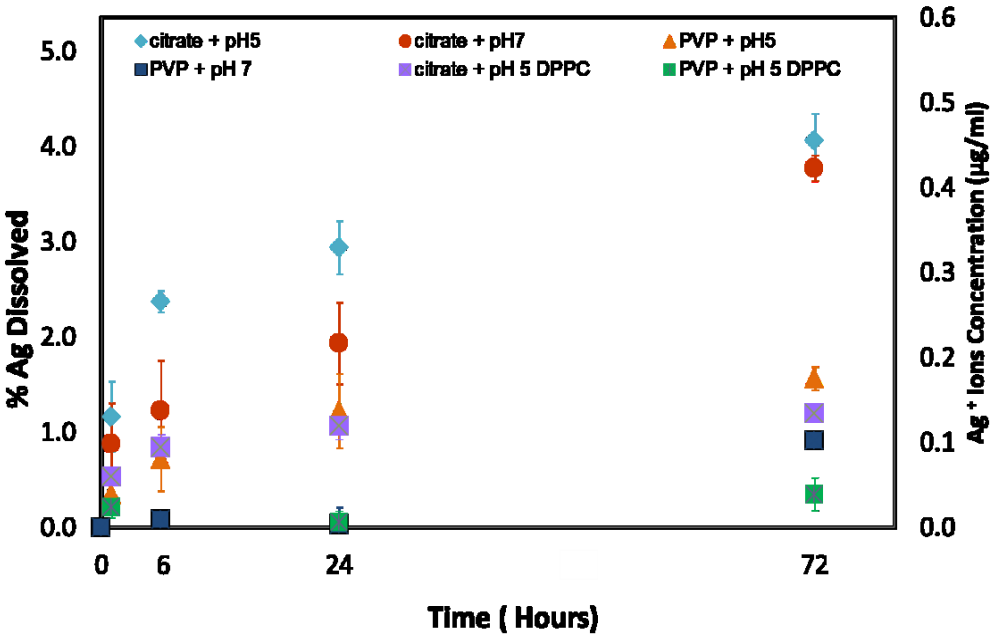

Fig. 4.16: Ag^+ Ion Release Study: 20nm AgNPs incubated in perchlorate acid/perchlorate buffer solutions (pH 5 and 7) over the course of 72 hours. The citrate stabilized particles demonstrated the greatest percent Ag dissolved at pH 5 over the time course.

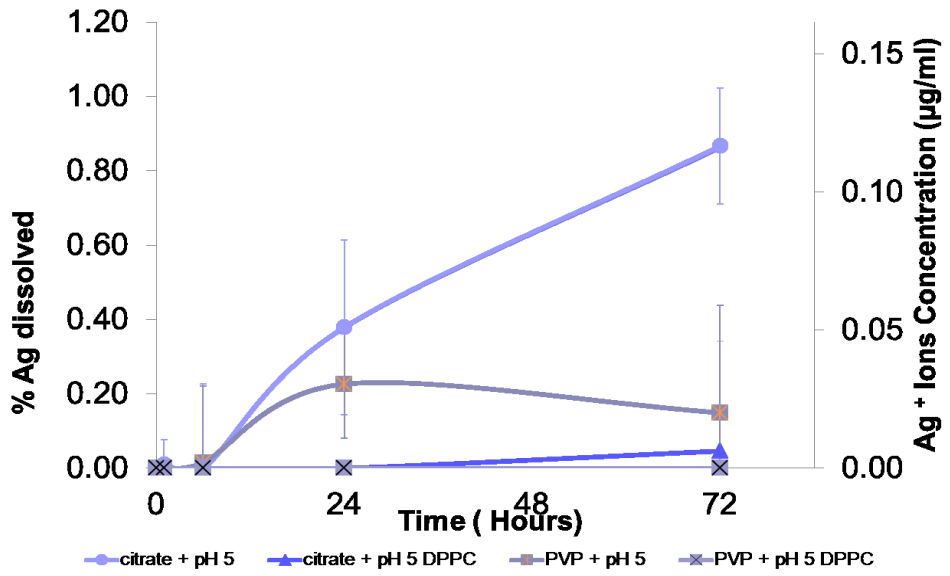

Fig. 4.17: Ag^{+} Ion Release Study with DPPC: 110 nm AgNPs incubated in perchlorate acid/perchlorate buffer solutions (pH 5 and 7) over the course of 72 hours with and without DPPC. Citrate stabilized particles demonstrated the highest % Ag dissolved over the entire time course. Dissolution from the 110nm citrate and PVP-stabilized AgNPs in pH 7 (with or without DPPC) was below the detection limit showing that negligible dissolution had occurred.

Having established that the particles were relatively stable against dissolution in perchlorate buffer solution (pH 7), their morphology and the effect of surfactant addition were assessed by TEM (Fig. 4.18). Regardless of stabilization, or the presence of the model surfactant DPPC, 20 nm AgNPs displayed a greater tendency to aggregate than the 110 nm particles, as expected due to surface energy considerations. Evidence of particle aggregation and significant *coarsening* was also observed for the 20 nm particles with both capping agents (Fig. 4.18 C&G). The limited aggregation of 110 nm AgNPs observed in buffer (Fig. 4.18 A&E) was completely lost upon addition of DPPC (Fig. 4.18 B&F). DPPC also had a dramatic effect on the 20 nm AgNPs with only small clusters of the AgNPs formed and no coarsening was observed (Fig. 4.18 D&H). In the lung, smaller-sized citrate- or PVP – AgNPs (20 nm) may form less stable agglomerates, potentially increasing the surface area available for biological interaction with proteins, lipids and inorganic ions in the lung fluid milieu, as well as for oxidative reactions[216, 308].

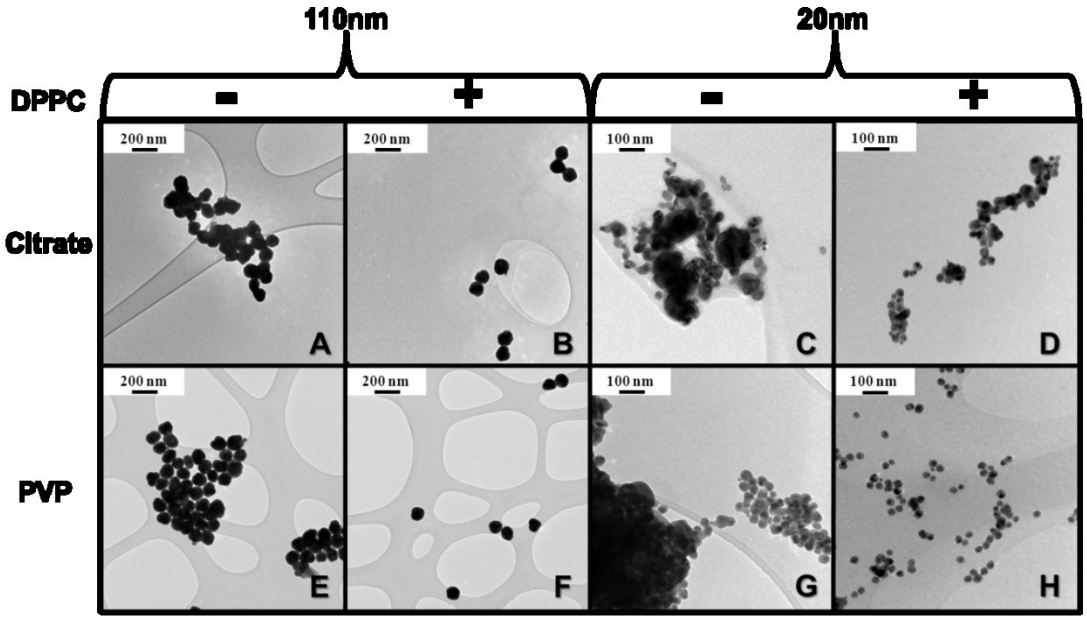

Fig. 4.18: AgNP Morphology and the Effect of Surfactant Addition by Transmission Electron Microscopy: TEM images of citrate vs. PVP stabilized AgNPs (20 and 110nm) incubated in pH 5 solution with, and without, DPPC at 37°C for 24 hours (magnification at 20 x). The addition of DPPC decreased particle aggregation in all instances; however, NPs size was the predominant factor in particle aggregation.

In comparison, the Ag20-PVP NP formed smaller aggregates and in some areas, the Ag20-PVP within the aggregates had fused together (Fig. 4.18G). The citrate-coated AgNP were stabilized by electrostatic repulsion attributed to the deprotonation of citrate carboxylic acid groups[309-311]. PVP is a non-ionic polymer, which stabilizes the AgNP by steric hindrance. The PVP-stabilized AgNP were less affected by electrolytes, therefore they had higher dispersion stability in biological media (Fig. 4.18H)[312].

Size, charge, solubility and surface modifications of metallic NPs have been linked to NPs toxicity[57, 313]. *In vitro* studies in this work could be used to predict differences between the bio-reactivity of AgNMs with different sizes and surface coatings in the lung *in vivo*. Smaller AgNP (15-30 nm) have been reported to be more toxic than larger ones (55 nm) in *murine* and human models due to their high reactivity with biological systems resulting from their larger specific surface areas[95, 314, 315]. *In vitro* dissolution studies in this work showed higher rates of dissolution for the 20 nm particles in perchlorate buffers with a reduced dissolution

rate in DPPC, suggesting that surfactant interaction stabilised the surface conditions, preventing oxidation, which would otherwise lead to the release of Ag^+. The rate of dissolution for the 110 nm particle was negligible, indicating that the release of Ag^+ ions may play an important role in the increased toxicity of the 20 nm nanoparticles. Thus, size, surface charge, chemical composition of NPs have to be considered in the understanding of NP cytotoxicity, which has important implications for the safe use of coated silver nanoparticles in commercial and consumer preparations[316, 317].

4.4 Summary

In summary, TEM images and *in situ* SAXS showed that AgNPs suspended in media containing DPPC, the primary lipid constituent of LLF were stabilised against coarsening and aggregation. Nevertheless, the presence of DPPC surfactant did not significantly affect the total amount of silver released over the pH range 3.0-7.0 after two weeks. These results enhance the understanding of the stability of NPs in the deep lung, and may be utilised for making predictions of how the aggregation state and stability of AgNPs changes in the LLF, thereby affecting the pulmonary system with regard to both respiratory physiology and host immunity. Furthermore, these studies also suggest that stabilisation of the AgNPs by coatings, prior to interaction with surfactant molecules in the lung lining fluid, is an important consideration. More generally, these results highlight the need to consider NPs size, surface coatings and their interaction with biological molecules (in this case lipids) in order to understand the downstream effects in humans and the environment. In particular, detailed characterisation of whether, and how, engineered nanomaterials (ENMs) change in their physicochemical properties within a biological system or the environment will be essential to make informed predictions about the mechanisms toxicity of ENMs.

5.0 Neurotoxicology: Microglia Response to AgNMs and Their Interaction with Enzymes in the Central Nervous System (CNS)

5.1 Overview

The extensive use of silver nanomaterials (AgNMs) in various emerging markets will lead to their significant release into the environment during industrial manufacturing, washing, use and product disposal. AgNMs as potential occupational and environmental hazards may raise health and safety concerns. For this reason, there is a need to assess the interaction of NMs with biological systems precisely for early prediction of NMs cytotoxicity. In relation to neurotoxicity, studies have shown that silver nanoparticles (AgNPs) can cross the blood brain barrier (BBB) *via* the systemic blood supply and localise inside the brain, causing neurodegeneration. However, much less is known about the distribution of AgNMs and their interaction with protein complexes inside brain cells. Here, interaction of microglia with AgNMs of two morphologies, spheres and wires, as well as their uptake and cytotoxicity were investigated. TEM analysis identified cellular uptake of both Ag formats, but neither increased production of reactive oxygen species (ROS) nor affected cell viability or mitochondrial activity. STEM - EDX analysis demonstrated the formation of silver sulphide (Ag_2S) within the cells, possibly facilitating metal detoxification and limiting cell death by protection against free radicals. In comparison between these two morphologies of AgNMs, NPs showed a significant anti-inflammatory effect, reducing ROS, nitrite generation and pro-inflammatory cytokine synthesis, which might be due to their higher Ag^+ ions release in the cellular environment. Confocal microscopy revealed that AgNM-treated microglia upregulated the expression of cystathionine γ-lyase (CSE), a major hydrogen sulphide (H_2S)-producing enzyme in the central nervous system (CNS), suggesting enhanced Ag^+ - induced liberation of cofactors which may increase the enzymatic activity. This may also occur due to the insufficient concentration of H_2S available to interact with Ag^+ ions, inducing upregulation of H_2S producing enzymes to achieve chemical equilibrium condition in the CNS. These findings demonstrate that Ag_2S formation regulated by CSE in the CNS acts as an ion trap for free Ag^+, significantly limiting short term toxicity effects – with important consequences for the neuro-safety of AgNMs. Therefore, not only NPs uptake into cells, but also fundamental understanding of the NPs-protein complex is

necessary for optimizing particular NPs features for favourable bioavailability and biodistribution.

5.2 Experimental Methods

5.2.1 Nanomaterials Synthesis and Characterisation

Silver nanoparticles (AgNPs) were synthesised *via* a chemical bath reduction method in which trisodium citrate ($Na_3C_6H_5O_7$) (Fisher Scientific, UK) served a dual role as both reductant and stabilizer. Briefly, $AgNO_3$ (1.0×10^{-3} M) (Sigma-Aldrich, UK) solution was added into the preheated DI-water (180 mL). Then, $Na_3C_6H_5O_7$ (1.0×10^{-3} M) solution was added dropwise to the $AgNO_3$ solution as soon as the boiling commenced. The colour of the solution slowly turned into grayish yellow, indicating the reduction of the Ag^+ ions. The solution was heated continuously for an additional 20 minutes, and then cooled to room temperature. In order to remove impurities and excess citrate, the AgNPs suspensions were washed with DI water and centrifuged at a relative centrifugal force maximum value (RCF_{max}) of 10,000 g. This washing process was repeated three times to ensure no citrate remained in the solutions. Finally, citrate-coated AgNPs were suspended in DI water based on the desired concentration of nanoparticles in the suspension. These purified particles were sealed, stored in the dark and kept in a refrigerator. The cleanliness of synthesised particles was confirmed with Energy Dispersive X-ray Spectroscopy (EDS) to ensure that sulphidation of AgNPs had not occurred [278] and impurities, such as $Na^+$and Cl^- were removed by the washing process. Silver nanowires (AgNWs) were prepared *via* a modified polyol pathway through the reduction of $AgNO_3$ with ethylene glycol in the presence of poly(vinyl pyrrolodone), PVP (Sigma-Aldrich, UK). Full characterisation of the physicochemical properties of the PVP- coated AgNWs used in this study was previously reported by Chen *et al.*[21].

5.2.2 Cell Culture and Treatments

Microglia experiments were carried out on the immortalized embryonic mouse microglia N9 cell line, first developed by Dr. Ricciardi-Castagnoli *et al.* [318] and given as a kind gift by Dr. Deanna Taylor, Imperial College London. N9 microglia reliably replicate cultured primary microglia with respect to NO production, cytokine synthesis and expression of cell surface markers[319-321]. N9 microglia were cultured in Dulbecco's Modified Eagle's medium (DMEM, Sigma) with 5% Fetal

Calf Serum (FCS, Sigma), 8 mM L-glutamine (Sigma) and 50 U/mL Penicillin and 50 µg/mL streptomycin (Sigma) (termed full DMEM) at 37^{o}C in a humidified atmosphere with 5 % CO_2.

Microglia cells were plated either in 96-well plates or onto glass coverslips in 24-well plates (at 10,000 or 50,000 cells per well, respectively) and incubated for 24 hr before experimentation began to allow them to readopt a resting phenotype. Microglia were then washed with serum-free RPMI (Sigma) (with 8mM L-glutamine and 50 U/mL Penicillin and 50 µg/mL streptomycin; termed SF-RPMI) and incubated with AgNPs or AgNWs in SF-RPMI for 1 h (pulse) at 37 ^{o}C with or without lipopolysaccharide (LPS) (500 ng/mL). The cells were then washed with SF-RPMI and incubated in SF-RPMI for a further hour. Then, they were incubated in full DMEM for 4 or 24 h (chase) before analysis (*i.e.* experimental end-point).

5.2.3 Cell Viability Assays

5.2.3.1 MTS Assay

MTS is a chromogenic assay which involves the bioreduction of the tetrazolium compound 3-(4, 5-dimethylthiazol-2-yl)-5-(3-carboxymethoxyphenyl)-2-(4-sulfophenyl)-2H-tetrazolium by NADH in viable cells into a colored formazan product. Therefore, the cellular metabolic activity can be quantified spectrophotometrically by measuring the absorbance of the formazan product.

At the experimental end-point, cells plated in 96 well plates were washed and incubated at 37^{o}C with fresh full DMEM (100 µL) containing MTS reagent (Promega, UK) (10 µL) for 2-3 h before the optical density (at 490 nm) was quantified with a plate reader. Cell viability was determined by comparing the optical density of compound-treated cells *vs.* control cells.

5.2.3.2 LDH Assay

Lactate dehydrogenase (LDH) is a soluble cytosolic enzyme which catalyses the oxidation of lactate to pyruvate. Once cells lose their membrane integrity due to stress or injury, LDH is rapidly released into the extracellular medium. Thus, membrane damage and cytotoxicity can be assessed by the quantification of released LDH from cells.

At the experimental end-point, extracellular medium (50 μL) from cells plated in 24 well plates was transferred to a 96-well plates and incubated with LDH reaction mixture (50 μL) (Promega, UK). Following 10-20 minutes incubation (at 37^{o}C), the optical density (at 490 nm) was quantified with a plate reader to determine LDH concentration in the extracellular medium. To control for lower LDH release due to a sparser cell population following cytotoxicity, total LDH (*i.e.* intracellular plus released LDH) was also quantified by lysing cells in the original culture medium (with 10 μL lysing buffer, Promega, UK) and the cell medium incubated with LDH reaction mixture as before. The amount of released LDH was then normalized against the total amount of LDH in the culture well.

5.2.4 Cytokine Release

Tumor necrosis factor alpha (TNFα) and interleukin-6 (IL-6) are pro-inflammatory cytokines produced by activated microglia cells, therefore indicate a microglial inflammatory phenotype. At the experimental end-point, TNFα and IL-6 release was measured in the cell culture medium using commercially available ELISA kits (Peprotech, UK) according to the manufacturer's instruction.

5.2.5 Intracellular ROS Release

Intracellular ROS levels were detected using the 2′,7′-Dichlorofluorescin diacetate (DCFH-DA) assay (Sigma, UK). DCFH-DA is a lipophilic cell permeable compound that is deacetylated in the cytoplasm by cellular esterases to DCF, which is then oxidised by free radicals, including hydroxyl, alkoxyl, peroxyl, carbonate and nitrate radicals to produce a fluorescence signal.

For ROS quantification, N9 microglia cells were seeded in dark, flat transparent bottomed 96 well plates (10,000 cells per well) as above (see 'cell culture and treatment section'). At the experimental end-point, cell media was removed and replaced with 25 μM DCFDA diluted in full DMEM without phenol red for 45min at 37 ^{o}C protected from light. Cells were then washed twice with PBS before measurement of fluorescence (at emission 485 nm and excitation 535 nm) in a microplate reader.

5.2.6 Mitochondria Membrane Potential Quantification

Mitochondrial membrane potential (MMP) was determined using the red-orange fluorescent dye tetramethylrhodamine ethyl ester perchlorate (TMRE) (Sigma, UK).

This lipophilic, positively-charged dye enters cells and is sequestered by healthy mitochondria with a negative charge. Conversely, depolarized or inactive mitochondria lose their membrane potential, leading to a loss of their negative charge and ability to sequester TMRE. Therefore, the polarization state of mitochondria can be assessed by the amount of orange-red fluorescence inside cells.

At the experimental end-point, cells in 96 well plates were rinsed twice in PBS and incubated in 500 nM TMRE for 20 mins at 37 ^{o}C in the dark, followed by rinsing with 0.2 % bovine serum albumin (BSA) in PBS prior to fluorescence measurement with excitation at 549 nm and emission at 575 nm using a microplate reader.

5.2.7 Western Blotting

Protein expression was quantified through immunostaining of Western blots (WB) from N9 lysates. Cells seeded in 6 well plates (at 500,000 cells per well) were lysed with RIPA buffer (Sigma, UK) with 10% protein inhibitor cocktail (Aprotinin, Bestatin, E-64, Leupeptin, Pepstatin, AEBSF) (Sigma, UK) at the experimental end-point. The lysates (20 μg) were resolved by SDS-PAGE (10 % gel) and transferred to PVDF membranes. After blocking with 5 % BSA in TBS-T (2 h at room temperature), the WB were stained with anti-CBS (1:5000, SantaCruz, USA), anti-CSE (1:5000, SantaCruz, USA), anti-MPST (1:1000, SantaCruz, USA) or anti-β-actin (1:20000, Abcam, UK) (all in 1 % BSA/TBS-T) overnight at 4 ^{o}C. The WB was then incubated with horse radish peroxidase (HRP)-anti-mouse secondary antibody (1:2000 in 1 % BSA/TBS-T, Sigma, UK) for 2 h at room temperature. Immunodetection was visualized through enhanced chemiluminescence.

5.2.8 Cellular Uptake of AgNMs

5.2.8.1 Transmission electron microscopy

N9 Microglia cells were seeded in 24 well plates and exposed to 50 μg/ml AgNPs/AgNWs for 24 h. After 24 h exposure, the cells were rinsed with HEPES buffer and fixed in freshly prepared 2.5 % glutaraldehyde for 1 h at 4 ºC. Each sample was dehydrated in a graded ethanol series (50 %, 70 %, 90 % and 100 % volume ratio of ethanol to DI water) for 5 min x 3 times each, followed by acetronitrile (Sigma) for an additional 10 min each, all at room temperature. After dehydration, samples were progressively infiltrated with 50 % and 75 % Quetol-based araldite resin/ethanol solution (Agar scientific, UK) overnight and finally

100 % resin for 4 days with fresh resin replaced daily. The specimens were then cured at 60 ºC for 24 h before cutting by an ultramicrotome (Leica ultracut UCT, Wien, Austria). Ultrathin cell monolayers (approximately 50 – 100 nm) were cut directly with a 35º glass knife and each section was examined in a JEOL 2000 transmission electron microscopy (TEM) at an accelerating voltage of 80 kV.

Multiple cells (> 100 per sample) from each sample were surveyed using an FEI Titan 80-300 scanning transmission electron microscopy (STEM) operated at 80 kV, fitted with a Cs (image corrector and a SiLi Energy Dispersive X-Ray (EDX) spectrometer (EDAX, Leicester UK). STEM – high angle annular dark field (HAADF)/ EDX analyses were performed on non-stained samples. STEM experiments were performed with a convergence semi-angle of 14 mrad and inner and outer HAADF collection angles of 49 and 239 mrad, respectively. The probe diameter was < 0.5 nm.

5.2.8.2 Focused Ion Beam (FIB) - Secondary Electron Microscopy (SEM) - EDX

To confirm the uptake and the intracellular location of AgNMs, a search of NMs inside the cells was performed by milling into the cell at the inspection region for SEM analysis. Before beginning the focused ion beam (FIB) milling, the sample was coated by a metallic layer to protect against unwanted beam-damage. Specimen milling and imaging was accomplished using a FIB 200 TEM (FEI Company, USA) equipped with a Ga^+ ion source. After the FIB process, samples were transferred and analysed using the SEM-EDS system (Auriga 40) equipped with in-lens and backscattered (BSE) detectors as well as an X-ray analyser for EDS sensitive to carbon and other higher atomic weight elements.

5.2.8.3 Confocal microscopy

To assess expression of H_2S-producing enzymes (CBS, CSE and MPST) in microglia N9 cells following AgNMs treatment, cells seeded on cover slips in 24 well-plates were washed with freshly prepared Dulbecco's phosphate buffer saline (PBS) at the experimental end-point, followed by fixation using ice cold methanol. The cells were blocked (1% BSA in PBS, pH 7.4) for 30 minutes at room temperature and incubated with primary antibodies (1:200 dilution) in blocking solution at 4 °C overnight. Following washing with PBS (x3) cells were incubated with the fluorescently-labelled secondary antibodies diluted in blocking solution

(1:200 dilution) for 1 h at the room temperature. Following further washings, the nuclei were counter stained with Hoechst 33342 (blue). The glass cover slips were mounted onto the microscope slides with SlowFade® antifade reagent and visualized using Leica SP5 inverted confocal microscope (Leica, Germany). To quantify the amount of the enzymes, the fluorescent intensity of the enzyme in the cells was measured using Fiji (Image J) analysis software, and the data were expressed as mean fluorescent intensity (MFI) with the standard deviation (± SD). Cells (40 cells) were observed for each sample and three separate experiments were performed with a total number of 120 observed cells.

5.2.9 TOF-SIMS Analysis of AgNMs Uptake in Microglial Cells

Prior to SIMS analysis the microglia cells (S1- controlled sample), AgNWs (70 nm in diameter) + microglia cells (S2) and AgNPs (110 nm in diameter) + microglia cells (S3) were seeded on 13 mm diameter glass cover slips. The samples were critical point dried to preserve their surface structure. The spectra and imaging data were acquired using a TOF-SIMS 5 instrument (ION-TOF, Germany) equipped with a bismuth primary ion source and a C_{60}^+ sputter ion source. Sputtering by C_{60}^+ was performed on a 500 μm x 500 μm area at energy of 10 keV. The current on the target was 0.6 nA. The timing scheme consisted of a sputter cycle of 0.5 s before acquisition, followed with pausing of 1 s for each scan in imaging mode. Sample imaging was performed within an area of 300 μm x 300 μm at 25 keV using Bi_3^+ cluster ions. Each scan provides an image with 256 x 256 pixels. The target current was 0.59 pA.

5.2.10 Statistical Analysis

The data were analysed by One-way Anova with Tukey's post-hoc test using SPSS package software. Differences between different samples were considered statistically significant at $p < 0.05$. Data are presented as means ± SD.

* The cell culture and cell viability assays experiments were led by Gonzalez Carter, Daniel at Hammersmith hospital campus, Imperial College. Whereas, the confocal imaging was led by Ruenraroengsak, Pakatip at South Kensington campus, Imperial College.

5.3 Results and Discussion

5.3.1 Characterisation of AgNMs

Both AgNPs and AgNWs used in this analysis were synthesised in-house and characterised using TEM, STEM-EDS, SAED and zeta potential. Fig. 5.1 showed

the morphology of AgNPs/ AgNWs and their size ditributions characterised by TEM or SEM techniques. SAED patterns (Fig. S2) revealed that as-synthesised NPs have characteristic lattice spacings 0.236 nm, 0.204 nm, and 0.145 nm, corresponding to the (111), (200) and (220) planes of metallic silver (Ref.#01-087-0597). EDX analysis taken from the AgNPs (Fig. S3) confirmed that all impurities had been removed after washing with DI water and no sulfidation had occurred on as-synthesised AgNPs. Whereas, PVP-capped AgNWs were synthesized *via* a polyol process and their physicochemical characteristics were thoroughly characterised as shown in Table 1.

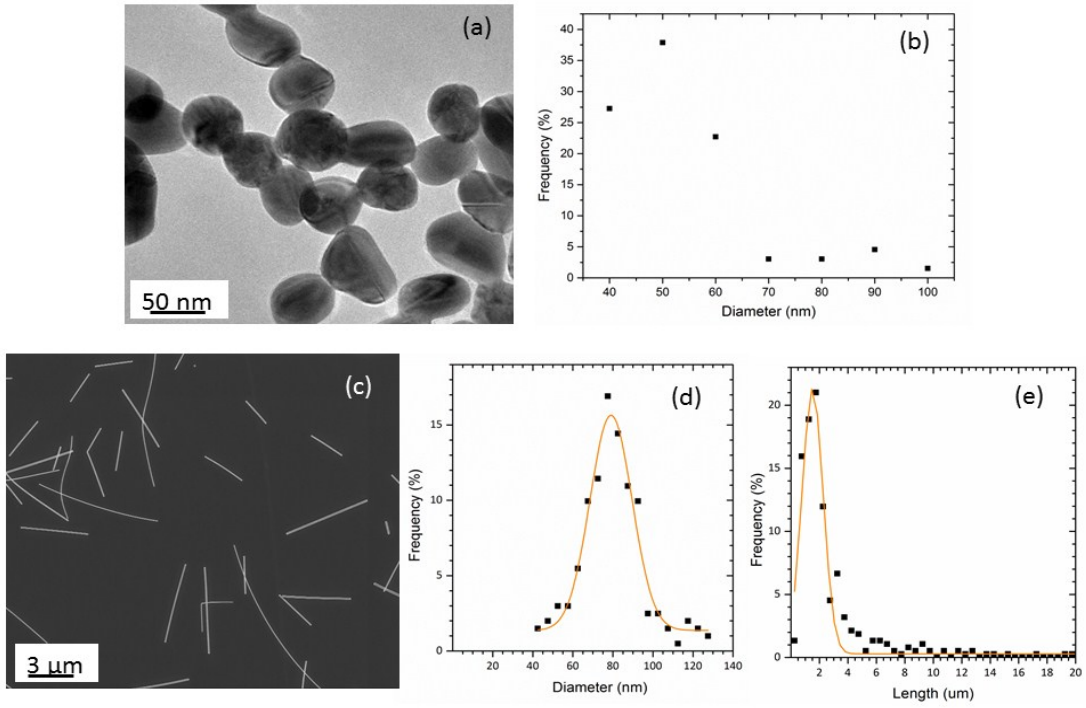

Fig. 5.1: Characterization of the as-synthesised AgNMs. (a) TEM image of as-synthesised AgNPs, and (b) their size distributions. (c) SEM image of the AgNWs prepared by a modified polyol pathway through the reduction of $AgNO_3$ with ethylene glycol in the presence of PVP and their (d) diameter and (e) length distribution.

Table 5.1: Summary of the physicochemical characteristics of AgNPs and AgNWs.

Material	**Silver Nanopaticles (AgNPs)**	**Silver Nanowires (AgNWs)**
Average Size	59 nm (40 – 100 nm) in diameter	72 nm (36 - 108 nm) in diameter 1.5 µm (0.1 - 3.1µm) in length
Capping Agent	Citrate	PVP (poly(vinyl pyrrolidone)) average molecular weight $M_w \approx 360k$
Surface Charge	- 27.8 ± 0.1 mV	- 14.8 ± 0.1 mV

5.3.2 Cellular Uptake of AgNMs

To investigate the consequences of exposure of N9 microglia to AgNMs, cells treated with AgNPs/NWs (50 μg/mL) were subjected to SEM and TEM. SEM backscattered images demonstrated that a large amount of Ag was found in microglia (Fig. 5.2b). Similarly, TEM showed AgNPs were found in microglia cells after an hour pulse chased then incubate for a further 24 h. NPs were observed within the cytoplasm and also found within endosome and lysosome-like vesicles. As observed in Fig. 5.2d, most of NPs agglomerated and formed larger-sized particles, probably due to the lower intracellular pH and thermodynamic driving force to minimise its total surface energy[60]. Furthermore, the interaction of NPs with salts in the RPMI cell culture medium may also affect their colloidal stability. The distribution of AgNWs was similar to that found for the AgNPs. Translocation of NWs across the plasma membrane after a 1 h pulse has been previously reported by Chen *et al.*[21]. The mechanism of 'needle-like' piercing into cells has been demonstrated for functionalised carbon nanotubes (CNTs)[209, 322]. However, 24 h after the exposure pulse, the 'needle-like' morphology of AgNWs was not retained but dissolved forming spherical-shaped particles in the cells (Fig. 5.2f).

The intracellular changes in the chemistry and morphology of both NPs and NWs were analysed using HAADF STEM – EDS after pulse chased for 1 h prior to a further 24 h exposure. The C_s - corrected STEM in conjunction with HAADF and EDX detector has dramatically improved the capability of atomic scale analysis (chemical and morphological features of AgNMs in microglia) with better resolution and quality than the conventional techniques. Fig. 5.2 shows the HAADF STEM images and EDX spectra of AgNPs and AgNWs-treated microglia. AgNMs were stored in vacuum prior to STEM-EDX characterisation and precautions were taken to ensure that the AgNMs were not sulphidised in the ambient air during TEM imaging nor interact with cell culture media[59]. Furthermore, we also avoided the use of heavy metal staining techniques which may affect the observed morphology of AgNMs and accelerate oxidation of AgNMs.

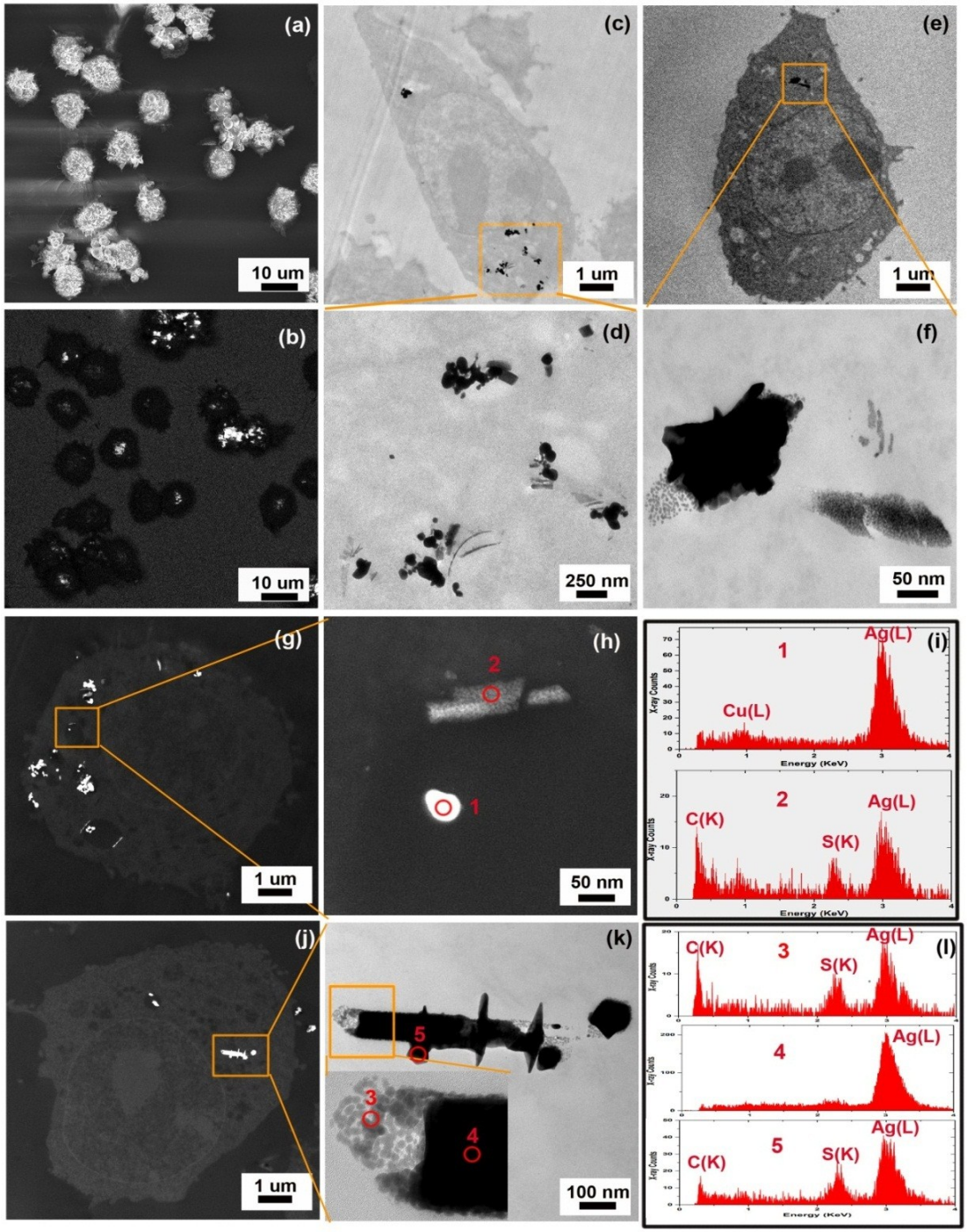

Fig. 5.2: AgNP/NW uptake by N9 microglia following 1hr pulse AgNP/NW treatment (50 µg/mL) with 24 hr chase. SEM images of AgNPs in N9 microglia cells in lens (a) and EBS (b) mode showing intense uptake of AgNPs; TEM images showing the cellular uptake of AgNPs (c - d) and AgNWs(e - f) by microglia cells using unstained cell sections; HAADF - STEM images showing the cellular distribution of AgNPs (g) and a corresponding higher resolution HAADF-STEM image (h) taken from the boxed area in (g). STEM-EDX spectra (i) taken from corresponding areas 1-2 marked in (g). HAADF-STEM image of AgNWs in microglia cells (j) and a high magnification image (k) of the selected area in (j). STEM-EDX spectra (l) collected from areas 3-5 marked in (k). (N: nucleus; C: cytoplasm; E/L: endosome/lysosome; ES: extracellular space).

The STEM-EDX spectrum (Fig. 5.2i) taken from the precipitates surrounding the AgNPs detected Ag(L) peaks and S(K) peaks, further confirming the interaction between Ag and S and the re-precipitation of highly insoluble Ag_2S (k_{sp}= 5.92 x 10 [51]). In contrast, the bulk of the AgNPs was pure Ag (Fig. 5.2h). Similarly to the AgNPs, changes in composition of AgNWs were also observed after their uptake by microglia cells. Substantial dissolution of diffuse Ag was seen at the two ends of AgNWs (Fig. 5.2k). Particles had coalesced with each other to form a shell coating around some of the AgNWs and were also found sulfurized by S-species inside the cells over the 1 day post- exposure. The observed greater dissolution at the tips of NWs might due to the close-packed surface structure that has higher surface energy and surface defects density compared to the bulk or longitudinal axis of NWs. In this study, STEM-EDS confirmed AgNPs/AgNWs uptake by microglia cells, where the composition of Ag was transformed to Ag_2S. The binding of Ag to organic ligands forming complexes, such as silver sulphide and silver thiosulphate inside the cellular environment may support the observed TEM results[323].

5.3.3 Effect of AgNMs on Microglia Cell Viability and Reactivity

The cytotoxicity of AgNMs on microglia cells was assessed using the MTS (Fig. 5.3a) and LDH assays (Fig. 5.3b). Neither AgNP nor AgNWs showed a clear dose dependent toxicity at concentration 6.25 – 50 μg/ml after a 1 h pulse exposure and 24 h chase. NPs were observed to affect the cells much more by depositing around them and causing cells to aggregate (data not shown). Furthermore, a similar AgNPs/NWs treatment did not significantly affect the mitochondria membrane potential (see SI), echoing cell viability results. The cellular internalisation of AgNMs, followed by their dissolution and transformation to Ag_2S can be correlated with the insignificant changes in microglia cell viability.

The effect of AgNMs-treatment on microglia inflammation was assessed under resting and LPS-activated conditions. AgNM by themselves did not affect pro-inflammatory cytokine (TNFα and IL-6) release or mitochondrial membrane potential (Fig. S5). Furthermore, on their own, AgNM slightly decreased the basal production of ROS (Fig. S5). In contrast, simultaneous treatment of microglia with LPS (500 ng/mL) and AgNMs led to a reduction of inflammatory markers compared to LPS treatment alone. However, the anti-inflammatory effect varied between

AgNPs and AgNWs. Accordingly, AgNPs were able to reduce the LPS-induced production of ROS, TNFα and nitric oxide (Fig. 5.3d-f), while AgNW were only able to reduce TNFα production (Fig. 5.3e).

From these data, we chose to study the cellular uptake of AgNMs (NWs vs. NPs) at the highest non-cytotoxicity concentration, 50 μg/ml (*i.e.* in the absence of overt inflammation/toxicity) for further microscopic analysis. Thus, the cellular uptake of the NPs/NPs and their interaction with enzymes can be detected using TEM, SEM and confocal fluorescence microscopy studies.

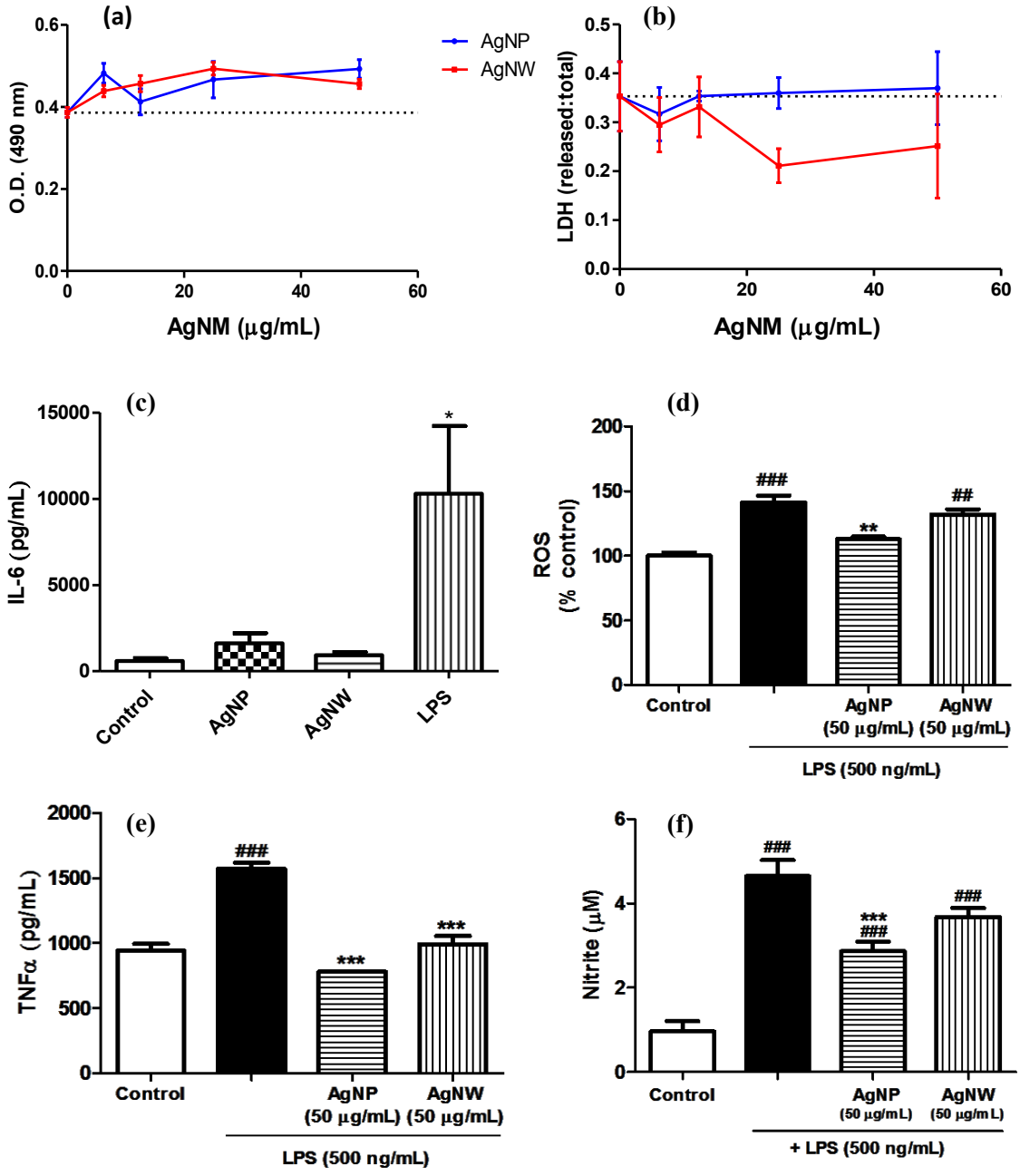

Fig. 5.3: Modulation of microglial cell viability and reactivity following AgNP/NW treatment. N9 microglia cells were treated with AgNPs/AgNWs with or without LPS (500 ng/mL) for a 1 h pulse followed by a 24 h chase. Cell viability was assessed through MTS assay (a) and LDH release assay. Microglial pro-inflammatory response was assessed through quantification of ROS production (d), TNFα release (e) and nitric oxide production (f). Data is presented as mean ± SEM of three independent experiments; ##, ### indicate $p < 0.01$, 0.005, respectively, *vs.* control; ** and *** indicate $p < 0.01$, 0.005, respectively, *vs.* LPS treatment as assessed by a one-way ANOVA with Tukey's post-hoc test.

5.3.4 TOF-SIMS Analysis of AgNMs Uptake in Microglial Cells

Time – of – flight secondary ion mass spectrometry (TOF-SIMS) is a surface analysis technique that is increasingly being used to investigate a wide range of biologically relevant samples, such as lipids[324, 325], cells and tissues[326, 327], DNA[328] and organisms[329]. In this technique, the sample surface is bombarded by a focused primary ion beam (1 – 40 keV), leading to the ejection of secondary ions which are accelerated by a potential of 2000 V into the flight tube. The ions which all now possess the same kinetic energy (KE) are allowed to drift through a field-free flight tube, of length L, until striking a detector. As the ions all have the same kinetic energy, the time taken for the ions to strike the detector determines their mass, and the mass to charge ratio (m/z) can be accurately determined.

TOF-SIMS spectra are calibrated internally using low mass fragment ions with a mass accuracy below 10 ppm. Mass spectra with high mass resolution and chemical maps with sub-micron spatial resolution are produced by rastering an ion beam across the sample surface. Unlike confocal microscopy, SIMS can be regarded as a 'discovery' technique as it is possible to obtain the full chemical composition of analytes without prior knowledge. Furthermore, it allows both organic and inorganic species to be investigated at the same time, with high spatial resolution capability up to 200 nm. By analysing the same microglia area using TOF-SIMS, FIB-SEM-EDS and fluorescence techniques, it was possible to map the spatial localisation of Ag and amino acids in the glial cells.

In this study, TOF-SIMS analysis was used to study the cellular uptake of AgNMs and their interaction with H_2S producing enzymes in microglia cells. SIMS is an ultrahigh vacuum (UHV) technique, therefore sample preparation is vital to maintain the native cellular chemical distribution and morphology of biological samples. Microglia cells were critical point dried (CPD) with liquid carbon dioxide after dehydrating with ethanol. To preserve sample morphology using CPD method, water was replaced by exchange fluids (*e.g.* ethanol or acetone) and in turn replacing the exchange fluid with liquid CO_2. Then, the liquid CO_2 converted to the gaseous phase at critical point (31 ºC; 74 bars) without changing density. Therefore, surface tension effects which may distort morphology and ultra-structure can be eliminated. The aim of this work was to understand which enzymes are responsible for sulphidising AgNMs in microglia cells. Few techniques are available to provide spatiality

resolved information about the chemistry of nanoparticles and their ion intensity in the cells.

5.3.4.1 Setting optimisation

The microglial uptake of AgNMs and their possible interaction with protein fragments were studied using ToF-SIMS analysis. In order to assess the capability of ToF-SIMS in detecting and imaging both organic and inorganic compounds in cells, samples prepared by critical point dry (CPD) method, were analysed. Fig. 5.4 illustrates the TOF-SIMS ion images of (a) total ion signals, (b) amino acid, $C_4H_8N^+$ signal and (c) Ag^+ signals originating from N9 microglia cells after the uptake of AgNWs (25 µg/ml, 24 h) using the 25 keV Bi_3^+ ion beam. Microglia cells were identified in the TOF-SIMS images and $C_4H_8N^+$ ion (m/z 70) was mapped to represent the amino acid. This signal was obtained mainly from those areas where the cells were visible. However, the Ag^+ signal could not be detected because the concentration of Ag was too low or because the samples surfaces were covered with contaminants.

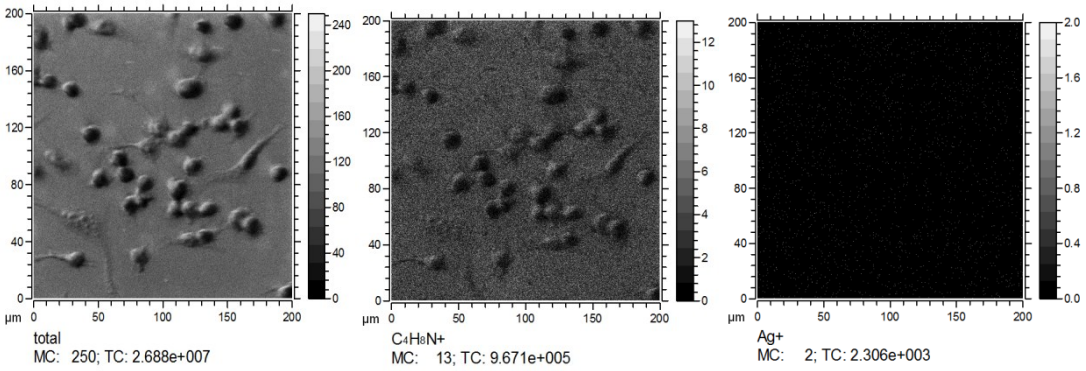

Fig. 5.4: TOF-SIMS images of (a) total, (b) amino acid and (c) Ag^+ ion signal from AgNWs in the N9 microglia cells samples.

In order to examine the distribution of AgNWs inside the microglia cells, the cells were ion beam milled using the Ga^+ ion beam and then secondary ions were analysed using the SIMS detector installed on the FIB instrument (FIB 200TEM). FIB-SIMS analysis confirmed the presence of Ag inside cells by ion beam milling 14 cells from the samples, to expose to the cross section of the cells as shown in Fig. 5.5. Using FIB-SIMS, a ratio which should correspond to the natural abundance for the Ag isotope, ^{107}Ag, i.e. 0.518 was plotted (Fig. 5.5d). The data were smoothed using a 5-

point moving average method and the result was within the error of 5 %. Using this method, Ag^{+} was successfully detected in the cells[330].

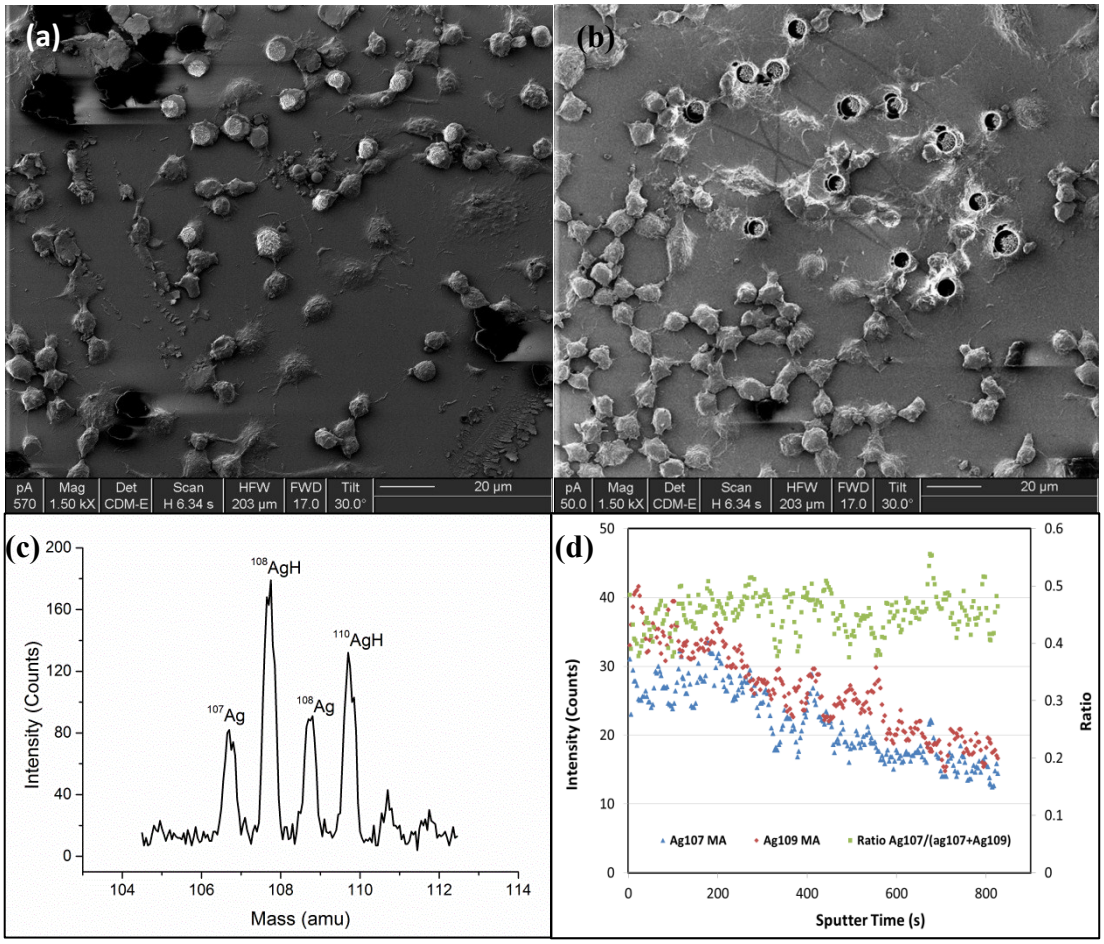

Fig. 5.5: Secondary electron mode (SEM) images of microglial cells exposed (25 µg/ml, 24 h) (a) before and (b) after sputtering with Ga^{+} ion beam; (c) Mass spectrum of Ag^{+} ions and (d) the depth profile data taken from the total signal from Ag^{+} after sputtering 14 cells using a FIB –SIMS instrument.

Using the FIB-SIMS imaging, Ag signals were confirmed by milling through the critically point dried cells. The factors contributing to difficulties in detecting Ag signals above the signal to noise ratio using TOF-SIMS were investigated. There are several hypotheses regarding the undetectable signal of Ag:

(i) Ag has a low satiation probability (*i.e.* the ionisation probability is very low).

(ii) In SIMS surface analysis, only 0.01 % of the sputtered material is ionised and the volume of Ag to be detected is too low. Thus, small volumes of material and low ionisation probabilities might be the factor of undetectable Ag signal.

(iii) Ag may be embedded inside the cells since SIMS is a surface analysis technique with a depth resolution < 1 nm. FIB cross-sectioning is required to enhance the Ag signal intensity.

5.3.4.2 C_{60} sputtering prior to SIMS analysis

The introduction of polyatomic ion beams, C_{60}^+ has been associated with relatively lower surface damage, improving detection limits, and enhanced efficiency of the analysis[331]. The increase in sputtered secondary ion species is because each atom within the C_{60} cluster carries a fraction of the total energy when an ion is accelerated and impacts the surface. For instance, in the case of C_{60}^+, there will be up to 60 separate collisions of approximately 250 eV, instead of a single particle with 15 keV bombarding the surface. This energy is deposited much closer to the surface and thus increases the sputter yield, leading to an increase in secondary ion yield[331]. Fig. 5.6 compares the yields of amino acids or protein fragments before and after the use of C_{60}^+ sputtering on the surface with repeated sputter cycles that erode the sample surface layer-by-layer. The localised signal of Cys was clearly seen in Fig. 5.6b after C_{60}^+ sputtering process. The signals of organic materials were significantly improved by the C_{60}^+ ion beam, eliminating poly (dimethylsiloxane) (PDMS) or impurities which are commonly found during the SIMS analysis.

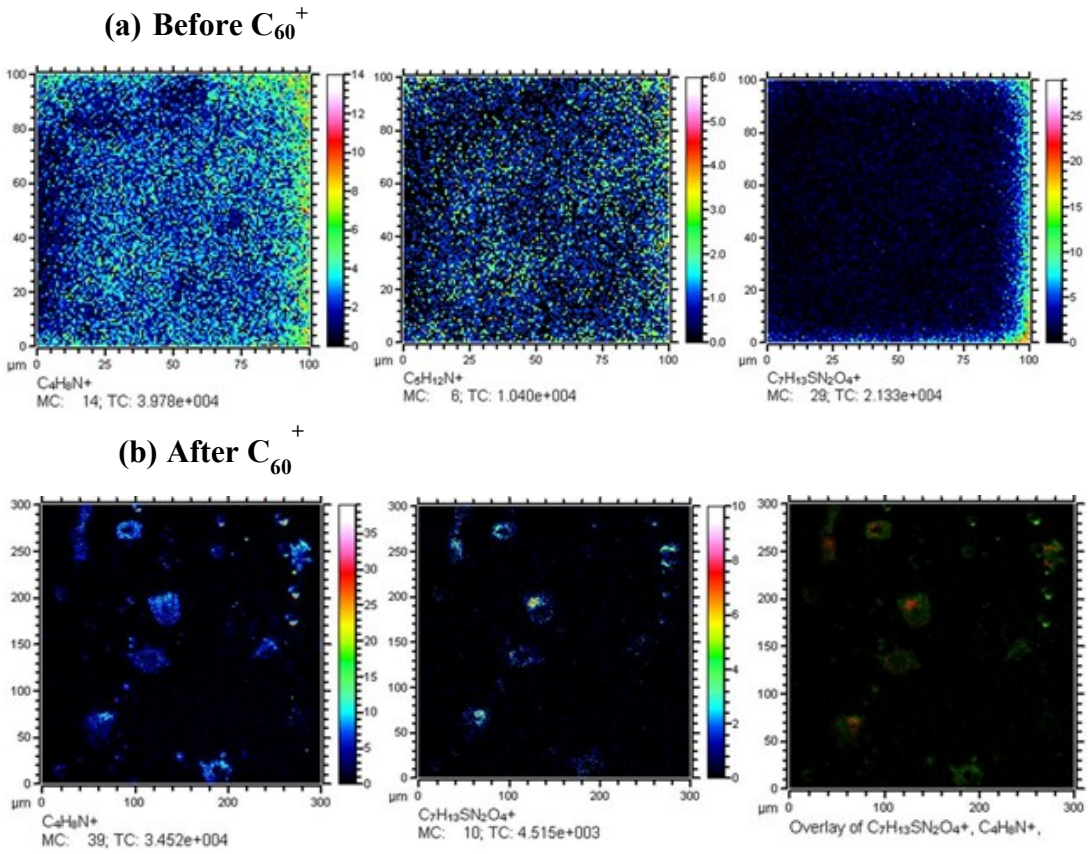

Fig. 5.6: TOF-SIMS images of control microglia cells (a) before and (b) after C_{60}^+ sputtering. $C_4H_8N^+$ and $C_5H_{12}N^+$ were used for identification of cells, originating from fragmentation of amino acids and the $C_7H_{13}SN_2O_4^+$ fragment was used for identification of cystathionine (Cys) (Resolution: 256 pixels x 256 pixels).

5.3.4.3 SEM-FIB-SIMS-EDS Analysis of the Cellular uptake of AgNWs

Cellular uptake of AgNMs by N9 cells was examined by TOF-SIMS and then correlated to the FIB-SEM morphology images. ToF-SIMS analysis was performed in both spectral and imaging modes. The ability of ToF-SIMS analysis to detect the PC, S, Ag and enzymes fragments signals is confirmed and their individual signals are shown in Fig. 5.8. Detection limit of Ag in cells is unknown and Ag is well-known for its low ionisation yield. Therefore, a high concentration of AgNWs (50 µg/ml) was chosen for the SIMS study

The amino acid ($C_4H_8N^+$) signal (blue) illustrated the morphology of the cells (Fig. 5.7). AgNWs with a diameter of 70 nm and lengths of 1 - 4 µm were identified as red signals in SIMS, agreeing well with AgNWs areas in SEM images. Fig. 5.7(b)

shows a SIMS image of 256 pixels x 256 pixels over a surface of 100 μm x 100 μm with a primary ion beam current of 0.5 pA; the lateral resolution of the SIMS image = 100 μm / 256 pixels = 390 nm per pixel. Therefore, AgNWs with lengths larger than a pixel size (~ 390 nm) can be detected by SIMS. However, the increasing ion beam doses causes the sample begin to charge when the images were zoomed in as shown in Fig. 5.7(c). Thereby, the Ag signals were not localised in the cell areas and interfere with the background signals. Furthermore, cellular uptake of individual AgNPs (diameter 50 nm) couldn't be analysed by the ToF-SIMS technique due to the lateral resolution limitation.

The presence of Ag and enzymes was clearly identified in overlay of the SIMS images of Ag^+ and enzyme (CBE, CSE and MPST) fragment signal ions (Fig. 5.8g & h). All these images were normalised to the total ion counts for the given pixel. For the interaction between Ag and enzymes, it is challenging to differentiate the secondary ions signals from the CSE and MPST fragments since they have similar ligands (see Table S2 and S3). Although SIMS can detect certain groups of molecules, such as lipids[325] at the nanometer scale and at attomolar concentration [332], it is less sensitive to large molecules with high mass: charge ratio (m/z). Moreover, the matrix effect and varying ionisation probabilities of different molecules can be complicated, leading to difficulties in absolute quantifications using current TOF-SIMS instrumentation[333, 334].

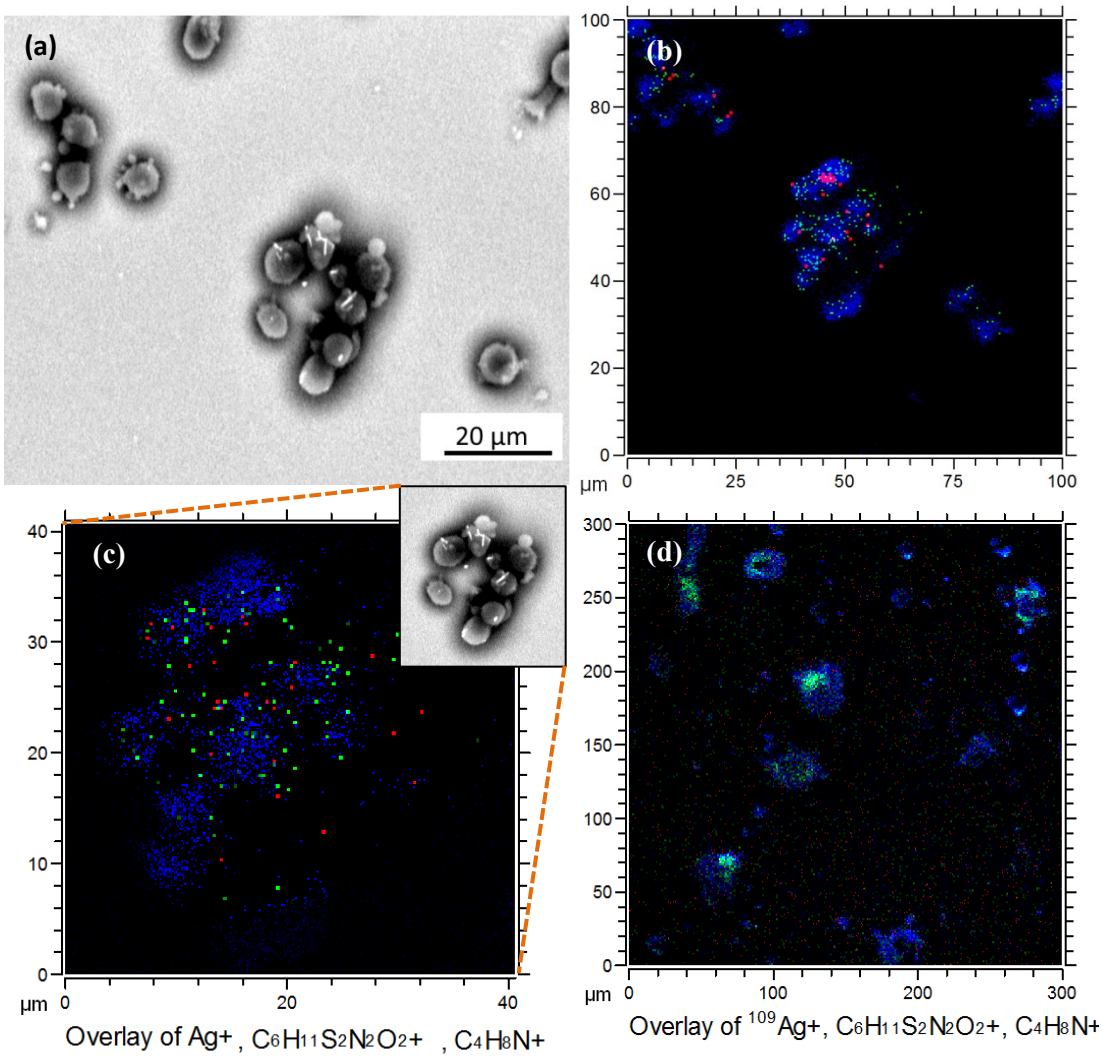

Fig. 5.7: (a) SEM and (b) SIMS images of silver nanowires (D=70 nm, L= 1 - 4 um, C=50µg/ml) uptake in microglial cells, (c) magnified areas (40 um x 40 um^2) of the boxed area and (d) control samples - microglia cells. Amino acid fragment ($C_4H_8N^+$): Blue; Cys fragment ($C_6H_{13}N_2O_4S^+$): Green; Ag signal: Red (256 pixels x 256 pixels).

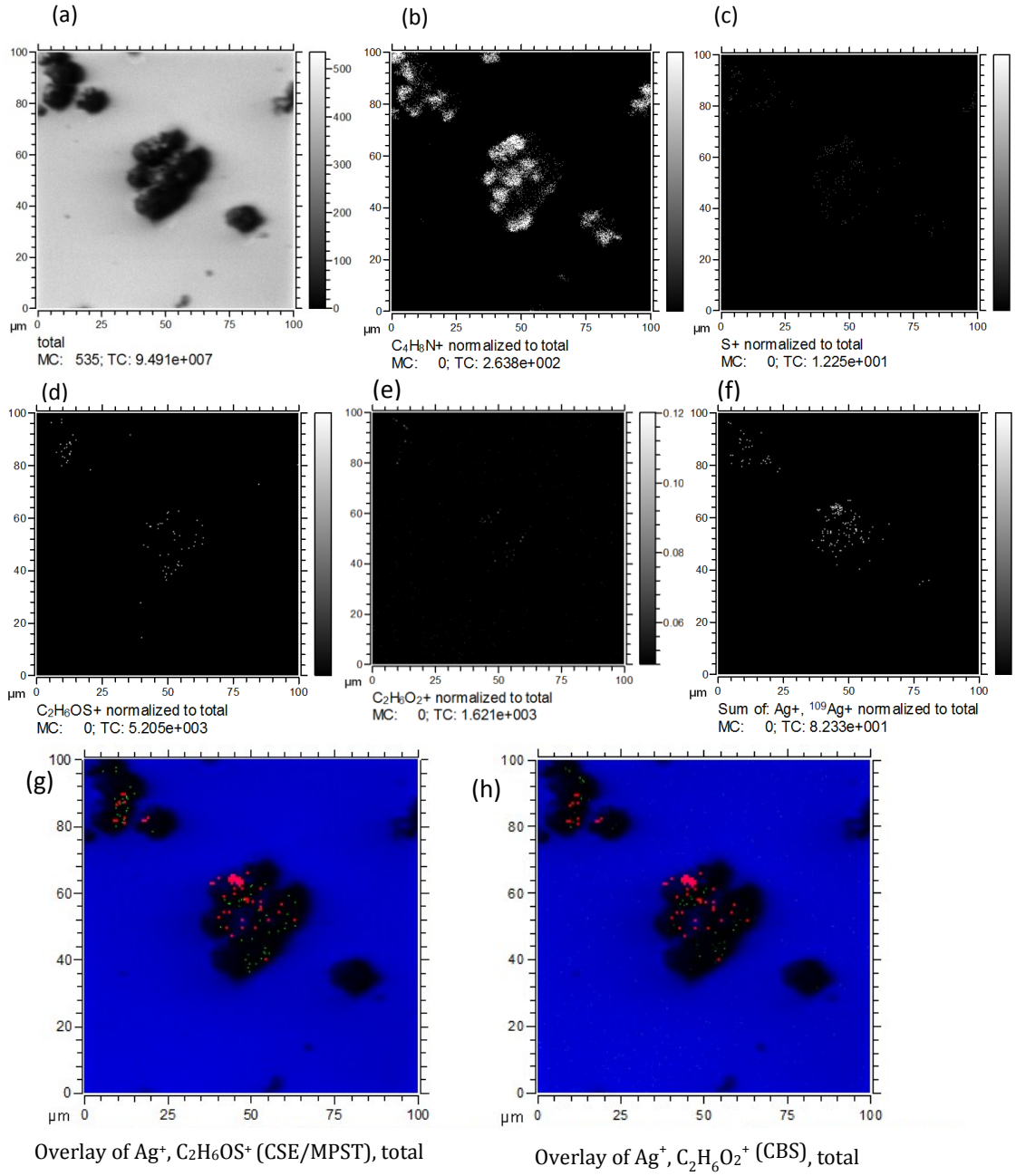

Fig. 5.8: TOF-SIMS imaging (positive ion mode) of (a) microglia cells (24 h), pooled signals of (b) amino acid fragment ions, (c) S^+ ions, (d) CSE or MPST enzymes fragment ions, (e) CBS enzyme fragment ions and (f) sum of Ag^+ ions; Overlay images of Ag ions (red) and (g) CSE or MPST enzymes fragment, $C_2H_6OS^+$ and (h) CBS enzyme fragment, $C_2H_6O_2^+$ (Green). Colour scale bars, with amplitude as number of counts are indicated to the right of each ion image. The amplitude of the colour scale corresponding to the maximum number of count (mc) and the total number of counts (tc) recorded for the specified m/z (it is the sum of counts in all pixels). Field of view: 100 µm x 100 µm.

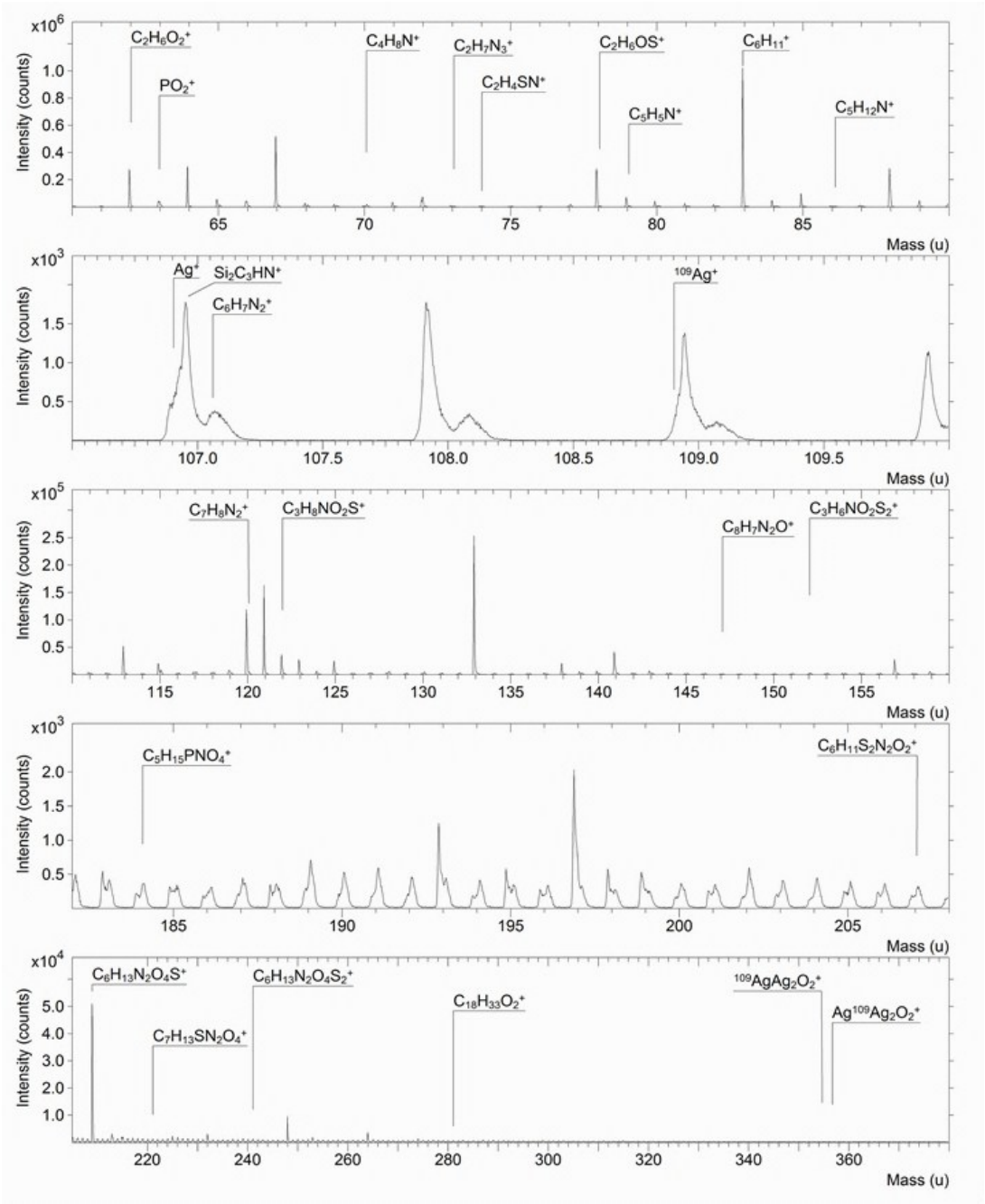

Fig. 5.9: Secondary-ion spectrum (positive polarity) obtained from control microglial cells after sputtering with C_{60}^{+}.

Fig. 5.9 and 5.10 show typical mass spectra recorded after C_{60}^{+} sputtering and the mass spectrum verifies that the C_{60}^{+} sputtering does not destroy all molecular information on the sample surface. All peak assignments were confirmed by comparison with reference spectra recorded with the pure substance. Ag^{+} ions peaks were clearly seen in the ion spectrum of AgNWs in microglia cells samples (Fig. 5.10) but none of the Ag peaks could be observed in controlled samples (Fig. 5.9). In

order to compare the Ag and S signals in microglia cells between these two samples, the ion intensities were normalised to the total ion intensity as shown in Table 5.2.

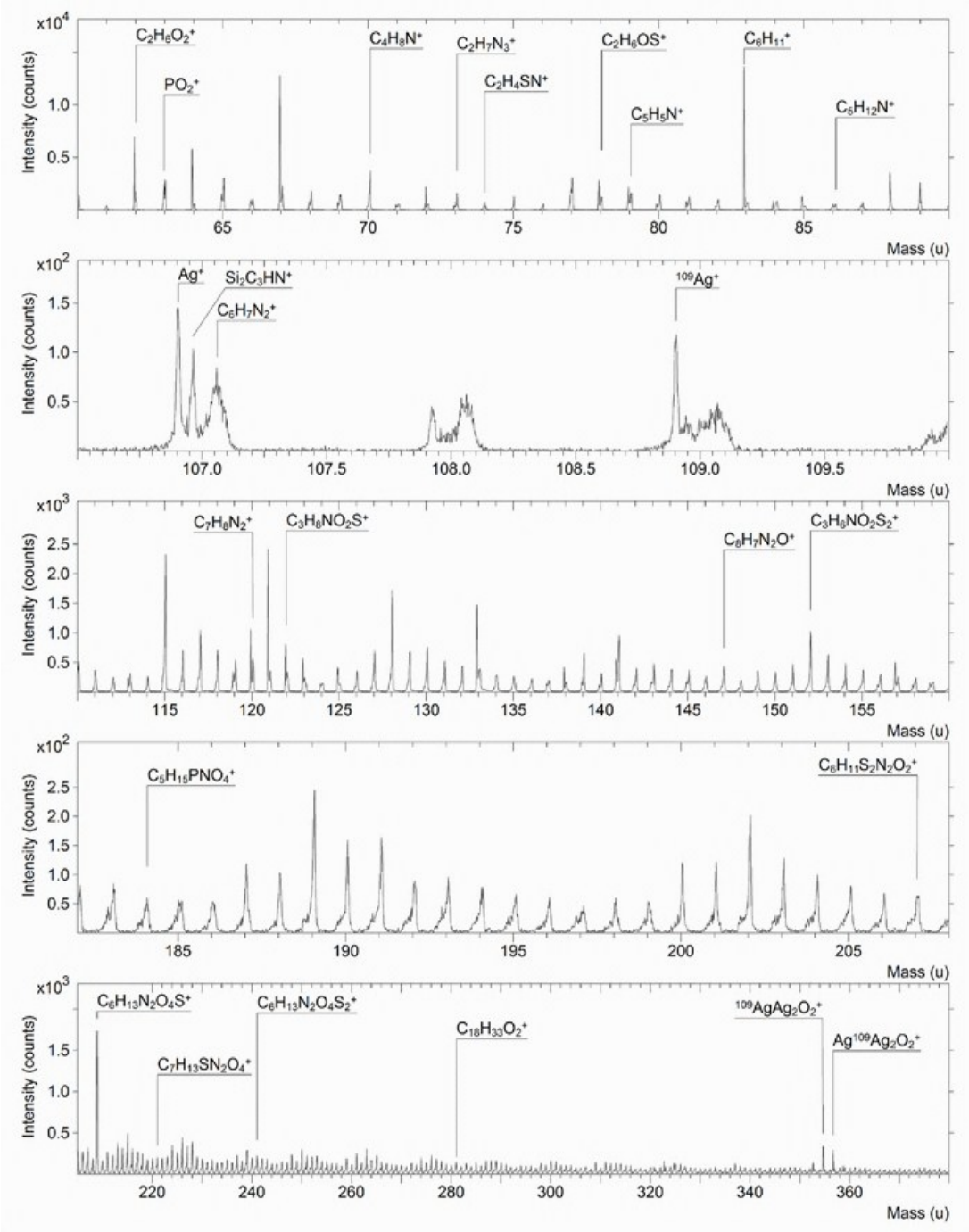

Fig. 5.10: Secondary-ion spectrum (positive polarity) recorded from AgNWs in microglia cells after sputtering with $C_{60}^{+\cdot}$.

Table 5.2: Comparison of Ag, ^{109}Ag and S ion intensity between control cells and microglia cells exposed to AgNWs (1 h pulsed + 24 h exposure) after normalising to total ion intensity.

Positive secondary ions (Normalised with total ion intensity)	Control microglia cells (Counts)	AgNWs in microglia cells (Counts)
Ag^+	5.47E-5	5.21E-4
$^{109}Ag^+$	3.69E-5	2.94E-4
S^+	3.59E-6	6.59E-5

The intensity counts of Ag^+ and $^{109}Ag^+$ in control cells were significantly lower compared to AgNWs in microglia cells. The Ag counts in control cell samples might be due to the mass interference. In contrast, the intensity count of S^+ ions was found to be higher when the microglia cells were treated with AgNWs. It has previously been demonstrated that metallisation of the organic samples will help to improve the secondary ion yields of intact molecular ions in SIMS, which is named as metal assisted (MetA) SIMS[335, 336]. Adriaensen, L. *et al.*[337] found a considerable increase in secondary ion yield by metal deposition in TOF-SIMS measurements. Several hypotheses have been proposed to verify the increase of S species with the cellular uptake of AgNWs in the microglia:

- Mobile analytes may migrate onto AgNWs[338].
- Molecular dynamics simulations have shown that metal increases ionisation or desorption by cooperative elevation of analyte molecules and metal atoms[339].
- Ag is a noble metal and is an electron donor, acting as a good cationizing agent to improve ion yields[340, 341].

In this work, the sample surface was bombarded with a Bi_3^+ primary ion beam rather than a conventional mono-atomic ion source (*e.g.* Cs^+ or Ga^+) to enhance the molecular signal. Moreover, polyatomic ion beams generate relatively low surface or sub-surface damage compared to mono-atomic ion beams, improving the efficiency of the SIMS analysis and its detection limits[342, 343]. Whereas, Cs^+ or Ga^+ have been shown not to be an ideal ion to sputter tissues or biological samples due to the amount of surface damage and fragmentation of large molecular ions.

FIB cross-sectioning is required to expose AgNMs which were embedded inside the cells. The FIB is equipped with a FEG - SEM detector, therefore slice and view cross-sectioning images were performed before and after FIB cross-sectioning. As illustrated in Fig. 5.11, the FIB cross –sectioned area was marked and an SEM image taken from the same cell. Approximately 20 cells were randomly selected for FIB prior to the SEM-EDS analysis. The cell morphology was captured using a SEM detector installed in FIB 200TEM to ensure that the top of the cells had been removed to reveal the AgNWs embedded inside the cells for further analysis. Although a thin layer of carbon coating was deposited before FIB milling, carbon coating on the topside of cells were removed during the milling process, thus the surface would be free of carbon and not affect the SIMS surface analysis.

Five cells were selected for FIB cross-sectioning (Fig. 5.12) and SIMS ion image overlay of Ag (red), CSE/MPST enzymes (green) and the amino acid fragment (blue) signals were found in the cells. The sum of the Ag ion signals from SIMS analysis (see Fig. 5.12d) was correlated with the SEM-EBS image (Fig. 5.12e). The protein and enzymes signals couldn't be detected from the cells, possibly because they were destroyed by the high energy focused Ga^+ ion beam during FIB. This was further confirmed by taking measurements from several other cells which had been FIB-cross-sectioned as shown in Fig. 5.12. Apart from Ag signal (red), other localised signals of PC (blue) and enzymes (green) couldn't be found in the cells. However, these protein signals were detected from cells without the FIB cross-sectioning process. Again, these results demonstrated that FIB is not suitable for analysing protein or PC signals before the SIMS analysis, but it may be used to characterise inorganic samples.

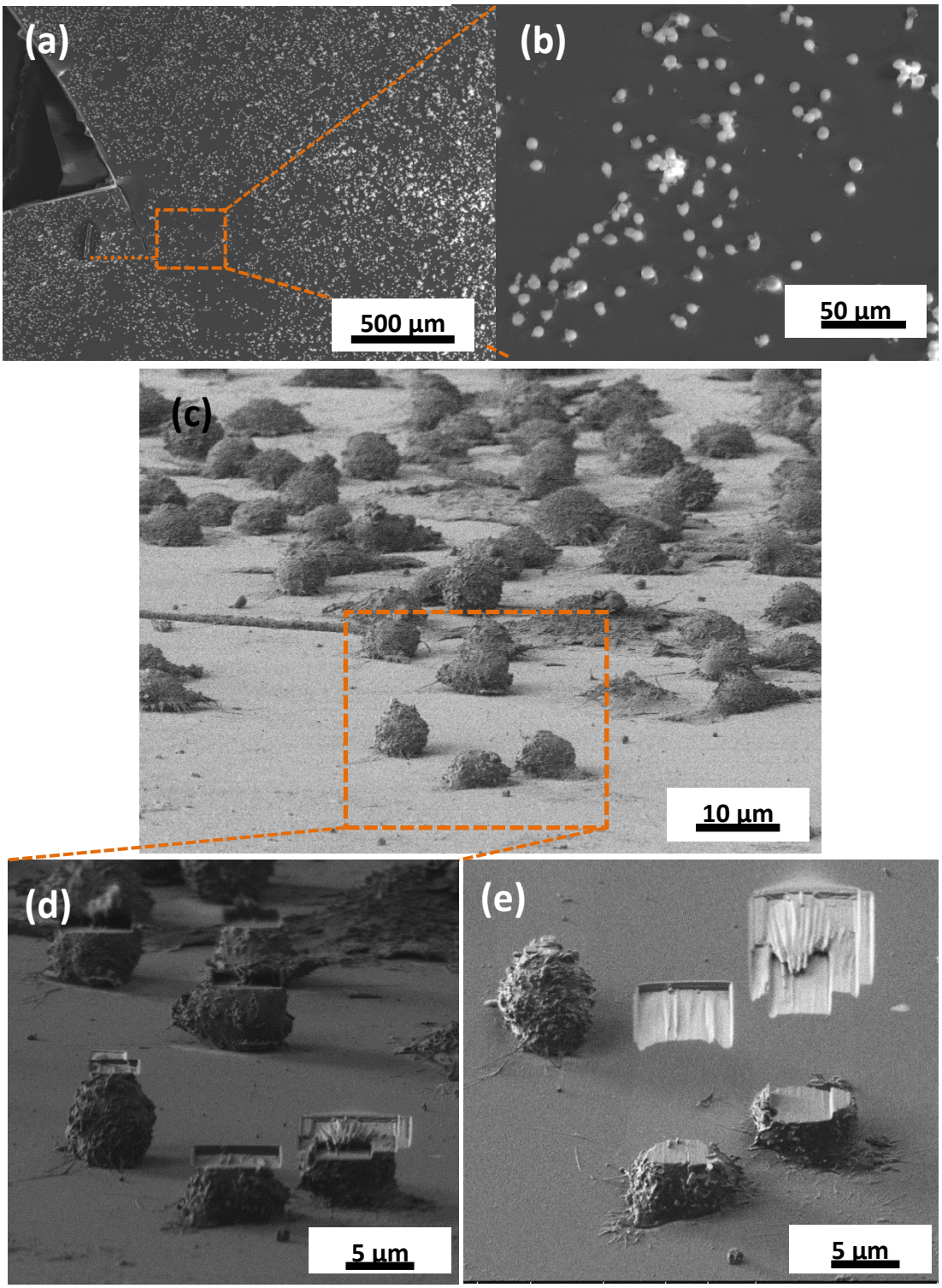

Fig. 5.11: SEM images of microglial cells exposed to AgNWs at (a) lower and (b) higher magnification, (c) before FIB and (d) after FIB (side view) and (e) after FIB (top view).

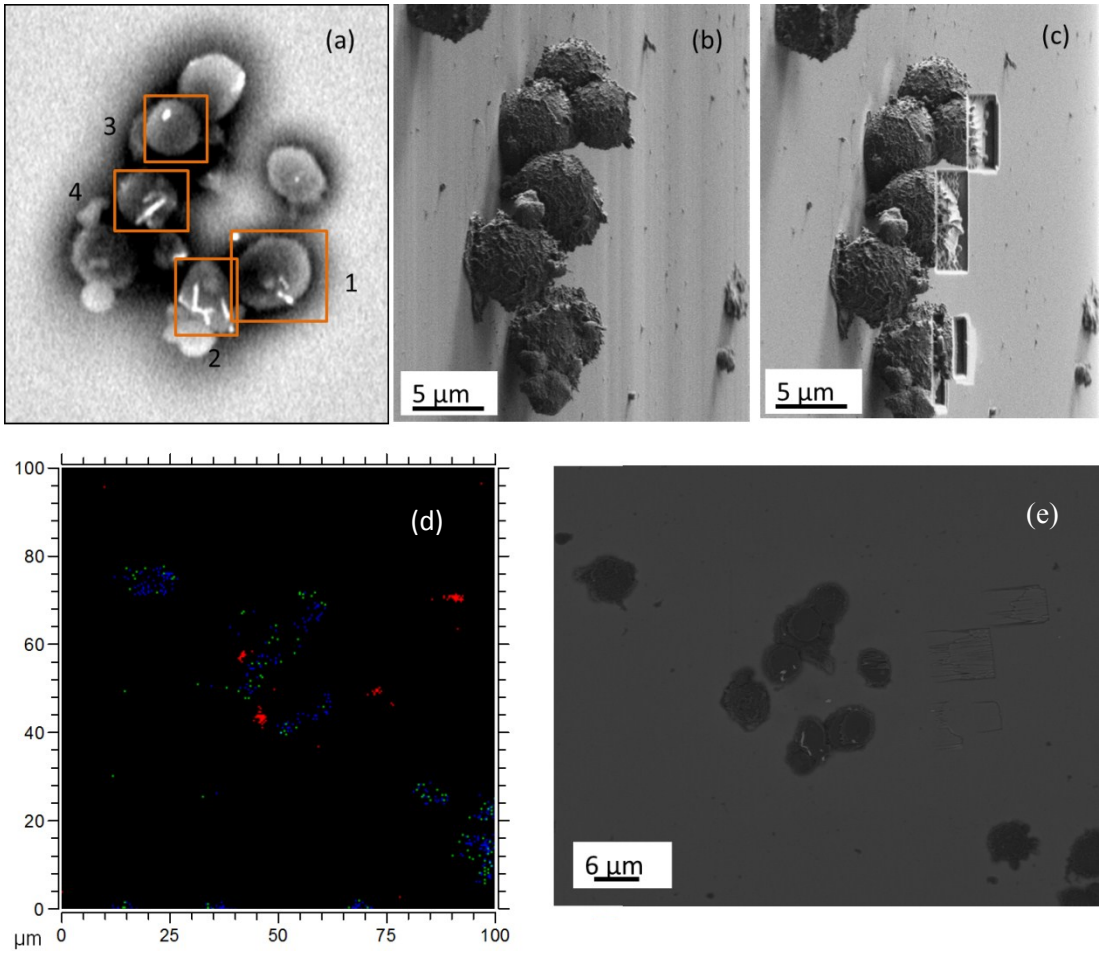

Fig. 5.12: (a) Secondary ion image acquired in high current branched mode, showing AgNWs on the surface of microglia cells; SEM (SE mode) images of microglia (b) before and (c) after the FIB cross-sectioning process, (d) overlay image showing the signal intensities of Ag^+ (red), a CSE/MPST enzymes fragment (green) and amino acid fragment (blue) and (e) a SEM image taken from the same region as the SIMS image.

Fig. 5.13 illustrated the SEM images and EDS spectra of AgNPs and AgNWs in microglia cells after 1 h pulse chase + 24 h exposure. The interaction of AgNMs with S species inside the cellular environment was also confirmed by FIB-SEM-EDS analysis. As shown in Fig. 5.11, the FIB cross - sectioning area was marked and their associated SEM image was captured to identify the inspection area. Approximately 20 cells were randomly selected for the FIB cross-sectioning process prior to the SEM-EDS analysis and the side view of the cell is shown in Fig. 5.13 (d). After FIB operation, cellular uptake of AgNWs was analysed by SEM-EBS imaging and their

chemical composition were further examined by EDS. As shown in EDS analysis, a higher intensity counts of S was found within the Ag areas as compared to the background signals inside cells. This might be due to the binding of Ag to S species forming complexes, such as silver sulphide and silver thiosulphate inside the cellular environment[323], supporting the observed TEM results. In this study, the intracellular internalisation of AgNMs, followed with their dissolution and transformation to Ag_2S can be correlated with the cell viability and oxidative stress results.

Even though correlation between Ag and protein inside microglia cells couldn't be analysed using the FIB-SIMS analysis, the chemical composition of Ag and S were determined using the SEM-EDS technique as shown in Fig. 5.13. The EDS data confirmed the interaction between Ag and S species in the cells, which is highly insoluble and limits their short-term toxicology effects[21]. The comparison between these analysing techniques is summarised in Table 5.3. It can be concluded that the combination of ToF-SIMS/confocal/ FIB-SEM-EDX analysis is an extremely powerful approach for analysing the uptake of NPs and their transformation in biological samples.

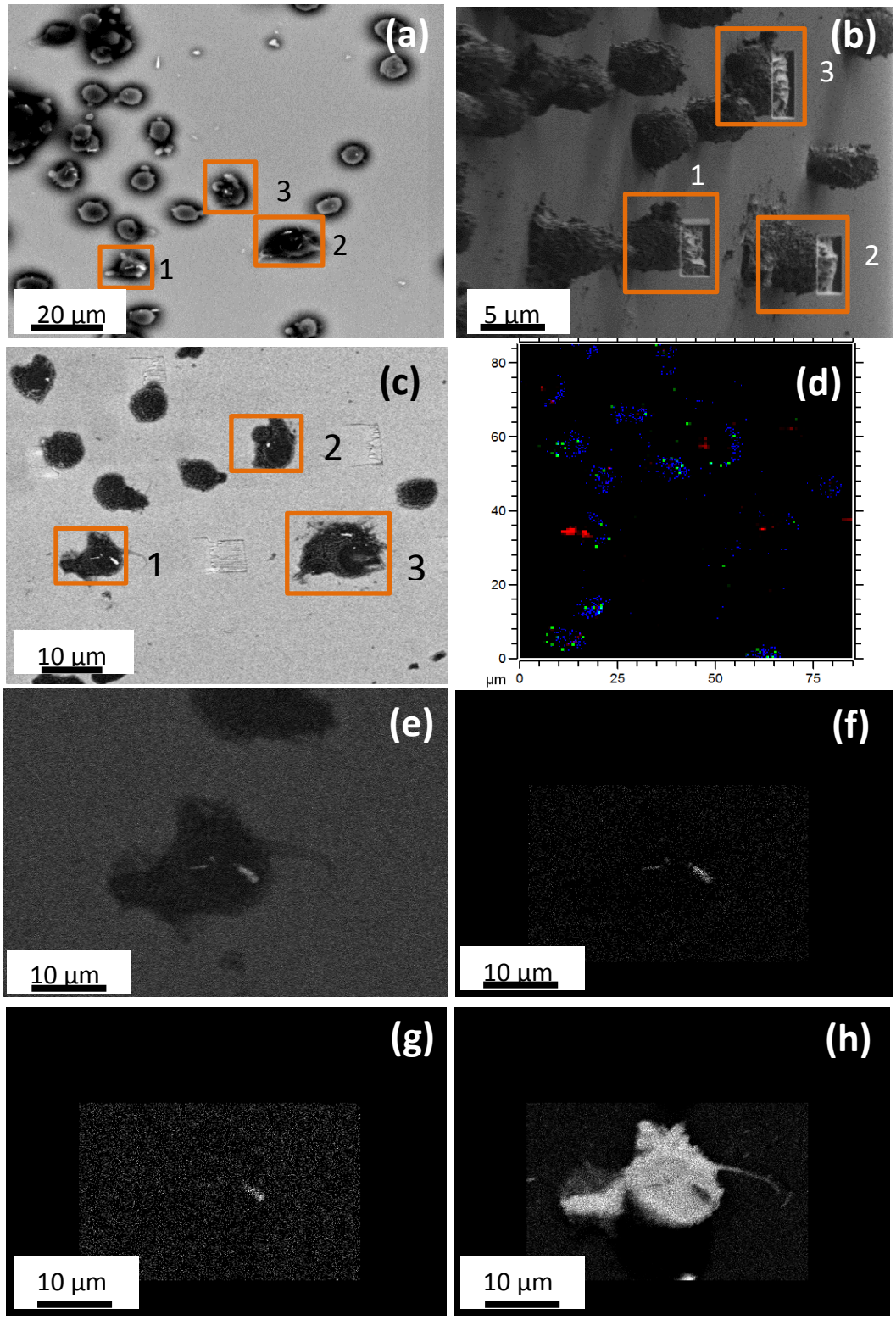

Fig. 5.13: SEM images of AgNPs in microglial cells (a) before and (b) after being FIB crossed section; (c) cellular uptake of AgNWs was imaged using SEM - BSE mode; (d) overlay SIMS image show signal intensities of Ag^{+} (red), CSE/MPST enzymes fragment (green) and amino acid (blue); (e) SEM- BSE image of AgNWs (D= 70 nm; L= 1-4 µm) in microglial cells and the EDS mapping of (f) Ag La1, (g) S Ka1 and (h) C Ka1.

Table 5.3: Comparison between ToF-SIMS, confocal and TEM microscopy techniques.

Techniques	ToF- SIMS	Confocal	TEM
Sample preparation	Critical point dry (no washing steps)	Bind with primary antibodies then fluorescent-labelled with secondary antibodies	Glutaraldehyde fixation, dehydrate with ethanol, acetone and then infiltrate with resin.
Cross-sectioning	FIB cross section to expose Ag in cells with Ga ion beam	Adjust the depth with focus	Microtome to 90 nm thickness so they are electron transparent
Analytes identification	The full chemical composition of analytes can be obtained without prior knowledge. The ion fragments can be identified by mass spectrum ranged from 1 to 10000 m/z.	Need to specify the examined analytes for choosing the primary antibodies	NPs can be identified at specific location in cells (nucleus, cytoplasm, endosome/lysosome) by EDS
Enzyme + Ag analysis	The specific type of enzymes with similar ligands is hard to differentiate; SIMS less sensitive to large protein molecules or fragments	Good correlation of Ag + enzyme signals	Only Ag can be identified; negative staining is required to examine the protein structures of biological complexes.
Depth (D) / Spatial (S) Resolution	D < 1nm S > 200 nm	D ≤ 200 µm S: 300 – 400 nm	D ~ 90 nm S : atomic scale

5.3.5 Regulation of Enzyme Activity through Interactions with AgNMs

5.3.5.1 Confocal Analysis

The expression of enzymes and their colocalisation with AgNPs/NWs were observed using confocal microscopy. Since AgNMs have the capacity to scatter light, their uptake in cells can be monitored directly using confocal microscopy. Fig. 5.14 and 5.15 illustrate the upregulation of H_2S producing enzymes in microglia following 4 and 24 h treatment with AgNMs, respectively. Results show that the baseline signal of CSE was stronger than that of CBS and MPST within the non-treated control cells following 4 and 24 h exposures, suggesting the CSE enzyme could be a major H_2S producer in microglia cells. At 4 h, although the signal of the CSE was not affected by the presence of AgNMs, its signal did increase following 24 h exposure (Fig. 5.15). While CBS signal was more diffuse at 4 h, with the small amount of the AgNP interaction and this appeared to be confined with negligible interaction after 24 h exposure. For MPST, the enzyme was weakly detected in both NPs/NWs-treated and non-treated cells.

As shown in Fig. 5.16k, quantitative confocal analysis revealed that CSE level was upregulated by the AgNPs, with a threefold increase observed compared to the control non-treated cells. On the other hand, AgNWs did not cause a significant upregulation of CSE protein level in microglial cells. In the case of CBS (Fig. 5.16j), neither AgNPs nor AgNWs significantly affected the enzyme levels. Unlike CBS and CSE, the MPST signal was hardly seen in the microglial cells. To confirm the qualitative results obtained with the confocal analysis, the upregulation of enzyme expression was quantified through Western blot immunostaining.

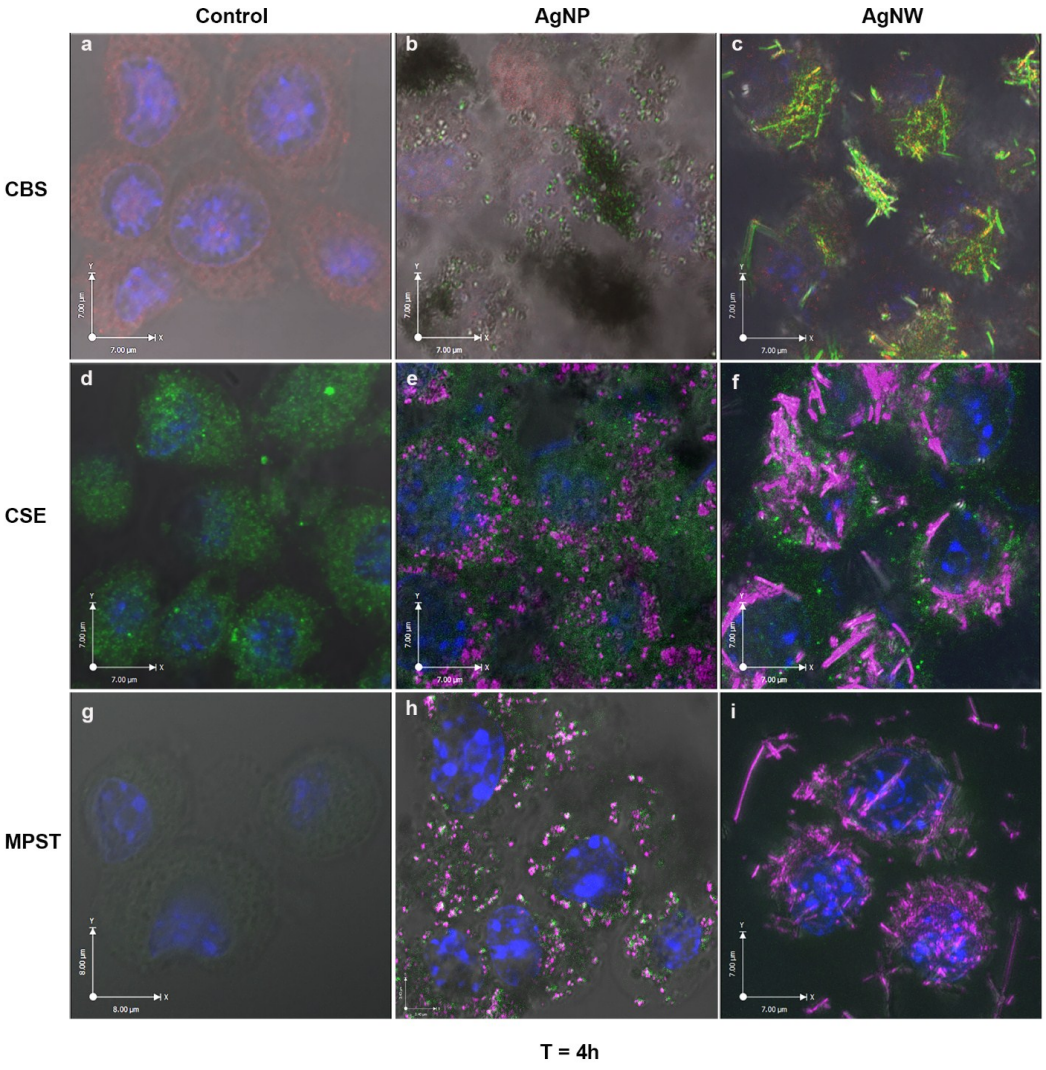

Fig. 5.14: The cellular uptake and distribution of AgNPs and AgNWs (50 µg/ml) together with CBS, CSE and MPST enzymes in microglia cells after 4 h exposure: confocal analysis on CBS enzymes (red) in (a) controlled microglia cells and (b-c) microglia uptake of AgNMs (blue – DAPI-stained nuclei, red – CBS enzymes, green - AgNPs/ AgNWs); CSE enzymes (green) in (d) controlled cells and (e-f) microglia uptake of AgNMs. ; MPST enzymes (green) in (g) controlled cells and (h-i) microglia uptake of AgNMs. (blue – DAPI-stained nuclei, green - florescent labelled enzymes and magenta – AgNPs/AgNWs).

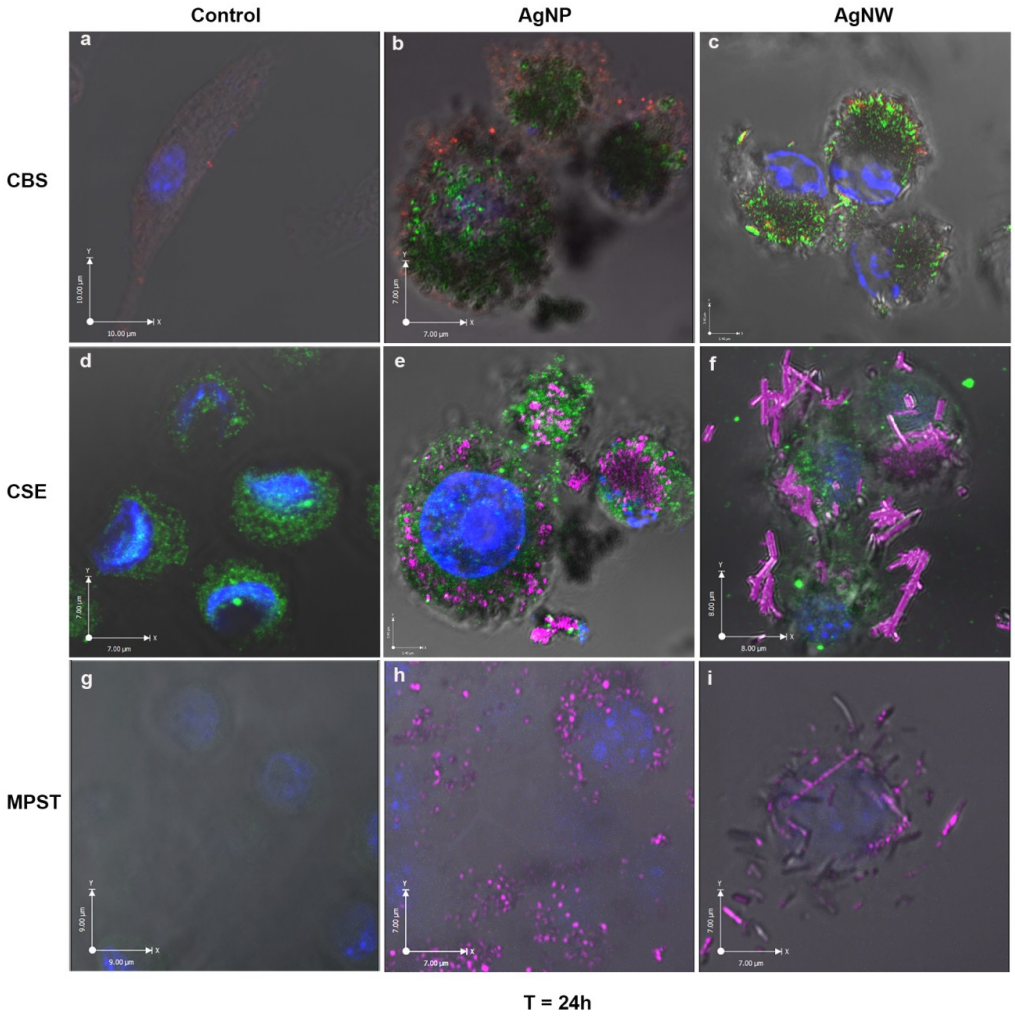

Fig. 5.15: The cellular uptake and distribution of AgNPs and AgNWs (50 µg/ml) together with CBS, CSE and MPST enzymes in microglia cells after 24 h exposure: confocal analysis on CBS enzymes (red) in (a) controlled microglia cells and (b-c) microglia uptake of AgNMs (blue – DAPI-stained nuclei, red – CBS enzymes, green - AgNPs/ AgNWs); CSE enzymes (green) in (d) controlled cells and (e-f) microglia uptake of AgNMs; MPST enzymes (green) in (g) controlled cells and (h-i) microglia uptake of AgNMs. (blue – DAPI-stained nuclei, green - florescent labelled enzymes and magenta – AgNPs/AgNWs).

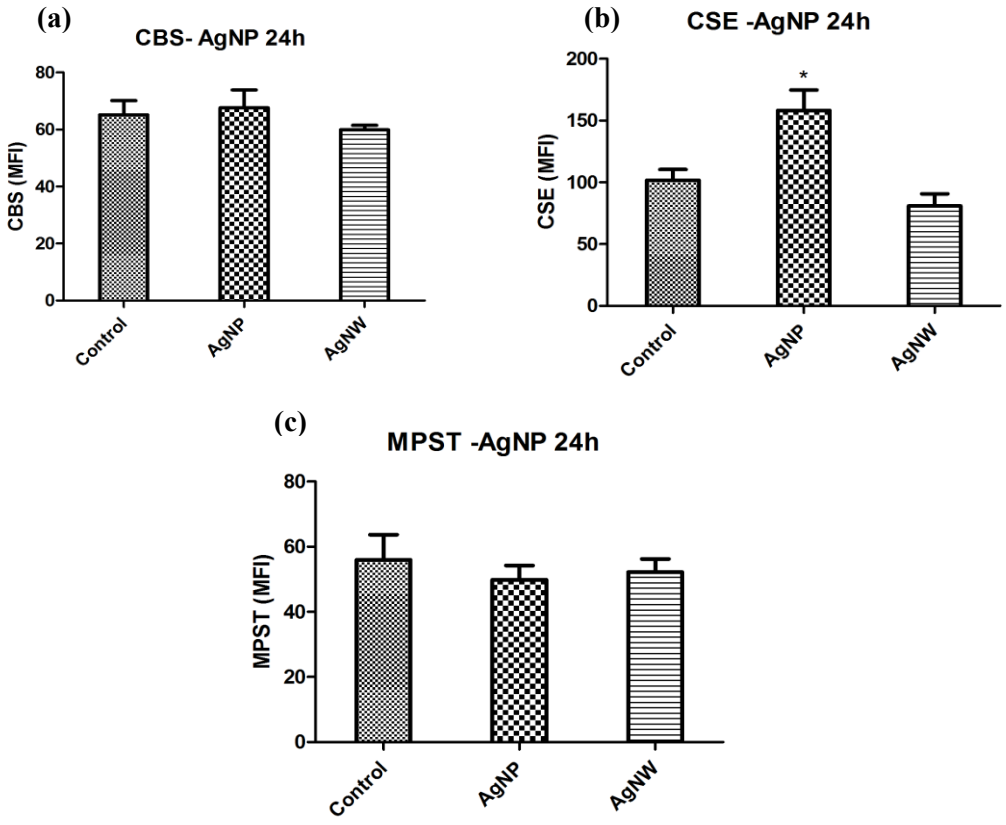

Fig. 5.16: The mean fluorescent intensity of the CBS (a), CSE (b) and MPST (c) enzymes measured in control non-treated N9 cells and the N9 cells exposed to AgNPs and AgNWs for 24 h. A significant increase of the mean fluorescent intensity of the CSE enzyme was detected within cell exposed to AgNPs after a 1 h pulse exposure and 24 h chase (n = 3 with 120 total observed cells, *$p < 0.05$).

5.3.5.2 Western Blot immunodetection

As shown in Fig. 5.17, the quantitative Western blot data result was consistent with the confocal analysis data, showing the expression of CBS does not change with either LPS or AgNM treatment but CSE is increased with LPS and AgNPs, demonstrating the reliability of confocal analysis data. Also, the increasing of the CSE enzyme protein level by AgNPs was correlated with the decreased in LPS-induced microglia activity after exposing to 50 µg/ml AgNPs (1 h pulse followed with 24 h chase) (Fig. 5.2)

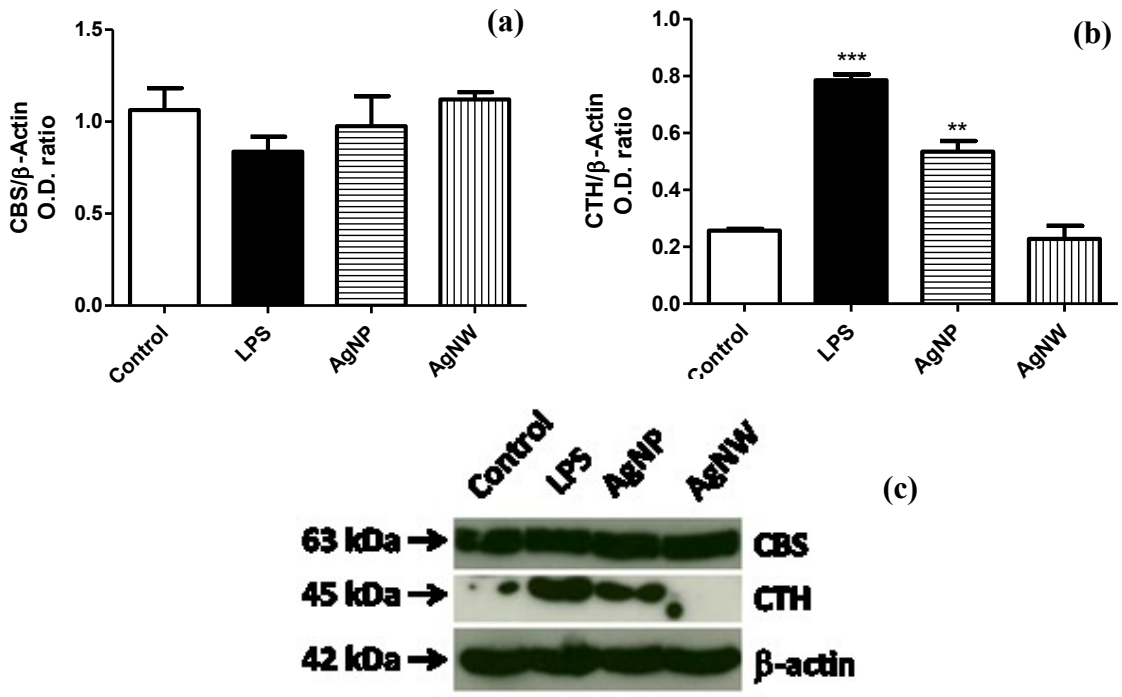

Fig. 5.17: Effect of AgNMs on the expression of (a) CBS and (b) CSE compared to beta-actin (loading control) by Western blot analysis, n=3; (c) representative Western blots showing AgNPs upregulated the CSE protein levels in microglia cells (1 h pulse followed with 24 h chase).

5.4 Discussion

Recently, researchers have reported that exposure to severe air pollutants with high levels of NPs is associated with human brain inflammation and Aβ42 accumulation, causing neuronal dysfunction[20, 344] and potentially Parkinson's disease[345]. For example, TiO_2 NPs can directly enter the brain of mice through the olfactory bulb following intranasal administration, causing increased lipid peroxidation, inflammation and pathological changes to the tissues[185]. An *et al.* [346] found that CuO-NPs impaired hippocampal long-term potentiation, as well as causing decreased memory and learning abilities of Wistar rats when they were treated with CuO-NPs *via* intraperitoneal injection for 2 weeks. Furthermore, AgNPs have been shown to induce cell death through apoptosis when exposed to cerebellum granule cells with contaminant oxidative stress[347]. Since apoptosis and changes in dopamine concentrations play a role in neurodegenerative diseases, there is a strong evidence to suggest that AgNPs may cause neurodegeneration[348].

In our study, the cellular uptake of AgNMs inside microglia cells and their chemical transformation into Ag_2S was investigated using TEM imaging analysis.

The HAADF STEM-EDX analysis demonstrates that AgNMs can be transformed into Ag_2S by S-containing salts and protein components, which may affect their neurotoxicity and also upregulate the major H_2S producing enzyme (CSE) levels to achieve the equilibrium in the system. From TEM, the localisation of AgNMs as large clusters was mainly found in cellular vesicles suggesting that endocytic pathways are involved in the internalisation of AgNMs into microglia cells[349]. Once AgNMs enter cells, they are not thermodynamically stable in the intracellular environment and tend to dissolve into Ag^+ ions that interact with natural organic macromolecules or inorganic ligands. Ag acts differently from other metal ions (*e.g.* Zn and Fe) and is likely to bind with complex protein thiol groups or ligands in the medium such as Cl^-, PO_4^{3-}, S^{2-} and SO_4^{2-}, forming insoluble silver compounds, *e.g.* silver sulphide, silver oxide and silver chloride. Since the solubility of Ag_2S (pKsp = 50.83) is extremely low, this highly stable Ag compound strongly affects the surface properties of AgNMs and inhibits further oxidation of Ag[21].

The sulfidation of AgNMs is a complex process and may occur *via* two chemical pathways, depending on the sulfide concentration in the cellular environment. According to Liu *et al.*, the Ag sulfidation is dominated by the indirect reaction if sulfide concentration < 0.025 μg/ml. At higher sulfide concentration (> 0.025 μg/ml), the mechanism switches to the direct sulfidation reaction where the reaction rate increases with the increasing of sulfide concentration. The below reactions show the competing of these two chemical and transport pathways of AgNMs sulfidation before transforming into the thermodynamically stable sulfide phases:

(1) Direct route (particle-fluid heterogeneous reaction – equation (5.1a - c)) - AgNMs direct oxysulfidation reaction rate increases with the increasing of sulfide concentration.

$$4Ag + O_2 + 2H_2S \longrightarrow 2Ag_2S + H_2O \quad (5.1a)$$

$$4Ag + O_2 + 2HS^- \longrightarrow 2Ag_2S + 2OH^- \quad (5.1b)$$

$$4Ag + O_2 + 4H^+ + 2S_2^- \longrightarrow 2Ag_2S + 2H_2O \quad (5.1c)$$

(2) Indirect route (oxidative dissolution (equation 5.2a) and precipitation (equation 5.2b - d)) - dissolution of AgNMs is initiated by oxygen chemisorption accompanied by electron transfer[60]. The cooperative effect of both dissolved oxygen and protons by thermodynamic analysis can be representing in following heterogeneous oxidation reaction stoichiometry:

$$2Ag + ½\ O + 2H^+ \leftrightarrow 2Ag^+ + H_2O \quad (5.2a)$$

While Ag ions are released from AgNPs or AgNWs, they diffuse into cellular environment rapidly and form sulfide precipitation:

$$2Ag^+ + H_2S \longrightarrow Ag_2S + 2H^+ \quad (5.2b)$$

$$2Ag^+ + HS^- \longrightarrow Ag_2S + H^+ \quad (5.2c)$$

$$2Ag^+ + S^{2-} \longrightarrow Ag_2S \quad (5.2d)$$

So far, it has been established that Ag ions (Ag^+) are a key determinant of toxicity[41], thus sequestering Ag as nontoxic Ag-protein complexes or Ag_2S species could act as a detoxification mechanism. As shown in STEM-EDS analysis, Ag_2S-NPs could be produced by either the direct route (particle-fluid reaction) or by the indirect route (oxidative dissolution followed by sulphide precipitation). At the early stage, Ag ions dissolve from the AgNMs, and then diffuse into the cellular environment before precipitating as Ag_2S particles. Therefore, initial stage of AgNMs transformation is mainly dominated by the indirect pathway.

Since dissolution of Ag ions increases with time, Ag^+ ions will either grow on the existing Ag_2S nuclei to grow larger-sized Ag_2S particles or precipitate as new Ag_2S NPs. In addition, sulphide species (*e.g.* H_2S, HS^- and S_2^-) may attack the outer layer of AgNMs surface *via* the direct particle-fluid reaction, leading to the formation of small Ag_2S particle surrounding NWs surface as shown in Fig. 5.2k. This can explain why no significant effect of either AgNPs or AgNWs was seen on microglia cell viability even up to the concentration of 50 μg/mL. Our studies also demonstrated no significant reduction in mitochondrial function nor a rise in ROS concentration exerted by the AgNMs on microglia cells. Recent studies showed that AgNPs may induce toxicity in neurons and cause neurotoxicity[350]. Although AgNPs can traverse into the brain and induce toxicity in neurons, our studies showed that neither AgNPs nor AgNWs activate the microglia. Nevertheless, a significant decrease in LPS-induced microglia reactivity was observed in AgNP-treated cells, as evidenced by decreased production of pro-inflammatory cytokines

and a significant reduction in ROS and nitrite production compared to NWs. The discrepancy between the two nanomaterials might be due to the larger surface area to volume ratio of NP, leading to higher dissolution rates than NWs, as shown in ICP dissolution data (Fig. S4, SI).

In previous studies Ag ions have been shown to be toxic to neurons. However, our study shows that AgNM could decrease local neuroinflammation by damping down microglia activation, thereby reducing inflammatory injury to neighbouring neuronal cells. In addition, our study also indicates AgNPs may upregulate the enzymatic activity responsible for producing H_2S, which has been shown to exert neuroprotection through its anti-inflammatory[351, 352], antioxidant[353, 354] and anti-apoptotic[355] effects. H_2S producing enzymes (CBS, CSE and MPST) have different types of ligands (shown in Table S1-3, SI). Mammalian CBS is the only pyridoxal-5'-phosphate (PLP)-dependent enzyme containing a heme cofactor which has been suggested to serve some type of allosteric function and regulate enzymatic activity via the hema redox state. The heme cofactor acts as a weak redox sensor, mildly increasing activity under oxidizing conditions. If the AgNMs cause an increase in oxidative stress when they are exposed to the cells (at a time point< 24 h or > 24 h), this will increase the activity of the enzyme[356].

Unlike CBS, the other two H_2S producing enzymes do not have metal binding ligands but contain S- group in their ligand. In the confocal microscopy studies, the increased florescence intensity of CSE enzymes (24 h) were observed in microglia cells exposed to Ag, but negligible enhanced signal was observed for CBS. The increased fluorescence intensity of the CSE enzymes could be a consequence of the potential binding of Ag to the S - groups of the enzymes. Nevertheless, the MPST signal was not clearly observed in the microglial cells if compared to the CBS and CSE,

The higher enzymatic levels may also link with the enhanced Ag-induced liberation of Zn^{2+} ion cofactors. Recent studies have claimed that Ag^{+} ions have a much higher affinity to metallothionine (MTs) and displace Zn^{2+} which has a multifunctional role in cell metabolism and wound healing[357]. It is well established that released Zn^{2+} ions act as cofactors in essential metalloenzymes[358, 359]. Metal ion cofactors catalyse thousands of enzymatic reactions ranging from Lewis acid catalysis to

electron transfer and redox catalysis. Zinc can easily adopt three or four amino acid side chains and substrates in a variety of coordination geometries. Moreover, Zn^{2+} ions serve as actual catalytic centre of enzymes, contributing directly to the catalytic mechanism or maintaining the structural integrity of the enzyme. Nevertheless, they may not participate directly in the catalysis step, but act as co-catalysts by binding in proximity to each other, where one plays a catalytic role and the other metal ions enhance the activity of the catalytic site of the enzyme. Like Zn, Ag or released Ag^{+} ions are able to interact and bind with metallothionine (MT) which has a unique structure and is present in all living cells[360]. MT, a powerful cysteine-rich protein, regulates cellular metal homeostasis by binding to toxic metals and plays a cytoprotective role. There are 4 different types of MTs (MT-1, MT-2, MT-3 and MT-4) that have affinities in different organ systems. MT-1 and MT-2 are widely expressed isoforms in mammals and MT-4 is concentrated in epithelial tissues, upper stomach and GI tract. While, MT-3 is mainly expressed in the brain and it has a specific neuronal growth inhibitory activity.

To date, it is known that MT-3 is significantly decreased in Alzheimer's disease (AD) brains, indicating its role in AD pathology[361]. MT was found as an inducible antioxidant protein that assisted in reducing cytokine-induced ROS production, protecting DNA breakage and depletion of NAD^{+} [362]. These studies showed no significant increase of cellular ROS production in AgNMs-treated microglia which is in agreement to previous studies[363]. Saydam *et al.* [364, 365] and Heuchel *et al.* [364, 365] suggested that metal responsive element-binding transcription factor 1 (MTF-1), also known as metal – regulator transcription factor 1 plays a vital role in the response to heavy or transition metal induced stress by regulating the expression of MT genes and inducing MT synthesis. An increase in MTs is associated with the scavenging of metal ions, thereby limiting the excess ROS generated by metals and preventing cell damage[84, 366]. Furthermore, AgNPs exposure has been reported to strongly upregulate the expression of MT in astrocytes and no significant increases of cellular ROS production or in the GSSG content[363]. This may also support the explanation why microglial cells are able to internalise the AgNMs with no sign of acute cytotoxicity.

According to Le Chatelier's principle, a system normally readjusts itself to counteract internal or external factors such as changes in concentration, pressure or volume and establishes a new equilibrium system. Considering the concentration of Ag^+ ions is increasing with time, insoluble Ag_2S may settle out of the reaction as a precipitate and reduction of H_2S levels occur. There is a scientific consensus on the key function of H_2S in protecting neurons in neurodegenerative diseases[367, 368]. H_2S has also been recognised as a novel gaseous mediator, acting as neuromodulator and neuroprotective agent in the central nervous system. Therefore, H_2S synthesizing enzymes become activated in order to maintain the chemical equilibrium of H_2S in the brain for signalling, neurotransmitter or relaxation functions as the amount of gasotransmitter H_2S is reduced and reached insufficient levels in brain tissues. This equilibrium mechanism demonstrates how reducing levels of H_2S induce the upregulation of specific enzymes. Consistent with this idea, the confocal imaging and Western blots analysis data show enhanced fluorescence intensity of these enzymes in microglia cells treated with AgNPs.

In summary, microglia plays a prominent role in regulating metal homeostasis and in protecting the brain against potentially toxic metals. Although a large quantity of silver was found in cultured N9 microglia cells treated with AgNMs, these studies showed that both AgNPs and AgNWs neither alter mitochondria potential nor compromise microglia cell viability or induce oxidative stress even at high doses. Furthermore, AgNPs are able to decrease the LPS-induced microglia reactivity, reducing ROS and nitrite production, as well as pro-inflammatory cytokine release. This suggests nanoparticle-derived silver ions may not release from microglia but are likely to bind with proteins, such as cellular sulfur species and MTs to prevent AgNP-induced neurotoxicity even at high doses. A similar observation was also seen by Tambuyzer *et al.*[369] and Oshiro *et al.*[370], showing glial cells can accumulate inorganic metals and protect neurons from oxidative stress by suppressing Tf-IU and proliferating. In contrast, Trickler *et al.*[187] demonstrated exposure of primary rat brain microvessel endothelial cells to AgNPs results in cerebral microvascular dysfunction, inducing brain inflammation. Therefore, it appears that the disparities might result from exposure of different cell types (species differences or tissue origin of the cells) to different surface coating or dimensions of AgNMs and differences in exposure time. In-depth studies are clearly needed to

assess the potential advantageous properties of AgNP as well as their toxicity in order to safely commercialise nano-Ag in various applications. Importantly, neurotoxicity of NPs is necessary to consider in the occupational health exposure risk assessment since there is strong evidence to suggest that inhaled NPs can reach the brain and may impair neurological function[20, 176, 344, 347]. The outcomes of this study can be used to inform regulators about which classes of commercially available AgNPs are safe to handle and to make informed decisions about how to design future classes of "safe" AgNPs.

6.0 Conclusions and Recommendations for Future Study

The aim of the work presented in the thesis is to address some of the controversies regarding the effect of the physicochemical properties of AgNPs on their electrochemical stability as well as their toxicity in two major organs, the lung and brain. The development of new nanometrology methods to measure elements in cells and the interactions between nanoparticles and surfactants were also discussed in the work. This chapter highlights the key contributions of the study and proposes some ideas for future work.

6.1 Conclusions

The widespread use of silver nanomaterials (AgNMs) in various consumer products, ranging from electronic and photonic devices to textiles, food storage containers, and antiseptic and antibacterial sprays, has raised concerns about their long-term stability and potential adverse effects on human health.

In this work, the effects of NPs size, solution pH and applied potential on the AgNPs electrochemical stability were examined and the changes to their surface chemistry or oxidation states were studied in different media (varied pH, potential, particle size). Dispersed silver nanoparticles with a controlled size distribution were prepared on boron-doped diamond substrates *via* magnetron sputtering with size-filtering capability. Particles synthesised *via* magnetron sputtering were compared to those produced by electrodeposition and e-beam evaporation. The potential (E) *vs.* pH experimental data showed that smaller-sized NPs were more stable than larger particles, contradicting the theoretical calculations. This might be affected by the interaction of NPs with the substrate, passivation effects on NPs surface, the variation in the surface coverage of AgNPs, and variable boron concentrations at substrates. However, smaller-sized NPs (*e.g.* 5.2 nm in diameter) followed the same E-pH relationship of bulk Ag, where their anodic potentials (E) were not pH-dependent in acidic solutions, but decreasing E was found at higher pH ($\geq$ 10). XPS confirmed the expected changes of Ag oxidation state as a function of solution pH. These fundamental studies on the dissolution behaviour of AgNPs can be correlated with the chemical reaction involved in cellular environments (*i.e.* oxygenated aqueous media with pH ranges from 1.5 to 7.5).

Whether AgNPs dissolve and release Ag^+ ions, or coarsen to form large aggregates, is critical in determining their potential toxicity. The stability of AgNPs in

dipalmitoylphosphatidylcholine (DPPC), the major component of pulmonary surfactant, was investigated as a function of pH. The kinetics of Ag^+ ion release was found strongly dependent on pH. A decrease in pH promoted particle aggregation and coarsening but the addition of DPPC delayed the release of Ag^+ ions and improved the dispersion of the AgNPs. The direct attachment of a DPPC to a particle surface as a semi-permeable layer was confirmed using TEM. Furthermore, these *in vitro* studies showed that the release rate of Ag^+ ions and the aggregation of NPs were affected by the NPs sizes, surface charges and chemical coating of NPs, suggesting these factors may affect their cellular uptake, translocation, clearance and toxic effects in the pulmonary system. These observations of nanoparticle - lipid interactions may be used to predict the biocompatibility, biodistribution and therapeutic efficacy of this class of NPs in the lung. Understanding the nature of the stability of NPs in lung lining fluids (LLF) could allow researchers to manipulate NPs to achieve a specific medical function and have important implications for predicting the potential reactivity of AgNPs in the lung and the environment.

There are some controversies in the literature about whether interactions of AgNMs with cellular components may affect their biological activity. In this work, NP transformation, following internalisation into cells, was investigated using different techniques, including TEM-EDX, SIMS, FIB-SEM-EDX and confocal microscopy. AgNPs may interact with sulphur containing salts or proteins (*e.g.* MTs), forming highly insoluble Ag_2S. Therefore, no significant increase in ROS production or reduction in cell viability was observed in AgNMs-treated microglia, up to the highest dose of 50 μg/ml. Moreover, AgNMs activated the H_2S producing enzymes (CSE and MPST) to achieve the chemical equilibrium condition of H_2S in the central nervous system. Investigating the interaction of AgNMs with proteins, enzymes or gaseous transmitter (*e.g.* H_2S) and their possible transformation within the cellular environment provides a better understanding of the mechanisms involved in AgNMs toxicity. The data gathered from the *in vitro* works can be used as a complementary method to *in vivo* studies, enabling the design of safe consumer products without jeopardising human health and the environment.

6.2 Future Work

The *in vitro* studies presented in this thesis have shown that the interaction of AgNMs with LLF, sulphide species or proteins may alter their surface chemistry. There are several open questions that still need to be addressed, with respect to stability and toxicity of AgNMs. These proposed avenues for future research are described below:

- For the complete theoretical calculation of the electrochemical stability of AgNPs as a function of size and pH, surface stress ($f_{\mathrm{AgO/Ag}}$), molar volume of the solid ($\Omega_{\mathrm{AgO/Ag}}$) and surface free energy per unit area ($\gamma_{\mathrm{AgO/Ag}}$) of silver oxides are required in the evaluation of $E_{AgO/Ag}$. To date, these important parameters, *i.e.* $f_{\mathrm{AgO/Ag}}$ and $\gamma_{\mathrm{AgO/Ag}}$ could not be found in the literature, but they can be obtained by using first-principle calculations, as shown in *Tang et al*.[252].
- Stability of AgNPs in pulmonary surfactant as presented in Chapter 4 can be extended by examining how physicochemical properties of NPs (*e.g.* size, shape, surface chemistry and surface reactivity) alter their bioreactivity. Furthermore, how the binding of lung lining fluid composition (both phospholipid and surfactant protein content) on in-house prepared AgNPs affect their toxicity can also be investigated.
- The organ (lung) effects (*e.g.* pulmonary elastance) of size, surface chemistry and shape of AgNMs can be assessed to determine the ability of AgNPs in disrupting the pulmonary function. Moreover, it is important to develop methods to track different form of Ag that has reached each organ (i.e. distinguish between ionic Ag^{+}, metallic AgNPs or Ag compounds) and their transformation *in vivo*.
- As observed, AgNMs were localised inside the brain microglia cells, however, the pathways by which the AgNMs enter the brain, *i.e.* whether this occurs by transport across the olfactory nerve or through from the vasculature into the brain *via* the BBB and its dependence on the physicochemistry of the particles is not fully understood. This line of research can be extended by investigating whether, and by which route, AgNPs with different physicochemical properties (such as surface coatings, particle sizes and morphology), access the brain tissue, and whether localisation in the brain

can be linked to brain disease following nasal inhalation. Animal studies should also be performed to validate which classes of AgNPs can translocate into the brain.

- The H_2S concentration in microglia cells couldn't be measured using Lazar Micro Sulfide/Hydrogen Sulfide Electrode measurement system (Lazarlab) due to a calibration error. Therefore, the effect of AgNPs vs. AgNWs in altering the Ag^+ ions and H_2S in microglia cells can be studied by using Ag^+ and H_2S sensitive dyes if they become available.
- The beam size of the TOF-SIMS is > 1 um and each pixel size (imaging) is > 100 nm. NanoSIMS may be an ideal option to study the nano-Ag inside the cells due to its high sensitivity and high lateral resolution (< 50 nm). The co-linear optics of the NanoSIMS allows the primary ion beam focus to a very small spot down to less than 50 nm spot size, providing very high lateral resolution analysis. It also helps in collecting most of the sputtered secondary ions, increasing secondary ion yield. Besides, the high mass resolution of the mass analyser allows the separation of the isotope (mass) of interest from interfering isotopes or molecular clusters with very close masses. The high mass molecules (*e.g.* cholesterol or enzymes fragments), which are commonly found in biological samples can be detected with nanoSIMS. A new set of samples (AgNWs and AgNPs in microglia) can be prepared *via* resin embedded and microtome methods for the nanoSIMS analysis to increase the signals of Ag and S^-.

Ultimately, the information generated through this study will be used to inform regulators and the government about which classes of AgNPs are safe to produce and how they might be designed to reduce any hazard associated with their handling. These data can be useful for researchers designing nanodrugs informing them of their potential hazards and risks in order that they can develop safe nanomaterials.

7.0 References

1. Roco, M.C., *The long view of nanotechnology development: the National Nanotechnology Initiative at 10 years.* Journal of Nanoparticle Research, 2011. **13**(2): p. 427-445.

2. Pourbaix, M., *Atlas of electrochemical equilibria in aqueous solutions*. 1966: Oxford : Pergamon Press

3. Kolb, D.M., G.E. Engelmann, and J.C. Ziegler, *On the unusual electrochemical stability of nanofabricated copper clusters.* Angewandte Chemie-International Edition, 2000. **39**(6): p. 1123-+.

4. Plieth, W.J., *Electrochemical properties of small clusters of metal atoms and their role in surface enhanced raman-scattering.* Journal of Physical Chemistry, 1982. **86**(16): p. 3166-3170.

5. Couvreur, P., *Nanoparticles in drug delivery: Past, present and future.* Advanced Drug Delivery Reviews, 2013. **65**(1): p. 21-23.

6. Tetley, T.D., *Health effects of nanomaterials.* Biochemical Society, 2007. **35**(3): p. 527-531.

7. Hussain, S.M. and J.J. Schlager, *Safety Evaluation of Silver Nanoparticles: Inhalation Model for Chronic Exposure.* Toxicological Sciences, 2009. **108**(2): p. 223-224.

8. Oberdorster, G., *Pulmonary effects of inhaled ultrafine particles.* International Archives of Occupational and Environmental Health, 2001. **74**(1): p. 1-8.

9. Calderon-Garciduenas, L., et al., *Brain inflammation and Alzheimer's-like pathology in individuals exposed to severe air pollution.* Toxicologic Pathology, 2004. **32**(6): p. 650-658.

10. Park, H.J., et al., *Silver-ion-mediated reactive oxygen species generation affecting bactericidal activity.* Water Research, 2009. **43**(4): p. 1027-1032.

11. Li, J.J., et al., *Nanoparticle-induced pulmonary toxicity.* Experimental Biology and Medicine, 2010. **235**(9): p. 1025-1033.

12. Oberdorster, G., et al., *Principles for characterizing the potential human health effects from exposure to nanomaterials: elements of a screening strategy.* Particle and fibre toxicology, 2005. **2**: p. 8-8.

13. Fubini, B., M. Ghiazza, and I. Fenoglio, *Physico-chemical features of engineered nanoparticles relevant to their toxicity.* Nanotoxicology, 2010. **4**(4): p. 347-363.

14. Suresh, A.K., et al., *Cytotoxicity Induced by Engineered Silver Nanocrystallites Is Dependent on Surface Coatings and Cell Types.* Langmuir, 2012. **28**(5): p. 2727-2735.

15. Murdock, R.C., et al., *Characterization of nanomaterial dispersion in solution prior to In vitro exposure using dynamic light scattering technique.* Toxicological Sciences, 2008. **101**(2): p. 239-253.

16. Warheit, D.B., *How meaningful are the results of nanotoxicity studies in the absence of adequate material characterization?* Toxicological Sciences, 2008. **101**(2): p. 183-185.

17. Park, S.H., et al., *Effects of silver nanoparticles on the fluidity of bilayer in phospholipid liposome.* Colloids and Surfaces B-Biointerfaces, 2005. **44**(2-3): p. 117-122.

18. MacCuspie, R.I., A.J. Allen, and V.A. Hackley, *Dispersion stabilization of silver nanoparticles in synthetic lung fluid studied under in situ conditions.* Nanotoxicology, 2011. **5**(2): p. 140-156.

19. Lee, H.-Y., et al., *Genomics-based screening of differentially expressed genes in the brains of mice exposed to silver nanoparticles via inhalation.* Journal of Nanoparticle Research, 2010. **12**(5): p. 1567-1578.

20. Hadrup, N., et al., *The similar neurotoxic effects of nanoparticulate and ionic silver in vivo and in vitro.* Neurotoxicology, 2012. **33**(3): p. 416-423.

21. Chen, S., et al., *Sulfidation of silver nanowires inside human alveolar epithelial cells: a potential detoxification mechanism.* Nanoscale, 2013. **5**(20): p. 9839-9847.

22. *'Plenty of room' revisited.* Nature nanotechnology, 2009. **4**(12): p. 781-781.

23. Bhushan, B., *Introduction to nanotechnology*, ed. n. ed. 2007, New York: Springer. 1-12.

24. Taniguchi, N., *On the Basic Concept of 'Nano-Technology'*. 1974: London, Proc. Intl. Conf. Prod. Part II, British Society of Precision Engineering.

25. Park, B., *Current and Future Applications of Nanotechnology*. 2007: Nanotechnology: Consequences for Human Health and the Environment. Issues in Environment Science and Technology. RCS Publishing.

26. Drexler, K.E., *Engines of Creation: The coming era of nanotechnology.* . 1996: Fourth Estate.

27. Smalley, R.E., *Discovering the fullerenes (Nobel lecture).* Angewandte Chemie-International Edition in English, 1997. **36**(15): p. 1595-1601.

28. Iijima, S., *Helical microtubules of graphitic carbon.* Nature, 1991. **354**(6348): p. 56-58.

29. *Analysis. Project on Emerging Nanotechnologies. Analysis. This is the first publicly available on-line inventory of nanotechnology-based consumer products. 2009 Ref Type: Report*.

30. Kim, J.S., et al., *Antimicrobial effects of silver nanoparticles.* Nanomedicine-Nanotechnology Biology and Medicine, 2007. **3**(1): p. 95-101.

31. Dirix, Y., et al., *Oriented pearl-necklace arrays of metallic nanoparticles in polymers: A new route toward polarization-dependent color filters.* Advanced Materials, 1999. **11**(3): p. 223-+.

32. Wiley, B., Y. Sun, and Y. Xia, *Synthesis of silver wanostructures with controlled shapes and properties.* Accounts of Chemical Research, 2007. **40**(10): p. 1067-1076.

33. Ma, P.C., B.Z. Tang, and J.-K. Kim, *Effect of CNT decoration with silver nanoparticles on electrical conductivity of CNT-polymer composites.* Carbon, 2008. **46**(11): p. 1497-1505.

34. Benn, T.M. and P. Westerhoff, *Nanoparticle silver released into water from commercially available sock fabrics.* Environmental Science & Technology, 2008. **42**(11): p. 4133-4139.

35. Mitrano, D.M., et al., *Presence of Nanoparticles in Wash Water from Conventional Silver and Nano-silver Textiles.* Acs Nano, 2014. **8**(7): p. 7208-7219.

36. Park, J., et al., *Size dependent macrophage responses and toxicological effects of Ag nanoparticles.* Chemical Communications, 2011. **47**(15): p. 4382-4384.

37. Gliga, A.R., et al., *Size-dependent cytotoxicity of silver nanoparticles in human lung cells: the role of cellular uptake, agglomeration and Ag release.* Particle and Fibre Toxicology, 2014. **11**: p. 17.

38. Powers, C.M., et al., *Silver exposure in developing zebrafish (Danio rerio): Persistent effects on larval behavior and survival.* Neurotoxicology and Teratology, 2010. **32**(3): p. 391-397.

39. Schrand, A.M., et al., *Metal-based nanoparticles and their toxicity assessment.* Wiley Interdisciplinary Reviews-Nanomedicine and Nanobiotechnology, 2010. **2**(5): p. 544-568.

40. Reidy, B., et al., *Mechanisms of Silver Nanoparticle Release, Transformation and Toxicity: A Critical Review of Current Knowledge and Recommendations for Future Studies and Applications.* Materials, 2013. **6**(6): p. 2295-2350.

41. Xiu, Z.M., et al., *Negligible Particle-Specific Antibacterial Activity of Silver Nanoparticles.* Nano Letters, 2012. **12**(8): p. 4271-4275.

42. Liu, J., et al., *Chemical Transformations of Nanosilver in Biological Environments.* Acs Nano, 2012. **6**(11): p. 9887-9899.

43. Jin, X., et al., *High-Throughput Screening of Silver Nanoparticle Stability and Bacterial Inactivation in Aquatic Media: Influence of Specific Ions.* Environmental Science & Technology, 2010. **44**(19): p. 7321-7328.

44. Fabrega, J., et al., *Silver Nanoparticle Impact on Bacterial Growth: Effect of pH, Concentration, and Organic Matter.* Environmental Science & Technology, 2009. **43**(19): p. 7285-7290.

45. Taglietti, A., et al., *Antibacterial Activity of Glutathione-Coated Silver Nanoparticles against Gram Positive and Gram Negative Bacteria.* Langmuir, 2012. **28**(21): p. 8140-8148.

46. Ivask, A., et al., *Toxicity Mechanisms in Escherichia coli Vary for Silver Nanoparticles and Differ from Ionic Silver.* Acs Nano, 2014. **8**(1): p. 374-386.

47. Bondarenko, O., et al., *Particle-Cell Contact Enhances Antibacterial Activity of Silver Nanoparticles.* Plos One, 2013. **8**(5).

48. Cronholm, P., et al., *Intracellular Uptake and Toxicity of Ag and CuO Nanoparticles: A Comparison Between Nanoparticles and their Corresponding Metal Ions.* Small, 2013. **9**(7): p. 970-982.

49. Liu, J.Y. and R.H. Hurt, *Ion Release Kinetics and Particle Persistence in Aqueous Nano-Silver Colloids.* Environmental Science & Technology, 2010. **44**(6): p. 2169-2175.

50. Zhang, W., et al., *Modeling the Primary Size Effects of Citrate-Coated Silver Nanoparticles on Their Ion Release Kinetics.* Environmental Science & Technology, 2011. **45**(10): p. 4422-4428.

51. Lee, Y.-J., et al., *Ion-release kinetics and ecotoxicity effects of silver nanoparticles.* Environmental Toxicology and Chemistry, 2012. **31**(1): p. 155-159.

52. Yang, X.Y., et al., *Mechanism of Silver Nanoparticle Toxicity Is Dependent on Dissolved Silver and Surface Coating in Caenorhabditis elegans.* Environmental Science & Technology, 2012. **46**(2): p. 1119-1127.

53. Seitz, F., et al., *Effects of silver nanoparticle properties, media pH and dissolved organic matter on toxicity to Daphnia magna.* Ecotoxicology and environmental safety, 2015. **111**: p. 263-70.

54. Glover, R.D., J.M. Miller, and J.E. Hutchison, *Generation of Metal Nanoparticles from Silver and Copper Objects: Nanoparticle Dynamics on Surfaces and Potential Sources of Nanoparticles in the Environment.* Acs Nano, 2011. **5**(11): p. 8950-8957.

55. Khan, S.S., A. Mukherjee, and N. Chandrasekaran, *Impact of exopolysaccharides on the stability of silver nanoparticles in water.* Water Research, 2011. **45**(16): p. 5184-5190.

56. Kittler, S., et al., *Toxicity of Silver Nanoparticles Increases during Storage Because of Slow Dissolution under Release of Silver Ions.* Chemistry of Materials, 2010. **22**(16): p. 4548-4554.

57. Mayer, A., et al., *The role of nanoparticle size in hemocompatibility.* Toxicology, 2009. **258**(2-3): p. 139-147.

58. Oberdorster, G., E. Oberdorster, and J. Oberdorster, *Nanotoxicology: An emerging discipline evolving from studies of ultrafine particles.* Environmental Health Perspectives, 2005. **113**(7): p. 823-839.

59. Chen, S., et al., *High-Resolution Analytical Electron Microscopy Reveals Cell Culture Media-Induced Changes to the Chemistry of Silver Nanowires.* Environmental Science & Technology, 2013. **47**(23): p. 13813-13821.

60. Leo, B.F., et al., *The Stability of Silver Nanoparticles in a Model of Pulmonary Surfactant.* Environmental Science & Technology, 2013. **47**(19): p. 11232-11240.

61. Wang, X., et al., *Use of Coated Silver Nanoparticles to Understand the Relationship of Particle Dissolution and Bioavailability to Cell and Lung Toxicological Potential.* Small, 2014. **10**(2): p. 385-398.

62. Henglein, A., *Small-particle research-Physicochemical properties of extremely small colloidal metal and semiconductor particles.* Chemical Reviews, 1989. **89**(8): p. 1861-1873.

63. Ng, K.H., H. Liu, and R.M. Penner, *Subnanometer silver clusters exhibiting unexpected electrochemical metastability on graphite.* Langmuir, 2000. **16**(8): p. 4016-4023.

64. Kolb, D.M., R. Ullmann, and T. Will, *Nanofabrication of small copper clusters on gold(111) electrodes by a scanning tunneling microscope.* Science, 1997. **275**(5303): p. 1097-1099.

65. Kolb, D.M. and F.C. Simeone, *Electrochemical nanostructuring with an STM: A status report.* Electrochimica Acta, 2005. **50**(15): p. 2989-2996.

66. Nielinger, M. and H. Baltruschat, *Local formation of an alloy by atomic contact between the STM tip and the substrate surface.* Chemphyschem, 2003. **4**(9): p. 1022-1024.

67. Del Popolo, M., et al., *Generation of palladium clusters on Au(111) electrodes: Experiments and simulations.* Applied Physics Letters, 2002. **81**(14): p. 2635-2637.

68. Maupai, S., et al., *Tip-induced nanostructuring of Au3Cu(001) with an electrochemical scanning tunneling microscope.* Journal of the Electrochemical Society, 2003. **150**(3): p. C111-C114.

69. Lakbub, J., et al., *Electrochemical Behaviors of Single Gold Nanoparticles.* Electroanalysis, 2011. **23**(10): p. 2270-2274.

70. Tang, L., et al., *Electrochemical Stability of Nanometer-Scale Pt Particles in Acidic Environments.* Journal of the American Chemical Society, 2010. **132**(2): p. 596-600.

71. Holby, E.F., et al., *Pt nanoparticle stability in PEM fuel cells: influence of particle size distribution and crossover hydrogen.* Energy & Environmental Science, 2009. **2**(8): p. 865-871.

72. Campbell, C.T., S.C. Parker, and D.E. Starr, *The effect of size-dependent nanoparticle energetics on catalyst sintering.* Science, 2002. **298**(5594): p. 811-814.

73. T, M.E.A.M.G., *Aulton's Pharmaceutics: The Design and Manufacture of Medicinies*. 2013: Elsevier.

74. Kwon, S.T. and G.L. Messing, *The effect of particle solubility on the strength of nanocrystalline agglomerates: Boehmite.* Nanostructured Materials, 1997. **8**(4): p. 399-418.

75. Mihranyan, A. and M. Stromme, *Solubility of fractal nanoparticles.* Surface Science, 2007. **601**(2): p. 315-319.

76. Auffan, M., et al., *Towards a definition of inorganic nanoparticles from an environmental, health and safety perspective.* Nature Nanotechnology, 2009. **4**(10): p. 634-641.

77. Han, B.C., C.R. Miranda, and G. Ceder, *Effect of particle size and surface structure on adsorption of O and OH on platinum nanoparticles: A first-principles study.* Physical Review B, 2008. **77**(7).

78. Som, C., et al., *Environmental and health effects of nanomaterials in nanotextiles and facade coatings.* Environment International, 2011. **37**(6): p. 1131-1142.

79. Panyala, N.R., E. Maria Pena-Mendez, and J. Havel, *Silver or silver nanoparticles: a hazardous threat to the environment and human health?* Journal of Applied Biomedicine, 2008. **6**(3): p. 117-129.

80. Schulte, P., et al., *Occupational risk management of engineered nanoparticles.* Journal of Occupational and Environmental Hygiene, 2008. **5**(4): p. 239-249.

81. Yokel, R.A. and R.C. MacPhail, *Engineered nanomaterials: exposures, hazards, and risk prevention.* Journal of Occupational Medicine and Toxicology, 2011. **6**.

82. Ayres, T.C. and J.W. Bond, *A chemical analysis examining the pharmacology of novel psychoactive substances freely available over the internet and their impact on public (ill) health. Legal highs or illegal highs?* Bmj Open, 2012. **2**(4).

83. Zimmer, A.T., P.A. Baron, and P. Biswas, *The influence of operating parameters on number-weighted aerosol size distribution generated from a gas metal arc welding process.* Journal of Aerosol Science, 2002. **33**(3): p. 519-531.

84. Dorman, D.C., et al., *Nasal toxicity of manganese sulfate and manganese phosphate in young male rats following subchronic (13-week) inhalation exposure.* Inhalation Toxicology, 2004. **16**(6-7): p. 481-488.

85. Hodgson, J.T. and A. Darnton, *The quantitative risks of mesothelioma and lung cancer in relation to asbestos exposure.* Annals of Occupational Hygiene, 2000. **44**(8): p. 565-601.

86. Camus, M., J. Siemiatycki, and B. Meek, *Nonoccupational exposure to Chrysotile asbestos and the risk of lung cancer.* New England Journal of Medicine, 1998. **338**(22): p. 1565-1571.

87. McDonald, J.C., *Health implication of environmental exposure to asbestos.* Environmental Health Perspectives, 1985. **62**(OCT): p. 319-328.

88. Schleh, C. and J.M. Hohlfeld, *Interaction of nanoparticles with the pulmonary surfactant system.* Inhalation toxicology, 2009. **21 Suppl 1**: p. 97-103.

89. Kumar, C., *Nanomaterials - Toxicity, Health and Environmental Issues.* 2006, VCH Verlag GmbH & Co, Weinheim: Wiley.

90. Peters, A., et al., *Translocation and potential neurological effects of fine and ultrafine particles a critical update.* Particle and fibre toxicology, 2006. **3**: p. 13-13.

91. Ng, A.W., A. Bidani, and T.A. Herring, *Innate host Defense of the lung: Effects of lung-lining fluid pH.* Lung, 2004. **182**(5): p. 297-317.

92. Oberdorster, G., *Toxicokinetics and effects of fibrous and nonfibrous particles.* Inhalation Toxicology, 2002. **14**(1): p. 29-56.

93. Rupper, A. and J. Cardelli, *Regulation of phagocytosis and endo-phagosomal trafficking pathways in Dictyostelium discoideum.* Biochimica Et Biophysica Acta-General Subjects, 2001. **1525**(3): p. 205-216.

94. Takenaka, S., et al., *Pulmonary and systemic distribution of inhaled ultrafine silver particles in rats.* Environmental Health Perspectives, 2001. **109**: p. 547-551.

95. Oberdoester, G., *Nanotoxicology: An Emerging Discipline Evolving from Studies of Ultrafine Particles (vol 113, pg 823, 2005).* Environmental Health Perspectives, 2010. **118**(9): p. A380-A380.

96. Muller, J., et al., *Respiratory toxicity of multi-wall carbon nanotubes.* Toxicology and Applied Pharmacology, 2005. **207**(3): p. 221-231.

97. Borm, P.J.A., R.P.F. Schins, and C. Albrecht, *Inhaled particles and lung cancer, part B: Paradigms and risk assessment.* International Journal of Cancer, 2004. **110**(1): p. 3-14.

98. Borm, P.J.A., et al., *The potential risks of nanomaterials: a review carried out for ECETOC.* Particle and fibre toxicology, 2006. **3**: p. 11-11.

99. Blundell, G., W.J. Henderson, and E.W. Price, *Soil particles in the tissues of the foot in endemic elephantiasis of the lower legs.*Annals of Tropical Medicine and Parasitology, 1989. **83**(4): p. 381-385.

100. Tinkle, S.S., et al., *Skin as a route of exposure and sensitization in chronic beryllium disease.* Environmental Health Perspectives, 2003. **111**(9): p. 1202-1208.

101. Toll, R., et al., *Penetration profile of microspheres in follicular targeting of terminal hair follicles.* Journal of Investigative Dermatology, 2004. **123**(1): p. 168-176.

102. Crosera, M., et al., *Nanoparticle dermal absorption and toxicity: a review of the literature.* International Archives of Occupational and Environmental Health, 2009. **82**(9): p. 1043-1055.

103. Lademann, J., et al., *Penetration of titanium dioxide microparticles in a sunscreen formulation into the horny layer and the follicular orifice.* Skin Pharmacology and Applied Skin Physiology, 1999. **12**(5): p. 247-256.

104. Larese, F.F., et al., *Human skin penetration of silver nanoparticles through intact and damaged skin.* Toxicology, 2009. **255**(1-2): p. 33-37.

105. Froehlich, E. and E. Roblegg, *Models for oral uptake of nanoparticles in consumer products.* Toxicology, 2012. **291**(1-3): p. 10-17.

106. Bouwmeester, H., et al., *Review of health safety aspects of nanotechnologies in food production.* Regulatory Toxicology and Pharmacology, 2009. **53**(1): p. 52-62.

107. Wang, B., et al., *Acute toxicity of nano- and micro-scale zinc powder in healthy adult mice.* Toxicology Letters, 2006. **161**(2): p. 115-123.

108. Bosi, S., et al., *Fullerene derivatives: an attractive tool for biological applications.* European Journal of Medicinal Chemistry, 2003. **38**(11-12): p. 913-923.

109. Oberdorster, G., J. Ferin, and B.E. Lehnert, *Correlation between particle-size, in-vivo particle persistence, and lung injury.* Environmental Health Perspectives, 1994. **102**: p. 173-179.

110. Wang, J., et al., *Acute toxicity and biodistribution of different sized titanium dioxide particles in mice after oral administration.* Toxicology Letters, 2007. **168**(2): p. 176-185.

111. Jani, P., et al., *Nanoparticle uptake by the rat gastrointestinal mucosa-quantitation and particle-size dependency.* Journal of Pharmacy and Pharmacology, 1990. **42**(12): p. 821-826.

112. Choi, H.S., et al., *Rapid translocation of nanoparticles from the lung airspaces to the body.* Nature Biotechnology, 2010. **28**(12): p. 1300-U113.

113. Choi, H.S., et al., *Design considerations for tumour-targeted nanoparticles.* Nature Nanotechnology, 2010. **5**(1): p. 42-47.

114. Burns, A.A., et al., *Fluorescent Silica Nanoparticles with Efficient Urinary Excretion for Nanomedicine.* Nano Letters, 2009. **9**(1): p. 442-448.

115. Baek, M., et al., *Pharmacokinetics, tissue distribution, and excretion of zinc oxide nanoparticles.* International Journal of Nanomedicine, 2012. **7**: p. 3081-3097.

116. Choi, H.S., et al., *Renal clearance of quantum dots.* Nature Biotechnology, 2007. **25**(10): p. 1165-1170.

117. Lei, R., et al., *Integrated metabolomic analysis of the nano-sized copper particle-induced hepatotoxicity and nephrotoxicity in rats: A rapid in vivo screening method for nanotoxicity.* Toxicology and Applied Pharmacology, 2008. **232**(2): p. 292-301.

118. Qi, W., et al., *Damaging Effects of Multi-walled Carbon Nanotubes on Pregnant Mice with Different Pregnancy Times.* Scientific Reports, 2014. **4**.

119. Huang, X., et al., *The Shape Effect of Mesoporous Silica Nanoparticles on Biodistribution, Clearance, and Biocompatibility in Vivo.* Acs Nano, 2011. **5**(7): p. 5390-5399.

120. Alexis, F., et al., *Factors affecting the clearance and biodistribution of polymeric nanoparticles.* Molecular Pharmaceutics, 2008. **5**(4): p. 505-515.

121. Wahajuddin and S. Arora, *Superparamagnetic iron oxide nanoparticles: magnetic nanoplatforms as drug carriers.* International Journal of Nanomedicine, 2012. **7**: p. 3445-3471.

122. Porter, D., et al., *A biocompatible medium for nanoparticle dispersion.* Nanotoxicology, 2008. **2**(3): p. 144-154.

123. Sager, T.M., et al., *Improved method to disperse nanoparticles for in vitro and in vivo investigation of toxicity.* Nanotoxicology, 2007. **1**(2): p. 118-129.

124. Bakshi, M.S., et al., *Metal nanoparticle pollutants interfere with pulmonary surfactant function in vitro.* Biophysical Journal, 2008. **94**(3): p. 855-868.

125. Roiter, Y., et al., *Interaction of nanoparticles with lipid membrane.* Nano Letters, 2008. **8**(3): p. 941-944.

126. Wang, B., et al., *Nanoparticle-induced surface reconstruction of phospholipid membranes.* Proceedings of the National Academy of Sciences of the United States of America, 2008. **105**(47): p. 18171-18175.

127. Guzman, E., et al., *Effect of Hydrophilic and Hydrophobic Nanoparticles on the Surface Pressure Response of DPPC Monolayers.* Journal of Physical Chemistry C, 2011. **115**(44): p. 21715-21722.

128. Yang, S.T., et al., *Biosafety and Bioapplication of Nanomaterials by Designing Protein-Nanoparticle Interaction.* Small, 2013.

129. Fenoglio, I., et al., *Multiple aspects of the interaction of biomacromolecules with inorganic surfaces.* Advanced Drug Delivery Reviews, 2011. **63**(13): p. 1186-1209.

130. Wells, M.A., et al., *Serum proteins prevent aggregation of Fe2O3 and ZnO nanoparticles.* Nanotoxicology, 2012. **6**(8): p. 837-846.

131. Harishchandra, R.K., M. Saleem, and H.-J. Galla, *Nanoparticle interaction with model lung surfactant monolayers.* J. R. Soc. Interface, 2010. **7**: p. S15–S26.

132. Stebounova, L.V., E. Guio, and V.H. Grassian, *Silver nanoparticles in simulated biological media: a study of aggregation, sedimentation, and dissolution.* Journal of Nanoparticle Research, 2011. **13**(1): p. 233-244.

133. Yin, L.Y., et al., *More than the ions: The effect of Silver Nanoparticles on Lodium multiflorum. . Environ. Sci. Technol*., 2011. **45**: p. 2360-2367.

134. El Badawy, A.M., et al., *Surface Charge-Dependent Toxicity of Silver Nanoparticles.* Environmental Science & Technology, 2011. **45**(1): p. 283-287.

135. Levard, C., et al., *Sulfidation Processes of PVP-Coated Silver Nanoparticles in Aqueous Solution: Impact on Dissolution Rate.* Environmental Science & Technology, 2011. **45**(12): p. 5260-5266.

136. Elzey, S. and V.H. Grassian, *Agglomeration, isolation and dissolution of commercially manufactured silver nanoparticles in aqueous environments.* Journal of Nanoparticle Research, 2010. **12**(5): p. 1945-1958.

137. Muller, K.H., et al., *pH-Dependent Toxicity of High Aspect Ratio ZnO Nanowires in Macrophages Due to Intracellular Dissolution.* Acs Nano, 2010. **4**(11): p. 6767-6779.

138. Rooney, S.A., S.L. Young, and C.R. Mendelson, *Molecular and cellular processing of lung surfactant.* Faseb Journal, 1994. **8**(12): p. 957-967.

139. Creuwels, L., L.M.G. vanGolde, and H.P. Haagsman, *The pulmonary surfactant system: Biochemical and clinical aspects.* Lung, 1997. **175**(1): p. 1-39.

140. Griese, M., *Pulmonary surfactant in health and human lung diseases: state of the art.* European Respiratory Journal, 1999. **13**(6): p. 1455-1476.

141. Sager, T.M. and V. Castranova, *Surface area of particle administered versus mass in determining the pulmonary toxicity of ultrafine and fine carbon black: comparison to ultrafine titanium dioxide.* Particle and Fibre Toxicology, 2009. **6**.

142. Veldhuizen, R., et al., *The role of lipids in pulmonary surfactant.* Biochimica Et Biophysica Acta-Molecular Basis of Disease, 1998. **1408**(2-3): p. 90-108.

143. Leonenko, Z.V., et al., *Investigation of temperature-induced phase transitions in DOPC and DPPC phospholipid bilayers using temperature-controlled scanning force microscopy.* Biophysical Journal, 2004. **86**(6): p. 3783-3793.

144. Tristram-Nagle, S. and J.F. Nagle, *Lipid bilayers: thermodynamics, structure, fluctuations, and interactions.* Chemistry and Physics of Lipids, 2004. **127**(1): p. 3-14.

145. Rappolt, M. and G. Rapp, *Structure of the stable and metastable ripple phase of dipalmitoylphosphatidylcholine.* European Biophysics Journal with Biophysics Letters, 1996. **24**(6): p. 381-386.

146. Goerke, J. and J. Gonzales, *Temperature-dependence of dipalmitoyl phosphatidylcholine monolayer stability.* Journal of Applied Physiology, 1981. **51**(5): p. 1108-1114.

147. Zuo, Y.Y. and F. Possmayer, *How does pulmonary surfactant reduce surface tension to very low values?* Journal of Applied Physiology, 2007. **102**(5): p. 1733-1734.

148. Notter, R.H., *Lung Surfactants:Basic Science and Clinical Applications*. 2000, New York: Marcel Dekker.

149. Richter, R., A. Mukhopadhyay, and A. Brisson, *Pathways of lipid vesicle deposition on solid surfaces: A combined QCM-D and AFM study.* Biophysical Journal, 2003. **85**(5): p. 3035-3047.

150. McConnell, H.M., et al., *Supported planar investigation of nanoparticle interaction with a model pulmonary surfactant monolayer.* Biochimica Et Biophysica Acta, 1986. **864**(1): p. 95-106.

151. Sachan, A.K., et al., *High-Resolution Investigation of Nanoparticle Interaction with a Model Pulmonary Surfactant Monolayer.* Acs Nano, 2012. **6**(2): p. 1677-1687.

152. Sutariya, V.B. and Y. Pathak, *Biointeractions of Nanomaterials*. 2014: CRC Press.

153. Lynch, I., A. Salvati, and K.A. Dawson, *PROTEIN-NANOPARTICLE INTERACTIONS What does the cell see?* Nature Nanotechnology, 2009. **4**(9): p. 546-547.

154. Monopoli, M.P., et al., *Biomolecular coronas provide the biological identity of nanosized materials.* Nature Nanotechnology, 2012. **7**(12): p. 779-786.

155. Lundqvist, M., et al., *Nanoparticle size and surface properties determine the protein corona with possible implications for biological impacts.* Proceedings of the

National Academy of Sciences of the United States of America, 2008. **105**(38): p. 14265-14270.

156. Lynch, I. and K.A. Dawson, *Protein-nanoparticle interactions.* Nano Today, 2008. **3**(1-2): p. 40-47.

157. Owens, D.E. and N.A. Peppas, *Opsonization, biodistribution, and pharmacokinetics of polymeric nanoparticles.* International Journal of Pharmaceutics, 2006. **307**(1): p. 93-102.

158. Roser, M., D. Fischer, and T. Kissel, *Surface-modified biodegradable albumin nano- and microspheres. II: effect of surface charges on in vitro phagocytosis and biodistribution in rats.* European Journal of Pharmaceutics and Biopharmaceutics, 1998. **46**(3): p. 255-263.

159. Mueller, R.H., et al., *In-vitro characterization of polymethylmethacrylate nanoparticles and correlation to their in-vivo fate.*. Journal of Controlled Release, 1992. **20**(3): p. 237-246.

160. Carstensen, H., R.H. Muller, and B.W. Muller, *Particle-size, surface hydrophobicity and interaction with serum of parenteral fat emulsions and model-drug carriers as parameters related to RES uptake.*. Clinical Nutrition, 1992. **11**(5): p. 289-297.

161. Cedervall, T., et al., *Detailed identification of plasma proteins adsorbed on copolymer nanoparticles.* Angewandte Chemie-International Edition, 2007. **46**(30): p. 5754-5756.

162. Sant, S., S. Poulin, and P. Hildgen, *Effect of polymer architecture on surface properties, plasma protein adsorption, and cellular interactions of pegylated nanoparticles.* Journal of Biomedical Materials Research Part A, 2008. **87A**(4): p. 885-895.

163. Kreuter, J., *Nanoparticulate systems for brain delivery of drugs.* Advanced Drug Delivery Reviews, 2001. **47**(1): p. 65-81.

164. Muller, R.H. and C.M. Keck, *Challenges and solutions for the delivery of biotech drugs - a review of drug nanocrystal technology and lipid nanoparticles.* Journal of Biotechnology, 2004. **113**(1-3): p. 151-170.

165. Olivier, J.-C., *Drug transport to brain with targeted nanoparticles.* NeuroRx : the journal of the American Society for Experimental NeuroTherapeutics, 2005. **2**(1): p. 108-19.

166. Goppert, T.M. and R.H. Muller, *Polysorbate-stabilized solid lipid nanoparticles as colloidal carriers for intravenous targeting of drugs to the brain: Comparison of plasma protein adsorption patterns.* Journal of Drug Targeting, 2005. **13**(3): p. 179-187.

167. Mueller, R.H. and S. Heinemann, *Surface modelling of microparticles as parenteral systems with high tissue affinity.* Paperback APV; Bioadhesion: Possibilities and future trends, 1990. **25**: p. 202-213.

168. Kim, H.R., et al., *Analysis of plasma protein adsorption onto PEGylated nanoparticles by complementary methods: 2-DE, CE and protein Lab-on-chip((R)) system.* Electrophoresis, 2007. **28**(13): p. 2252-2261.

169. Lemarchand, C., et al., *Influence of polysaccharide coating on the interactions of nanoparticles with biological systems.* Biomaterials, 2006. **27**(1): p. 108-118.

170. Peracchia, M.T., et al., *Stealth (R) PEGylated polycyanoacrylate nanoparticles for intravenous administration and splenic targeting.* Journal of Controlled Release, 1999. **60**(1): p. 121-128.

171. Paciotti, G.F., et al., *Colloidal gold: A novel nanoparticle vector for tumor directed drug delivery.* Drug Delivery, 2004. **11**(3): p. 169-183.

172. Zahr, A.S., C.A. Davis, and M.V. Pishko, *Macrophage uptake of core-shell nanoparticles surface modified with poly(ethylene glycol).* Langmuir, 2006. **22**(19): p. 8178-8185.

173. Liu, G., et al., *Nanoparticle and other metal chelation therapeutics in Alzheimer disease.* Biochimica Et Biophysica Acta-Molecular Basis of Disease, 2005. **1741**(3): p. 246-252.

174. Cui, Z.R., et al., *Novel D-penicillamine carrying nanoparticles for metal chelation therapy in Alzheimer's and other CNS diseases.* European Journal of Pharmaceutics and Biopharmaceutics, 2005. **59**(2): p. 263-272.

175. Stoehr, L.C., et al., *Shape matters: effects of silver nanospheres and wires on human alveolar epithelial cells.* Particle and Fibre Toxicology, 2011. **8**.

176. Soderstjerna, E., et al., *Gold- and Silver Nanoparticles Affect the Growth Characteristics of Human Embryonic Neural Precursor Cells.* Plos One, 2013. **8**(3).

177. AshaRani, P.V., et al., *Cytotoxicity and Genotoxicity of Silver Nanoparticles in Human Cells.* Acs Nano, 2009. **3**(2): p. 279-290.

178. Park, M.V.D.Z., et al., *The effect of particle size on the cytotoxicity, inflammation, developmental toxicity and genotoxicity of silver nanoparticles.* Biomaterials, 2011. **32**(36): p. 9810-9817.

179. Marambio-Jones, C. and E.M.V. Hoek, *A review of the antibacterial effects of silver nanomaterials and potential implications for human health and the environment.* Journal of Nanoparticle Research, 2010. **12**(5): p. 1531-1551.

180. Chen, X. and H.J. Schluesener, *Nanosilver: A nanoproduct in medical application.* Toxicology Letters, 2008. **176**(1): p. 1-12.

181. Nowack, B., H.F. Krug, and M. Height, *120 Years of Nanosilver History: Implications for Policy Makers.* Environmental Science & Technology, 2011. **45**(4): p. 1177-1183.

182. Oberdorster, G., et al., *Translocation of inhaled ultrafine particles to the brain.* Inhalation Toxicology, 2004. **16**(6-7): p. 437-445.

183. Elder, A., et al., *Translocation of inhaled ultrafine manganese oxide particles to the central nervous system.* Environmental Health Perspectives, 2006. **114**(8): p. 1172-1178.

184. Yu, L.E., et al., *Translocation and effects of gold nanoparticles after inhalation exposure in rats.* Nanotoxicology, 2007. **1**(3): p. 235-242.

185. Wang, J., et al., *Time-dependent translocation and potential impairment on central nervous system by intranasally instilled TiO2 nanoparticles.* Toxicology, 2008. **254**(1-2): p. 82-90.

186. Buzea, C., Pacheco, II, and K. Robbie, *Nanomaterials and nanoparticles: Sources and toxicity.* Biointerphases, 2007. **2**(4): p. MR17-MR71.

187. Trickler, W.J., et al., *Silver Nanoparticle Induced Blood-Brain Barrier Inflammation and Increased Permeability in Primary Rat Brain Microvessel Endothelial Cells.* Toxicological Sciences, 2010. **118**(1): p. 160-170.

188. Kim, Y.S., et al., *Twenty-eight-day oral toxicity, genotoxicity, and gender-related tissue distribution of silver nanoparticles in Sprague-Dawley rats.* Inhalation Toxicology, 2008. **20**(6): p. 575-583.

189. Tang, J., et al., *Distribution, Translocation and Accumulation of Silver Nanoparticles in Rats.* Journal of Nanoscience and Nanotechnology, 2009. **9**(8): p. 4924-4932.

190. Kawaguchi, H., et al., *Phagocytosis of latex-particles by leukocytes. l. Dependence of phagocytosis on the size and surface-potential of particles.* Biomaterials, 1986. **7**(1): p. 61-66.

191. Gratton, S.E.A., et al., *The effect of particle design on cellular internalization pathways.* Proceedings of the National Academy of Sciences of the United States of America, 2008. **105**(33): p. 11613-11618.

192. Sharma, G., et al., *Polymer particle shape independently influences binding and internalization by macrophages.* Journal of Controlled Release, 2010. **147**(3): p. 408-412.

193. Champion, J.A., A. Walker, and S. Mitragotri, *Role of particle size in phagocytosis of polymeric microspheres.* Pharmaceutical Research, 2008. **25**(8): p. 1815-1821.

194. Kreyling, W.G., et al., *Translocation of ultrafine insoluble iridium particles from lung epithelium to extrapulmonary organs is size dependent but very low.* Journal of Toxicology and Environmental Health-Part A, 2002. **65**(20): p. 1513-1530.

195. Kato, T., et al., *Evidence that exogenous substances can be phagocytized by alveolar epithelial cells and transported into blood capillaries.* Cell and Tissue Research, 2003. **311**(1): p. 47-51.

196. Davda, J. and V. Labhasetwar, *Characterization of nanoparticle uptake by endothelial cells.* International Journal of Pharmaceutics, 2002. **233**(1-2): p. 51-59.

197. Voigt, J., J. Christensen, and V.P. Shastri, *Differential uptake of nanoparticles by endothelial cells through polyelectrolytes with affinity for caveolae.* Proceedings of the National Academy of Sciences of the United States of America, 2014. **111**(8): p. 2942-2947.

198. Bannunah, A.M., et al., *Mechanisms of Nanoparticle Internalization and Transport Across an Intestinal Epithelial Cell Model: Effect of Size and Surface Charge.* Molecular Pharmaceutics, 2014. **11**(12): p. 4363-4373.

199. Des Rieux, A., et al., *Nanoparticles as potential oral delivery systems of proteins and vaccines: A mechanistic approach.* Journal of Controlled Release, 2006. **116**(1): p. 1-27.

200. Kotov, N.A., et al., *Nanomaterials for Neural Interfaces.* Advanced Materials, 2009. **21**(40): p. 3970-4004.

201. Verma, A. and F. Stellacci, *Effect of Surface Properties on Nanoparticle-Cell Interactions.* Small, 2010. **6**(1): p. 12-21.

202. Liu, X., et al., *Surface and Size Effects on Cell Interaction of Gold Nanoparticles with Both Phagocytic and Nonphagocytic Cells.* Langmuir, 2013. **29**(29): p. 9138-9148.

203. Tabata, Y. and Y. Ikada, *Effect of the size and surface-charge of polymer microspheres on their phagocytosis by macrophage.* Biomaterials, 1988. **9**(4): p. 356-362.

204. Chu, Z., et al., *Unambiguous observation of shape effects on cellular fate of nanoparticles.* Scientific Reports, 2014. **4**.

205. Huang, X., et al., *The effect of the shape of mesoporous silica nanoparticles on cellular uptake and cell function.* Biomaterials, 2010. **31**(3): p. 438-448.

206. Yanes, R.E., et al., *Involvement of Lysosomal Exocytosis in the Excretion of Mesoporous Silica Nanoparticles and Enhancement of the Drug Delivery Effect by Exocytosis Inhibition.* Small, 2013. **9**(5): p. 697-704.

207. Garcia-Aonso, J., et al., *Cellular Internalization of Silver Nanoparticles in Gut Epithelia of the Estuarine Polychaete Nereis diversicolor.* Environmental Science & Technology, 2011. **45**(10): p. 4630-4636.

208. Conner, S.D. and S.L. Schmid, *Regulated portals of entry into the cell.* Nature, 2003. **422**(6927): p. 37-44.

209. Al-Jamal, K.T., et al., *Cellular uptake mechanisms of functionalised multi-walled carbon nanotubes by 3D electron tomography imaging.* Nanoscale, 2011. **3**(6): p. 2627-2635.

210. Uttara, B., et al., *Oxidative Stress and Neurodegenerative Diseases: A Review of Upstream and Downstream Antioxidant Therapeutic Options.* Current Neuropharmacology, 2009. **7**(1): p. 65-74.

211. Festjens, N., T. Vanden Berghe, and P. Vandenabeele, *Necrosis, a well-orchestrated form of cell demise: Signalling cascades, important mediators and concomitant immune response.* Biochimica Et Biophysica Acta-Bioenergetics, 2006. **1757**(9-10): p. 1371-1387.

212. Valko, M., et al., *Free radicals and antioxidants in normal physiological functions and human disease.* International Journal of Biochemistry & Cell Biology, 2007. **39**(1): p. 44-84.

213. Valko, M., et al., *Free radicals, metals and antioxidants in oxidative stress-induced cancer.* Chemico-Biological Interactions, 2006. **160**(1): p. 1-40.

214. Pujalte, I., et al., *Cytotoxicity and oxidative stress induced by different metallic nanoparticles on human kidney cells.* Particle and Fibre Toxicology, 2011. **8**.

215. Zhang, T., et al., *Cytotoxic Potential of Silver Nanoparticles.* Yonsei Medical Journal, 2014. **55**(2): p. 283-291.

216. Saptarshi, S.R., A. Duschl, and A.L. Lopata, *Interaction of nanoparticles with proteins: relation to bio-reactivity of the nanoparticle.* Journal of Nanobiotechnology, 2013. **11**.

217. Leonard, S., et al., *Cobalt-mediated generation of reactive oxygen species and its possible mechanism.* Journal of Inorganic Biochemistry, 1998. **70**(3-4): p. 239-244.

218. Yin, J.-J., et al., *Dual Role of Selected Antioxidants Found in Dietary Supplements: Crossover between Anti- and Pro-Oxidant Activities in the Presence of Copper.* Journal of Agricultural and Food Chemistry, 2012. **60**(10): p. 2554-2561.

219. Risom, L., P. Moller, and S. Loft, *Oxidative stress-induced DNA damage by particulate air pollution.* Mutation Research-Fundamental and Molecular Mechanisms of Mutagenesis, 2005. **592**(1-2): p. 119-137.

220. McCarthy, J., et al., *Mechanisms of Toxicity of Amorphous Silica Nanoparticles on Human Lung Submucosal Cells in Vitro: Protective Effects of Fisetin.* Chemical Research in Toxicology, 2012. **25**(10): p. 2227-2235.

221. Nguyen, K.C., et al. *Comparison of toxicity of uncoated and coated silver nanoparticles*. in *3rd International Conference on Safe Production and Use of Nanomaterials (Nanosafe)*. 2012. Minatec, Grenoble, FRANCE.

222. Pan, Y., et al., *Gold Nanoparticles of Diameter 1.4 nm Trigger Necrosis by Oxidative Stress and Mitochondrial Damage.* Small, 2009. **5**(18): p. 2067-2076.

223. Foldbjerg, R., D.A. Dang, and H. Autrup, *Cytotoxicity and genotoxicity of silver nanoparticles in the human lung cancer cell line, A549.* Archives of Toxicology, 2011. **85**(7): p. 743-750.

224. Halliwell, B., *Antioxidant defence mechanisms: From the beginning to the end (of the beginning).* Free Radical Research, 1999. **31**(4): p. 261-272.

225. Mecocci, P., U. Macgarvey, and M.F. Beal, *Oxidative damage to mitochondrial-DNA is increased in Alzheimers-disease.*. Annals of Neurology, 1994. **36**(5): p. 747-751.

226. Aruoma, O.I., *Free radicals, oxidative stress, and antioxidants in human health and disease.* Journal of the American Oil Chemists Society, 1998. **75**(2): p. 199-212.

227. Bagchi, D., et al., *Free radicals and grape seed proanthocyanidin extract: importance in human health and disease prevention.* Toxicology, 2000. **148**(2-3): p. 187-197.

228. Sioutas, C., R.J. Delfino, and M. Singh, *Exposure assessment for atmospheric ultrafine particles (UFPs) and implications in epidemiologic research.* Environmental Health Perspectives, 2005. **113**(8): p. 947-955.

229. Schubert, D., et al., *Cerium and yttrium oxide nanoparticles are neuroprotective.* Biochemical and Biophysical Research Communications, 2006. **342**(1): p. 86-91.

230. Hackenberg, S., et al., *Silver nanoparticles: Evaluation of DNA damage, toxicity and functional impairment in human mesenchymal stem cells.* Toxicology Letters, 2011. **201**(1): p. 27-33.

231. Froehlich, E., *Cellular Targets and Mechanisms in the Cytotoxic Action of Non-biodegradable Engineered Nanoparticles.* Current Drug Metabolism, 2013. **14**(9): p. 976-988.

232. Froehlich, E., *The role of surface charge in cellular uptake and cytotoxicity of medical nanoparticles.* International Journal of Nanomedicine, 2012. **7**: p. 5577-5591.

233. Yang, G., et al., *H(2)S as a physiologic vasorelaxant: Hypertension in mice with deletion of cystathionine gamma-lyase.* Science, 2008. **322**(5901): p. 587-590.

234. Wallace, J.L., *Hydrogen sulfide-releasing anti-inflammatory drugs.* Trends in Pharmacological Sciences, 2007. **28**(10): p. 501-505.

235. McGeer, E.G. and P.L. McGeer, *Neuroinflammation in Alzheimer's Disease and Mild Cognitive Impairment: A Field in Its Infancy.* Journal of Alzheimers Disease, 2010. **19**(1): p. 355-361.

236. Suzuki, K., et al., *Hydrogen sulfide replacement therapy protects the vascular endothelium in hyperglycemia by preserving mitochondrial function.* Proceedings of the National Academy of Sciences of the United States of America, 2011. **108**(33): p. 13829-13834.

237. Kamoun, P., et al., *Endogenous hydrogen sulfide overproduction in Down syndrome.* American Journal of Medical Genetics Part A, 2003. **116A**(3): p. 310-311.

238. Jha, S., et al., *Hydrogen sulfide attenuates hepatic ischemia-reperfusion injury: role of antioxidant and antiapoptotic signaling.* American Journal of Physiology-Heart and Circulatory Physiology, 2008. **295**(2): p. H801-H806.

239. Lee, S.W., et al., *Hydrogen sulphide regulates calcium homeostasis in microglial cells.* Glia, 2006. **54**(2): p. 116-124.

240. Kabil, O., et al., *The Quantitative Significance of the Transsulfuration Enzymes for H2S Production in Murine Tissues.* Antioxidants & Redox Signaling, 2011. **15**(2): p. 363-372.

241. *Nanoparticles in Biotechnology, Drug Development and Drug Delivery*. 2012.

242. Krug, H.F., *Nanosafety Research—Are We on the Right Track?* Angew. Chem. Int. Ed., 2014. **53**: p. 12304-12319.

243. MacPhail, R.C., E.A. Grulke, and R.A. Yokel, *Assessing nanoparticle risk poses prodigious challenges.* Wiley Interdisciplinary Reviews-Nanomedicine and Nanobiotechnology, 2013. **5**(4): p. 374-387.

244. Olson, K.R., *The therapeutic potential of hydrogen sulfide: separating hype from hope.* American Journal of Physiology-Regulatory Integrative and Comparative Physiology, 2011. **301**(2): p. R297-R312.

245. Guo, S.J. and E.K. Wang, *Noble metal nanomaterials: Controllable synthesis and application in fuel cells and analytical sensors.* Nano Today, 2011. **6**(3): p. 240-264.

246. Guo, D.J. and H.L. Li, *Highly dispersed Ag nanoparticles on functional MWNT surfaces for methanol oxidation in alkaline solution.* Carbon, 2005. **43**(6): p. 1259-1264.

247. Banerjee, A., R. Theron, and R.W.J. Scott, *Design, synthesis, catalytic application, and strategic redispersion of plasmonic silver nanoparticles in ionic liquid media.* Journal of Molecular Catalysis a-Chemical, 2014. **393**: p. 105-111.

248. McFarland, A.D. and R.P. Van Duyne, *Single silver nanoparticles as real-time optical sensors with zeptomole sensitivity.* Nano Letters, 2003. **3**(8): p. 1057-1062.

249. Lee, K.S. and M.A. El-Sayed, *Gold and silver nanoparticles in sensing and imaging: Sensitivity of plasmon response to size, shape, and metal composition.* Journal of Physical Chemistry B, 2006. **110**(39): p. 19220-19225.

250. Isse, A.A., et al., *Relevance of electron transfer mechanism in electrocatalysis: the reduction of organic halides at silver electrodes.* Chemical Communications, 2006(3): p. 344-346.

251. Isse, A.A., et al., *Electrocatalysis and electron transfer mechanisms in the reduction of organic halides at Ag.* Journal of Applied Electrochemistry, 2009. **39**(11): p. 2217-2225.

252. Tang, L., et al., *Electrochemical Stability of Elemental Metal Nanoparticles.* Journal of the American Chemical Society, 2010. **132**(33): p. 11722-11726.

253. Singh, G., et al., *Measurement Methods to Detect, Characterize, and Quantify Engineered Nanomaterials in Foods.* Comprehensive Reviews in Food Science and Food Safety, 2014. **13**(4): p. 693-704.

254. Safavi, A., N. Maleki, and E. Farjami, *Electrodeposited Silver Nanoparticles on Carbon Ionic Liquid Electrode for Electrocatalytic Sensing of Hydrogen Peroxide.* Electroanalysis, 2009. **21**(13): p. 1533-1538.

255. Raj, S., P. Rai, and Y.-T. Yu, *Pulse electrophoresis deposition of Ag@SiO2 core-shell nanoparticles on FTO substrate.* Materials Letters, 2014. **117**: p. 116-119.

256. Zuo, J., *Deposition of Ag nanostructures on TiO2 thin films by RF magnetron sputtering.* Applied Surface Science, 2010. **256**(23): p. 7096-7101.

257. Nepijko, S.A., et al., *Growth of rodlike silver nanoparticles by vapor deposition of small clusters.* Chemphyschem, 2000. **1**(3): p. 140-+.

258. Nelson, G.W. and J.S. Foord, *Nanoparticle-Based Diamond Electrodes*, in *Novel Aspects of Diamond*, N. **Yang**, Editor. 2015, Springer. p. 165-204.

259. Kraft, A., *Doped diamond: A compact review on a new, versatile electrode material.* International Journal of Electrochemical Science, 2007. **2**(5): p. 355-385.

260. Yang, N., *Novel Aspects of Diamond: From Growth to Applications*. Vol. 121. 2015, Switzerland: Springerlink International Publishing.

261. Scheludko, A. and M. Todorova, Bull. Acad. Bulg. Sci. Phys., 1952. **3**: p. 61.

262. Nalwa, H.S., *Deposition and Processing*. Vol. 5. 2002, USA: Academic Press. 419.

263. Haberland, H., et al., *Thin-films from energetic cluster impact-A feasibility study.* Journal of Vacuum Science & Technology a-Vacuum Surfaces and Films, 1992. **10**(5): p. 3266-3271.

264. *"Database of Emperically Derivied Atomic Sensitivity Factors", in: UK Surface Analysis Forum (1998) <http://www.uksaf.org/data/sfactors.html>*.

265. Thompson, W.T., et al., *Pourbaix Diagrams for Multielement Systems*. 2000, <st1:place w:st="on"><st1:country-region w:st="on">Canada</st1:country-region>: John Wiley & Sons, Inc.

266. *A. Scheludko and M, Todorova, Izv. Bulg. Akad. Nauk. Ser. Phys. 3 (1952) 61.*

267. Liu, H., et al., *Size-selective electrodeposition of meso-scale metal particles: a general method.* Electrochimica Acta, 2001. **47**(5): p. 671-677.

268. Sandmann, G., H. Dietz, and W. Plieth, *Preparation of silver nanoparticles on ITO surfaces by a double-pulse method.* Journal of Electroanalytical Chemistry, 2000. **491**(1-2): p. 78-86.

269. *Mantis Deposition Limited, Oxford, Uk. http://www.mantisdeposition.com*.

270. Chen, Y.W.H.L.C., *Thermodynamics versus Kinetics in Nanosynthesis.* Angewandte Chemie International Edition, 2014.

271. Toh, H.S., et al., *The anodic stripping voltammetry of nanoparticles: electrochemical evidence for the surface agglomeration of silver nanoparticles.* Nanoscale, 2013. **5**(11): p. 4884-4893.

272. Moulder, F.F., W.F. Stickle, and P.E. Sobel, *Handbook of Photoelectron Spectroscopy*. 2003: Perkin-Elmer, Physical Electronics Division.

273. Briggs, D. and J.T. Grant, *"Polymer C1s Chemical Shifts", in: Surface Analysis by Auger and X-ray Photoelectron Spectroscopy*. 2003, Charlton, UK: IM Publications.

274. Wagner, C.D., A.V. Naumkin, and A. Kraut-Vass, *NIST X-ray Photoelectron Spectroscopy Database, in: N.I.o.S.a.T. (NIST) (Ed.)*. 2007, Washington, USA: Secretary of Commerce.

275. Wang, H., et al., *Electrochemical Determination of Tetracycline Using Molecularly Imprinted Polymer Modified Carbon Nanotube-Gold Nanoparticles Electrode.* Electroanalysis, 2011. **23**(8): p. 1863-1869.

276. Xie, F., et al., *Nanoscale control of Ag nanostructures for plasmonic fluorescence enhancement of near-infrared dyes.* Nano Research, 2013. **6**(7): p. 496-510.

277. Solomon, S.D., et al., *Synthesis and study of silver nanoparticles.* Journal of Chemical Education, 2007. **84**(2): p. 322-325.

278. Levard, C., et al., *Environmental Transformations of Silver Nanoparticles: Impact on Stability and Toxicity.* Environmental Science & Technology, 2012. **46**(13): p. 6900-6914.

279. De Carlo, S. and J.R. Harris, *Negative staining and cryo-negative staining of macromolecules and viruses for TEM.* Micron, 2011. **42**(2): p. 117-131.

280. Hammouda, B., *A new Guinier-Porod model.* Journal of Applied Crystallography, 2010. **43**: p. 716-719.

281. Demaurex, N., *pH homeostasis of cellular organelles.* News in Physiological Sciences, 2002. **17**: p. 1-5.

282. Cedervall, T., et al., *Understanding the nanoparticle-protein corona using methods to quantify exchange rates and affinities of proteins for nanoparticles.* Proceedings of the National Academy of Sciences of the United States of America, 2007. **104**(7): p. 2050-2055.

283. Leonenko, Z.V., et al., *Investigation of temperature-induced phase transitions in DOPC and DPPC phospholipid bilayers using temperature-controlled scanning force microscopy.* Biophys J, 2004. **86**(6): p. 3783-93.

284. Hayat, M.A., *Principles and Techniques of Electron Microscopy Biological Applications*. 4th ed. 2000: Cambridge University Press. 545.

285. Chen, K.L. and M. Elimelech, *Influence of humic acid on the aggregation kinetics of fullerene (C60) nanoparticles in monovalent and divalent electrolyte solutions.* Journal of Colloid and Interface Science, 2007. **309**(1): p. 126-134.

286. Avena, M.J., A.W.P. Vermeer, and L.K. Koopal, *Volume and structure of humic acids studied by viscometry pH and electrolyte concentration effects.* Colloids and Surfaces a-Physicochemical and Engineering Aspects, 1999. **151**(1-2): p. 213-224.

287. Takeno, N., *Atlas of Eh-pH Diagrams*, in *Geological Survey of Japan Report*. May 2005.

288. Zhang, W., et al., *Influence of dissolved oxygen on aggregation kinetics of citrate-coated silver nanoparticles.* Environmental Pollution, 2011. **159**(12): p. 3757-3762.

289. Bae, E., et al., *Bacteria cytotoxicity of the silver nanoparticle related to physicochemical metrics and agglomeration properties.* Environmental Toxicology and Chemistry, 2010. **29**(10): p. 2154-2160.

290. Gebel, E., *The Mysterious Fates of Nanoparticles: ES&T's Top Feature Article 2012.* Environ. Sci. Technol., 2013.

291. Damm, C. and H. Munstedt, *Kinetic aspects of the silver ion release from antimicrobial polyamide/silver nanocomposites.* Applied Physics a-Materials Science & Processing, 2008. **91**(3): p. 479-486.

292. French, R.A., et al., *Influence of Ionic Strength, pH, and Cation Valence on Aggregation Kinetics of Titanium Dioxide Nanoparticles.* Environmental Science & Technology, 2009. **43**(5): p. 1354-1359.

293. Lead, J.R., et al., *Determination of diffusion coefficients of humic substances by fluorescence correlation spectroscopy: Role of solution conditions.* Environmental Science & Technology, 2000. **34**(7): p. 1365-1369.

294. Olenin, A.Y., et al., *Formation of surface layers on silver nanoparticles in aqueous and water-organic media.* Colloid Journal, 2008. **70**(1): p. 71-76.

295. Ball, R.C., et al., *Universal kinetics in reaction-limited aggregation.* Physical Review Letters, 1987. **58**(3): p. 274-277.

296. Chen, K.L. and M. Elimelech, *Aggregation and deposition kinetics of fullerene (C-60) nanoparticles.* Langmuir, 2006. **22**(26): p. 10994-11001.

297. Derjaguin, B.V. and L. Landau, *Theory of the stability of strongly charged lyophobic sols and of the adhesion of strongly charged particles in solution of electrolytes.* Acta Physicochimica (USSR), 1941. **14**: p. 633.

298. Verwey, E.J.W. and J.T.G. Overbeek, *Theory of the stability of lyophobic colloids*. 1948, Amsterdam: Elsevier.

299. Petosa, A.R., et al., *Aggregation and Deposition of Engineered Nanomaterials in Aquatic Environments: Role of Physicochemical Interactions.* Environmental Science & Technology, 2010. **44**(17): p. 6532-6549.

300. Sperling, R.A. and Parak, W.J., *Surface modification, functionalization and bioconjugation of colloidal inorganic nanoparticles.* Phil. Trans. R. Soc. A, 2009. **368**: p. 1333–1383.

301. Phenrat, T., et al., *Stabilization of aqueous nanoscale zerovalent iron dispersions by anionic polyelectrolytes: adsorbed anionic polyelectrolyte layer properties and their effect on aggregation and sedimentation.* J Nanopart Res, 2008. **10**: p. 795–814.

302. Chibowski, E., A. Szczes, and L. Holysz, *Changes of zeta potential and particles size of silica caused by DPPC adsorption and enzyme phospholipase A(2) presence.* Adsorption-Journal of the International Adsorption Society, 2010. **16**(4-5): p. 305-312.

303. Langner, M. and K. Kubica, *The electrostatics of lipid surfaces.* Chemistry and Physics of Lipids, 1999. **101**: p. 3-35.

304. Jones, M.N., *The surface-properties of phospholipid liposome systems and their characterization.* Advances in Colloid and Interface Science, 1995. **54**: p. 93-128.

305. Mashaghi, A., et al., *Hydration strongly affects the molecular and electronic structure of membrane phospholipids.* Journal of Chemical Physics, 2012. **136**(11).

306. Mashaghi, A., et al., *Interfacial Water Facilitates Energy Transfer by Inducing Extended Vibrations in Membrane Lipids.* Journal of Physical Chemistry B, 2012. **116**(22): p. 6455-6460.

307. Porter, D., et al., *A compatible medium for nanoparticle dispersion.* Nanotoxicology, 2008. **2**: p. 144-154.

308. Kwon, J.Y., P. Koedrith, and Y.R. Seo, *Current investigations into the genotoxicity of zinc oxide and silica nanoparticles in mammalian models in vitro and in vivo:*

carcinogenic/genotoxic potential, relevant mechanisms and biomarkers, artifacts, and limitations. International Journal of Nanomedicine, 2014. **9**: p. 271-286.

309. Roemer, I., et al., *Aggregation and dispersion of silver nanoparticles in exposure media for aquatic toxicity tests.* Journal of Chromatography A, 2011. **1218**(27): p. 4226-4233.

310. Tejamaya, M., et al., *Stability of Citrate, PVP, and PEG Coated Silver Nanoparticles in Ecotoxicology Media.* Environmental Science & Technology, 2012. **46**(13): p. 7011-7017.

311. Tolaymat, T.M., et al., *An evidence-based environmental perspective of manufactured silver nanoparticle in syntheses and applications: A systematic review and critical appraisal of peer-reviewed scientific papers.* Science of the Total Environment, 2010. **408**(5): p. 999-1006.

312. Huynh, K.A. and K.L. Chen, *Aggregation Kinetics of Citrate and Polyvinylpyrrolidone Coated Silver Nanoparticles in Monovalent and Divalent Electrolyte Solutions.* Environmental Science & Technology, 2011. **45**(13): p. 5564-5571.

313. Hanley, C., et al., *The Influences of Cell Type and ZnO Nanoparticle Size on Immune Cell Cytotoxicity and Cytokine Induction.* Nanoscale Research Letters, 2009. **4**(12): p. 1409-1420.

314. Carlson, C., et al., *Unique Cellular Interaction of Silver Nanoparticles: Size-Dependent Generation of Reactive Oxygen Species.* Journal of Physical Chemistry B, 2008. **112**(43): p. 13608-13619.

315. Foldbjerg, R., et al., *PVP-coated silver nanoparticles and silver ions induce reactive oxygen species, apoptosis and necrosis in THP-1 monocytes.* Toxicology Letters, 2009. **190**(2): p. 156-162.

316. Hussain, S.M., et al., *In vitro toxicity of nanoparticles in BRL 3A rat liver cells.* Toxicology in Vitro, 2005. **19**(7): p. 975-983.

317. Park, S., et al., *Cellular toxicity of various inhalable metal nanoparticles on human alveolar epithelial cells.* Inhalation Toxicology, 2007. **19**: p. 59-65.

318. Righi, M., et al., *Monokine production by microglial cell clones.* Eur J Immunol, 1989. **19**(8): p. 1443-8.

319. Bulgarelli, I., et al., *Desacyl-ghrelin and synthetic GH-secretagogues modulate the production of inflammatory cytokines in mouse microglia cells stimulated by beta-amyloid fibrils.* J Neurosci Res, 2009. **87**(12): p. 2718-27.

320. Bureau, G., F. Longpre, and M.G. Martinoli, *Resveratrol and quercetin, two natural polyphenols, reduce apoptotic neuronal cell death induced by neuroinflammation.* J Neurosci Res, 2008. **86**(2): p. 403-10.

321. Chang, L.C., et al., *Inhibition of nitric oxide production by the carbazole compound LCY-2-CHO via blockade of activator protein-1 and CCAAT/enhancer-binding protein activation in microglia.* Biochem Pharmacol, 2008. **76**(4): p. 507-19.

322. Lacerda, L., et al., *Translocation mechanisms of chemically functionalised carbon nanotubes across plasma membranes.* Biomaterials, 2012. **33**(11): p. 3334-3343.

323. Leblanc, G.A., et al., *The influence of speciation on the toxicity of silver to fathead minnow (Phmephalespromelas).* Environmental Toxicology and Chemistry, 1984. **3**(1): p. 37-46.

324. Kraft, M.L. and H.A. Klitzing, *Imaging lipids with secondary ion mass spectrometry.* Biochimica Et Biophysica Acta-Molecular and Cell Biology of Lipids, 2014. **1841**(8): p. 1108-1119.

325. Touboul, D. and A. Brunelle, *TOF-SIMS Imaging of Lipids on Rat Brain Sections.* Methods in molecular biology (Clifton, N.J.), 2015. **1203**: p. 21-7.

326. Hanrieder, J., et al., *Time-of-Flight Secondary Ion Mass Spectrometry Based Molecular Histology of Human Spinal Cord Tissue and Motor Neurons.* Analytical Chemistry, 2013. **85**(18): p. 8741-8748.

327. Sole-Domenech, S., et al., *Localization of cholesterol, amyloid and glia in Alzheimer's disease transgenic mouse brain tissue using time-of-flight secondary ion mass spectrometry (ToF-SIMS) and immunofluorescence imaging.* Acta Neuropathologica, 2013. **125**(1): p. 145-157.

328. Lee, C.-Y., et al., *Fluorescence, XPS, and TOF-SIMS surface chemical state image analysis of DNA microarrays.* Journal of the American Chemical Society, 2007. **129**(30): p. 9429-9438.

329. Geier, F.M., et al., *ToF-SIMS analysis of biomolecules in the model organism Caenorhabditis elegans.* Surface and Interface Analysis, 2013. **45**(1): p. 234-236.

330. Woodland, S.J., et al., *Accurate measurement of silver isotopic compositions in geological materials including low Pd/Ag meteorites.* Geochimica Et Cosmochimica Acta, 2005. **69**(8): p. 2153-2163.

331. Jones, E.A., et al., *ToF-SIMS analysis of bio-systems: Are polyatomic primary ions the solution?* Applied Surface Science, 2006. **252**(19): p. 6844-6854.

332. Braun, R.M., et al., *Spatially resolved detection of attomole quantities of organic molecules localized in picoliter vials using time-of-flight secondary ion mass spectrometry.* Analytical Chemistry, 1999. **71**(16): p. 3318-3324.

333. Wittmaack, K., *Unified explanation for secondary-ion yields and mechanism of the SIMS matrix effect-comment..* Journal of Applied Physics, 1981. **52**(1): p. 527-529.

334. Vickerman, J.C. and D. Briggs, *ToF-SIMS: Materials Analysis by Mass Spectrometry*. 2013: IM Publications, 2013.

335. Delcorte, A., et al., *Sample metallization for performance improvement in desorption/ionization of kilodalton molecules: Quantitative evaluation, imaging secondary ion MS, and laser ablation.* Analytical Chemistry, 2003. **75**(24): p. 6875-6885.

336. Delcorte, A., N. Medard, and P. Bertrand, *Organic secondary ion mass spectrometry: Sensitivity enhancement by gold deposition.* Analytical Chemistry, 2002. **74**(19): p. 4955-4968.

337. Adriaensen, L., F. Vangaever, and R. Gijbels, *Metal-assisted secondary ion mass spectrometry: Influence of Ag and Au deposition on molecular ion yields.* Analytical Chemistry, 2004. **76**(22): p. 6777-6785.

338. Hagenhoff, B., *SurfaceSpectra and IM: Chichester*, in *ToF-SIMS: surface analysis by mass spectrometry*, J.C. Vickerman and D. Briggs, Eds., Editors. 2001. p. 293.

339. Delcorte, A., et al., *Kiloelectronvolt particle-induced emission and fragmentation of polystyrene molecules adsorbed on silver: Insights from molecular dynamics.* Journal of Physical Chemistry B, 2000. **104**(12): p. 2673-2691.

340. Nygren, H., et al., *A cell preparation method allowing subcellular localization of cholesterol and phosphocholine with imaging TOF-SIMS.* Colloids and Surfaces B-Biointerfaces, 2003. **30**(1-2): p. 87-92.

341. Mahoney, C.M., *Cluster secondary ion mass spectrometry of polymers and related materials.* Mass Spectrometry Reviews, 2010. **29**(2): p. 247-293.

342. Magnusson, Y., et al., *Lipid imaging of human skeletal muscle using TOF-SIMS with bismuth cluster ion as a primary ion source.* Clinical Physiology and Functional Imaging, 2008. **28**(3): p. 202-209.

343. Weibel, D., et al., *A C-60 primary ion beam system for time of flight secondary ion mass spectrometry: Its development and secondary ion yield characteristics.* Analytical Chemistry, 2003. **75**(7): p. 1754-1764.

344. Ranft, U., et al., *Long-term exposure to traffic-related particulate matter impairs cognitive function in the elderly.* Environmental Research, 2009. **109**(8): p. 1004-1011.

345. Li, X., et al., *SiO2 nanoparticles change colour preference and cause Parkinson's-like behaviour in zebrafish.* Scientific Reports, 2014. **4**.

346. An, L., et al., *Cognitive impairment in rats induced by nano-CuO and its possible mechanisms.* Toxicology Letters, 2012. **213**(2): p. 220-227.

347. Yin, N., et al., *Silver Nanoparticle Exposure Attenuates the Viability of Rat Cerebellum Granule Cells through Apoptosis Coupled to Oxidative Stress.* Small, 2013. **9**(9-10): p. 1831-1841.

348. Ehringer, H. and O. Hornykiewicz, *Distribution of noradrenaline and dopamine (3-hydroxytyramine) in the human brain and their behavior in diseases of the extrapyramidal system.* Klinische Wochenschrift, 1960. **38**: p. 1236-9.

349. Ahlberg, S., et al., *PVP-coated, negatively charged silver nanoparticles: A multi-center study of their physicochemical characteristics, cell culture and in vivo experiments.* Beilstein Journal of Nanotechnology, 2014. **5**: p. 1944-1965.

350. Xu, F., et al., *Silver nanoparticles (AgNPs) cause degeneration of cytoskeleton and disrupt synaptic machinery of cultured cortical neurons.* Molecular Brain, 2013. **6**.

351. Dufton, N., et al., *Hydrogen sulfide and resolution of acute inflammation: A comparative study utilizing a novel fluorescent probe.* Scientific Reports, 2012. **2**.

352. Du, C., et al., *Downregulation of cystathionine beta-synthase/hydrogen sulfide contributes to rotenone-induced microglia polarization toward M1 type.* Biochemical and Biophysical Research Communications, 2014. **451**(2): p. 239-245.

353. Li, L., P. Rose, and P.K. Moore, *Hydrogen Sulfide and Cell Signaling.* Annual Review of Pharmacology and Toxicology, Vol 51, 2011, 2011. **51**: p. 169-187.

354. Lee Predmore, B., D. Joseph Lefer, and G. Gojon, *Hydrogen Sulfide in Biochemistry and Medicine.* Antioxidants & Redox Signaling, 2012. **17**(1): p. 119-140.

355. Sen, N., et al., *Hydrogen Sulfide-Linked Sulfhydration of NF-kappa B Mediates Its Antiapoptotic Actions.* Molecular Cell, 2012. **45**(1): p. 13-24.

356. Soderstjerna, E., et al., *Silver and Gold Nanoparticles Exposure to In Vitro Cultured Retina - Studies on Nanoparticle Internalization, Apoptosis, Oxidative Stress, Glial- and Microglial Activity.* Plos One, 2014. **9**(8).

357. Lansdown, A.B.G., et al., *Silver aids healing in the sterile skin wound: experimental studies in the laboratory rat.* British Journal of Dermatology, 1997. **137**(5): p. 728-735.

358. Sharonova, I.N., V.S. Vorobjev, and H.L. Haas, *Interaction between copper and zinc at GABA(A) receptors in acutely isolated cerebellar Purkinje cells of the rat.* British Journal of Pharmacology, 2000. **130**(4): p. 851-856.

359. Lazarczyk, M. and M. Favre, *Role of Zn(2+) Ions in Host-Virus Interactions.* Journal of Virology, 2008. **82**(23): p. 11486-11494.

360. Thirumoorthy, N., et al., *A Review of Metallothionein Isoforms and their Role in Pathophysiology.* World Journal of Surgical Oncology, 2011. **9**.

361. McCord, M.C. and E. Aizenman, *The role of intracellular zinc release in aging, oxidative stress, and Alzheimer's disease.* Frontiers in Aging Neuroscience, 2014. **6**.

362. Min, K.-S., *The physiological significance of metallothionein in oxidative stress.* Yakugaku Zasshi-Journal of the Pharmaceutical Society of Japan, 2007. **127**(4): p. 695-702.

363. Luther, E.M., et al., *Upregulation of Metallothioneins After Exposure of Cultured Primary Astrocytes to Silver Nanoparticles.* Neurochemical Research, 2012. **37**(8): p. 1639-1648.

364. Saydam, N., et al., *Heat and heavy metal stress synergize to mediate transcriptional hyperactivation by metal-responsive transcription factor MTF-1.* Journal of Biological Chemistry, 2003. **278**(34): p. 31879-31883.

365. Heuchel, R., et al., *The transcription factor MTF-1 is essential for basal and heavy metal-induced metallothionein gene-expression.* Embo Journal, 1994. **13**(12): p. 2870-2875.

366. Min, K.S., *The Physiological Significance of Metallothionein in Oxidative Stress*. 2006: The Pharmaceutical Society of Japan.

367. Kida, K., et al., *Inhaled Hydrogen Sulfide Prevents Neurodegeneration and Movement Disorder in a Mouse Model of Parkinson's Disease.* Antioxidants & Redox Signaling, 2011. **15**(2): p. 343-352.

368. Abe, K. and H. Kimura, *Hydrogen Sulfide: Its production and functions.* J. Neurosci., 1996. **16**: p. 1066-1071.

369. Tambuyzer, B.R., P. Ponsaerts, and E.J. Nouwen, *Microglia: gatekeepers of central nervous system immunology.* Journal of Leukocyte Biology, 2009. **85**(3): p. 352-370.

370. Oshiro, S., et al., *Glial cells contribute more to iron and aluminum accumulation but are more resistant to oxidative stress than neuronal cells.* Biochimica Et Biophysica Acta-Molecular Basis of Disease, 2000. **1502**(3): p. 405-414.

Appendices

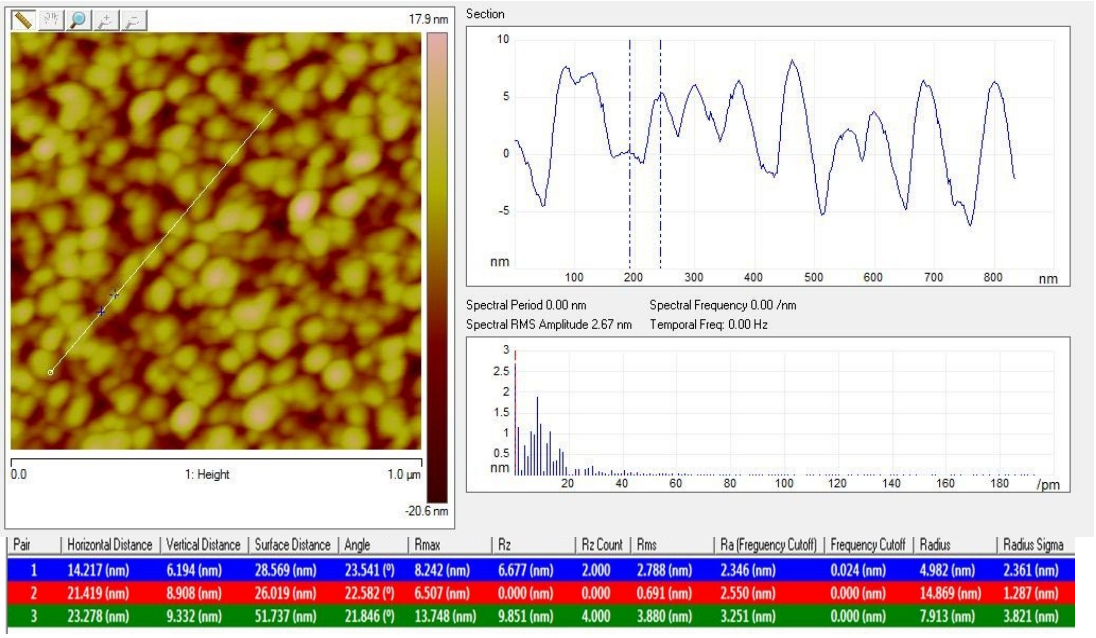

Pair	Horizontal Distance	Vertical Distance	Surface Distance	Angle	Rmax	Rz	Rz Count	Rms	Ra (Frequency Cutoff)	Frequency Cutoff	Radius	Radius Sigma
1	14.217 (nm)	6.194 (nm)	28.569 (nm)	23.541 (°)	8.242 (nm)	6.677 (nm)	2.000	2.788 (nm)	2.346 (nm)	0.024 (nm)	4.982 (nm)	2.361 (nm)
2	21.419 (nm)	8.908 (nm)	26.019 (nm)	22.582 (°)	6.507 (nm)	0.000 (nm)	0.000	0.691 (nm)	2.550 (nm)	0.000 (nm)	14.869 (nm)	1.287 (nm)
3	23.278 (nm)	9.332 (nm)	51.737 (nm)	21.846 (°)	13.748 (nm)	9.851 (nm)	4.000	3.880 (nm)	3.251 (nm)	0.000 (nm)	7.913 (nm)	3.821 (nm)

Fig. S1: AFM and height profile of AgNPs synthesised *via* magnetron sputtering with size-filtering at 5 nm. The average height of NPs is 7.0 ±1.9 nm calculated using Image J (n= 30).

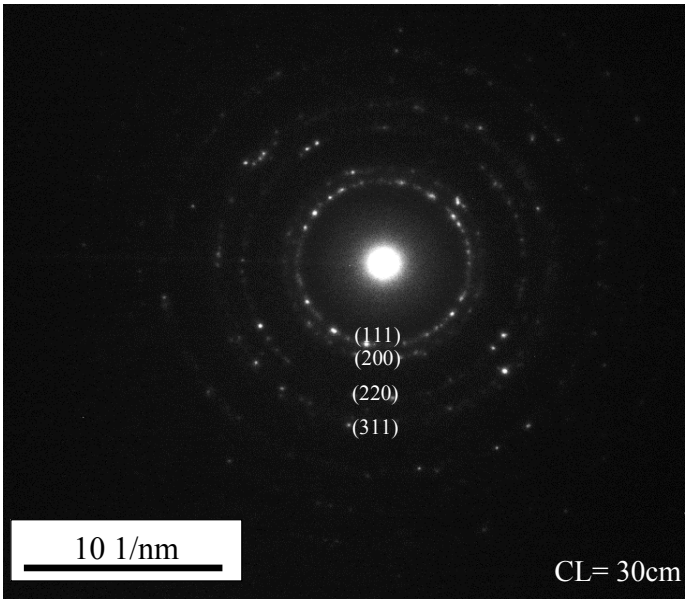

Fig. S2: Indexed selected area electron diffraction (SAED) patterns of AgNPs incubated in DI water. The selective aperture size used was 100 nm in diameter.

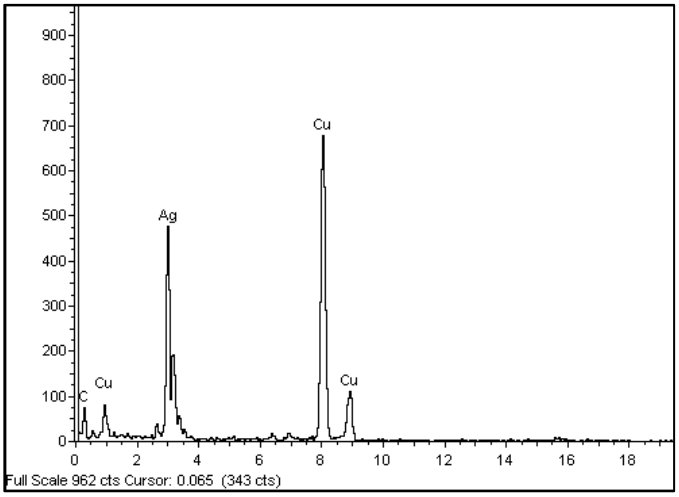

Fig. S3: EDS spectrum of as – synthesised 20 nm AgNPs.

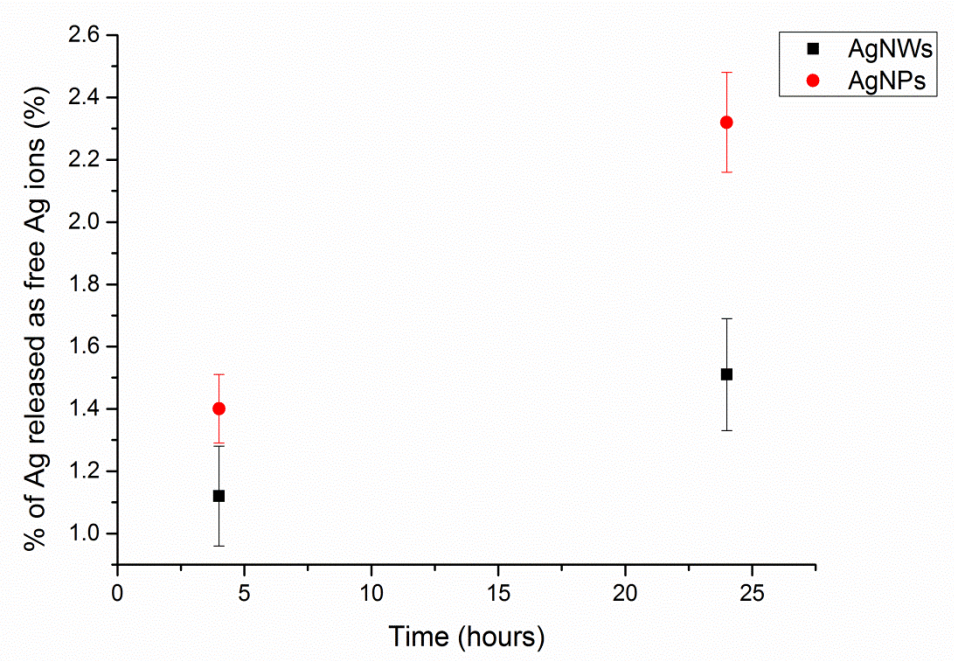

Fig. S4: ICP-OES analysis to assess the amount of free Ag^{+} ions released from AgNMs in non-interacting perchlorate buffer solution (pH 5).

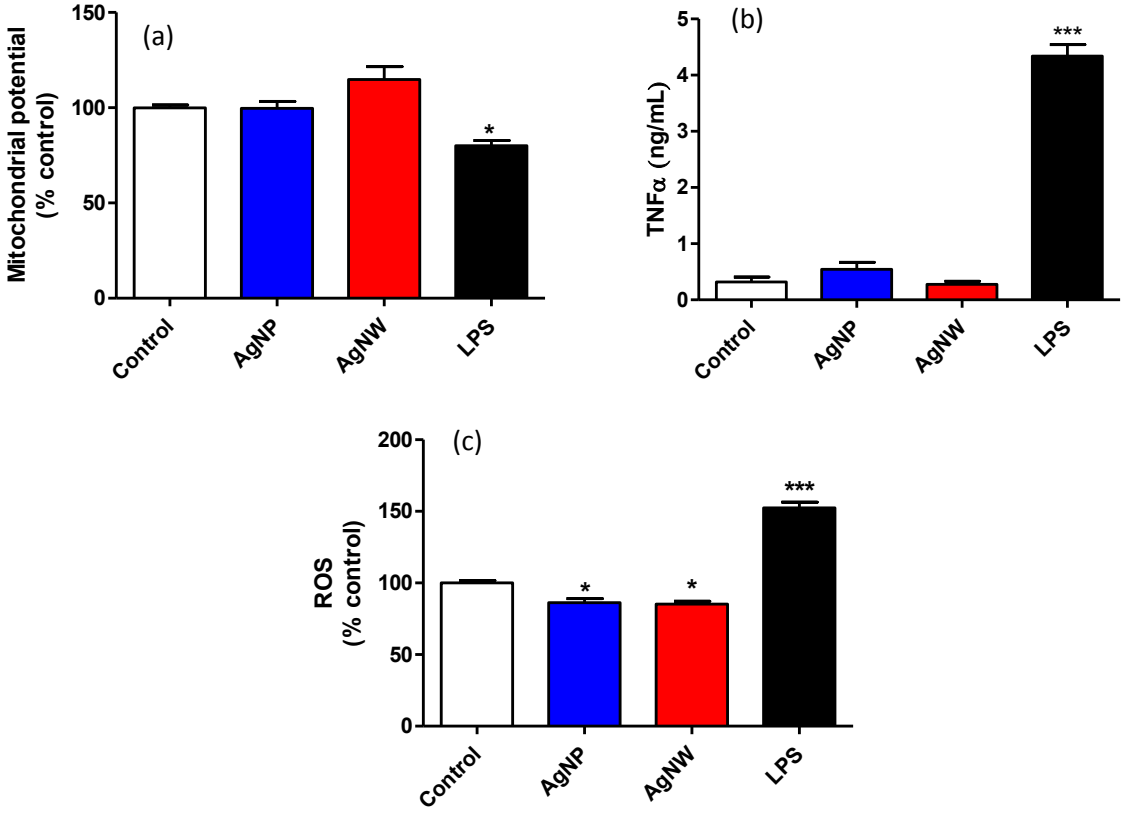

Fig. S5: (a) Mitochondria membrane potential (MMP), (b) ROS generation and (c) release of TNF-α in microglia cells after treated with AgNPs/AgNWs for 1 h, followed with rinsing and then left cells for 24 h before assessing the toxicity (n = 3 replicates).

Table S1: List of ligands which are found in the CBS enzyme structures (source: European Protein Data Bank)

Cystathionine-β-synthase (CBS) (Enzyme Commission number, EC 4.2.1.22)

LIGAND	**FORMULA**	**SYSTEMATIC NAME**
PLP	$C_8 H_{10} N O_6 P$	PYRIDOXAL-5'-PHOSPHATE
HEM	$C_{34} H_{32} Fe N_4 O_4$	PROTOPORPHYRIN IX CONTAINING FE
NA	Na	SODIUM ION
MPD	$C_6 H_{14} O_2$	(4S)-2-METHYL-2, 4-PENTANEDIOL
ACT	$C_2 H_3 O_2$	ACETATE ION
PE4	$C_{16} H_{34} O_8$	2-(2-[2-(2-(2-[2-(2-ETHOXY-ETHOXY)-ETHOXY]-ETHOXY-ETHOXY)-ETHOXY]-ETHOXY)-ETHANOL
KOU	$C_{11} H_{15} N_2 O_8 P$	(E)-N-((3-hydroxy-2-methyl-5-[(phosphonooxy)methyl]pyridin-4-yl)methylidene)-L-serine
SEP	$C_3 H_8 N O_6 P$	PHOSPHOSERINE
P1T	$C_{11} H_{15} N_2 O_7 P$	2-[((3-HYDROXY-2-METHYL-5-[(PHOSPHONOOXY)METHYL]PYRIDIN-4-YL)METHYL)AMINO]ACRYLIC ACID
EDO	$C_2 H_6 O_2$	1,2-ETHANEDIOL
OAS	$C_5 H_9 N O_4$	O-ACETYLSERINE

Table S2: List of ligands which are found in the CSE enzyme structures (source: European Protein Data Bank).

Cystathionine ϒ-lyase (CSE) (EC 4.4.1.1)

LIGAND	FORMULA	SYSTEMATIC_NAME
GOL	$C_3 H_8 O_3$	GLYCEROL
PLP	$C_8 H_{10} N O_6 P$	PYRIDOXAL-5'-PHOSPHATE
0JO	$C_{11} H_{13} N_2 O_7 P$	2-{[(E)-{3-hydroxy-2-methyl-5-[(phosphonooxy)methyl]pyridin-4-yl}methylidene]amino}prop-2-enoic acid
SO4	$O_4 S$	SULFATE ION
SER	$C_3 H_7 N O_3$	SERINE
PYR	$C_3 H_4 O_3$	PYRUVIC ACID
NAK	$C_3 H_5 N O_2$	AMINO-ACRYLATE
KOU	$C_{11} H_{15} N_2 O_8 P$	(E)-N-({3-hydroxy-2-methyl-5-[(phosphonooxy)methyl]pyridin-4-yl}methylidene)-L-serine
2AG	$C_5 H_9 N O_2$	(2S)-2-aminopent-4-enoic acid
NO3	$N O_3$	NITRATE ION
PEG	$C_4 H_{10} O_3$	DI(HYDROXYETHYL)ETHER
BCT	$C H O_3$	BICARBONATE ION
BME	$C_2 H_6 O S$	BETA-MERCAPTOETHANOL
CO3	$C O_3$	CARBONATE ION

Table S3: List of ligands which are found in the MPST enzyme structures (source: European Protein Data Bank).

3-mercaptopyruvate sulfurtransferase (MPST**)** (EC 2.8.2.1)

LIGAND	FORMULA	SYSTEMATIC_NAME
GOL	C3 H8 O3	GLYCEROL
SO4	$O_4 S$	SULFATE ION
PYR	$C_3 H_4 O_3$	PYRUVIC ACID